

Copyright
By
Mariana Costa Dionisio
2010

**The Dissertation Committee for Mariana Costa Dionisio
certifies that this is the approved version of the following dissertation:**

The Characterization of Regional Ozone Transport

Committee:

David T. Allen, Supervisor

Elena McDonald-Buller

Roger T. Bonnecaze

Michael E. Webber

Thomas F. Edgar

The Characterization of Regional Ozone Transport

by

Mariana Costa Dionisio, B.S.

Dissertation

Presented to the Faculty of the Graduate School of

The University of Texas at Austin

in Partial Fulfillment

of the Requirements

for the Degree of

Doctor of Philosophy

The University of Texas at Austin

May, 2010

Dedication

This dissertation is dedicated to my family for their continuous love and encouragement.

Acknowledgements

I would like to express sincere gratitude to my advisor, Dr. David T. Allen, for his continuous guidance and support. I am also deeply grateful for the dedicated assistance and advice of Dr. Elena McDonald-Buller.

I would like to extend sincere and special gratitude to Dr. Dave Sullivan, Gary McGaughey, and Dr. Yosuke Kimura for all of their combined diligent assistance and support, which made my work possible. A special thank you is also extended to my friends at the Center for Energy and Environmental Resources.

I deeply thank my family for their unconditional love, encouragement, and support.

The Characterization of Regional Ozone Transport

Mariana Costa Dionisio, Ph.D.

The University of Texas at Austin, 2010

Supervisor: David T. Allen

Among the most ubiquitous and persistent air quality problems facing urban areas are high concentrations of gas phase oxidants and fine particulate matter. Ozone and particulate matter concentrations in urban areas are significantly influenced by other factors in addition to local emissions, such as regional transport spanning distances as large as 1000 kilometers. Despite the importance of regional transport in meeting air quality standards, to date most analyses of regional transport have focused only on short duration episodes, or semi-quantitative assessments. The development and evaluation of seasonal, quantitative assessments of regional pollutant transport, based on modeling calculations and observational data is the topic of this dissertation.

The observational data available through the Texas Air Quality Studies in 2000 and 2006 provide a unique opportunity to develop, evaluate, and improve methods for characterizing regional air pollutant transport. Measurements collected during these studies are used as the primary observational basis for characterizing regional ozone transport and to evaluate the performance of photochemical models. Results suggest that measurements (from aircraft and surface monitors) and the photochemical model provide consistent estimates of the magnitude of ozone transport. On this basis, photochemical modeling is used to determine potential impacts of regional ozone transport in Texas, under varying meteorological and photochemical conditions, as well as to characterize the dominant chemical and physical processes within urban plumes.

While qualitative studies and limited quantitative analyses have been performed to assess regional ozone transport, this work includes the first detailed quantitative characterization of the importance of ozone transport over the course of an entire ozone season using both photochemical modeling and ambient data. Results demonstrate that

urban plumes in Texas are capable of transporting significant amounts of ozone over distances spanning hundreds of kilometers. Furthermore, on a seasonal basis, there are a number of days characterized by high contributions from inter-city transport coinciding with high total ozone concentrations, suggesting that the role of inter-city transport will remain significant for many areas to demonstrate attainment of the NAAQS for ozone. Results also indicate that reductions in the impacts of inter-city transport are possible by decreases in emissions from source regions.

Table of Contents

List of Tables	xii
List of Figures	xxi
Chapter 1: Introduction	1
1.1 References.....	6
Chapter 2: Literature Review	7
2.1 Introduction.....	7
2.2 Ozone Formation	7
2.3 Surface Monitoring Data.....	12
2.4 Aircraft LIDAR Data	15
2.5 Satellite Data.....	18
2.6 Back Trajectory Analyses.....	18
2.7 Photochemical Modeling Techniques.....	28
2.8 The Impact of Ozone Transport on Federal Air Quality Policy	37
2.9 References.....	39
Chapter 3: Assessing the Magnitude of Regional Ozone Transport on a Seasonal Basis: Photochemical Modeling*	44
3.1 Introduction.....	44
3.2 Methodology	46
3.2.1 Description of the Photochemical Model	46
3.2.2 CAMx 2002 Seasonal Model Description and Inputs	49
3.2.3 CAMx 2006 Model Description and Inputs.....	51
3.3 Results.....	56
3.3.1 CAMx Seasonal Episode: May 1 st to September 30 th , 2002.....	56
3.3.2 Photochemical Modeling Results for 2006.....	66
3.4 Conclusions.....	75
3.5 References.....	77
Chapter 4: Use of a Rural Monitoring Network and Photochemical Modeling to Characterize Regional Ozone Concentrations	78

4.1	Introduction.....	78
4.2	Rural Monitoring Network	79
4.3	Observed Regional Ozone Concentration Gradients	82
4.4	Diurnal Patterns of Rural Ozone Concentrations.....	87
4.5	Photochemical Model Description and Inputs	89
4.6	Comparison of Ambient Data to Photochemical Modeling Results.....	91
4.7	Photochemical Modeling NO _x Emissions Sensitivity Analyses	96
	4.7.1 CAMx Process Analysis Methodology	103
	4.7.2 CAMx Process Analysis Results	107
4.8	Implications of Diurnal Patterns of Rural Ozone Concentrations	116
4.9	Conclusions.....	119
4.10	References.....	121
Chapter 5: Intercomparison of Ambient Data and Photochemical Modeling to Characterize Pollutant Transport in Plumes		124
5.1	Introduction.....	124
5.2	Observational Characterizations of Ozone Transport: Data from Airborne LIDAR and Surface Monitors.....	125
	5.2.1 Ozone Flux Calculation Method with Surface Monitor Data	127
	5.2.2 Estimation of the Planetary Boundary Layer Height.....	129
	5.2.3 Estimation of the Horizontal Extent of the Urban Plume	133
	5.2.4 Estimation of Wind Speeds.....	136
	5.2.5 Estimation of Background and Downwind Ozone	140
5.3	Ozone Flux Calculation Results.....	141
	5.3.1 Example of Ozone Flux Calculation with Data from Surface Monitors.....	141
	5.3.2 Results of Ozone Flux Calculations with Data from Surface Monitors and LIDAR.....	147
5.4	Photochemical Modeling Datasets.....	148
	5.4.1 Ozone Flux Calculations with Photochemical Modeling Data ..	150
5.5	Conclusions.....	158
5.6	References.....	160
Chapter 6: Reconciling Modeling Approaches for Apportioning Regional Sources with Ambient Data.....		162

6.1	Introduction.....	162
6.2	Ozone Formation and Plume Characterization in Houston	163
6.3	Photochemical Model Description and Inputs.....	167
6.4	Aircraft LIDAR Datasets	168
6.5	CAMx Source Apportionment Methodology	169
6.6	CAMx Process Analysis Methodology.....	172
6.7	Process Analysis Results and Discussion	173
	6.7.1 Results for the Houston Ship Channel plume (Plume A)	175
	6.7.2 Results for the Texas City Plume (Plume B).....	182
	6.7.3 Analysis of Zero-order Decay.....	188
6.8	Source Apportionment Results and Discussion.....	196
6.9	Conclusions.....	203
6.10	References.....	204
Chapter 7: Recommendations for Future Work.....		206
7.1	Introduction.....	206
7.2	Future Work Recommendations for the Use of Ambient Data and Photochemical Modeling to Characterize Regional Ozone Concentrations.	207
7.3	Future Work Recommendations for the Use of Surface Monitors and Photochemical Modeling to Characterize Pollutant Transport in Plumes	207
7.4	Future Work Recommendations for Reconciling Modeling Approaches for Apportioning Regional Sources with Ambient Data	210
7.5	References.....	211
Appendix A: Vertical Grid Structures for CAMx 2002 and 2006 Simulations		212
A.1	References.....	214
Appendix B: Continued Analysis of Photochemical Modeling Results for May 1st - September 30th, 2002.....		215
B.1	References.....	222
Appendix C: Further Analysis of Photochemical Modeling Results for August 13th- September 15th, 2006.....		223
C.1	References.....	240

Appendix D: CAMx Process Analysis Results for September 6th, 2000	241
Appendix E: A Comparison of Airborne LIDAR and Surface Measurements of Ozone Concentrations on September 6th, 2000	245
E.1 References.....	254
Appendix F: Parameters of Ozone Flux Calculations Based on Data from Surface Monitors.....	255
F.1 Estimates of Background and Downwind Ozone and Wind Speeds	255
F.2 Estimates of Horizontal Plume Width	262
F.3 References.....	267
Bibliography	268
Vita	277

List of Tables

Table 2-1. Range of monthly 90 th percentile daily peak one-hour zone concentrations for four monitors near Houston-Galveston-Brazoria (TCEQ, 2009). The data shown is for May through September of each indicated year. Maximum values for each year are highlighted in boldface type.....	13
Table 2-2. Ozone flux estimates derived with airborne LIDAR measurements (Senff et al., 2007). Results for each day are shown for the flight transect corresponding to the highest calculated ozone flux.....	17
Table 2-3. Frequency of ozone transport events in Texas from Northeast/East continental origins (TCEQ, 2009).	25
Table 2-4. Average APCA contributions to 8-hour ozone exceedances in the DFW area during August 15 th -22 nd , 1999 (ENVIRON, 2004a).	32
Table 2-5. Results of simulations in which all anthropogenic emissions in Texas were set equal to zero (Webb et al., 2002).	33
Table 3-1. Dimensions of CAMx model grid domains and sub-domains (TCEQ, 2009a).	53
Table 3-2. Maximum and average values of maximum differences in 8-hour ozone concentrations (as calculated by Equation 3.1) and differences in peak 8-hour ozone concentrations (as calculated by Equation 3.2) between the CAMx base case and zero-out case. Results are based on modeling output from May 1 st -September 29 th , 2002.	58
Table 3-3. Correlations of CAMx zero-out maximum 8-hour ozone differences.	58
Table 3-4. Percentage of days with predicted maximum 8-hour ozone differences between the CAMx base case and zero-out scenario (as calculated by Equation 3.1) within the specified ranges. Results are included for 152 days within the CAMx modeling period of May 1 st -September 29 th , 2002.	60
Table 3-5. Percentage of days with predicted maximum 8-hour ozone differences between the CAMx base case and zero-out simulations (as calculated by Equation 3.1) within the specified ranges. Days included for each region (specified as “total days”) are characterized by local surface measurements of 8-hour ozone concentrations above 70 ppb during May 1 st -September 29 th , 2002.....	61

Table 3-6. Ambient and modeled maximum 8-hour ozone concentrations and maximum differences in 8-hour ozone concentrations between the CAMx base case and zero-out case (as calculated by Equation 3.1) for DFW. Results are shown for days with the ten highest ambient 8-hour ozone concentrations during May 1 st –September 29 th , 2002.....	62
Table 3-7. Ambient and modeled maximum 8-hour ozone concentrations and maximum differences in 8-hour ozone concentrations between the CAMx base case and zero-out case (as calculated by Equation 3.1) for Austin. Results are shown for days with the ten highest ambient 8-hour ozone concentrations during May 1 st –September 29 th , 2002.....	63
Table 3-8. Ambient and modeled maximum 8-hour ozone concentrations and maximum differences in 8-hour ozone concentrations between the CAMx base case and zero-out case (as calculated by Equation 3.1) for San Antonio. Results are shown for days with the ten highest ambient 8-hour ozone concentrations during May 1 st –September 29 th , 2002.....	63
Table 3-9. Ambient and modeled maximum 8-hour ozone concentrations and maximum differences in 8-hour ozone concentrations between the CAMx base case and zero-out case (as calculated by Equation 3.1) for Victoria. Results are shown for days with the ten highest ambient 8-hour ozone concentrations during May 1 st –September 29 th , 2002.....	64
Table 3-10. Ambient and modeled maximum 8-hour ozone concentrations and maximum differences in 8-hour ozone concentrations between the CAMx base case and zero-out case (as calculated by Equation 3.1) for DFW. Results are shown for days with the ten highest 8-hour ozone differences between the base case and zero-out case, during May 1 st –September 29 th , 2002.....	65
Table 3-11. Ambient and modeled maximum 8-hour ozone concentrations and maximum differences in 8-hour ozone concentrations between the CAMx base case and zero-out case (as calculated by Equation 3.1) for Austin. Results are shown for days with the ten highest 8-hour ozone differences between the base case and zero-out case, during May 1 st –September 29 th , 2002.....	65
Table 3-12. Ambient and modeled maximum 8-hour ozone concentrations and maximum differences in 8-hour ozone concentrations between the CAMx base case and zero-out case (as calculated by Equation 3.1) for San Antonio. Results are shown for days with the ten highest 8-hour ozone differences between the base case and zero-out case, during May 1 st –September 29 th , 2002.....	66

Table 3-13. Ambient and modeled maximum 8-hour ozone concentrations and maximum differences in 8-hour ozone concentrations between the CAMx base case and zero-out case (as calculated by Equation 3.1) for Victoria. Results are shown for days with the ten highest 8-hour ozone differences between the base case and zero-out case, during May 1 st –September 29 th , 2002.....	66
Table 3-14. Maximum and average values of maximum differences in 8-hour ozone concentrations (as calculated by Equation 3.1) and differences in peak 8-hour ozone concentrations (as calculated by Equation 3.2) between the CAMx base case and zero-out case. Results are based on modeling output from August 13 th -September 14 th , 2006 and 2002.....	68
Table 3-15. Correlations of CAMx zero-out maximum 8-hour ozone differences for August 13 th -September 14 th , 2006.	69
Table 3-16. Percentage of days with predicted maximum 8-hour ozone differences between the CAMx base case and zero-out simulation (as calculated by Equation 3.1) within the specified ranges. Results are included for 33 days within the CAMx modeling periods of August 13 th –September 14 th , 2006 and 2002.....	70
Table 3-17. Percentage of days with predicted maximum 8-hour ozone differences between the CAMx base case and zero-out simulation (as calculated by Equation 3.1) within the specified ranges. Days included for each region (specified as “total days”) are characterized by local surface measurements of 8-hour ozone concentrations above 70 ppb during August 13 th –September 14 th , 2006 and 2002.....	71
Table 3-18. Ambient and modeled maximum 8-hour ozone concentrations and maximum differences in 8-hour ozone concentrations between the CAMx base case and zero-out case (as calculated by Equation 3.1) for DFW. Results are shown for days with the ten highest ambient 8-hour ozone concentrations during August 13 th –September 14 th , 2006.	72
Table 3-19. Ambient and modeled maximum 8-hour ozone concentrations and maximum differences in 8-hour ozone concentrations between the CAMx base case and zero-out case (as calculated by Equation 3.1) for Austin. Results are shown for days with the ten highest ambient 8-hour ozone concentrations during August 13 th –September 14 th , 2006.	73
Table 3-20. Ambient and modeled maximum 8-hour ozone concentrations and maximum differences in 8-hour ozone concentrations between the CAMx base case and zero-out case (as calculated by Equation 3.1) for DFW. Results are shown for days with the ten highest 8-hour ozone differences between the base case and zero-out case, during August 13 th –September 14 th , 2006.	73

Table 3-21. Ambient and modeled maximum 8-hour ozone concentrations and maximum differences in 8-hour ozone concentrations between the CAMx base case and zero-out case (as calculated by Equation 3.1) for Austin. Results are shown for days with the ten highest 8-hour ozone differences between the base case and zero-out case, during August 13 th –September 14 th , 2006.	74
Table 4-1. TexAQS II monitoring sites, locations, and types of measurements collected (TCEQ, 2008c).....	81
Table 4-2. CAMx and MM5 vertical grid structures based on 28 sigma-p levels. Heights (m) are above sea level according to a standard atmosphere; pressure is in millibars.	90
Table 4-3. Process information reported by the IPR option (ENVIRON, 2004).....	104
Table 4-4. CAMx predictions of surface layer night-time (averaged from 10:00 pm-6:00 am) wind speeds (in mph) for grid cells corresponding to the Cypress River and Longview monitoring sites. Results are shown for August 13 th -22 nd , 1999.	105
Table 4-5. CAMx initial and final total ozone concentrations (ppb) and total formation/depletion contributions (ppb) for 10:00 pm-6:00 am on August 16 th -17 th and 18 th -19 th , 1999. Results are shown for the Cypress River monitoring site, averaged over the first three vertical layers in the CAMx 12-km modeling domain.....	110
Table 4-6. CAMx initial and final total ozone concentrations (ppb) and total formation/depletion contributions (ppb) for 10:00 pm-6:00 am on August 16 th -17 th and 18 th -19 th , 1999. Results are shown for the Longview monitoring site, averaged over the first three vertical layers in the CAMx 12-km modeling domain.....	110
Table 4-7. CAMx initial and final total ozone concentrations (ppb) and total formation/depletion contributions (ppb) for 10:00 pm-6:00 am on August 16 th -17 th and 18 th -19 th , 1999. Results are shown for the Cypress River monitoring site, averaged over the first three vertical layers in the CAMx 12-km domain, for the case study involving a 10-fold increase in NO _x emissions in rural East Texas counties.....	115
Table 4-8. CAMx initial and final total ozone concentrations (ppb) and total formation/depletion contributions (ppb) for 10:00 pm-6:00 am on August 16 th -17 th and 18 th -19 th , 1999. Results are shown for the Longview monitoring site, averaged over the first three vertical layers in the CAMx 12-km domain, for the case study involving a 10-fold increase in NO _x emissions in rural East Texas counties.....	115

Table 5-1. Approximations of PBL depth used in ozone flux calculations as estimated from wind profiler data, as well as those computed with aircraft LIDAR measurements (Senff et al., 2007).....	132
Table 5-2. Comparison of horizontal extent of the urban plume estimated from the AQF modeling results versus estimates obtained from aircraft LIDAR measurements calculated by Senff et al. (2007).	135
Table 5-3. Wind speeds (in m/s) implemented in computations of ozone flux, as approximated by wind profilers, surface monitors, and the HYSPLIT application.....	140
Table 5-4. Surface monitor estimates of ozone concentrations, wind speed, and plume dimensions implemented in ozone flux computations with Equation 5.2. Estimates of similar parameters based on LIDAR and wind profiler measurements (provided by Senff et al., 2007) that were implemented in ozone flux computations with LIDAR data (using Equation 5.1) are also shown.	145
Table 5-5. Ozone flux (in molecules of ozone per second) computed with ambient measurements from airborne LIDAR (according to Equation 5.1) and surface monitors (according to Equation 5.2)..	148
Table 5-6. Ozone flux (in molecules of ozone per second) computed with modeled CAMx predictions and ambient measurements from airborne LIDAR and surface monitors. Calculations with data from surface monitors and CAMx were performed according to Equation 5.2, and LIDAR-derived results were computed based on Equation 5.1.	154
Table 5-7. Ozone flux (in molecules of ozone per second) computed with CAMx predictions and airborne LIDAR measurements according to Equation 5.1. Results are shown for September 6 th , 2000, for the NOAA DC-3 flight transect indicated in Figure 5-18.....	158
Table 6-1. Summary of anthropogenic and biogenic VOC and NO _x emissions in tons per day for all source regions on September 6 th , 2000.....	171
Table 6-2. Maximum hourly percent difference and standard deviations for total ozone production/loss ratios at all receptor sites for Plume A.	190
Table 6-3. Maximum hourly percent difference and standard deviations for total ozone production/loss ratios at all receptor sites for Plume B.	190
Table 6-4. CAMx hourly surface layer wind speeds (m/s) at the receptor sites for Plume A from 10:00-16:00 CST on September 6 th , 2000.....	191

Table 6-5. CAMx hourly surface layer wind speeds (m/s) at the receptor sites for Plume B from 10:00-16:00 CST on September 6 th , 2000.	192
Table 6-6. OSAT ozone contributions to Plume A for 13:00 CST on September 6 th , 2000. All contributions are in ppb of ozone. Relative source rankings are also listed next to each value in parenthesis.	196
Table 6-7. APCA ozone contributions to Plume A for 13:00 CST on September 6 th , 2000. All contributions are in ppb of ozone. Relative source rankings are also listed next to each value in parenthesis.	196
Table 6-8. OSAT ozone contributions to Plume B for 13:00 CST on September 6 th , 2000. All contributions are in ppb of ozone. Relative source rankings are also listed next to each value in parenthesis.	197
Table 6-9. APCA ozone contributions to Plume B for 13:00 CST on September 6 th , 2000. All contributions are in ppb of ozone. Relative source rankings are also listed next to each value in parenthesis.	197
Table A-1. MM5 and CAMx vertical grid structures based on 28 sigma-p levels. Heights are in meters above ground level (agl) according to a standard atmosphere; pressure is in millibars (ENVIRON, 2006). This vertical grid structure was used for the modeling period of May 1 st - September 30 th , 2002, and results were discussed in Chapter 3.	212
Table A-2. MM5 and CAMx vertical grid structures. Heights are in meters above ground level (agl) according to a standard atmosphere (ENVIRON, 2006). This vertical grid structure was used for the modeling period of August 13 th - September 15 th , 2006, and results were discussed in Chapter 3.	213
Table B-1. For each region, the fourth highest predicted 8-hour ozone concentrations are listed for May 1 st -September 29 th , 2002. These concentrations are ranked by CAMx output from the base case and zero-out case.	215
Table C-1. Ambient 1-hour ozone concentrations are shown for Italy High School CAMS 650, averaged from August 13 th -September 15 th , 2006. The ambient 1-hour ozone concentrations for CAMS 650 are also shown for August 19 th , 2006... ..	235
Table D-1. CAMx PA results for receptor site a1 from 10:00-16:00 CST on September 6 th , 2000. Initial and final concentrations of ozone are shown in units of ppb. Chemistry, advection, diffusion, and deposition terms are shown in units of ppb/hr.	241

Table D-2. CAMx PA results for receptor site a2 from 10:00-16:00 CST on September 6 th , 2000. Initial and final concentrations of ozone are shown in units of ppb. Chemistry, advection, diffusion, and deposition terms are shown in units of ppb/hr.	241
Table D-3. CAMx PA results for receptor site a3 from 10:00-16:00 CST on September 6 th , 2000. Initial and final concentrations of ozone are shown in units of ppb. Chemistry, advection, diffusion, and deposition terms are shown in units of ppb/hr.	242
Table D-4. CAMx PA results for receptor site a4 from 10:00-16:00 CST on September 6 th , 2000. Initial and final concentrations of ozone are shown in units of ppb. Chemistry, advection, diffusion, and deposition terms are shown in units of ppb/hr.	242
Table D-5. CAMx PA results for receptor site a5 from 10:00-16:00 CST on September 6 th , 2000. Initial and final concentrations of ozone are shown in units of ppb. Chemistry, advection, diffusion, and deposition terms are shown in units of ppb/hr.	242
Table D-6. CAMx PA results for receptor site b1 from 10:00-16:00 CST on September 6 th , 2000. Initial and final concentrations of ozone are shown in units of ppb. Chemistry, advection, diffusion, and deposition terms are shown in units of ppb/hr.	243
Table D-7. CAMx PA results for receptor site b2 from 10:00-16:00 CST on September 6 th , 2000. Initial and final concentrations of ozone are shown in units of ppb. Chemistry, advection, diffusion, and deposition terms are shown in units of ppb/hr.	243
Table D-8. CAMx PA results for receptor site b3 from 10:00-16:00 CST on September 6 th , 2000. Initial and final concentrations of ozone are shown in units of ppb. Chemistry, advection, diffusion, and deposition terms are shown in units of ppb/hr.	243
Table D-9. CAMx PA results for receptor site b4 from 10:00-16:00 CST on September 6 th , 2000. Initial and final concentrations of ozone are shown in units of ppb. Chemistry, advection, diffusion, and deposition terms are shown in units of ppb/hr.	244
Table D-10. CAMx PA results for receptor site b5 from 10:00-16:00 CST on September 6 th , 2000. Initial and final concentrations of ozone are shown in units of ppb. Chemistry, advection, diffusion, and deposition terms are shown in units of ppb/hr.	244

Table F-1. One-hour average wind speeds (m/s) and ozone concentrations (ppb) for surface monitors upwind and downwind of the DFW area for 16:00 CST on September 13 th , 2006. LIDAR-based results are also shown for this day for measurements collected along the flight transect indicated in Figure F-1, with data corresponding to a flight time of 15:50-16:30 CST.	256
Table F-2. One-hour average wind speeds (m/s) and ozone concentrations (ppb) for surface monitors upwind and downwind of the Houston area for 17:00 CST on August 12 th , 2006. LIDAR-based results are also shown for this day for measurements collected along the flight transect indicated in Figure F-2, with data corresponding to a flight time of 16:57-17:34 CST.	257
Table F-3. One-hour average wind speeds (m/s) and ozone concentrations (ppb) for surface monitors upwind and downwind of the Houston area for 17:00 CST on August 14 th , 2006. LIDAR-based results are also shown for this day for measurements collected along the flight transect indicated in Figure F-3, with data corresponding to a flight time of 16:59-17:26 CST.	258
Table F-4. One-hour average wind speeds (m/s) and ozone concentrations (ppb) for surface monitors upwind and downwind of the Houston area for 17:00 CST on August 30 th , 2006. LIDAR-based results are also shown for this day for measurements collected along the flight transect indicated in Figure F-4, with data corresponding to a flight time of 17:10-17:43 CST.	259
Table F-5. Hourly wind speeds (m/s) and ozone concentrations (ppb) for surface monitors and CAMx grid cells corresponding to the locations of these monitors, upwind and downwind of the Houston area for 16:00 CST on August 28 th , 2000. LIDAR-based results are also shown for this day for measurements collected along the flight transect indicated in Figure F-5, with data corresponding to a flight time of 16:11-16:40 CST.....	260
Table F-6. Hourly wind speeds (m/s) and ozone concentrations (ppb) for surface monitors and CAMx grid cells corresponding to the locations of these monitors, upwind and downwind of the Houston area for 14:00 CST on September 6 th , 2000. LIDAR-based results are also shown for this day for measurements collected along the flight transect indicated in Figure F-6, with data corresponding to a flight time of 14:13-14:43 CST.....	261
Table F-7. Geographical coordinates of surface monitors used to estimate horizontal plume width with the AQF model, as illustrated in Figures F-7 through F-10. Approximations of plume width (in km) are shown for the 2006 case study days, along with LIDAR-derived estimated ranges of plume width (in km).....	264

Table F-8. CAMx surface layer grid cell i and j coordinates, and the corresponding latitude and longitude coordinates, for the grid cells within the 4-km modeling domain that were selected to estimate plume widths on August 28th and September 6th, 2000. 266

List of Figures

Figure 1-1. Regions that currently violate the NAAQS for ozone and particulate matter (PM-2.5) (http://www.epa.gov/ozonepollution/actions.html).	1
Figure 1-2. Regions that violate a projected NAAQS for ground-level 8-hour ozone in the range of 0.60–0.70 ppm (http://www.epa.gov/ozonepollution/actions.html).	2
Figure 1-3. Six-year average local and background components of the 8-hour maximum ozone concentrations for the DFW area for 1998-2003 (Nielsen-Gammon et al., 2005).	4
Figure 2-1. Typical diurnal cycle of ozone formation (TCEQ, 2009).	11
Figure 2-2. Contribution of regional background ozone to ozone concentrations observed in Dallas-Fort Worth during an ozone episode in August, 1999 (Breitenbach, 2003).	14
Figure 2-3. Trajectory residence time analysis results for high ozone days in DFW (daily maximum 8-hour ozone concentrations greater than 100 ppb) (ENVIRON, 2004a).	20
Figure 2-4. Trajectory residence time analysis results for low ozone days in DFW (daily maximum 8-hour ozone concentrations less than 50 ppb) (ENVIRON, 2004a).	21
Figure 2-5. Trajectory residence time in percent for the lowest 20% 8-hour ozone days (McGaughey et al., 2006a). Colors represent the percentage of time that air parcels advecting into DFW spent in the location.	23
Figure 2-6. Trajectory residence time in percent for the highest 20% 8-hour ozone days (McGaughey et al., 2006a). Colors represent the percentage of time that air parcels advecting into DFW spent in the location.	23
Figure 2-7. HYSPLIT 48-hour backward trajectory for winds arriving in Houston at 00:00 UTC on September 1 st , 2008. Source winds originate at an altitude of 1500 meters.	24
Figure 2-8. The leading principal component, PC1, plotted in its positive orientation with amplitude equal to one standard deviation (Nielsen-Gammon et al., 2005)....	26

Figure 2-9. Mean centerlines of six 60-hour HYSPLIT back trajectory clusters for winds arriving in Houston at 18:00 UTC, at 300 meters above ground level (Sullivan, 2009). Results are shown for the peak months of the Houston ozone season, May through October, for 2000 to 2007. The clusters are categorized by the predominant wind direction as follows: 0. (not shown) far southerly fetch; 1. red, SE fetch; 2. blue, S/SE fetch; 3. green, northerly fetch; 4. cyan, short fetch; 5. magenta, NE fetch; 6. yellow, easterly fetch. The relative percentage of the number of trajectories included in each cluster is also shown.	27
Figure 2-10. Difference in 8-hour average ozone concentrations between a base case simulation and a scenario with anthropogenic emissions in the 8-county Houston-Galveston non-attainment area set equal to zero for July 2 nd , 1996 (McDonald-Buller et al., 2000).....	34
Figure 2-11. Differences in ozone concentrations between a base case simulation and a scenario where all NO _x emissions from electricity generating units were set equal to zero. Results are shown for September 7 th , 1993 (Nobel et al., 2001).	35
Figure 3-1. CAMx 36-km and 12-km (smaller rectangle outlined in red) modeling domains for the seasonal ozone model from May 1 st -September 30 th , 2002 (ENVIRON, 2006).....	50
Figure 3-2. The CAMx 12-km nested modeling domain is shown, with selected counties for the Austin, Victoria, DFW, San Antonio, and HGB areas designated by the colors shown in the legend.....	51
Figure 3.3. CAMx horizontal grid configuration for the model simulation during August 13 th -September 15 th , 2006 (TCEQ, 2009a).	53
Figure 3-4. Maximum 8-hour ozone differences between the CAMx base case and the zero-out case (as calculated by Equation 3.1) for May 1 st -September 29 th , 2002.....	57
Figure 3-5. Number of days characterized by maximum 8-hour ozone differences between the CAMx base case and zero-out scenario (as calculated by Equation 3.1) within the specified ranges. Results are included for the CAMx modeling period of May 1 st -September 29 th , 2002.	59
Figure 3-6. Maximum 8-hour ozone differences between the CAMx base case and the zero-out case (as calculated by Equation 3.1) for August 13 th -September 14 th , 2006.	68

Figure 4-1. Map of Texas showing the locations of routine surface monitors and monitors implemented as part of the TexAQS II field study (TCEQ, 2008c).	80
Figure 4-2. “Flux Line” established by the locations of TexAQS II monitoring sites implemented on the Texas-Louisiana border (Allen and Olaguer, 2004). ..	81
Figure 4-3. Surfer rural ozone contour plot showing the 75 th percentile daily 8-hour maximum ozone concentrations. Locations of rural monitoring stations are also shown (Sullivan et al., 2006).	84
Figure 4-4. Contour plot of ozone concentrations at 14:30 CST on September 26 th , 2005.	85
Figure 4-5. HYSPLIT 48-hour back-trajectories for 16:00 CST on October 17 th , 2005, from the Dallas-Fort Worth area at elevations of 300, 1000, and 1500 meters.	86
Figure 4-6. Regional contour plot of ozone concentrations on Oct. 17 th , 2005, 16:00 CST, with and without TexAQS II monitoring sites.....	86
Figure 4-7. Ozone concentration diurnal patterns for rural Northeast Texas monitoring sites and Big Bend.	88
Figure 4-8. Locations of rural Northeast Texas surface monitors in relation to natural gas production density.....	89
Figure 4-9. CAMx horizontal modeling domain for the August 13 th -22 nd , 1999 episode, including a 36-km regional grid and nested 12-km and 4-km fine grids (ENVIRON, 2003).	90
Figure 4-10. Time series of one-hour average ozone concentrations (in ppb) measured by the Tyler, Longview, and Cypress River surface monitors for August 13 th -22 nd , 1999. Photochemical modeling results are also shown for surface layer grid cells within the CAMx 12-km domain that correspond to the locations of these monitors.....	92
Figure 4-11. Hourly ambient surface monitor ozone concentrations and corresponding CAMx photochemical modeling predictions (in ppb) for the Cypress River monitoring site during August 13 th -22 nd , 1999.	93
Figure 4-12. Hourly ambient surface monitor ozone concentrations and corresponding CAMx photochemical modeling predictions (in ppb) for the Longview monitoring site during August 13 th -22 nd , 1999.	93

Figure 4-13. Hourly ambient surface monitor NO concentrations and corresponding CAMx photochemical modeling predictions (in ppb) for the Cypress River monitor during August 13 th -22 nd , 1999.....	95
Figure 4-14. Hourly ambient surface monitor NO concentrations and corresponding CAMx photochemical modeling predictions (in ppb) for the Longview monitor during August 13 th -22 nd , 1999.....	95
Figure 4-15. Comparison of CAMx modeled NO _x emission levels in tons per hour at 10:00 CST on August 17 th , 1999, to locations of dense natural gas production levels in Northeast Texas.....	96
Figure 4-16. CAMx surface layer 12-km domain for simulations involving an increase in NO _x emissions in Panola and Freestone counties. Results are shown for August 17 th , 1999.....	97
Figure 4-17. CAMx surface layer 12-km domain for simulations involving an increase in NO _x emissions in East Texas counties (excluding the Houston and DFW urban areas). Results are shown for August 17 th , 1999.	97
Figure 4-18. Hourly ambient surface monitor NO concentrations and corresponding CAMx photochemical modeling predictions (in ppb) for NO _x sensitivity studies for the Cypress River monitoring site during August 13 th -22 nd , 1999.	98
Figure 4-19. Difference between hourly surface layer NO _x emissions (ton/hr) for the CAMx 12-km domain associated with a 2-fold increase in low-level NO _x emissions in Panola and Freestone counties versus the base case. Results are presented for the hour with the maximum difference in NO _x emissions on August 17 th , 1999.....	99
Figure 4-20. Difference between hourly surface layer NO _x emissions (ton/hr) for the CAMx 12-km domain associated with a 10-fold increase in low-level NO _x emissions in Panola and Freestone counties versus the base case. Results are presented for the hour with the maximum difference in NO _x emissions on August 17 th , 1999.....	99
Figure 4-21. Difference between hourly surface layer NO _x emissions (ton/hr) for the CAMx 12-km domain associated with a 2-fold increase in low-level NO _x emissions in Eastern Texas counties (excluding the Houston and Dallas urban areas) versus the base case. Results are presented for the hour with the maximum difference in NO _x emissions on August 17 th , 1999.	100

Figure 4-22. Difference between hourly surface layer NO_x emissions (ton/hr) for the CAMx 12-km domain associated with a 10-fold increase in low-level NO_x emissions in Eastern Texas counties (excluding the Houston and Dallas urban areas) versus the base case. Results are presented for the hour with the maximum difference in NO_x emissions on August 17th, 1999. 100

Figure 4-23. Hourly ambient surface monitor ozone concentrations and corresponding CAMx photochemical modeling predictions (in ppb) for the Cypress River monitoring site during August 13th-22nd, 1999. 101

Figure 4-24. Difference in hourly surface layer ozone concentrations (ppb) for grid cells within the CAMx 12-km domain resulting from a 2-fold increase in low-level NO_x emissions in Panola and Freestone counties, relative to the base case. Results are shown for 14:00 CST on August 17th, 1999. 102

Figure 4-25. Difference in hourly surface layer ozone concentrations (ppb) for grid cells within the CAMx 12-km domain resulting from a 10-fold increase in low-level NO_x emissions in Eastern Texas counties, relative to the base case (excluding the Houston and Dallas urban areas). Results are shown for 15:00 CST on August 17th, 1999. 102

Figure 4-26. HYSPLIT 48-hour back trajectories from the Cypress River surface monitor at initial altitudes of 100, 500, and 1000 meters for 12:00 UTC on August 17th, 1999. 106

Figure 4-27. HYSPLIT 48-hour back trajectories from the Cypress River surface monitor at initial altitudes of 100, 500, and 1000 meters for 12:00 UTC on August 19th, 1999. 107

Figure 4-28. CAMx 12-km domain PA results for the Cypress River monitoring site on August 16th, 1999. Total ozone concentrations (ppb) and rates of formation/depletion (ppb/hr) are shown. 108

Figure 4-29. CAMx 12-km domain PA results for the Cypress River monitoring site on August 17th, 1999. Total ozone concentrations (ppb) and rates of formation/depletion (ppb/hr) are shown. 108

Figure 4-30. CAMx 12-km domain PA results for the Cypress River monitoring site on August 18th, 1999. Total ozone concentrations (ppb) and rates of formation/depletion (ppb/hr) are shown. 109

Figure 4-31. CAMx 12-km domain PA results for the Cypress River monitoring site on August 19th, 1999. Total ozone concentrations (ppb) and rates of formation/depletion (ppb/hr) are shown. 109

Figure 4-32. CAMx 12-km domain PA results for the Cypress River monitoring site on August 17th, 1999. Total NO concentrations (ppb) and rates of formation/depletion (ppb/hr) are shown. 112

Figure 4-33. CAMx 12-km domain PA results for the Cypress River monitoring site on August 16th, 1999, for the case involving a 10-fold increase in NO_x emissions in rural East Texas counties. Total ozone concentrations (ppb) and rates of formation/depletion (ppb/hr) are shown. 113

Figure 4-34. CAMx 12-km domain PA results for the Cypress River monitoring site on August 17th, 1999, for the case involving a 10-fold increase in NO_x emissions in rural East Texas counties. Total ozone concentrations (ppb) and rates of formation/depletion (ppb/hr) are shown. 113

Figure 4-35. CAMx 12-km domain PA results for the Cypress River monitoring site on August 18th, 1999, for the case involving a 10-fold increase in NO_x emissions in rural East Texas counties. Total ozone concentrations (ppb) and rates of formation/depletion (ppb/hr) are shown. 114

Figure 4-36. CAMx 12-km domain PA results for the Cypress River monitoring site on August 19th, 1999, for the case involving a 10-fold increase in NO_x emissions in rural East Texas counties. Total ozone concentrations (ppb) and rates of formation/depletion (ppb/hr) are shown. 114

Figure 4-37. Hourly ambient and CAMx-predicted ozone concentrations (in ppb) for the Cypress River monitor during August 13th-22nd, 1999. Modeled results are shown for the CAMx base case and for the sensitivity study involving decreased K_v values at Panola and Freestone counties within the first three vertical layers in the CAMx 12-km domain. 118

Figure 4-38. Hourly ambient and CAMx-predicted ozone concentrations (in ppb) for the Longview monitor during August 13th-22nd, 1999. Modeled results are shown for the CAMx base case and for the sensitivity study involving decreased K_v values at Panola and Freestone counties within the first three vertical layers in the CAMx 12-km domain. 119

Figure 5-1. LIDAR data collected by the NOAA Twin Otter for the second flight transect on August 14th, 2006 (Senff et al., 2007). 126

Figure 5-2. Illustration of the “box” model for ozone flux calculations with surface monitor data. 128

Figure 5-3. Radar profiler summaries of planetary boundary layer diurnal patterns during TexAQS II (Wilczak et al., 2007). 130

Figure 5-4. Geographical locations of radar profilers used in the TexAQS II analysis of diurnal patterns of average PBL heights (Wilczak et al., 2007).	131
Figure 5-5. Air Quality Forecast 1-hour daily maximum ozone concentrations for the Houston-Galveston 4-km modeling domain on August 12 th , 2006. The surface monitors used to approximate the width of the plume (C559 and C552) are indicated.	134
Figure 5-6. CAMx-predicted 1-hour surface layer ozone concentrations for the 4-km domain at 13:00 CST on September 6 th , 2000. The CAMx i and j coordinates for two grid cells that were selected to estimate the horizontal extent of the plume are indicated, and the NOAA DC-3 flight track for this day is also shown.	135
Figure 5-7. HYSPLIT 24-hour forward wind trajectory estimates from the Houston region beginning at 14:00 UTC on August 12 th , 2006. Trajectories are estimated at initial heights of 200, 500, and 1000 meters.	137
Figure 5-8. HYSPLIT 24-hour forward wind trajectory estimates from the Houston region beginning at 14:00 UTC on August 30 th , 2006. Trajectories are estimated at initial heights of 200, 500, and 1000 meters.	138
Figure 5-9. HYSPLIT 24-hour forward wind trajectory estimates from the Dallas region beginning at 14:00 UTC on September 13 th , 2006. Trajectories are estimated at initial heights of 200, 500, and 1000 meters.	139
Figure 5-10. HYSPLIT 24-hour forward wind trajectory estimates from the Houston region beginning at 14:00 UTC on September 6 th , 2000. Trajectories are estimated at initial heights of 200, 500, and 1000 meters.	139
Figure 5-11. Ozone concentrations from the NOAA Twin Otter flight on August 12 th , 2006 (Senff et al., 2007). The locations of the upwind and downwind surface monitors used to calculate ozone flux are also shown in red and blue, respectively.	142
Figure 5-12. Surface monitor locations in the Houston and Galveston areas that were operational in 2006 (CAPCO et al., 2004). The locations of the upwind and downwind surface monitors used to calculate ozone flux on August 12 th , 2006, are circled in red and blue, respectively.	143
Figure 5-13. Ozone concentrations from the NOAA Twin Otter flight on August 30 th , 2006 (Senff et al., 2007). The locations of the upwind and downwind surface monitors used to calculate ozone flux are also shown in red and blue, respectively.	146

Figure 5-14. CAMx photochemical modeling horizontal domains and vertical layer structure for the August 22 nd –September 6 th , 2000 episode.	150
Figure 5-15. Ozone concentrations from the NOAA DC-3 flights on August 28 th and September 6 th , 2000 (Senff et al., 2007).	151
Figure 5-16. Surface monitoring stations in the HGB area that were operational during 2000 (CAPCO et al., 2004). The locations of the upwind and downwind surface monitors used to calculate ozone flux on September 6 th , 2000, are circled in red and blue, respectively.	152
Figure 5-17. HYSPLIT 24-hour forward wind trajectory estimates from the Houston region beginning at 14:00 UTC on August 28 th , 2000. Trajectories are estimated at initial heights of 200, 500, and 1000 meters.	153
Figure 5-18. Ozone concentrations (vertically averaged over 200-1000 mMSL) from the NOAA DC-3 LIDAR on September 6 th , 2000. The figure illustrates average concentrations from 10-second sampling within the 4-km HGBPA CAMx grid domain. The DC-3 flight track is provided for reference (McGaughey et al., 2005).	155
Figure 5-19. Ozone concentrations (vertically averaged over 200-1000 mMSL) observed by the NOAA DC-3 LIDAR and predicted by CAMx on September 6 th , 2000. Results are shown for the DC-3 flight transect corresponding to a flight time of approximately 12:14-12:39 CST.	156
Figure 5-20. Vertical contour plot of modeled one-hour average ozone concentrations on the 4-km HGBPA CAMx grid domain, corresponding to the NOAA DC-3 flight transect indicated in Figure 5-18 (McGaughey et al., 2005).	157
Figure 6-1. Measurements of ozone concentrations collected by the LIDAR during the NOAA DC-3 flight on September 6 th , 2000 (Senff et al., 2007). The contours represent ozone concentrations vertically averaged over an approximate depth of 200-1000 meters above mean sea level.	165
Figure 6-2. One-hour average ozone concentrations measured by surface monitors in the HGB area and the CAMS 87 monitor in Victoria (McGaughey et al., 2005).	166
Figure 6-3. CAMx photochemical modeling horizontal domains for the August 22 nd –September 6 th , 2000 episode.	168

Figure 6-4. CAMx-predicted 1-hour surface layer ozone concentrations for the 4-km domain at 13:00 CST on September 6th, 2000. The locations of the selected source and receptor regions used for the source apportionment study are also shown, as well as the NOAA DC-3 aircraft flight track for this day..... 171

Figure 6-5. Relative anthropogenic and biogenic VOC and NO_x emissions in tons per day for all source regions on September 6th, 2000, superimposed on the CAMx 4-km domain. The NOAA DC-3 aircraft flight track for this day is also shown. 172

Figure 6-6. Average CAMx and LIDAR vertically averaged total ozone concentrations at the receptor regions selected in the centerline of Plume A (Houston Ship Channel source) and Plume B (Texas City source). 174

Figure 6-7. CAMx PA results for September 6th, 2000, for Plume A at receptor location a1. Results show hourly ozone concentrations in ppb and ozone production and loss rates in ppb/hr. 176

Figure 6-8. CAMx PA results for September 6th, 2000, for Plume A at receptor location a2. Results show hourly ozone concentrations in ppb and ozone production and loss rates in ppb/hr. 178

Figure 6-9. CAMx PA results for September 6th, 2000, for Plume A at receptor location a3. Results show hourly ozone concentrations in ppb and ozone production and loss rates in ppb/hr. 178

Figure 6-10. CAMx PA results for September 6th, 2000, for Plume A at receptor location a4. Results show hourly ozone concentrations in ppb and ozone production and loss rates in ppb/hr. 179

Figure 6-11. CAMx PA results for September 6th, 2000, for Plume A at receptor location a5. Results show hourly ozone concentrations in ppb and ozone production and loss rates in ppb/hr. 179

Figure 6-12. CAMx PA results for September 6th, 2000, for Plume B at receptor location b1. Results show hourly ozone concentrations in ppb and ozone production and loss rates in ppb/hr. 183

Figure 6-13. CAMx PA results for September 6th, 2000, for Plume B at receptor location b2. Results show hourly ozone concentrations in ppb and ozone production and loss rates in ppb/hr. 184

Figure 6-14. CAMx PA results for September 6th, 2000, for Plume B at receptor location b3. Results show hourly ozone concentrations in ppb and ozone production and loss rates in ppb/hr. 184

Figure 6-15. CAMx PA results for September 6 th , 2000, for Plume B at receptor location b4. Results show hourly ozone concentrations in ppb and ozone production and loss rates in ppb/hr.	185
Figure 6-16. CAMx PA results for September 6 th , 2000, for Plume B at receptor location b5. Results show hourly ozone concentrations in ppb and ozone production and loss rates in ppb/hr.	185
Figure 6-17. CAMx surface layer PA results of total ozone production rates vs. loss rates for all Plume A receptor sites during the NOAA DC-3 flight hours of 10:00–16:00 CST on September 6 th , 2000. A linear regression was performed for the data at each hour.	188
Figure 6-18. CAMx surface layer PA results of total ozone production rates vs. loss rates for all Plume B receptor sites during the NOAA DC-3 flight hours of 10:00–16:00 CST on September 6 th , 2000. A linear regression was performed for the data at each hour.	189
Figure 6-19. CAMx PA hourly ozone production rates from 10:00-16:00 CST by vertical diffusion (solid curves) and losses by vertical advection (dashed curves) for all receptor sites in Plume A, in ppb/hr.....	193
Figure 6-20. CAMx PA hourly ozone production rates from 10:00-16:00 CST by vertical diffusion (solid curves) and losses by vertical advection (dashed curves) for all receptor sites in Plume B, in ppb/hr.....	193
Figure 6-21. Radar profiler summaries of planetary boundary layer diurnal patterns during TexAQS II (Wilczak et al., 2007).	194
Figure 6-22. Geographical locations of radar profilers used in the TexAQS II analysis of diurnal patterns of average PBL heights (Wilczak et al., 2007).	195
Figure 6-23. APCA contributions (in ppb and percentage) from anthropogenic NO _x and VOC for Sources 1 and 8. Results are shown for receptor site a1 at 13:00 CST on September 6 th , 2000.	199
Figure 6-24. OSAT contributions (in ppb and percentage) from anthropogenic NO _x and VOC, and biogenic VOC, for Sources 1 and 8. Results are shown for receptor site a1 at 13:00 CST on September 6 th , 2000.....	199
Figure 6-25. Plume A APCA and OSAT contributions in (ppb of ozone) from Source 1 (Ship Channel) for all “a” receptor regions. Results are shown for 13:00 CST on September 6 th , 2000.	200

Figure 6-26. Plume B APCA and OSAT contributions in (ppb of ozone) from Source 2 (Texas City) for all “b” receptor regions. Results are shown for 13:00 CST on September 6 th , 2000.	202
Figure B-1. Maximum ambient and modeled (base case) 8-hour ozone concentrations are shown for DFW for May 1 st -September 29 th , 2002. The maximum difference between modeled base case and zero-out case 8-hour ozone concentrations (as calculated by Equation 3.1) for DFW are also shown.....	216
Figure B-2. HYSPLIT 48-hour back trajectories for winds arriving in DFW at 22:00 UTC and 500 magl for August 7 th , 2002.	219
Figure B-3. HYSPLIT 48-hour back trajectories for winds arriving in DFW at 22:00 UTC and 500 magl for August 19 th , 2002.	220
Figure C-1. Maximum 8-hour ozone differences between the CAMx base case and the zero-out case (as calculated by Equation 3.1) for August 13 th -September 14 th , 2002, for the DFW and Austin regions.....	224
Figure C-2. HYSPLIT 24-hour back trajectories for winds arriving in Austin at 22:00 UTC and 500 magl for August 18 th , 2006.	225
Figure C-3. HYSPLIT 24-hour back trajectories for winds arriving in DFW at 22:00 UTC and 500 magl for August 19 th , 2006.	226
Figure C-4. CAMx differences in 1-hour ozone concentrations between the base case and zero-out case. Results are shown for the 12-km grid domain, at 12:00 CST on August 18 th , 2006.....	227
Figure C-5. CAMx differences in 1-hour ozone concentrations between the base case and zero-out case. Results are shown for the 12-km grid domain, at 16:00 CST on August 18 th , 2006.....	227
Figure C-6. CAMx differences in 1-hour ozone concentrations between the base case and zero-out case. Results are shown for the 12-km grid domain, at 20:00 CST on August 18 th , 2006.....	228
Figure C-7. CAMx differences in 1-hour ozone concentrations between the base case and zero-out case. Results are shown for the 12-km grid domain, at 0:00 CST on August 19 th , 2006.....	229
Figure C-8. CAMx differences in 1-hour ozone concentrations between the base case and zero-out case. Results are shown for the 12-km grid domain, at 4:00 CST on August 19 th , 2006.....	229

Figure C-9. CAMx differences in 1-hour ozone concentrations between the base case and zero-out case. Results are shown for the 12-km grid domain, at 7:00 CST on August 19 th , 2006.....	230
Figure C-10. Modeled and ambient surface monitor maximum 8-hour ozone concentrations for DFW and Austin from August 13 th -September 14 th , 2006. CAMx modeling results are shown for the base case.....	231
Figure C-11. Geographic locations of surface monitors in Austin and surrounding areas. Surface monitors that measured elevated ozone on August 18 th , 2006 (CAMS 674, 3, and 601) are circled in red.....	233
Figure C-12. Geographic locations of surface monitors for the DFW region. The location of the Italy High School surface monitor, CAMS 650, is indicated.	234
Figure C-13. Surfer contour plot of interpolated ambient 8-hour maximum ozone concentrations for August 18 th , 2006. HYSPLIT 72-hour back trajectories are also shown for six origins in East Texas, at 18:00 UTC and an altitude of 300 magl.	236
Figure C-14. Surfer contour plot of interpolated ambient 8-hour maximum ozone concentrations for August 19 th , 2006. HYSPLIT 72-hour back trajectories are also shown for six origins in East Texas, at 18:00 UTC and an altitude of 300 magl.	237
Figure C-15. Surfer contour plot of interpolated ambient 1-hour average ozone concentrations for 14:00 CST on August 18 th , 2006.	238
Figure C-16. Surfer contour plot of interpolated ambient 1-hour average ozone concentrations for 15:00 CST on August 18 th , 2006.	238
Figure C-17. Surfer contour plot of interpolated ambient 1-hour average ozone concentrations for 16:00 CST on August 18 th , 2006.	239
Figure C-18. Surfer contour plot of interpolated ambient 1-hour average ozone concentrations for 17:00 CST on August 18 th , 2006.	239
Figure E-1. Ozone concentrations (vertically averaged from 200-1000 mMSL) from the NOAA DC-3 flight on September 6 th , 2000 (Senff et al., 2007). The locations of the surface monitors used for calculating ozone flux on this day are shown in magenta. The flight transects examined in this analysis are specified, corresponding to flight times from 16:57-17:14 UTC and 20:13-20:43 UTC.	246

Figure E-2. Continuous Ambient Monitoring Stations (CAMS) in the Houston area that were operational during 2000 (CAPCO et al., 2004). Surface monitors that were used to estimate background and peak ozone concentrations on September 6th, 2000, are circled in blue and red, respectively. 247

Figure E-3. Vertically averaged LIDAR and surface monitor measurements of ozone concentrations (ppb) for September 6th, 2000. Results are shown for the flight transect indicated in Figure E-1 from 20:13-20:43 UTC. The 5-minute measurements are shown for the surface monitors circled in Figure E-2. The dashed lines represent the mean ozone concentration for each surface monitor, based on 5-minute measurements from 20:00-21:00 UTC. 248

Figure E-4. Vertically averaged LIDAR and surface monitor measurements of ozone concentrations (ppb) for a portion of the flight transect from 20:13-20:43 UTC on September 6th, 2000. The mean and one standard deviation of these measurements are shown as the dashed lines and error bars, respectively. These statistics were calculated for thirteen 10-second LIDAR measurements from 20:28:25-20:31:05 UTC, and for thirteen 5-minute measurements recorded by each surface monitor (CAMS 409, 410, and 53) from 20:00-21:00 UTC. 250

Figure E-5. Vertically averaged LIDAR and CAMS 610 surface measurements of ozone concentrations (ppb) for a portion of the flight transect from 16:57-17:14 UTC on September 6th, 2000. The mean and one standard deviation of these measurements are shown as the dashed lines and error bars, respectively. These statistics were calculated for thirteen 10-second LIDAR measurements (from 16:57:55-17:00:05 UTC) and thirteen 5-minute CAMS 610 measurements (from 16:55-17:55 UTC). 252

Figure F-1. Ozone concentrations from the NOAA Twin Otter flight downwind of DFW on September 13th, 2006 (Senff et al., 2007). The locations of the upwind and downwind surface monitors used to calculate ozone flux are also shown in red and blue, respectively. 256

Figure F-2. Ozone concentrations from the NOAA Twin Otter flight downwind of Houston on August 12th, 2006 (Senff et al., 2007). The locations of the upwind and downwind surface monitors used to calculate ozone flux are also shown in red and blue, respectively. 257

Figure F-3. Ozone concentrations from the NOAA Twin Otter flight downwind of Houston on August 14th, 2006 (Senff et al., 2007). The locations of the upwind and downwind surface monitors used to calculate ozone flux are also shown in red and blue, respectively. 258

Figure F-4. Ozone concentrations from the NOAA Twin Otter flight downwind of Houston on August 30th, 2006 (Senff et al., 2007). The locations of the upwind and downwind surface monitors used to calculate ozone flux are also shown in red and blue, respectively. 259

Figure F-5. Ozone concentrations from the NOAA DC-3 flight downwind of Houston on August 28th, 2000 (Senff et al., 2007). The locations of the upwind and downwind surface monitors used to calculate ozone flux are also shown in red and blue, respectively. 260

Figure F-6. Ozone concentrations from the NOAA DC-3 flight downwind of Houston on September 6th, 2000 (Senff et al., 2007). The locations of the upwind and downwind surface monitors used to calculate ozone flux are also shown in red and blue, respectively. 261

Figure F-7. Air Quality Forecast 1-hour daily maximum ozone concentrations for the Houston-Galveston 4-km modeling domain on August 12th, 2006. The surface monitors used to approximate the width of the plume (C559 and C552) are indicated. 262

Figure F-8. Air Quality Forecast 1-hour daily maximum ozone concentrations for the Houston-Galveston 4-km modeling domain on August 14th, 2006. The surface monitors used to approximate the width of the plume (C78 and C64) are indicated. 263

Figure F-9. Air Quality Forecast 1-hour daily maximum ozone concentrations for the Houston-Galveston 4-km modeling domain on August 30th, 2006. The surface monitors used to approximate the width of the plume (C618 and C96) are indicated. 263

Figure F-10. Air Quality Forecast 1-hour daily maximum ozone concentrations for the East Texas 12-km modeling domain on September 13th, 2006. The surface monitors used to approximate the width of the plume (C73 and C71) are indicated. 264

Figure F-11. Contour plot of ozone concentrations predicted by CAMx at 16:00 CST on August 28th, 2000. The x- and y-axes are in units of projected grid cell coordinates (i,j) within the CAMx 4-km modeling domain in the East-West and North-South directions, respectively. The coordinates of two CAMx grid cells that were selected to estimate the horizontal extent of the plume are indicated, and the NOAA DC-3 flight track for this day is also shown. 265

Chapter 1: Introduction

Among the most ubiquitous and persistent air quality problems facing urban areas are high concentrations of gas phase oxidants, especially ozone, and high concentrations of fine particulate matter. In the United States, approximately 140 million people (see Figure 1-1) live in regions that fail to meet national standards for air quality. The Clean Air Act, which was last amended in 1990, requires the Environmental Protection Agency (EPA) to establish standards for wide-spread pollutants from numerous and diverse sources considered harmful to public health and the environment. These standards, referred to as National Ambient Air Quality Standards (NAAQS), set limits for particulate matter concentrations averaged over a year and averaged over 24 hours, and ozone concentrations averaged over 8-hours. The ozone NAAQS is generally referred to as the 8-hour ozone standard.

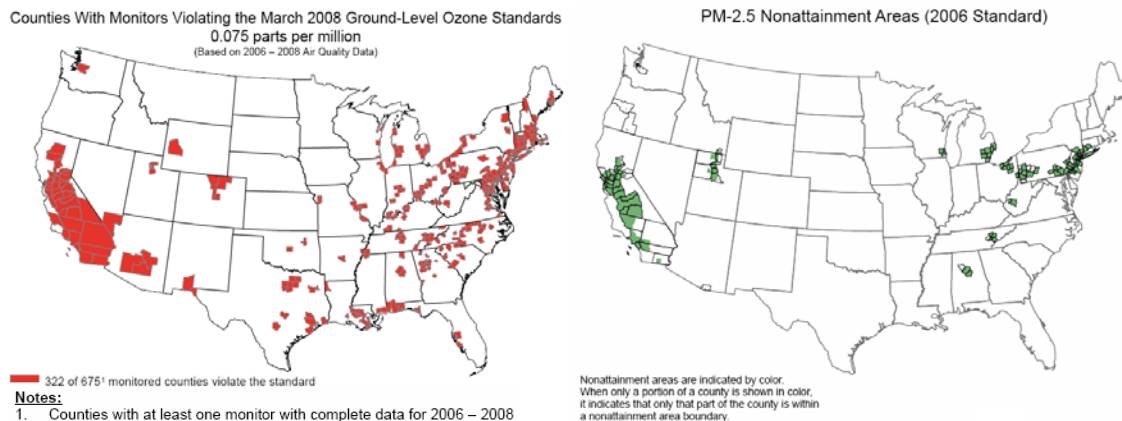


Figure 1-1. Regions that currently violate the NAAQS for ozone and particulate matter (PM-2.5) (<http://www.epa.gov/ozonepollution/actions.html>).

On March 12th, 2008, the EPA significantly strengthened the 8-hour NAAQS for ground-level ozone from 0.084 ppm to 0.075 ppm. On January 19th, 2010, in the Federal Register (Vol. 75, Number 11, page 2938), the EPA proposed to further strengthen this NAAQS to between 0.060 and 0.070 ppm. This would mean that the fourth highest daily maximum 8-hour ozone concentration each year, averaged over a three year period would need to be below 60-70 ppb for a region to be in attainment of the standard. Based on

2004-2006 air quality data, the number of counties in non-attainment of the previous 0.084 ppm 8-hour NAAQS is 85 (<http://www.epa.gov/ttn/airs/airsaqs/>). Based on 2006-2008 air quality data, Figure 1-1 illustrates the drastic increase in the number of non-attainment counties to 322 under the newly implemented 0.075 ppm 8-hour NAAQS, and this number of non-attainment counties is expected to increase further with future decreases in the NAAQS. Figure 1-2 shows that, on the same basis of 2006-2008 air quality data, the number of counties that are in violation of a projected NAAQS in the range of 0.060-0.070 ppm increases to 650 counties. It should be noted that the EPA will not designate areas as non-attainment based on these data, but likely on 2008-2010 data which are expected to reflect improvements in air quality.

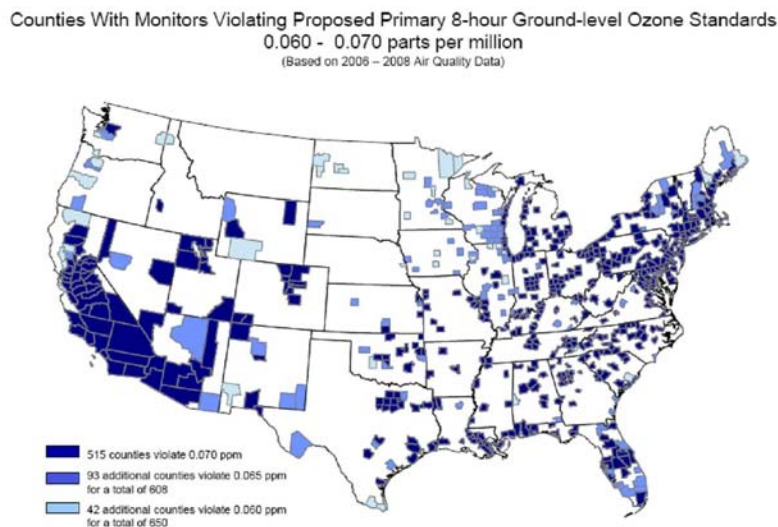


Figure 1-2. Regions that violate a projected NAAQS for ground-level 8-hour ozone in the range of 0.60–0.70 ppm (<http://www.epa.gov/ozonepollution/actions.html>).

The maps shown in Figures 1-1 and 1-2 illustrate the transformation of the challenge of attaining the ozone NAAQS from a local to a regional problem. The non-attainment areas identified in Figure 1-1 are relatively isolated urban areas except in the northeast and parts of California. In contrast, the map of Figure 1-2 shows non-attainment regions that are contiguous over large areas. It should be noted that Figure 1-2 understates the degree to which contiguous areas will become non-attainment. For example, in Texas, virtually every county east of I-35 would become non-attainment for

an ozone NAAQS of 60 ppb. Additionally, the map in Figure 1-2 only shows counties where ozone monitors are currently located.

While extensive research has drastically improved the understanding of local factors that contribute to air quality in urban areas, research has increasingly shown that ozone and particulate matter in urban areas are significantly influenced by regional, continental, and even global factors (Allen, 2007). Ozone in particular has a relatively long atmospheric lifetime and consequently can be transported over distances of hundreds of kilometers. In contrast to the increasingly regional nature of pollutant concentrations, and the increasingly regional nature of non-attainment regions, air quality planning and implementation of emission control programs have historically focused on metropolitan areas. However, recent research, including the findings presented in this work, suggests the need for strategies designed to maintain areas in accordance with the NAAQS to account for the characterization and impacts of regional transport of air pollutants. The formation of such strategies involves the use of computational and observational tools for quantitatively characterizing transport of air pollutants at regional and national scales. The development and evaluation of these tools, particularly for ozone, and their application to characterizing air pollution transport in Texas, is the topic of this study.

The importance of regional transport of ozone in Texas is illustrated in Figure 1-3, which shows maximum 8-hour average ozone concentrations measured by surface monitors in the Dallas-Fort Worth (DFW) area, as well as background ozone levels measured by monitors located upwind of the urban region. The data presented show 6-year averaged ozone concentrations in the DFW area as the sum of two components: background ozone and the local contribution. The background ozone is defined as the ozone level that would be attained if all local anthropogenic (man-made) emissions of ozone precursors were eliminated (Nielsen-Gammon et al., 2005). The local contribution can be expressed as the difference between the maximum 8-hour average ozone concentration and the background 8-hour average ozone concentration. Figure 1-3 illustrates that, on average, the local contribution is the smaller component of 8-hour maximum ozone concentrations in DFW, contributing to less than one-third of the total

ozone observed. However, as will be shown in this work, the relative contributions of local and regional sources of ozone can vary significantly from day to day.

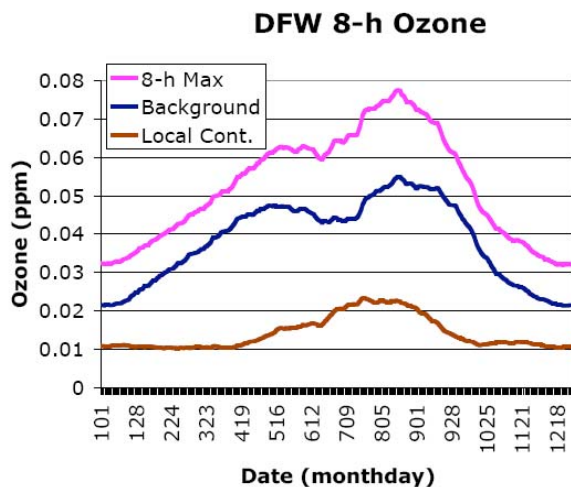


Figure 1-3. Six-year average local and background components of the 8-hour maximum ozone concentrations for the DFW area for 1998-2003 (Nielsen-Gammon et al., 2005).

Particulate matter transport over regional scales is also important. Air quality field data, collected as part of the fine particulate matter Supersites program (supported by the EPA) and other field measurement programs, have been used to assess the role of aerosol transport on fine particulate matter concentrations. Assessment of field data from cities including New York, Baltimore, Pittsburgh, Atlanta, Houston, St. Louis and Fresno indicated that, in virtually all of these regions, transport of aerosol over distances of 100-1000 km has a significant impact on urban particulate matter concentrations and plays a critical role in determining rural particulate matter concentrations (Allen et al., 2006). The EPA has conducted analyses for additional cities in the eastern U.S. that support this conclusion (Rao et al., 2002). In addition to the physical transport of aerosol particles, results from field studies have shown that the regional transport of aerosol precursors may lead to conditions conducive to large scale nucleation events. In some cases, these nucleation events have been correlated with the availability of sulfur dioxide and may therefore be categorized as sulfate formation events (Allen et al., 2006). These

phenomena begin to illustrate the principle, also expanded on in this work, that regional concentrations of air pollutants are influenced by both chemical and physical processes.

Although this study will focus on the transport of ozone over regional scales, the data analysis and modeling methods that can be used to characterize ozone and fine particulate transport over regional scales are very similar, and the methods developed in this work could be applied to either air pollutant. The focus will be on ozone because the intent is to describe the integration of detailed modeling and measurements. The most recent comprehensive field measurements available that included a focus on regional transport of air pollutants come from two air quality field studies in Texas, described in more detail in Chapter 4. Modeling of the regions in Texas encompassed by the field studies has been focused on ozone, largely because the state contains NAAQS non-attainment regions for ozone, but not for particulate matter.

The remainder of this dissertation describes ambient measurements and modeling approaches to characterize the regional transport of ozone. Chapter 2 provides a literature review of air pollutant transport at regional scales and the various methods that have been previously used to characterize that transport. Chapter 3 incorporates photochemical modeling and surface measurements to characterize the regional impacts of anthropogenic emissions from Houston on other metropolitan cities in Texas. Chapter 4 provides an assessment of regional ozone concentrations in the eastern half of Texas, based on a recent air quality field study. Chapter 5 describes the use of rural, ground-based monitoring to assess ozone transport, and compares the results to available aircraft-based measurements and photochemical modeling. Chapter 6 describes the application of ozone source apportionment tools, within the framework of photochemical models, and compares the results of these tools to aircraft-based measurements conducted during air quality field programs in Texas. Finally, Chapter 7 provides recommendations for future work.

1.1 REFERENCES

- Allen, D. T., and M.P. Fraser (2006), “An Overview of the Gulf Coast Aerosol Research and Characterization Study: The Houston Fine Particulate Matter Supersite”, *Journal of the Air and Waste Management Association*, 56, 456-466.
- Allen, D.T. (2007), “Rural Monitoring for Assessing Ozone Transport into Texas”, Final report submitted to the Texas Commission on Environmental Quality, New Technology Research and Development Program, satisfying tasks 1-4 of Grant Contract 582-5-65591-003, February 2007.
- U.S. Environmental Protection Agency, website reference for Figures 1.1 and 1.2, available at <http://www.epa.gov/ozonepollution/actions.html>, accessed March 2010.
- U.S. Environmental Protection Agency, NAAQS website reference, available at <http://www.epa.gov/ttn/airs/airsaqs/>, accessed March 2010.
- Neilsen-Gammon, J., J. Tobin, and A. McNiel (2005), “A Conceptual Model for Eight-Hour Ozone Exceedances in Houston Texas: Part I: Background Ozone Levels in East Texas”, Final report for Houston Advanced Research Center, Project H-12, January 2005.
- Rao, V, N. Frank, A. Rush, and F. Dimmick (2002), “Chemical Speciation of PM 2.5 in Urban and Rural Areas”, National Air Quality and Emissions Trends Report, Air and Waste Management Association Air Quality Measurements Conference, November 2002.

Chapter 2: Literature Review

2.1 INTRODUCTION

Air quality is influenced by both the transport of pollution over regional scales and pollutant generation by local sources. Therefore, a critical step in developing air quality strategies for reducing pollutant levels is to characterize the relative extents of local, regional, and global source contributions. This work will utilize measurements and modeling to characterize the relative extent of air pollutant sources, with a focus on ozone and its precursors. The measurement and modeling approaches can be broadly grouped into five categories:

- Surface monitoring data
- Aircraft data
- Satellite data
- Back trajectory modeling
- Photochemical modeling

The literature describing these approaches, along with a brief overview of ozone formation, is provided in the remainder of this Chapter.

2.2 OZONE FORMATION

Ozone is triatomic oxygen, a gas consisting of three oxygen atoms (O_3). Naturally occurring ozone is found in the stratosphere surrounding the earth and in the troposphere, near ground level. Stratospheric ozone forms high in the atmosphere in the presence of intense sunlight, which causes molecular (O_2) molecules to dissociate. The resulting oxygen atoms react with diatomic oxygen to form ozone. The ozone also photolyzes, and the production and loss due to photolysis generally results in a steady state concentration of ozone in the stratosphere. This “good ozone,” shields the earth from the harmful effects of the sun’s ultraviolet rays (TCEQ, 2009).

The formation of ozone in the troposphere is more complex than ozone formation in the stratosphere and involves reactions with hundreds of chemical precursors. The key reactions, as summarized by Seinfeld and Pandis (1998), are discussed here.

The formation of ozone in the troposphere results from only one known reaction: addition of atomic oxygen (O) to molecular oxygen (O₂) in the presence of a third "body", denoted as M in the reactions. The quantity M represents any "body" with mass, primarily nitrogen or oxygen molecules, but also particles, trace gas molecules, and surfaces of large objects. M absorbs energy from the reaction as heat, and the combination of O and O₂ into O₃ is not possible without this reaction.



The oxygen atoms are primarily generated by the photolysis of NO₂ by ultraviolet solar radiation (h_v), and, in the absence of sunlight, this process reverses and is known as ozone titration or "scavenging." The ozone formed by the reaction of atomic oxygen with diatomic oxygen can then regenerate NO₂ by reacting with NO (reaction 3) resulting in a cycling of ozone, NO, and NO₂.



The slower photolysis reaction (2) is generally the rate-limiting reaction for the nitrogen cycle and, as a result, ozone is not formed appreciably at night. Additionally, ozone concentrations are high during the summer months with high temperatures and intense solar radiation. The cycle time for the three reactions described above is only a few minutes during daylight hours. Depending on emission rates and meteorological conditions, ozone generally accumulates over the course of several hours. Therefore, the nitrogen cycle operates relatively fast enough to adequately approximate the photostationary-state ozone concentration as shown in equation (4), derived from reactions 1-3.

$$[\text{O}_3] \approx \left(\frac{k_2}{k_3} \right) \times \left(\frac{\text{NO}_2}{\text{NO}} \right) \quad (4)$$

where k_2 and k_3 are the rate constants for reactions 2 and 3 (units of sec^{-1} and $(\text{conc} \cdot \text{sec})^{-1}$). Under the assumptions of typical urban pollutant concentrations and that equilibrium could be reached in the ambient air, a concentration ratio of 10:1 for $[\text{NO}_2]/[\text{NO}]$ would be required to generate about 0.1 ppm of ozone.

The NO_2 to NO emission ratio is approximately 1:10; therefore, the nitrogen cycle alone does not generate high ozone concentrations observed in urban areas. Therefore, for ozone to accumulate according to the photostationary-state equation, an additional reaction pathway that will not simultaneously consume ozone is necessary to convert NO to NO_2 . The photochemical oxidation of volatile organic compounds (VOCs), such as hydrocarbons and aldehydes, provides that pathway.

Hydrocarbons and other VOCs are oxidized in the atmosphere by a series of reactions that form carbon monoxide (CO), carbon dioxide (CO_2), and water. Intermediate steps in this overall oxidation process involve cyclic stages driven by the hydroxyl radical (OH) reacting with the parent hydrocarbon, partially oxidized intermediate compounds, and other VOCs. The hydroxyl radical is consistently present in the ambient air. It is formed by photolysis from ozone in the presence of water vapor and also from nitrous acid, hydrogen peroxide, and other sources.

The VOC oxidation cycle typically begins with reaction 5, by OH reacting with a hydrocarbon or another VOC. In the sequence of reactions 5-7 below, “R” can be hydrogen or an organic fragment. R can also be generated by photolysis of VOCs with molecules containing the carbonyl ($\text{C}=\text{O}$) bond.



This is followed by a reaction with ambient oxygen, which generates the peroxy radical (RO_2).



The key reaction in the VOC oxidation cycle is the conversion of NO to NO₂, which occurs through the fast radical transfer reaction with NO shown in reaction (7). This reaction produces the NO₂ required for ozone formation, along with an oxidized hydrocarbon (RO).



The relative amounts of VOCs and NO_x at a particular location, known as the VOC/NO_x ratio, is a determining factor of whether NO_x behaves as a net ozone generator or a net ozone inhibitor. When the VOC/NO_x ratio in the ambient air is low (an abundance of NO_x is present), NO_x effectively inhibits ozone formation. In such cases, the amount of VOCs tends to limit the amount of ozone formed, and the ozone formation is called "VOC-limited" or "radical-limited", since it is the VOC reaction with hydroxyl radical that is frequently the rate limiting step in VOC oxidation. When the VOC/NO_x ratio is high, NO_x tends to generate ozone. In this case, the amount of NO_x available to participate in reaction 7 tends to limit the amount of ozone formed, and ozone formation is called "NO_x-limited". The VOC/NO_x ratio can differ substantially by location and throughout the day within a geographic area. Furthermore, the VOC/NO_x ratio measured near the ground may not accurately represent the ratio in the air aloft, where most tropospheric ozone is generated.

In the context of the work presented in this dissertation, VOC/ NO_x ratios in rural and upwind areas may be quite different than VOC/NO_x ratios in urban areas. This causes changes in chemistry as air masses are transported into or from urban areas that can make identification of limiting chemical processes challenging. Additionally, winds from one source may transport NO_x emissions over an area, while winds from a different direction may direct VOC emissions over that area. Therefore, meteorological considerations, along with types and locations of emissions sources, are essential in formulating effective air quality policies that account for regional pollutant transport.

Figure 2-1 illustrates the typical daily, or diurnal, cycle of ozone formation. Low levels of ozone are present before sunrise, followed by an increase during the morning and into the afternoon, then declining to low (background) levels again after sunset. During morning hours, NO_x and VOC emissions begin to mix with precursors remaining

from the previous day. As the sun heats the atmosphere, providing energy in the form of light, this mixture begins to generate ozone, with maximum ozone concentrations typically occurring in the afternoon. As the solar energy dissipates in the evening, ozone concentrations at ground level decrease to very low values at night-time due to NO titration and deposition processes. For rural regions with relatively low NO_x emissions, this titration does not occur to the same extent as in urban regions where night-time NO_x emissions are high. This phenomenon will be further addressed for rural regions in East Texas in Chapter 4.

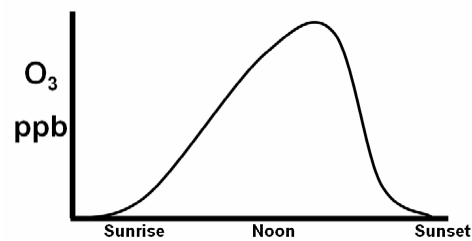


Figure 2-1. Typical diurnal cycle of ozone formation (TCEQ, 2009).

The temporal evolution of ozone concentrations near the surface is also strongly affected by the diurnal variation of the well-mixed atmospheric boundary layer (Zhang et al., 1999). Concentration is determined by the quantity of emissions and volume of well-mixed air, which in turn is dependant on wind speed and the depth of this well-mixed layer, also known as the mixing height. The mixing height determines the available volume of air in which pollutants emitted near the surface are primarily concentrated. For a fixed mass of precursor emissions, a lower mixing height contains a smaller volume of air, resulting in a more concentrated, and thus more reactive, air parcel (TCEQ, 2009). Conversely, a higher mixing height with a larger volume of air dilutes precursor levels, resulting in a less reactive parcel. Mixing heights can experience significant variability depending on geography, meteorology, as well as on a temporal basis; therefore, much research has been dedicated to developing techniques for estimating mixing heights. In this dissertation, Chapter 5 will illustrate the importance of accurate mixing height estimates in relation to pollutant flux calculations.

2.3 SURFACE MONITORING DATA

As described briefly in Chapter 1, one simple approach to characterizing regional transport of air pollutants is to compare measurements of surface air pollutant concentrations upwind of urban areas to measurements within and downwind of urban areas. In Texas, ground-based monitoring stations have been installed in urban regions for decades, and, in the past several years, monitors have been installed by the air quality group at the University of Texas in rural regions along the Texas geographic boundaries including the Gulf coast, as well as upwind and downwind of urban regions. A detailed description of the network will be provided in Chapter 4. Briefly, the surface monitoring instruments collect ambient concentrations for various chemical compounds such as ozone and NO_x, particulate matter (PM), visibility, and meteorological parameters such as wind speed, temperature, and relative humidity. All of the continuous surface pollution and meteorological data are reported in near real-time through the Texas Commission on Environmental Quality (TCEQ) Leading Environmental Analysis and Display System (LEADS), and to the EPA AIRNow Web-accessible data system.

Several analyses using data from surface monitors have been performed to estimate the levels of ozone transported into a region so that the amount of ozone that can be controlled (locally-produced ozone) can be quantified. Because ozone precursor compounds also exist under natural conditions, ozone is created and destroyed on a natural cycle according to atmospheric chemical conditions, even in the absence of anthropogenic (man-made) precursor sources. Ozone is also produced from anthropogenic sources at continental and hemispheric scales and collectively this natural ozone and anthropogenic continental scale ozone is known as background ozone. Background ozone levels transported into Texas are regularly as high as 60 ppb, and often higher (TCEQ, 2009). The need to quantify background ozone levels is essential given that a large metropolitan area, such as Houston, regularly generates enough local ozone to exceed the NAAQS when high background levels are present (TCEQ, 2009).

While local emissions and meteorology act in tandem to elevate ozone levels in the Houston-Galveston-Brazoria (HGB) area, background ozone is a substantial contributor, accounting for over half of the total ozone during periods when peak ozone

levels are observed (TCEQ, 2009). One study (TCEQ, 2009) identified the range of 90th percentile ozone concentrations recorded at four selected surface monitors surrounding the HGB region, shown in Table 2-1 below. These monitors were selected to represent background concentrations transported into HGB from various directions within Texas, as well as outside of the state. To isolate ozone being transported into the state and avoid undue impacts from nearby industrial sources, measurements at the selected monitors were restricted by wind direction. Results of this study indicate that 90th percentile ozone concentrations can exceed 80 ppb at any of these monitoring sites.

Table 2-1. Range of monthly 90th percentile daily peak one-hour zone concentrations for four monitors near Houston-Galveston-Brazoria (TCEQ, 2009). The data shown is for May through September of each indicated year. Maximum values for each year are highlighted in boldface type.

year	Hamshire C64/C654		Karnack C85/AFHP303		SETPRC Mauriceville 42 C642/C311/C665		West Orange C9/A141	
	min	max	min	max	min	max	min	max
	ppb	ppb	ppb	ppb	ppb	ppb	ppb	ppb
2000	38	74	.	.	56	81	43	83
2001	50	71	.	54	45	69	57	68
2002	51	62	58	84	40	68	53	69
2003	30	68	60	64	39	61	38	66
2004	43	71	39	66	30	61	41	66
2005	55	79	62	75	43	76	52	75
2006	45	76	42	78	32	63	43	75
2007	37	62	55	67	40	62	47	69
2008	40	62	.	65	47	70	50	60
9-year period	30	79	39	84	30	81	38	83

A second case study involving the use of surface monitoring data was performed by the TCEQ to analyze daily upwind/downwind ozone concentrations in the DFW area during an air pollution episode in August of 1999; the results of the analysis are illustrated in Figure 2-2. For each day included in this episode, the regional (or background) contribution to DFW elevated ozone levels is estimated as the lowest peak ozone concentration observed at any regional surface monitor for that particular day

(Breitenbach, 2003). The difference between this background ozone concentration and the highest peak concentration at any of the region's monitors is considered to be a locally generated contribution (Breitenbach, 2003). This approach assumes that monitors are broadly distributed throughout the urban area in a sufficient manner such that at least one sensor will never be influenced by local emissions (Nielsen-Gammon et al., 2005). The data shown here reveals that, on these days, the background ozone levels account for more than half of the total daily maximum ozone values. Figure 1-3 also showed that, for the six years of surface monitoring data averaged in that study, the local contribution is the smaller component of the 8-hour maximum ozone concentrations in DFW, contributing to less than one-third of the total ozone observed (Nielsen-Gammon et al., 2005).

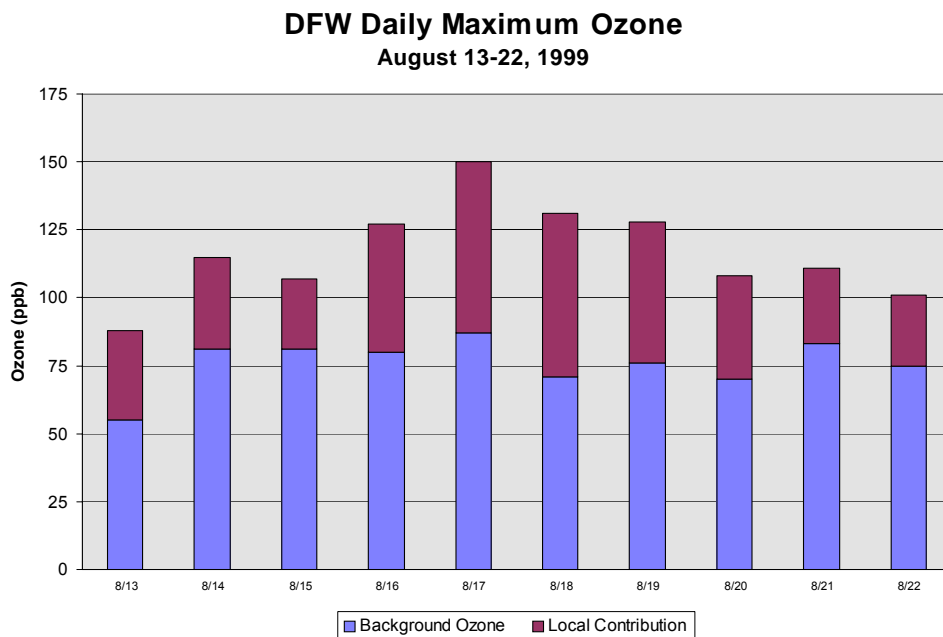


Figure 2-2. Contribution of regional background ozone to ozone concentrations observed in Dallas-Fort Worth during an ozone episode in August, 1999 (Breitenbach, 2003).

In another study, the data from surface monitors was used to investigate the relationship between ground-level ozone and ozone trapped aloft in the night-time residual layer (Zhang et al., 1999). To identify the processes that govern the temporal

evolution of the ground-level ozone concentrations, rates of change in surface ozone concentrations were examined between an urban site and a rural site, both located in New York, using all available observational data from June through August, 1995. The peak values of these rates of change during early morning hours at the rural site suggested that ozone aloft in the night-time residual layer exerts a major influence on the temporal evolution of the ground-level ozone concentration through vertical mixing processes (Zhang et al., 1999).

It should be noted that there are various shortcomings of using only ground-based observations for monitoring air quality. One shortcoming is the relatively small number of monitors that are used to characterize very large upwind and downwind regions. Another is that the analysis ignores the dynamics of ozone formation and accumulation processes. For example, the Nielsen-Gammon methods and the TCEQ methods may not strictly estimate background ozone, as defined above, because they do not discount any potential recirculation of pollutants generated by local emissions (TCEQ, 2009). Additionally, measurements of background ozone alone may not be sufficient, since ozone precursors, which can react with each other and with local emissions to produce ozone, may also be present in transported air (TCEQ, 2009). Nevertheless, surface monitors in fixed locations provide a starting point for assessments of regional transport, and results from surface monitor networks in Texas will be described in more detail in Chapter 5. Additional approaches to estimating ozone transport that address some of the shortcomings of methods based on surface monitors will be described in later chapters. Larger spatial areas can be represented by aircraft and satellites, which are described in the next sections, but these measurements also have limitations.

2.4 AIRCRAFT LIDAR DATA

Data from aircraft flights that determine the horizontal and vertical distributions of pollutants is another source of observational data that has been used to characterize pollutant transport. One of the most powerful approaches, and one of the approaches to be used in this work, involves the use of an instrument known as a LIDAR (Light Detection and Ranging) sensor mounted on an aircraft. LIDAR is an optical remote

sensing technology that measures the properties of scattered light, by using laser pulses, to find range or other information of a distant target (Cracknell et al., 2007). Like the similar radar technology, which uses radio waves, the range to an object is quantified by measuring the time delay between transmission of a pulse and detection of the reflected signal. In LIDAR measurements of ozone, two laser signals are used. One wavelength is chosen to backscatter from particulate matter, providing ranging information. A second wavelength, which is also backscattered, but that is absorbed by ozone provides information on ozone concentrations. Coupled analysis of the aerosol backscatter and ozone absorbing wavelengths provides vertical profiles of pollutant concentrations. These are collected along horizontal flight paths, creating a two-dimensional mapping of pollutant concentrations along a pre-defined flight path, often with the purpose of characterizing the formation and transport of pollutants in plumes.

Several aircraft studies using techniques other than LIDAR have been performed during large-scale air quality studies to quantify regional ozone transport. Aircraft measurements taken as part of the North American Research Strategy for Tropospheric Ozone-Northeast field study, conducted during 1995-1997, reported ozone concentrations in excess of 80 ppb on a regional scale in the nocturnal residual layer during periods that experienced elevated ozone levels (Zhang et al., 1999). Given the regional extent of the polluted dome aloft during a typical ozone episode in the northeastern U.S. (on a horizontal spatial scale of about 600 km), these results demonstrated the importance of implementing emission reduction strategies on a regional scale (Zhang et al., 1999). During air quality field programs in Texas in 2000 and 2006, aircraft measured ozone concentrations upwind, across, and downwind of Dallas, Houston and Victoria. Results showed that, on some days, transported ozone can bring the Dallas and Houston areas close to an 8-hour exceedance of the NAAQS without any added contribution from local emissions (Kemball-Cook et al., 2009). In this work, the focus will be on LIDAR measurements because they provide the most detailed mappings available of the horizontal and vertical structure of ozone concentrations.

Airborne LIDAR data has been used to quantitatively characterize ozone flux downwind of metro areas in eastern Texas by NOAA (Senff et al., 2007). More

specifically, the purpose of these measurements was to use data from flight transects downwind of Houston and Dallas-Fort Worth to compute the total horizontal flux of ozone emitted by these urban regions for several days in August and September of 2006 and 2000. The ozone flux was calculated by integrating excess ozone in the plume (plume ozone minus background ozone) across the entire area between the surface and the top of the boundary layer and within the horizontal urban area plume boundaries. The boundary layer height was determined by an objective Haar wavelet method that detects the steep aerosol gradient at the top of the boundary layer in the LIDAR backscatter data. This integrated plume ozone was then multiplied by the horizontal wind speed, which was estimated from nearby wind profiler data, to yield ozone flux values in the units of molecules per second. Results of this analysis are presented in Table 2-2 below and are shown for the flight transect corresponding to the highest calculated ozone flux on each respective day. The calculations suggest the surprising finding that the excess ozone emitted by the Houston area does not vary much during the days with available airborne LIDAR data. In another surprising finding, results for 2006 are comparable with those from 2000, despite substantial emission reductions in the Houston urban area between 2000 and 2006. While the Dallas area emitted less excess ozone in comparison to Houston for the days in this study, the ozone flux remains on the same order of magnitude as Houston flux values.

Table 2-2. Ozone flux estimates derived with airborne LIDAR measurements (Senff et al., 2007). Results for each day are shown for the flight transect corresponding to the highest calculated ozone flux.

Metro Area	Date	Wind Direction	Wind Speed (m/s)	Time (CST)	Background Ozone (ppbv)	Ozone Production (ppbv)	Ozone Flux (molec O3/s)
Houston	8/12/2006	S	7.3	16:57 - 17:34	29	39	5.00E+26
Houston	8/14/2006	S	4.5	16:58 - 17:26	34	55	5.00E+26
Houston	8/30/2006	N	3.8	17:10 - 17:43	59	52	3.20E+26
Houston	8/28/2000	S	4.2	16:11 - 16:40	53	52	6.00E+26
Houston	9/6/2000	NE	5.2	14:13 - 14:43	69	46	3.60E+26
Dallas-Ft. Worth	9/13/2006	N	4.6	15:49 - 16:34	57	18	1.70E+26

These urban ozone flux measurements are among the first to become available for U.S. cities, and offer the opportunity to evaluate the performance of photochemical models for the same regions, during the same time periods. This inter-comparison between ozone LIDAR results and photochemical model predictions will be the topic of Chapter 5.

2.5 SATELLITE DATA

While not a primary focus of this dissertation, the use of satellite data is briefly discussed, since it is an emerging method for characterizing regional transport of pollutants, especially particulate matter. With the launch of NASA's MODerate resolution Imaging Spectroradiometer (MODIS), the transport of aerosol-borne pollutants has been monitored over land and ocean surfaces by using satellite observations. Results have demonstrated that MODIS data and its products are capable of detecting and qualitatively tracking the migration of particulate matter (Armistead et al., 2000). One case study in particular involves MODIS satellite imagery that was used to track continental haze migration into Texas during a particularly harmful episode which required health advisories to be issued for over 150 counties in Texas (Armistead et al., 2000). The satellite imagery successfully tracked the path of migration of the haze from its origin in the Northeast continental U.S. (over the Mississippi and Ohio Rivers) into Texas (Armistead et al., 2000). Additional uses of satellite data have included tracking of natural aerosol events (fires and dust storms).

These satellite based measurements are still semi-quantitative in their ability to characterize regional transport of pollutants, and therefore will not be a primary focus of this dissertation.

2.6 BACK TRAJECTORY ANALYSES

The analysis of back trajectories is among the simplest of modeling tools used to characterize air pollutant transport. Back trajectories are model results that estimate the hypothetical path an air parcel takes prior to arriving at a specific place and time. A tool

that has been frequently used for trajectory analyses is the HYbrid Single-Particle Lagrangian Integrated Trajectory (HYSPLIT) application based on archived meteorological wind data (Draxler et al., 2003). HYSPLIT was developed as a joint effort of the National Oceanic and Atmospheric Administration (NOAA) and Australia's Bureau of Meteorology. The application is capable of calculating trajectories either forward or backward in time, and hourly trajectories are generated using a three-dimensional meteorological data set. HYSPLIT also has the option to simultaneously generate wind trajectories from multiple starting locations. The analysis of multiple trajectories can distinguish between source areas or paths that lead to higher than average, or lower than average ozone concentrations (Sullivan, 2009). Complete documentation of the calculation methods used by HYSPLIT can be accessed from the official website (<http://www.arl.noaa.gov/ready/hysplit4.html>).

Several studies combining results from back trajectory analysis, source apportionments, and surface monitoring data with the purpose of generating residence time maps have been performed. The methodology involves the length of time back trajectories are calculated to have resided in various source regions. Uncertainties arise when applying this technique to the apportionment of ozone due to the cyclical, non-linear, and potentially rapid reaction mechanisms that are associated with ozone formation. Nevertheless, calculating ozone apportionments by trajectory residence time patterns may potentially provide qualitative results relating to regional transport patterns of ozone.

In 1995, the Air Quality Analysis Workgroup associated with OTAG (Ozone Transport Assessment Group) performed a back trajectory residence time analysis. The spatial characteristics of select long-term trajectory climatology were prepared by calculating the residence time (in hours) for each grid cell of back trajectories for six high elevation sites in the eastern U.S. for the summers of 1989 through 1995. Although the study had limitations (e.g., only six sites were examined, no consideration of emissions or chemical reactions, and simplified treatment of wind fields), it helped to identify where the air masses associated with both high and low ozone concentrations were likely to have previously resided.

Stoeckenius and Yarwood analyzed air parcel trajectory paths using HYSPLIT over a multi-state area centered on Dallas-Fort Worth over two historic periods to evaluate potential patterns in sources attributing to elevated ozone levels in the area (ENVIRON, 2004a). The study involved mapping back trajectories, generating residence time maps, and using a statistical model to associate trajectory paths with ozone concentrations based on data from June-September for 2000, 2001, and 2002. Total residence times for trajectories arriving in DFW on the afternoons of high and low ozone days (defined as days with 8-hour maximum ozone concentrations of 100 ppb or greater and 50 ppb and lower, respectively) are illustrated in Figures 2-3 and 2-4 below, respectively. Relative to low ozone days, results of this study show that trajectories on high ozone days have shorter fetches (corresponding to slower wind speeds) and spend more time in the south and southeast areas of DFW. Trajectories on low ozone days indicate dominant flow from the Gulf of Mexico and cover greater distances, which corresponds to higher wind speeds.

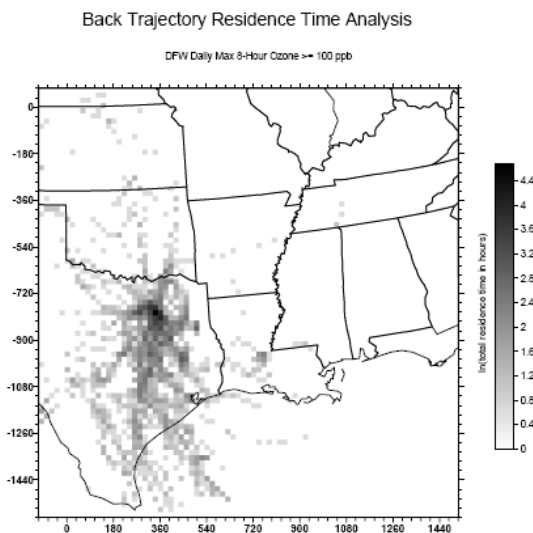


Figure 2-3. Trajectory residence time analysis results for high ozone days in DFW (daily maximum 8-hour ozone concentrations greater than 100 ppb) (ENVIRON, 2004a).

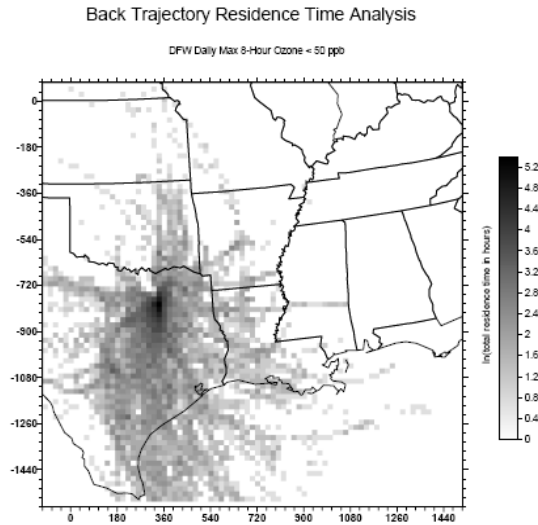


Figure 2-4. Trajectory residence time analysis results for low ozone days in DFW (daily maximum 8-hour ozone concentrations less than 50 ppb) (ENVIRON, 2004a).

The results of a more recent study visually summarized the geographic locations that are most frequently upwind of the DFW and HGB ozone non-attainment areas, which correspond to the potential source regions of background ozone entering these areas (McGaughey et al., 2006a). Residence time contour maps were created for each month during the period of April through October 2001 through 2005, to provide a mechanism for comparisons of climatological seasonal variability in regional transport patterns. The maps were also generated for all days with maximum ozone concentrations above 75 ppb and 85 ppb during the period and for the days that had maximum ozone concentrations within the highest and lowest 20th percentiles.

Five-day (120-hour) back trajectories were generated using HYSPLIT for all days included in the study. This five-day duration was selected to capture long-range transport not only within Texas, but also from more distant source regions such as the central and southeastern U.S., during conditions of relatively low wind speeds in the lower atmosphere. Daily maximum ozone concentrations averaged over 8 hours were compiled from DFW and HGB ground monitoring stations that were available during this time period. For each scenario, the residence time within each one degree latitude by one

degree longitude grid cell was calculated by summing the number of back trajectory hours with locations that occurred within that cell.

Figures 2-5 and 2-6 illustrate results for the DFW area with days in September that were characterized by the lowest and highest 20th percentile of maximum ozone concentrations, respectively. Figure 2-5 suggests that results for low ozone days are consistent with the long-range transport of relatively clean maritime air westward over the Gulf of Mexico, followed by southerly to southeasterly transport into the DFW region. In contrast, Figure 2-6 suggests that long-range transport from continental areas located to the east and northeast of Texas contributes to high ozone days. This is consistent with the clockwise flow around a surface ridge of high pressure that typically extends south into Texas during high ozone events (McGaughey et al., 2006b). The continental air transported into Texas most likely contained elevated concentrations of ozone and its precursors associated with both biogenic and anthropogenic emissions from upwind sources (McGaughey et al., 2006b). A similar analysis has been performed for the Texas ozone near non-attainment areas of Austin, Corpus Christi, San Antonio, Tyler/Longview/Marshall, and Victoria (McGaughey et al., 2006b).

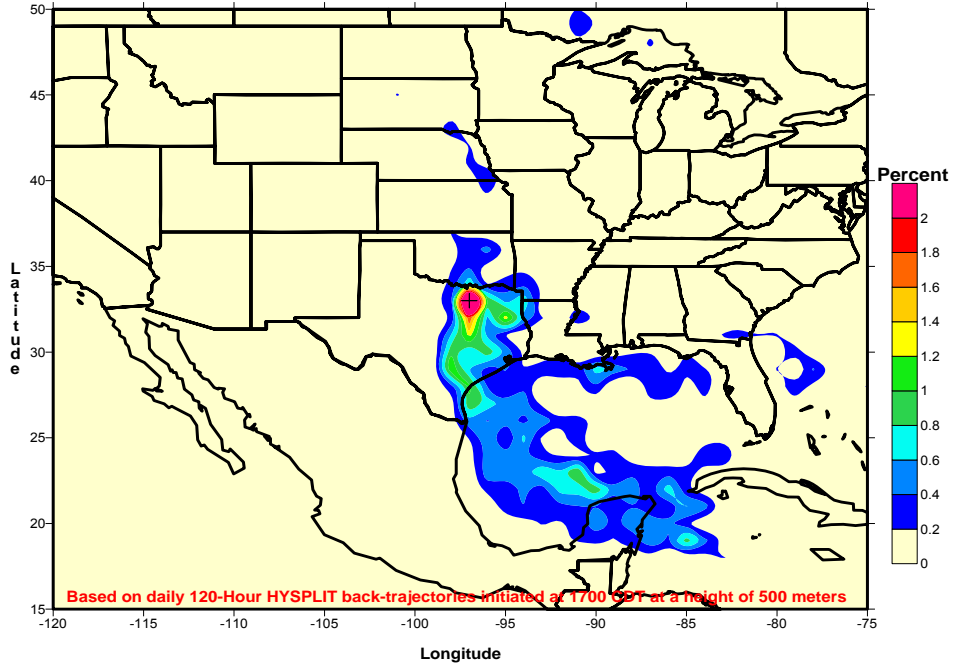


Figure 2-5. Trajectory residence time in percent for the lowest 20% 8-hour ozone days (McGaughey et al., 2006a). Colors represent the percentage of time that air parcels advecting into DFW spent in the location.

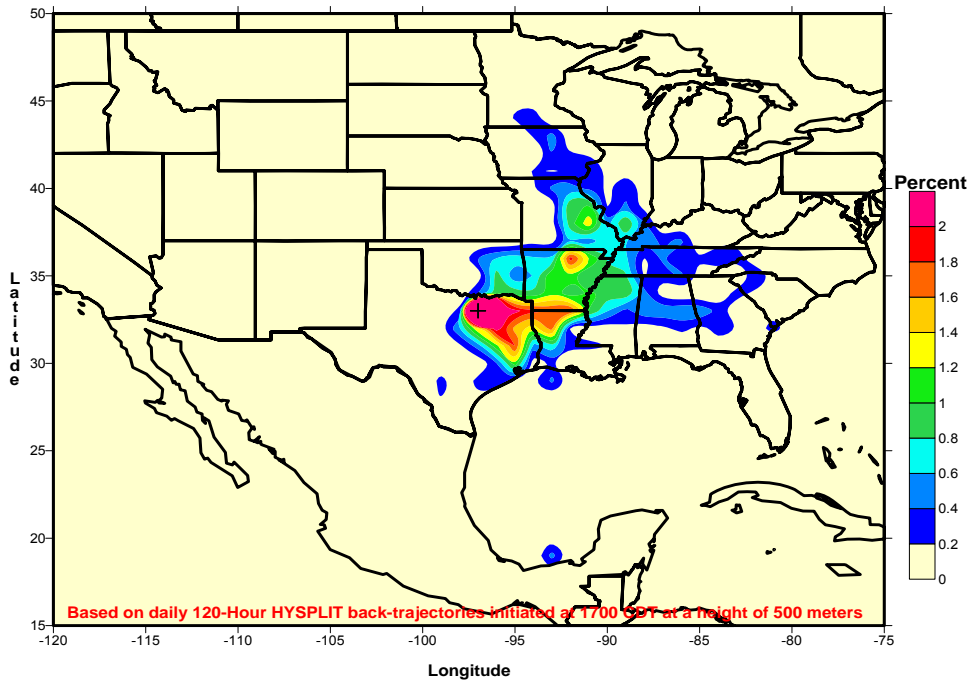


Figure 2-6. Trajectory residence time in percent for the highest 20% 8-hour ozone days (McGaughey et al., 2006a). Colors represent the percentage of time that air parcels advecting into DFW spent in the location.

Another study that used coupled HYSPLIT back trajectory analysis with observational data was performed by the TCEQ to investigate patterns of continental ozone transport into Texas for the summer months of May through September, 2004 through 2008 (TCEQ, 2009). Candidate days were selected by examining EPA AIRNow ozone plots and identifying days when 8-hour ozone levels exceeded 85 ppb in multiple states upwind of Texas, generally as far east as the Midwestern U.S. For these days, 48-hour back trajectories arriving at an altitude of 1500 meters were generated using the HYSPLIT model and EDAS (Eta Data Assimilation System) data, and the frequencies of identified transport days, by year, were computed. It should be noted that an unknown degree of uncertainty accompanies this approach, due to the visual identification procedure for identifying transport events from AIRNow ozone plots (TCEQ, 2009). Figure 2-7 shows a typical 48-hour HYSPLIT backward trajectory for a day characterized by winds originating from eastern/northeastern sources and arriving in Houston.

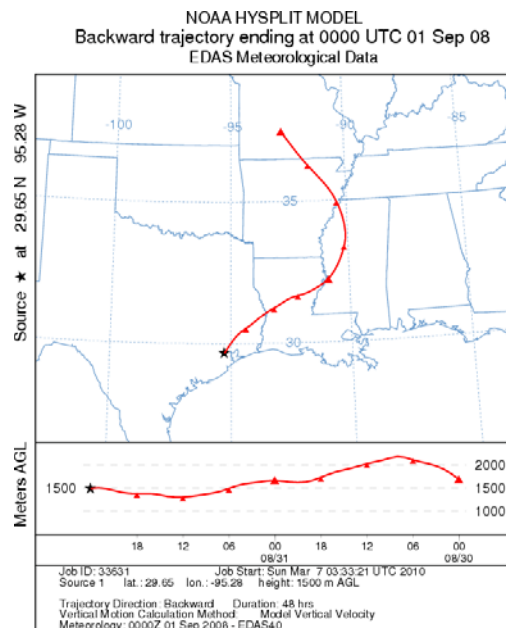


Figure 2-7. HYSPLIT 48-hour backward trajectory for winds arriving in Houston at 00:00 UTC on September 1st, 2008. Source winds originate at an altitude of 1500 meters.

As shown in Table 2-3, results of this study indicate the highest frequency totals of long-range transport into Texas from states located to the east and northeast occurred

in 2005 and 2006, with 22 and 34 days, respectively. Identified transport days are fewer in 2004, 2007 and 2008, suggesting that background ozone levels transported from eastern/northeastern states were lower, which would also be expected to reduce ozone levels in Texas for those years (TCEQ, 2009).

Table 2-3. Frequency of ozone transport events in Texas from Northeast/East continental origins (TCEQ, 2009).

	May	June	July	August	September	Total
2004	0	0	1	6	4	11
2005	6	3	4	8	13	34
2006	0	8	6	8	0	22
2007	1	3	0	0	4	8
2008	1	5	2	2	0	10
Total	8	19	13	24	21	85

Aside from using multiple trajectories for arbitrarily-defined high and low ozone days in an attempt to determine preferred directions of transport, an alternative approach that has been taken relates the wind direction to background ozone levels by principal component analysis (Nielsen-Gammon et al., 2005). Principal component analysis effectively reduces the dimensionality of a large data set into smaller, more manageable variables. One study incorporated principal component analysis to determine the dominant modes of large-scale wind patterns, which may be expected to strongly control background ozone, and define them as a small number of continuously-varying patterns. In this study, these wind patterns were represented by a set of graphs on a grid covering the area from eastern Texas to the lower Mississippi River valley, extending north to southwestern Kentucky. Each pattern, or principal component, was tested for correlations with background ozone levels.

The results of this study indicate that PC1, the leading principal component shown in Figure 2-8, represents the strongest mode of variability and corresponds to a vector oriented from the southwest (if positive) or northeast (if negative). It is therefore an indicator of the presence (or absence, in the positive orientation) of transport from the central and eastern continental United States. This principal component was found to be

most strongly correlated with background ozone levels, explaining background ozone variations of about 17 ppb in DFW and 20 ppb in the Houston/Galveston area.

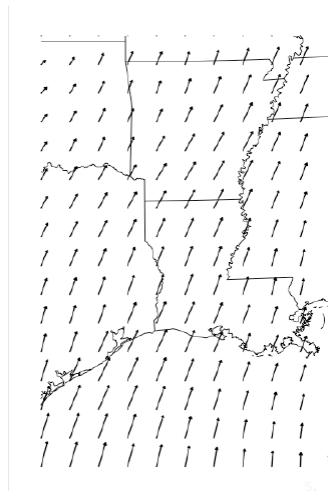


Figure 2-8. The leading principal component, PC1, plotted in its positive orientation with amplitude equal to one standard deviation (Nielsen-Gammon et al., 2005).

Yet another approach is called cluster analysis, which seeks to find particular recurring patterns and group the observed weather patterns into “clusters” (Nielsen-Gammon et al., 2005). This approach is appropriate when the atmosphere rapidly transitions from one mode to another, creating particular patterns of variability; however, when the atmosphere varies gradually and continuously as it tends to do during the summer in Texas, cluster analysis may only produce an arbitrary grouping of weather events with little or no underlying physical basis (Nielsen-Gammon et al., 2005).

A series of cluster analysis studies were done for the TCEQ (Sullivan, 2009) that addressed this shortcoming. The analyses incorporated HYSPLIT back trajectories along with EDAS and observational data from surface monitors to estimate the amount of ozone transported into the Houston area. Numerous 72-hour back trajectories were run starting at 12:00 CST in central Houston, at 300 meters above ground level, during the peak months of the ozone season in Houston (May 1st to October 31st, 2000 to 2007) (TCEQ, 2009). Six clusters were identified, and the mean centerline from each cluster is shown in Figure 2-9.

The trajectories were then compared to locally observed ozone concentrations in Houston as measured by twelve ozone surface monitoring sites that had near continuous operation from 2000 to 2007. Daily minimum and maximum peak 8-hour ozone concentrations were extracted for the twelve monitors and merged with the cluster classification that corresponded with that day. Following the approach used by Nielsen-Gammon et al. (2005), the minimum peak 8-hour average ozone concentration was selected to represent background ozone.

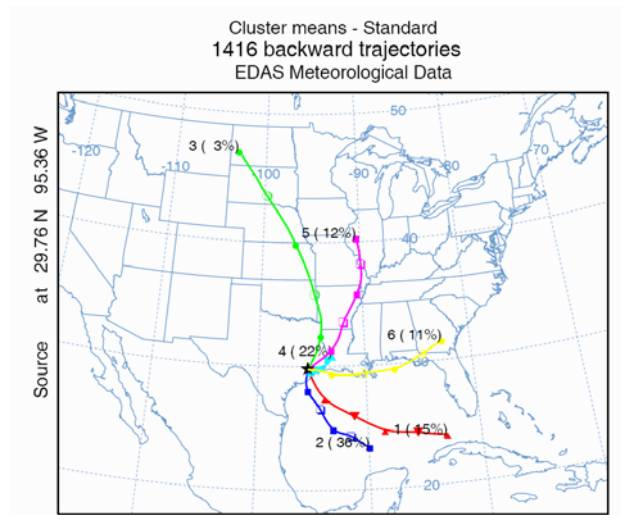


Figure 2-9. Mean centerlines of six 60-hour HYSPLIT back trajectory clusters for winds arriving in Houston at 18:00 UTC, at 300 meters above ground level (Sullivan, 2009). Results are shown for the peak months of the Houston ozone season, May through October, for 2000 to 2007. The clusters are categorized by the predominant wind direction as follows: 0. (not shown) far southerly fetch; 1. red, SE fetch; 2. blue, S/SE fetch; 3. green, northerly fetch; 4. cyan, short fetch; 5. magenta, NE fetch; 6. yellow, easterly fetch. The relative percentage of the number of trajectories included in each cluster is also shown.

The results of this study indicated that clusters from the northeast and those which were shorter in length (clusters 5 and 4 in Figure 2-9, respectively) accounted for not only the highest background ozone concentrations entering the Houston area, but also the highest local maximum ozone concentrations (TCEQ, 2009). Clusters that were from the south and southeast (clusters 1 and 2 in Figure 2-9, respectively) corresponded to days characterized by the lowest background ozone levels, likely due to clean air transported

from the Gulf of Mexico. A regression analysis showed that grouping average 8-hour ozone concentrations by directional back trajectory clusters can account for approximately 24 ppb and 30 ppb of variation in estimates of background concentrations and maximum ozone concentrations, respectively (Sullivan, 2009). Additional statistical analysis revealed a significant linear relationship between mean area minimum and maximum 8-hour average ozone concentrations by trajectory cluster, suggesting that trajectory cluster is an indicative factor of severity for both maximum and background ozone concentrations in the Houston area (Sullivan, 2009).

Taken collectively, these back trajectory analysis techniques provide a characterization of the types of wind patterns and source regions that lead to high concentrations of air pollutants. In their current form, however, they are primarily qualitative, suggesting the types of photochemical episodes that would be suitable for more detailed analyses. This has been valuable when the computational resources required by photochemical models limited detailed analyses to a few days to a week. Currently, long-term (seasonal and year-long) photochemical analyses are just becoming viable, and therefore systematic comparisons with photochemical models and a variety of back trajectory analyses need to be performed. This work will compare quantitative estimates of the extent, sources, and chemistry of regional ozone based on seasonal photochemical models to the results from these more qualitative tools.

2.7 PHOTOCHEMICAL MODELING TECHNIQUES

A variety of photochemical modeling tools have the ability to analyze the contributions of precursor emissions and transported ozone from different source regions (ENVIRON, 2004a). Photochemical modeling source apportionment studies have suggested that regional background ozone can significantly influence ozone concentrations (Webb et al., 2007). Due to the nonlinearity of the chemical mechanisms involved in ozone formation, as well as the fact that ozone formation involves the interaction between emissions that most likely come from varying sources, e.g., anthropogenic NO_x interacting with biogenic VOC, there is no single “correct” source apportionment analysis method.

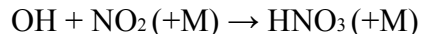
Photochemical modeling source apportionment tools belong to a category of mass balance analysis techniques, which have proven useful in identifying which sources contribute to ozone concentrations (Seigneur et al., 1999; Dunker et al., 2002b). Examples of other mass balance analysis techniques encountered in the literature include the Counter Species Method (Leone and Seinfeld, 1984); the Ozone Assignment Method (Bowman and Seinfeld, 1994); the Geographic Ozone Assessment Technology (Yarwood et al., 1997); the Ozone Precursor Assessment Technology (Yarwood et al., 1997); the Threaded Source Apportionment Modeling System (Deuel et al., 1997); the Decoupled Direct Method (Dunker, 1981); the zero-out analysis (EPA, 1999); the Ozone Source Apportionment Technology (Yarwood et al., 1997); and the Anthropogenic Precursor Culpability Assessment (Yarwood et al., 1997; Zhang et al., 2005). The source apportionment tools incorporated in this work include the final two from this list and are therefore discussed in further detail below.

Ozone Source Apportionment Technology (OSAT) is a photochemical modeling source apportionment method that provides information about the relationships between ozone concentrations and sources of precursors in the form of ozone source apportionments (ENVIRON, 2004a). It attributes all new ozone production to precursors that are present at the location (or source grouping) where ozone is being formed.

For each source grouping, ozone reaction tracers are used to track the fate of ozone precursor emissions of VOCs and NO_x , in addition to ozone formation attributed to these emissions. When ozone production at a given location and time is NO_x -limited, it makes sense to attribute ozone production to source groupings based on their contributions to the local NO_x and similarly to allocate based on VOC contributions when ozone formation is VOC-limited. Ozone production is allocated into VOC- or NO_x -limited fractions based on the ratio of hydrogen peroxide (H_2O_2) production to nitric acid (HNO_3) production (Webb et al., 2007). The following explanation for this basis is taken from the CAMx User Guide (ENVIRON, 2004b).

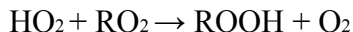
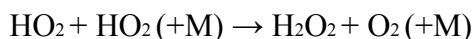
The sensitivity of ozone formation to VOCs and NO_x at any given time is attributable to the fate of radicals. The radical pool is often referred to as odd-hydrogen (HO_x) and is most usefully considered as the sum of OH,

HO₂ and RO₂ radicals. When NO_x is abundant, the main radical termination (i.e., HO_x removal) pathway is nitric acid formation, i.e.:



Under these conditions, ozone formation is limited by the rate at which radicals can be formed, which is generally referred to as the VOC-limited condition. Thus, nitric acid (HNO₃) production is indicative of VOC-limited ozone formation.

When NO_x is scarce, radical-radical reactions dominate the removal of HO_x, e.g.:



Under these conditions, ozone formation is limited by the availability of NO to react with HO₂ and RO₂ radicals, which is described as the NO_x-limited condition. HO₂ and RO₂ radicals that do not react with NO participate in peroxide formation. Thus, peroxide formation (H₂O₂ = hydrogen peroxide, or ROOH = organic hydroperoxides) is indicative of scarce NO_x, or NO_x-limited ozone formation.

Sillman (1995) has explored this situation to develop useful indicators of VOC vs. NO_x-limited ozone formation based on the ratio of peroxide production to nitric acid production. Sillman proposed that the transition between these conditions occurs when:

$$(\text{P}_{\text{H}_2\text{O}_2} + \text{P}_{\text{ROOH}}) / \text{P}_{\text{HNO}_3} = 0.5$$

The production rates of nitric acid (P_{HNO₃}) and hydrogen peroxide (P_{H₂O₂}) in each CAMx grid cell at each time step are readily accessible, but the production rate of organic peroxides (P_{ROOH}) is not readily accessible because the chemical mechanism does not explicitly track these species. The balance between P_{ROOH} and P_{H₂O₂} depends upon the relative production of HO₂ and RO₂ radicals, which is not highly variable within/across simulations. Accordingly, Sillman proposes the ratio above is equivalent to a transition point of:

$$\text{P}_{\text{H}_2\text{O}_2} / \text{P}_{\text{HNO}_3} = 0.35$$

In other words, when this ratio exceeds 0.35 ozone formation is NO_x-limited, and when this ratio is less than 0.35 ozone formation is VOC-limited. The photochemical model tracks the ozone produced at the same time that VOCs and NO_x from individual source groupings are consumed,

and based on the value of this ratio when the ozone is produced, assigns the ozone production to either VOC or NO_x emissions.

The Anthropogenic Precursor Culpability Assessment (APCA) is a variation of OSAT. OSAT apportions ozone formation based solely on the precursors that were present during ozone formation, whereas APCA modifies the OSAT method to account for the uncontrollable nature of biogenic emissions (emissions from vegetation). Ozone formation is only attributed to biogenic emissions by APCA when it is due to the interaction of biogenic VOCs with biogenic NO_x, resulting in greater ozone formation attributed to anthropogenic sources relative to biogenic sources when compared to the original OSAT tool. Both OSAT and APCA methods require that the sum of all source contributions add up to exactly 100% of the total ozone present, ensuring that all of the ozone is exactly accounted for (ENVIRON, 2004a).

The State of Texas and the EPA have also used zero-out analysis for assessing the impacts of transport (EPA, 1999). A zero-out modeling simulation is one in which anthropogenic emissions of ozone precursors (VOCs and NO_x) from a source region of interest are eliminated (or zeroed) in order to evaluate the impacts on ozone concentrations in another area (Webb et al., 2007). The resulting differences in ozone concentrations represent an estimate of the relative source contribution of the removed emissions source(s) to ozone levels. Unlike the OSAT and APCA methods, difficulties arise when determining source apportionments from zero-out differences because the sum of these differences over all sources does not equal the total ozone. Additionally, due to the fact that zero-out differences eliminate emissions within source areas, the chemistry of ozone formation can potentially be drastically altered, and separate runs must be performed for each emission source group to isolate each source region of interest. Nevertheless, the zero-out method can be evaluated easily over the entire modeling domain and has been widely used to evaluate source contributions to ozone levels (ENVIRON, 2004a).

Several source apportionment techniques were used in a study by Stoeckenius and Yarwood (ENVIRON, 2004a) to analyze the contributions of emissions from various regions in Texas and neighboring states to ozone concentrations above 85 ppb in the

DFW area based on modeling simulations of an ozone episode during August 13th-22nd, 1999 (Olague et al., 2007). OSAT results showed that biogenic emissions are a major contributor to ozone formation in Dallas-Fort Worth, reflecting the high contribution of biogenics to total VOC emissions (Olague et al., 2007). Results from the APCA analyses are illustrated in Table 2-4. On average, the continental ozone background (i.e. model boundary conditions) and transport from upwind sources had a larger contribution to elevated ozone levels during this episode (Olague et al., 2007). The results from zero-out analyses are consistent with APCA results in terms of rank ordering of source regions and locations of maximum impacts.

Table 2-4. Average APCA contributions to 8-hour ozone exceedances in the DFW area during August 15th-22nd, 1999 (ENVIRON, 2004a).

Source Category	Ozone Contribution (ppb)
Dallas-Fort Worth nonattainment area	40
Intra-state transport	12
Out-of-state transport	11
Horizontal and top boundary conditions	31
Total non-local contribution	54

ENVIRON (2005) also used the APCA technique with an updated photochemical model of the same 1999 time period. Results from this study indicated that, on average, anthropogenic emissions from other states contributed about 5 ppb on days with an 8-hour ozone exceedance in DFW (compare to 11 ppb in Table 2-4.).

The University of Texas at Austin (2004) performed a similar APCA analysis using the September 13th-20th, 1999 episode to evaluate the impacts of regional transport of ozone and its precursors for Austin and Victoria, Texas. These modeling simulations were designed to evaluate the impacts from boundary and initial conditions, geographic source regions, and emission source categories. The results support the conclusion that air quality in both cities is influenced by regional transport of ozone and its precursors from other areas within and outside the state of Texas. For each scenario, the boundary conditions were responsible for the maximum contribution to ozone concentrations, indicating the importance of the accuracy of these boundary conditions for photochemical

modeling. From these results, it may also be inferred that obtaining accurate estimates of ambient background ozone concentrations is also significant.

The application of various source apportionment techniques for an assessment of regional transport was performed as part of Texas Environmental Research Consortium (TERC) Project H60, a collaboration among ENVIRON, the University of North Carolina, and the University of Houston (Byun et al., 2006). Two modeling episodes were used in this study: June 19th-23rd, 2005 and August 30th-September 9th, 2005. The photochemical modeling simulations quantified the impact of regional transport on DFW ozone concentrations, revealing that the Texas intra-state contribution can exceed 15 ppb and is dominated by NO_x emissions, while the combination of contributions from neighboring states (Oklahoma, Arkansas, and Louisiana) contributed up to about 10 ppb. Results also showed that a 50% decrease in NO_x reductions in these neighboring states would be required to reduce daily maximum ozone concentrations in DFW by 4 ppb.

The results of a zero-out assessment performed by Webb et al. (2002) are shown in Table 2-5. For this analysis, photochemical modeling simulations were performed in which all of the anthropogenic (man-made) emissions in Texas were set equal to zero. The data in Table 2-5 shows the decreases in 8-hour average ozone concentrations that resulted in Houston. It is worthwhile to note that, while significant reductions in ozone concentrations can be achieved on most days by reducing emissions in Texas, there are days such as July 9th, 1995, when sources outside of Texas contribute to elevated ozone concentrations observed within the state.

Table 2-5. Results of simulations in which all anthropogenic emissions in Texas were set equal to zero (Webb et al., 2002).

Date simulated	Base case maximum 8-hour average ozone concentration in the Houston-Galveston area	All Texas “zero-out” maximum 8 hour average ozone concentration in the Houston-Galveston Area	Maximum difference between base case and all Texas “zero-out” in the Houston-Galveston Area
7/9/95	124	88	67
7/10/95	96	59	53
7/11/95	105	62	64
7/12/95	126	78	79

In another photochemical modeling zero-out analysis, McDonald-Buller et al. (2000) predicted ozone concentrations for several cases where all anthropogenic emissions in several cities in Texas were eliminated. Figure 2-10 shows the substantial differences in ozone concentrations that resulted when anthropogenic emissions in the 8-county Houston-Galveston non-attainment area were eliminated. Depending on the particular day (results are shown for July 2nd, 1996), differences in 8-hour ozone concentrations can be up to 20 ppb in Austin, 28 ppb in San Antonio, and up to 33 ppb and 71 ppb in Victoria and Beaumont-Port Arthur, respectively. Results from similar analyses performed for all other major urban areas in eastern Texas (Austin, DFW, and Beaumont-Port Arthur) indicate that all of these urban areas contribute to regional ozone concentration levels.

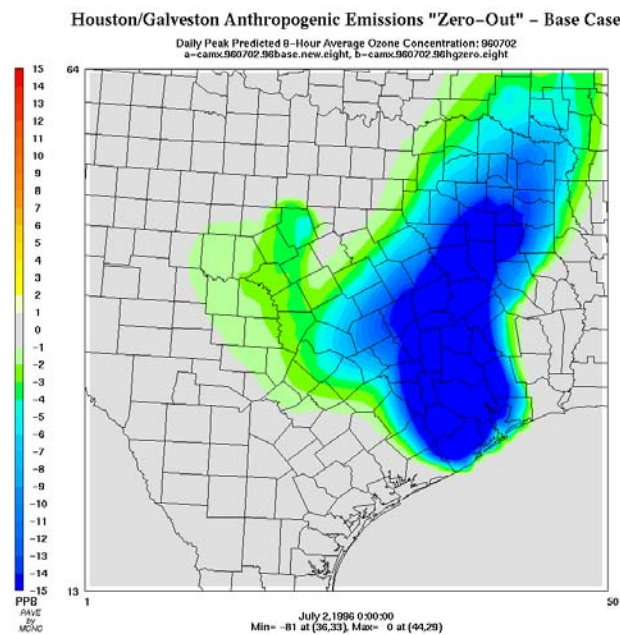


Figure 2-10. Difference in 8-hour average ozone concentrations between a base case simulation and a scenario with anthropogenic emissions in the 8-county Houston-Galveston non-attainment area set equal to zero for July 2nd, 1996 (McDonald-Buller et al., 2000).

In addition to contributions from major urban areas, ozone formation due to emissions in the rural regions of eastern Texas is also likely to be an important factor in determining regional ozone concentrations. Results of a study by Nobel et al. (2001)

support this finding. Figure 2-11 shows the difference in ozone concentrations between a base case simulation and a simulation, for the same day, where all NO_x emissions from electricity generating units in eastern Texas were set equal to zero. As the figure illustrates, the differences in ozone concentrations between the base case and the zero-out scenario can be more than 60 ppb in isolated areas and more than 30 ppb over larger regions.

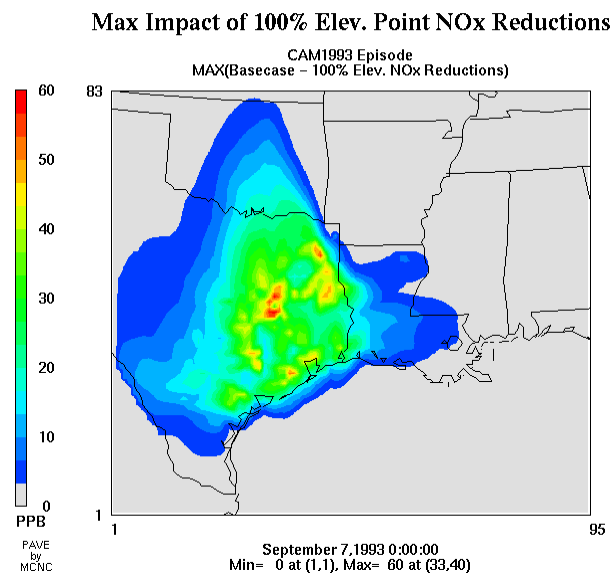


Figure 2-11. Differences in ozone concentrations between a base case simulation and a scenario where all NO_x emissions from electricity generating units were set equal to zero. Results are shown for September 7th, 1993 (Nobel et al., 2001).

Results from photochemical modeling source apportionment studies have also been relevant in formulating air quality regulatory policies. The EPA used the results of APCA and zero-out analyses as the technical foundation for the Clean Air Interstate Rule (CAIR), issued in March, 2005 (70 Fed. Reg. 231, 2 Dec. 2005). The EPA did not conclude that either approach was technically superior (Webb et al., 2007). The technical analysis primarily focused on the impacts of reducing emissions of sulfur dioxide and NO_x in 28 eastern states and the District of Columbia. The results of the EPA study concluded that the CAIR requires reduced emissions in upwind states that significantly

contributed to non-attainment of the NAAQS for ozone and fine particulate matter in downwind states (Webb et al., 2007).

In order to estimate the response of pollutant levels predicted by a photochemical model to changes in emissions, sensitivity analyses are generally useful to gain an understanding of which parameters and input variables (e.g., emission sources) influence the model output. Photochemical models provide various tools for advanced sensitivity analysis, and one in particular, known as the Direct Decouple Method (DDM), has been thoroughly discussed in the literature (Dunker, 1981, 1984; Milford et al., 1992; Gao et al., 1995; Yang et al., 1997). DDM uses local, time-dependant first-order derivatives to characterize the response of ozone concentrations to changes in input parameters such as emission levels and boundary/initial conditions (Dunker et al., 2002a, 2002b). More specifically, the method is based on the first-order sensitivity of species concentrations (S_p) to emissions, boundary concentrations, and initial concentrations by the following formula:

$$S_p(t) = \frac{\partial C_p(t)}{\partial \lambda}$$

where C_p is the time-varying concentration of species p and λ is an input parameter. The sensitivities reported by DDM are in units of ppb and represent the first

order term of the species concentration, $\frac{\partial C_p(t)}{\partial \lambda}(\lambda)$ (Webb et al., 2007).

The strengths and weaknesses of these source apportionment and sensitivity analysis techniques have been investigated in previous studies (Dunker et al., 2002a, b; Yarwood et al., 2003; Zhang et al., 2005; Webb et al., 2007). DDM and OSAT are both capable of quantifying the impacts of source regions and emission categories on local air quality. OSAT, unlike DDM, cannot account for negative sensitivities which were shown by Zhang et al. (2005) to cause inaccuracies when the influence of NO_x titration on ozone formation is significant (Webb et al., 2007). Additionally, due to the non-linear nature of ozone formation, source apportionment is not uniquely defined, whereas DDM sensitivity coefficients have a unique mathematical derivation (Webb et al., 2007). However, DDM first order coefficients alone are not necessarily accurate in representing non-linear

systems, and higher-order derivatives have been successful in more accurately characterizing the curvatures of such atmospheric responses (Hakami et al., 2003). This technique is referred to as High-order DDM (HDDM-3D), derived from the more conventional DDM-3D (Yang et al., 1997). Additionally, Zhang et al. (2005) found that DDM may be inaccurate for larger perturbations in input parameters and is better suited for small-to-moderate emission reductions of less than 40%. The computational intensity associated with DDM is also greater than OSAT and APCA. Zero-out analyses are an alternative brute-force approach for first-order sensitivities; however this requires that a separate modeling run be performed for each emission source group, which can also be a computational burden (Webb et al., 2007).

While all of these modeling tools have recognized limitations, results from these methods can provide a quantitative estimate of source contributions as well as a qualitative characterization of consistent patterns in the relative contributions of source areas. For this reason, they continue to be applied towards air quality planning initiatives and have in some cases (e.g., CAIR) provided the technical foundation for changes in air quality regulations.

2.8 IMPACTS OF OZONE TRANSPORT ON FEDERAL AIR QUALITY POLICY

The need for assessments of quantitative tools for regional pollutant transport is evident from the use of these tools in policy-making processes. Examples of commissions formed to address various transport pollutant control strategies within the U.S. include the Grand Canyon Visibility Transport Commission (GCVTC), Ozone Transport Commission (OTC) for the Northeastern U.S., and the Ozone Transport Assessment Group (OTAG), which covers regional ozone mitigation for the entire Eastern U.S.

In 1990, Congress amended the Clean Air Act and authorized further research and regional assessment reports on the issue of regional haze (Woodrow, 2000). Regional commissions formed to study and issue recommendations to EPA to address regional haze. Nine western states (Arizona, California, Colorado, Idaho, Nevada, New Mexico, Oregon, Utah, and Wyoming) were invited to participate in the GCVTC, which formed in

1991 to study, analyze, and make recommendations on regional haze affecting the Grand Canyon National Park and western U.S (Woodrow, 2000).

The OTC is another example of a multi-state organization created under the Clean Air Act (CAA) that incorporates several states in the northeastern U.S. with the purpose of coordinating reductions in air pollution that benefit the entire region. Primary responsibilities include advising the EPA on transport issues and developing and implementing regional solutions to the ground-level ozone problem in the Northeast and Mid-Atlantic regions. Current OTC members include Connecticut, Delaware, the District of Columbia, Maine, Maryland, Massachusetts, New Hampshire, New Jersey, New York, Pennsylvania, Rhode Island, Vermont, and Virginia.

OTAG is a partnership among the EPA, the Environmental Council of the States (ECOS), and various industrial and environmental groups. OTAG was established to assist states east of the Mississippi River in attaining the federal clean air standards for ozone and to develop regional strategies to address the issues within the area.

As ozone attainment becomes much more of a regional problem (as discussed in Chapter 1), the work of these groups will become increasingly important and tools for quantitatively assessing ozone transport on regional scales will become essential. As outlined in this Chapter, multiple observational tools and modeling tools have been applied to characterizing ozone transport. However, almost no studies have combined observational and modeling methods, and most studies have considered only limited study periods. This dissertation will examine how combinations of these observational and modeling tools can provide improved understanding of ozone transport.

2.9 REFERENCES

- Allen, D. T., G. McGaughey, and E. McDonald-Buller (2002), "Development of an Ozone Conceptual Model for Victoria", Final Report for Project UTA02-443, submitted to Capital Area Planning Council and TNRCC, October 2002.
- Armistead, R., and R. Dennis (2000), "NARSTO critical review of photochemical models and modeling", *Atmospheric Environment*, 34, 2283-2324.
- Bowman, F.M., and J.H. Seinfeld (1994), "Ozone Productivity of Atmospheric Organics", *Journal of Geophysical Research*, 99, 5309-5324.
- Breitenbach, P. (2003), "Dallas Fort Worth Ozone: Background and Transport Issues", Briefing for Science Coordinating Committee, Texas Commission on Environmental Quality, August 2003.
- Byun, D.W., et al. (2006), "Regional Air Pollution Transport Modeling: CMAQ HDDM Simulations", HARC Project H60 Final Report, August 2006.
- Cracknell, A.P., and H. Ladson (2007), *Introduction to Remote Sensing* (2nd edition), London: Taylor and Francis, ISBN 0849392551, OCLC 70765252.
- Deuel, H.P., R.E. Looker, and P.D. Guthrie (1997), "A UAM-V based threaded source-apportionment modeling system", Paper presented at the 90th Annual Meeting, Air and Waste Management Association, Toronto, Ontario, Canada, 8-13 June.
- Draxler, R.R. and G.D. Rolph (2003), HYSPLIT (HYbrid Single-Particle Lagrangian Integrated Trajectory), NOAA Air Resources Laboratory, Silver Spring, MD, Model access via the NOAA ARL READY website, available at <http://www.arl.noaa.gov/ready/hysplit4.html>, accessed March 2010.
- Dunker, A.M. (1981), "Efficient calculation of sensitivity coefficients for complex atmospheric models", *Atmospheric Environment*, 15, 1155-1161.
- Dunker, A.M. (1984), "The decoupled direct method for calculating sensitivity coefficients in chemical kinetics", *Journal of Chemical Physics*, 81, 2385.
- Dunker, A.M., G. Yarwood, J.P. Ortmann, and G. Wilson (2002a), "Comparison of source apportionment and source sensitivity of ozone in a three-dimensional air quality model", *Environmental Science & Technology*, 36, 2953-2964.

- Dunker, A.M., G. Yarwood, J.P. Ortmann, and G. Wilson (2002b), “The decoupled direct method for sensitivity analysis in a three-dimensional air quality model: Implementation, accuracy, and efficiency”, *Environmental Science & Technology*, *36*, 2965-2976.
- ENVIRON International Corporation (2002), “Conceptual Model of Ozone Formation in the Dallas/Fort Worth Ozone Non-Attainment Area”, Final report, Novato, CA, October 2002.
- ENVIRON International Corporation (2004a), “Dallas-Fort Worth Transport Project”, Final report prepared for the Houston Advanced Research Center (HARC), April 2004.
- ENVIRON International Corporation (2004b), User’s Guide – Comprehensive Air Quality Model with extensions (CAMx), Version 4.00, Novato, CA, available at <http://www.camx.com>.
- ENVIRON International Corporation (2005), “Dallas/Fort-Worth CAMx Modeling: Improved Model Performance and Transport Assessment”, Final report for HARC Project H35 (Phase 2), August 2005, available at http://www.tceq.state.tx.us/assets/public/implementation/air/am/docs/dfw/p1/H35_Phase2_FinalReport_20050831.pdf.
- Gao, D., W.R. Stockwell, and J.B. Milford (1995), “First-order sensitivity and uncertainty analysis for a regional-scale gas-phase chemical kinetic mechanism”, *Journal of Geophysical Research*, *100*, 23, 153-23, 166.
- Hakami, A., M.T. Odman., and A.G. Russell (2003), “High-order, direct sensitivity analysis of multidimensional air quality models”, *Environmental Science & Technology*, *37*, 2442-2452.
- Hakami, A., M.T. Odman, and A.G. Russell (2004), “Nonlinearity in atmospheric response: A direct sensitivity analysis approach”, *Journal of Geophysical Research*, *109*, D15303.
- Kemball-Cook, S., D. Parrish, T. Ryerson, U. Nopmongcol, J. Johnson, E. Tai, and G. Yarwood (2009), “Contributions of regional transport and local sources to ozone exceedances in Houston and Dallas: Comparison of results from a photochemical grid model to aircraft and surface measurements”, *Journal of Geophysical Research*, *114*, D00F02, doi: 10.1029/2008JD010248.
- Leone, J. A., and J. H. Seinfeld (1984), “Analysis of the characteristics of complex chemical reaction mechanisms: application to photochemical smog chemistry”, *Environmental Science & Technology*, *18*, 280–287, 1984.

- McDonald-Buller, E.C., A.A. Eusebi, Y. Kimura, M.M. Russell, and D.T. Allen (2000), "Impacts of Regional Control Strategies on Air Quality in Eastern and Central Texas: Zeroing Out Emissions in Each of the Non-Attainment and Near Non-Attainment Regions", Report submitted to the Texas Natural Resource Conservation Commission, January 2000.
- McGaughey, G., E. McDonald-Buller, and D.T. Allen (2002), "Development of an Ozone Conceptual Model for the Austin Area", Report submitted to the Capital Area Planning Council, and the Texas Natural Resource Conservation Commission, September 2002.
- McGaughey, G., C. Durrenberger, E.C. McDonald-Buller, and D.T. Allen (2005), "Assessing the Performance of the CAMx Photochemical Model: A Qualitative Comparison of Observed and Simulated Ozone Plumes on September 6, 2000 within the 4-km HGA Grid Domain", Report prepared for the City of Victoria, April 2005.
- McGaughey, G., C. Durrenberger, E.C. McDonald-Buller, and D.T. Allen (2006a), "Back-Trajectory Analyses on High and Low Ozone Days for the Dallas/Fort Worth and Houston/Galveston/Brazoria Ozone Nonattainment Areas for the Years 2001 through 2005", Report prepared for the TCEQ NTRD program, October 2006.
- McGaughey, G., C. Durrenberger, E.C. McDonald-Buller, and D.T. Allen (2006b), "Monthly Back-Trajectory Analyses on High and Low Ozone Days for the Texas Near Nonattainment Areas for the Years 2001 through 2005", Report prepared for the City of Victoria, August 2006.
- Milford, J.B., D. Gao, A.G. Russel, and G.J. McRae (1992), "Use of sensitivity analysis to compare chemical mechanisms for air quality modeling", *Environmental Science and Technology*, 26, 1179-1189.
- Neilsen-Gammon, J., J. Tobin, and A. McNiel (2005), "A Conceptual Model for Eight-Hour Ozone Exceedances in Houston Texas: Part I: Background Ozone Levels in East Texas", Final report for HARC project H-12, January 2005.
- Nobel, C.E., E. C. McDonald-Buller, Y. Kimura, and D.T. Allen (2001), "Accounting for spatial variation of ozone productivity in NOx emission trading," *Environmental Science and Technology*, 35, 4397-4407.
- Olaguer, E., H. Jeffries, G. Yarwood, and J. Pinto (2006), "Attaining the 8-hr Ozone Standard in East Texas: A Tale of Two Cities", *Journal of the Air & Waste Management Association (EM)*, October 2006 Issue, 26-30.
- OTCAIR reference, available at <http://www.otcair.org/>, accessed February 2008.

- Seigneur, C., B. Pun, and Y. Zhang (1999), "Review of methods for source apportionment in three-dimensional air quality models for particulate matter", *EPRI Tech. Rep. TR-112070*, Electr. Power Res. Inst., Palo Alto, CA.
- Seinfeld, J.H., and S.N. Pandis (1998), "Atmospheric Chemistry and Physics - from Air Pollution to Climate Change", John Wiley and Sons, New York, NY.
- Senff, C., et al. (2007), "Ozone Production and Flux Downwind of Houston and Dallas", Presented at the TexAQS II Principal Findings Data Analysis Workshop, May 2007.
- Sillman, S. (1995), "The Use of NO_y, H₂O₂, and HNO₃ as Indicators for Ozone – NO_x Hydrocarbon Sensitivity in Urban Locations", *Journal of Geophysical Research*, 100, 14,175-14,188.
- Sullivan, D. (2009), "Effects of Meteorology on Pollutant Trends", Final report to the Texas Commission on Environmental Quality, grant activities No. 582-5-86245-FY08-01, The University of Texas at Austin Center for Energy and Environmental Resources, Austin, TX, March 2009.
- Texas Commission on Environmental Quality, LEADS website reference, available at www.tceq.state.tx.us/air/monops, accessed January 2006.
- Texas Commission on Environmental Quality (2009), "Houston-Galveston-Brazoria Nonattainment Area Ozone Conceptual Model", Draft report prepared by the TCEQ Data Analysis Team, May 2009, available at http://www.tceq.state.tx.us/assets/public/implementation/air/am/modeling/hgb8h2/doc/HGB8H2_Conceptual_Model_20090519.pdf.
- The University of Texas at Austin (2004), "Analysis of the Impacts of Regional Transport on Air Quality in the Austin and Victoria Areas using Anthropogenic Precursor Culpability Assessment (APCA) Tool with the September 13-20, 1999 CAMx Photochemical Modeling Episode", The University of Texas at Austin Center for Energy and Environmental Resources Austin, TX, October 2004.
- U.S. Environmental Protection Agency (1999), "Draft Guidance on the Use of Models and Other Analyses in Attainment Demonstrations for the 8-hour Ozone NAAQS", EPA 454/R-99-004, U.S. Environmental Protection Agency, Research Triangle Park, NC.
- U.S. Environmental Protection Agency, OTAG website reference, available at <http://www.epa.gov/ttnnaqs/ozone/rto/otag/faq.html>, accessed February 2008.
- U.S. Environmental Protection Agency, AIRNow website reference, available at www.airnow.gov, accessed December 2008.

- Webb, A.M., C. Durrenberger, E.C. McDonald-Buller, and D.T. Allen (2002), "Texas Non-Attainment and Near Non-Attainment Zero-Out Modeling Runs for the July 7-12, 1995 episode", Report submitted to the Capital Area Planning Council and the Texas Natural Resource Conservation Commission, The University of Texas at Austin Center for Energy and Environmental Resources, Austin, TX, August 2002.
- Webb, A.M., C. Durrenberger, G. McGaughey, D.T. Allen, and E.C. McDonald-Buller (2007), "Comparison of Source Apportionment and Source Sensitivity Approaches for an Air Quality Analysis in Central and Southeast Texas", The University of Texas at Austin Center for Energy and Environmental Resources, Austin, TX, 2007.
- Woodrow, P. (2000), "Building Consensus among Multiple Parties: The Experience of the Grand Canyon Visibility Transport Commission", Final report prepared by CDR Associates, Boulder, Colorado.
- Yang, Y.J., J.G. Wilkinson, and A.G. Russell (1997), "Fast, direct sensitivity analysis of multidimensional photochemical models", *Environmental Science & Technology*, 31, 2859-2868.
- Yarwood, G., G. Wilson, R.E. Morris, and M.A. Yocke (1997), "User's guide to the ozone tool: Ozone source apportionment technology for UAM-IV", Report, S. Coast Air Quality Management District, Diamond Bar, CA.
- Yarwood, G., R.E. Morris, S. Lau, U. Ganesh, and G. Tonnesen (2003), "Guidance on the Application of CAMx Probing Tools", CRC Project A-37-2, Novato, CA.
- Zhang, J., and S. T. Rao (1999), "The role of vertical mixing in the temporal evolution of ground-level ozone concentrations," *Journal of Applied Meteorology*, 38, 12, 1674–1691.
- Zhang, Y., K. Vijayaraghavan, and C. Seigneur (2005), "Evaluation of three probing techniques in a three-dimensional air quality model", *Journal of Geophysical Research*, 110, D02305.

Chapter 3: Assessing the Magnitude of Regional Ozone Transport on a Seasonal Basis: Photochemical Modeling*

*a portion of this Chapter has been summarized and submitted for publication: Dionisio, M., E. McDonald-Buller, and D.T. Allen, “A Seasonal Analysis of Regional Transport of the Houston Urban Plume”, Extended Abstract 2010-A-919-AWMA, submitted for publication in the Proceedings of Air & Waste Management Association 103rd Annual Conference & Exhibition, Calgary, Alberta, Canada, June 2010.

3.1 INTRODUCTION

As mentioned in Chapter 1, ozone has a relatively long atmospheric lifetime and can be transported over distances of hundreds of kilometers. Recent research, in addition to the findings of this work, provides evidence that reducing the regional transport of ground-level ozone and ozone precursors will be necessary for many areas to attain the National Ambient Air Quality Standards (NAAQS), and suggests the need for regional approaches to air quality planning. The importance of these regional approaches will become increasingly critical as regulatory air quality standards undergo more stringent revisions. The goal of this Chapter will be to demonstrate, quantitatively, the importance of inter-city ozone transport over distances of hundreds of kilometers over the course of an entire ozone season. While qualitative analyses, and limited quantitative analyses have been performed to assess regional ozone transport, this work is the first detailed quantitative characterization of the importance of ozone transport over an entire ozone season using both photochemical modeling and ambient data. Regional transport of ozone in the State of Texas is used as a case study.

The State of Texas has consistently dealt with persistent regulatory ozone issues and has invested in large-scale research studies to characterize regional transport of air pollutants. For example, the Texas Air Quality Study performed in 2006 (TexAQS II) involved the establishment of a network of pollutant monitoring sites in the rural areas of eastern Texas. In comparison to the East Coast, where large urban areas are located in close proximity to one another, Texas contains multiple large urban regions separated by

largely rural regions. The addition of the rural monitoring network facilitated the tracking of plumes and long-range pollutant transport from sources within and outside of the state, and allowed pollutant concentrations to be measured in locations between urban areas, providing reasonable estimates of background ozone concentrations.

Furthermore, the Texas Commission on Environmental Quality (TCEQ) has adopted regional control strategies that required reductions from certain sources in counties outside of attainment areas. For example, air quality successes reported by the TCEQ include controls of NO_x and SO₂ emissions from power plants and stationary gas-fired engines in East Texas that have been implemented to improve air quality in DFW (<http://www.tceq.state.tx.us/implementation/air/airsuccess>). However, policies for precursor reductions for regional transport over larger scales, such as from Houston to Dallas, have not been adopted.

Plumes from urban areas in the State, such as the Houston-Galveston-Brazoria (HGB) region, are capable of making substantial contributions to the ozone, aerosol, and precursor concentrations in other urban and rural regions of the state. Among the findings of the TexAQS II study, the average ozone flux from Houston, emitted over the 8-hour photochemically active part of one day, is sufficient to produce a 10 ppb increase in ozone over an approximately 10,000 square mile area, assuming a 2-km deep boundary layer (Senff et al., 2007). While valuable, the measurements from aircraft and several of the rural surface monitors implemented during TexAQS II are only available for a small number of days. Photochemical models are capable of providing data on a more frequent basis, as well as predicting how air quality in a region will be affected by future emissions reductions resulting from federal, state, and local programs. Like all models of complex physical systems, there are uncertainties; nevertheless, photochemical models are recognized by Environmental Protection Agency (EPA) as the best tools available for developing plans to achieve clean air goals (<http://www.tceq.state.tx.us/implementation/air/airmod/overview>).

The work described in the remainder of this Chapter involves the combination of modeling tools and ambient measurements to characterize the behavior of diverse plumes originating from the HGB area, under varying meteorological and photochemical

conditions. A photochemical modeling source apportionment method was used to quantify the impacts of anthropogenic (man-made) emissions originating in HGB on four urban areas that currently violate or are close to violating the NAAQS for ozone: DFW, Austin, San Antonio, and Victoria. A seasonal photochemical modeling episode, spanning from May to September, 2002, was selected for a portion of this work to capture the potential impacts of plumes originating in Houston under various meteorological regimes. Similar analyses were performed for a more recent period in 2006, during which data from the rural monitoring network implemented as part of TexAQs II were available. The results presented in this Chapter will document the importance of the Houston urban plume on regional air quality. Subsequent chapters will then analyze the dominant chemical and physical processes associated with ozone transported in these plumes.

3.2 METHODOLOGY

3.2.1 Description of the Photochemical Model

Most 3-dimensional photochemical grid models used in air quality are designed to calculate concentrations of both inert and chemically reactive pollutant species by simulating atmospheric physical and chemical processes (ENVIRON, 2009). These calculations are based upon a governing continuity equation, which represents a mass balance in which all relevant processes (precursor emissions, transport, diffusion, chemical reactions, and removal processes) are mathematically expressed (ENVIRON, 2009).

The Comprehensive Air Quality Model with extensions (CAMx) is a U.S. EPA-approved Eulerian photochemical dispersion model that allows for an integrated assessment of gaseous and particulate air pollution over scales ranging from sub-urban to continental (ENVIRON, 2009). CAMx was selected for this work because it is currently being used by the State of Texas for attainment demonstrations in areas that have violated the NAAQS for ozone. A brief overview of the CAMx model governing algorithm and structure is presented here, summarized from the CAMx User Guide, which is publicly available at <http://www.camx.com>.

CAMx simulates the emission, dispersion, chemical reaction, and removal of pollutants in the troposphere by solving a concentration continuity equation for each chemical species (l) on a system of nested three-dimensional grids. The Eulerian continuity equation describes the time dependency of an average species concentration (c_l) within each grid cell volume as the sum of all applicable physical and chemical processes operating on that volume. This equation is expressed mathematically as a function of height (z) as:

$$\begin{aligned} \frac{\partial c_l}{\partial t} = & -\nabla_H \cdot V_H c_l + \left[\frac{\partial(c_l \eta)}{\partial z} - c_l \frac{\partial}{\partial z} \left(\frac{\partial h}{\partial t} \right) \right] + \nabla \cdot \rho K \nabla (c_l / \rho) \\ & + \left. \frac{\partial c_l}{\partial t} \right|_{Emission} + \left. \frac{\partial c_l}{\partial t} \right|_{Chemistry} + \left. \frac{\partial c_l}{\partial t} \right|_{Removal} \end{aligned}$$

where V_H is the horizontal wind vector, η is the net vertical “entrainment rate”, h is the layer interface height, ρ is atmospheric density, and K is the turbulent diffusion coefficient. The first term on the right-hand side represents horizontal advection, the second term represents net resolved vertical transport across an arbitrary space- and time-varying height grid, and the third term represents sub-grid scale turbulent diffusion. Chemistry is treated by simultaneously solving a set of reaction equations defined from specified chemical mechanisms, and removal includes both dry surface uptake (deposition) and wet scavenging by precipitation. Pollutant concentrations and state variables are defined at the center of each grid cell volume, representing the average values over the entire cell (known as an “Arakawa C” arrangement). Wind components, entrainment rates, and diffusion coefficients are defined at cell interfaces to represent the mass transfer entering and exiting each cell face.

CAMx incorporates two-way grid nesting, allowing for coarse grid spacing over a wide regional domain, while simultaneously applying fine grid nests where high resolution is desired. This grid nesting feature was applied to all CAMx simulations analyzed in this dissertation. Pollutant concentration information propagates into and out of all grid nests during model integration. Any number of grid nests can be specified in a single simulation, and grid spacing and vertical layer structures can vary from one grid nest to another. The nested grid capability allows for multiple air quality issues to be

addressed in the same model simulation, such as regional transport on the coarse grid scale, simultaneously providing fine resolution to address small-scale impacts in selected areas.

There are numerous “extensions” available within CAMx, including the source apportionment tools that are used in this work. Photochemical modeling source apportionment tools belong to a category of mass balance analysis techniques and are used to analyze the contributions of precursor emissions and transported ozone from various source regions. A detailed discussion of these methods and previous applications related to pollutant transport was included in Chapter 2. The work presented in this Chapter involves the zero-out method, which is briefly summarized here.

A zero-out model simulation is one in which anthropogenic emissions of ozone precursors (VOCs and NO_x) from a source region of interest are eliminated (or zeroed) in order to evaluate the impacts on ozone concentrations in another area (Webb et al., 2007). The resulting differences in ozone concentrations represent an estimate of the relative source contribution of the removed emissions source(s) to ozone levels. Difficulties arise because zero-out modeling does not provide source apportionments for non-linear systems (such as ozone formation); therefore, the sum of zero-out impacts over all sources will not equal the total concentration. Additionally, removing emissions sources has the potential to drastically alter the chemistry of ozone formation, and separate runs must be performed for each emission source group to isolate each source region of interest. Nevertheless, the zero-out method can be easily evaluated over the entire modeling domain and has been extensively used to evaluate source contributions to ozone levels (ENVIRON, 2009).

In this work, zero-out photochemical modeling simulations were performed with CAMx by eliminating all anthropogenic emissions in the 8-county HGB non-attainment area for periods during 2002 and 2006. A more detailed description of the nested grid arrangements and inputs used for each CAMx model simulation follows.

3.2.2 CAMx 2002 Seasonal Model Description and Inputs

ENVIRON has developed a CAMx seasonal ozone model for 2002, and model performance was evaluated during several high 8-hour ozone episodes (ENVIRON, 2006). This 2002 model is based on meteorology and emissions data developed by the Central Regional Air Planning Association (CENRAP) for annual modeling of regional haze and visibility (further information available at www.cenrap.org). The meteorological data have 36-km and 12-km resolution, thus the 2002 CAMx seasonal model does not include a 4-km grid. The model evaluation demonstrated that the performance of the model is generally within the EPA performance benchmarks, particularly on high ozone days, and is suitable for use in developing control strategies (ENVIRON, 2006). More specifically, the performance evaluation showed that the model has adequate resolution for characterizing regional contributions to ozone but lacks the fine resolution necessary to accurately represent local ozone contributions (ENVIRON, 2006).

Photochemical modeling was performed using version 4.31 of CAMx. The modeling period spans from May 1st to September 30th, 2002, at 36-km resolution with a two-way nested 12-km grid, as shown in Figure 3-1. The expanded 36-km coarse grid is outlined in black and spans the entire eastern U.S. and portions of Canada and Mexico. This grid has 69 grid cells in the east-west direction and 67 grid cells in the north-south direction. The 12-km nested grid, outlined in red, covers the eastern half of Texas and most of Louisiana, Mississippi, Arkansas, and Oklahoma. This grid has 96 grid cells in the east-west direction and 96 grid cells in the north-south direction. CAMx was run with 20 vertical layers (used for both grids) with the maximum height above 15 km and a surface layer thickness of 20 meters. The vertical grid structures for both CAMx and the meteorological model are shown in Appendix A.

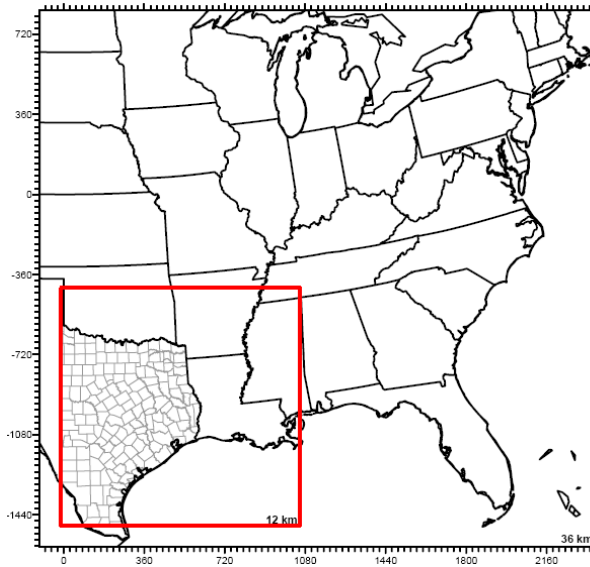


Figure 3-1. CAMx 36-km and 12-km (smaller rectangle outlined in red) modeling domains for the seasonal ozone model from May 1st-September 30th, 2002 (ENVIRON, 2006).

Meteorological inputs were developed with the Fifth-Generation Pennsylvania State University/National Center for Atmospheric Research (PSU/NCAR) Mesoscale Model (MM5). Biogenic emissions for 2002 were developed using the Global Biosphere Emissions and Interactions System (GloBEIS) model with MM5 temperatures and solar radiation derived from analysis of GOES satellite data and landuse/landcover (LULC) data developed for the TCEQ by ENVIRON (ENVIRON, 2006). The regional emission inventory data were developed from the CENRAP 2002 inventory data, which is based on the EPA 2002 National Emission Inventory with updates and corrections provided by CENRAP member states (which includes Texas) and the other Regional Planning Organizations (ENVIRON, 2006). The regional emission inventories were processed using the Emissions Processing System (EPS3) for the modeling domains shown in Figure 3-1.

As shown in Figure 3-2 below, five geographic regions were designated within the 12-km modeling domain as follows: the 5-county Austin area, Victoria county, the 8-county DFW area, the 4-county San Antonio area, and the 8-county HGB area. A base

case was run in addition to a zero-out case, in which all anthropogenic emissions from the 8-county HGB area were eliminated.

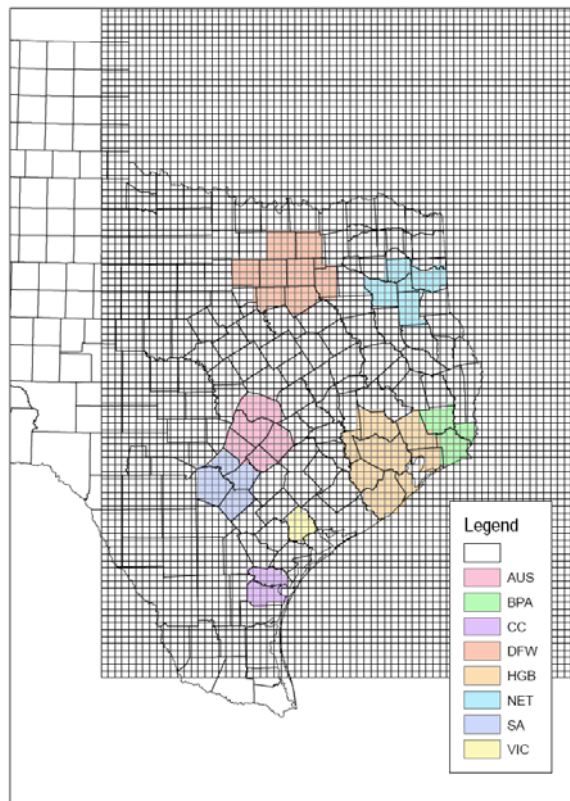


Figure 3-2. The CAMx 12-km nested modeling domain is shown, with selected counties for the Austin, Victoria, DFW, San Antonio, and HGB areas designated by the colors shown in the legend.

3.2.3 CAMx 2006 Model Description and Inputs

Because the TexAQS II field intensive provides an extraordinarily rich data base on which to evaluate hypotheses and validate modeling results, additional photochemical modeling episodes have been formulated for this period. The TCEQ has developed a model simulation using CAMx version 4.53 for August 13th through September 15th, 2006, with a focus to support attainment demonstration in HGB area for the ozone NAAQS.

Figure 3-3 depicts the horizontal modeling domains used in CAMx for this episode. The horizontal configurations of the 36-km (outlined in black) and 12-km (outlined in green) domains are similar to those shown in Figure 3-1. This configuration includes a nested 4-km grid encompassing both the Houston-Galveston and Beaumont-Port Arthur (HG/BPA) ozone non-attainment counties (outlined in blue). As mentioned in Section 3.2.1, the addition of nested domains with finer resolutions may result in more accurate replications of the ambient chemical reactions. Sensitivity analyses performed by the TCEQ and others for the now vacated 1-hour ozone SIP (December 2004) have suggested that a finer sub-domain within the 4-km HGB/BPA domain would be useful in order to resolve the narrow industrial plumes emanating from the Ship Channel and surrounding areas (TCEQ, 2009a). Therefore, this configuration includes a nested 2-km grid encompassing a major portion of the Houston-Galveston (HG) non-attainment counties (outlined in red).

Table 3-1 lists the dimensions for the CAMx grid domain and sub-grids. All of the grids are projected in a Lambert Conformal Projection (LCP) with the origin at 100 degrees W and 40 degrees N. The vertical configuration consists of a varying 28-layer structure within the 4-km horizontal domain and a varying 17-layer structure within the 12-km and 36-km horizontal domains (shown in Appendix A). The unique meteorology induced by the land/sea/bay effects and the unique mixture of industrial sources, which release pollutants across a wide range of elevations, indicated a need for finer resolution with more vertical layers, particularly near the surface, within the resolution 4-km domain (TCEQ, 2009a).

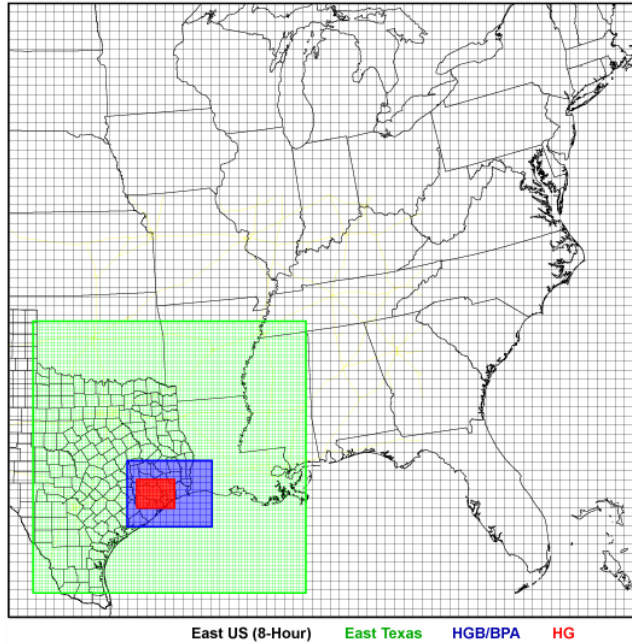


Figure 3.3. CAMx horizontal grid configuration for the model simulation during August 13th-September 15th, 2006 (TCEQ, 2009a).

Table 3-1. Dimensions of CAMx model grid domains and sub-domains (TCEQ, 2009a).

Domain Name	Cell Size (km)	Range (km)		Number of Cells	
		Easting	Northing	Easting	Northing
East US Domain	36 x 36	(-108,2376)	(-1584,828)	69	67
East Texas Sub-domain	12 x 12	(-12,1056)	(-1488,-420)	89	89
HGB/BPA Sub-domain	4 x 4	(-356,688)	(-1228,-968)	83	65
HG Sub-domain	2 x 2	(-394,542)	(-1154,-1042)	74	56

Similar to the 2002 seasonal model, biogenic emissions inputs were processed using version 3.1 of the GloBEIS biogenics emissions model (TCEQ, 2009a). The emissions modeling systems, including EPS3 and GloBEIS, use the same horizontal and vertical domains as CAMx, although the non-point source emissions categories within the 4-km domain are developed at a 2-km resolution and on-road mobile source emissions within the 36-km domain are developed at a 12-km resolution (TCEQ, 2009a).

The input to CAMx requires merged emissions files for both low-level and elevated emissions for each grid resolution, consisting of both biogenic and anthropogenic emissions. TCEQ provided one elevated point source file and four gridded low-level emission files for most simulation days. Several days in the episode were only modeled at the coarser 12-km resolution. Fine grid nests are typically applied where high resolution is needed for increased accuracy of results, although calculations are more rigorous for the finer grid domains. To minimize CAMx processing time, merged low-level emissions files with 4-km and 2-km resolutions were not created for several days during the episode that experienced relatively lower ozone concentrations in Houston. These low-level emission files contain emissions from all source categories merged into one emission rate for each modeled species and grid cell. TCEQ also provided gridded biogenic emissions files for the HG/BPA domain (see Figure 3-3) in 2-km resolution.

For this work, it was necessary to separate the low-level anthropogenic emissions from the merged emissions files as the zero-out procedure involved eliminating only these anthropogenic emissions from the HGB area. Files containing gridded biogenic emissions were only available for the 2-km Houston-Galveston (HG) nested grid, while low-level merged emissions files were available for all of the grid domains, but not for all of the days included in the modeled episode.

For the days with available emissions files on the 2-km fine grid resolution scale, isolating the anthropogenic emissions for this domain were relatively straightforward. The biogenic emissions were subtracted from the merged emissions to yield emissions representative of anthropogenic emissions. A factor of zero was then applied to the anthropogenic emissions for all grid cells included in the 8-county HGB region, which was defined in Figure 3-2. This “spatially-masked” anthropogenic emission file was re-merged with the biogenic emission file to yield the merged low-level emission file. For the HG/BPA 4-km domain, the biogenic emission file was first aggregated, or merged, into 4-km resolution. Following the same processing sequence as for the HG 2-km domain yielded the “zero-out” merged low level emission file for the 4-km domain.

For days when the HG/BPA 4-km domain and HG 2-km domain were disabled (i.e. CAMx only enables the EUS 36-km and ETX 12-km domains), it was necessary to

alter the emission rate in the 12-km resolution emission file. At the time of the simulation, biogenic emission files derived from 12-km GloBEIS modeling were not publicly available from TCEQ. Therefore, emissions in the 2-km resolution biogenic emission files were spatially aggregated into 12-km resolution and used as a surrogate for 12-km biogenic emission file. The same masking and re-merging procedures for the 2-km and 4-km resolution files were followed for 12-km resolution files for the days where ETX 12-km domain is the finest resolution domain covering the Houston Galveston 8-county region.

It should be noted that this aggregation method of averaging emissions over coarser resolutions do not generate the same emission rate as if the emissions had been distributed across these domains using an emissions model such as GloBEIS. GloBEIS calculates biogenic emission rates based as a non-linear function of various input parameters, such as land coverage and environmental conditions, for each grid cell at the specified resolution of the grid domain. Due to this non-linearity, the aggregation method results in a slight discrepancy from GloBEIS estimates when calculating emission rates for grid cells of a larger area within a coarser domain. Additionally, CAMx disregards emission rates from coarser resolution files if a nested grid of finer resolution exists for a particular geographic location. The HG/BPA 4-km domain and HG 2-km domain cover the region where the emission rate was modified for this work (the 8 counties in HGB). Therefore, no modifications for the ETX 12-km and EUS 36-km domains were needed for the days when all four domains are enabled in the CAMx model.

For the 12-km grid domain, however, the biogenic emissions files only contained emissions for the area which overlaps with 4-km grid. In order to successfully isolate anthropogenic emissions in the 12-km grid domain for the zero-out analysis, three emissions files were created containing the following:

1. All merged (biogenic and anthropogenic) emissions within the 12-km domain, excluding the HG/BPA 4-km domain. This was obtained by disabling emissions in all grid cells within the HG/BPA 4-km domain from the all-inclusive low-level emissions file.

2. Only biogenic emissions within the 12-km domain area that overlaps the HG/BPA 4-km domain, obtained by aggregating the 2-km resolution biogenic emissions file.
3. Only anthropogenic emissions within the 12-km domain area that overlaps the 8-county HGB region, obtained by the subtraction of “2” from “1”.

This successfully isolated HGB anthropogenic emissions for the 12-km grid domain. A factor of zero was then applied to these emissions for all grid cells included in the 8-county HGB region. Merging this resulting emissions file with the first and second files yields the appropriate configuration for the 12-km grid domain for the zero-out scenario, with only biogenic emissions present in the 8-county HGB region, and biogenic and anthropogenic emissions present in the remainder of the domain.

3.3 RESULTS

3.3.1 CAMx Seasonal Episode: May 1st to September 30th, 2002

The CAMx zero-out results are summarized as maximum differences in 8-hour ozone concentrations between the base case and the zero-out scenario over all grid cell hours, which is indicative of the quantitative impacts that anthropogenic precursor emissions from HGB had on four urban areas in East Texas during this seasonal period. This maximum zero-out difference was calculated by Equation 3.1 as:

$$\text{Maximum Difference} = \max_{g,h} \{ C_{g,h}^{\text{basecase}} - C_{g,h}^{\text{zero-out}} \} \quad (\text{Equation 3.1})$$

where $C_{g,h}$ is the modeled 8-hour ozone concentration (in ppb) in grid cell g at hour h . Figure 3-4 illustrates these maximum differences in 8-hour ozone concentrations for DFW, Austin, San Antonio, and Victoria for each day in the seasonal episode.

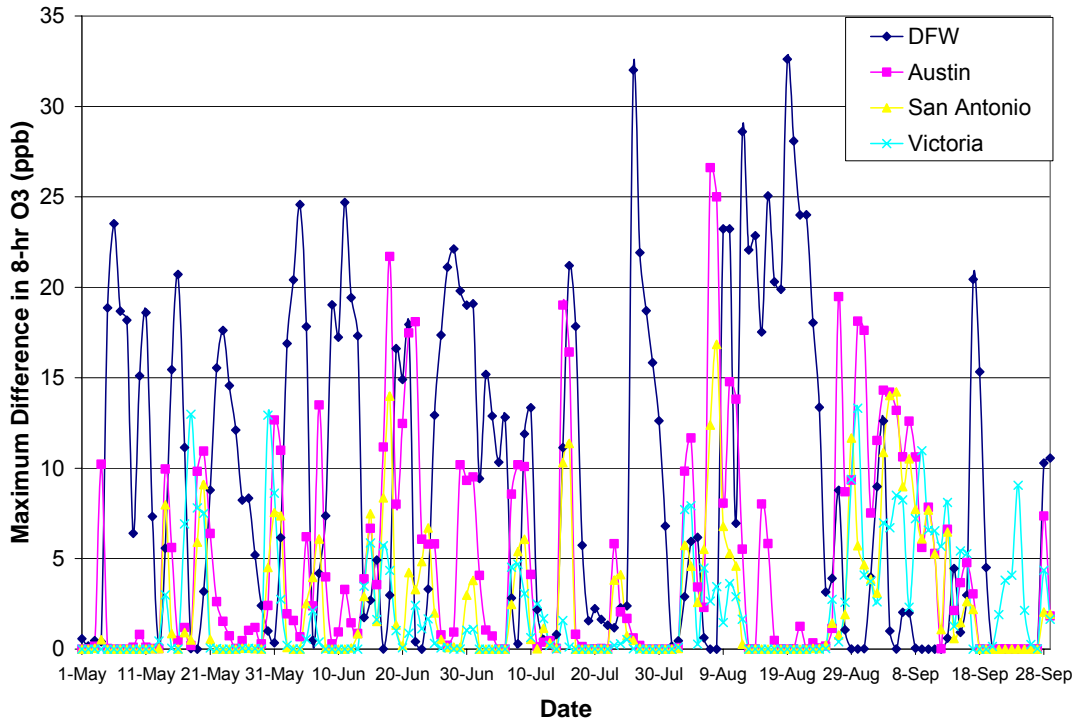


Figure 3-4. Maximum 8-hour ozone differences between the CAMx base case and the zero-out case (as calculated by Equation 3.1) for May 1st-September 29th, 2002.

Table 3-2 lists the seasonal peak and average maximum differences of 8-hour ozone concentrations. The average maximum difference is the average of the values calculated by Equation 3.1 across all days from May 1st-September 29th, 2002. Table 3-2 also shows the peak and average differences in the maximum 8-hour ozone concentrations for both modeling simulations. The difference in the maximum 8-hour ozone concentration is calculated by Equation 3.2 as:

$$\text{Difference in Maximum} = \left\{ \max[C_{g,h}^{\text{basecase}}] - \max[C_{g,h}^{\text{zero-out}}] \right\} \quad (\text{Equation 3.2})$$

where $C_{g,h}$ is the modeled 8-hour ozone concentration (in ppb) in grid cell g at hour h . The average difference in the maximum 8-hour ozone concentration is the average of the values calculated by Equation 3.2 across all days from May 1st-September 29th, 2002.

Table 3-2. Maximum and average values of maximum differences in 8-hour ozone concentrations (as calculated by Equation 3.1) and differences in peak 8-hour ozone concentrations (as calculated by Equation 3.2) between the CAMx base case and zero-out case. Results are based on modeling output from May 1st-September 29th, 2002.

Region	Highest Max Difference in 8-hr O3 (ppb)	Average Max Difference in O3 (ppb)	Highest Difference in Max 8-hour O3 (ppb)	Average Difference in Max 8-hour O3 (ppb)
DFW	33	9	12	2
Austin	27	5	10	1
San Antonio	17	2	6	1
Victoria	13	2	11	1

As evident in Figure 3-4 and Table 3-2, DFW experienced the largest magnitudes of 8-hour ozone concentration zero-out differences during this period, followed by Austin, San Antonio, and Victoria. The differences in predicted 8-hour maximum ozone concentrations are more evenly distributed among the regions. Correlations of the maximum 8-hour ozone zero-out differences were also examined to determine if, and to what extent, zero-out differences in ozone concentrations affect more than one region in East Texas on the same day. The coefficients of correlation are shown in Table 3-3. These data show the expected results that the effect on Austin is well correlated with San Antonio, the effect on San Antonio is well-correlated with Victoria (to a lesser extent), and the effect on DFW is negatively correlated with the other three regions.

Table 3-3. Correlations of CAMx zero-out maximum 8-hour ozone differences.

Correlations	Austin	San Antonio	DFW	Victoria
Austin	1.00			
San Antonio	0.75	1.00		
DFW	-0.24	-0.37	1.00	
Victoria	0.36	0.54	-0.46	1.00

While the data presented in Figure 3-4 also show a large variability in the maximum differences of 8-hour ozone concentrations between the base case and the zero-out case, these differences can be significant and can impact regions for a series of consecutive days. For example, from August 12th-23rd, DFW experienced predicted zero-

out differences in 8-hour ozone concentrations larger than 15 ppb. In order to investigate seasonal trends, examine the variation of HGB impacts on regional ozone concentrations, and draw conclusions from this extensive modeling period, results were further categorized in a variety of ways.

Figure 3-5 illustrates the distribution of the frequencies of maximum 8-hour ozone differences for each region that resulted from the zero-out method. Results are summarized as the number of days within the 152-day modeling period characterized by maximum 8-hour ozone differences falling within the specified ranges. It should be noted that these CAMx numerical results are carried out to three decimal places, although for simplicity this is not shown in the figure; therefore, a maximum ozone difference of 4.59 ppb, for example, would be grouped with the 0-5 ppb bin. Table 3-4 summarizes the same data on a percentage basis, based on 152 days included in the analysis.

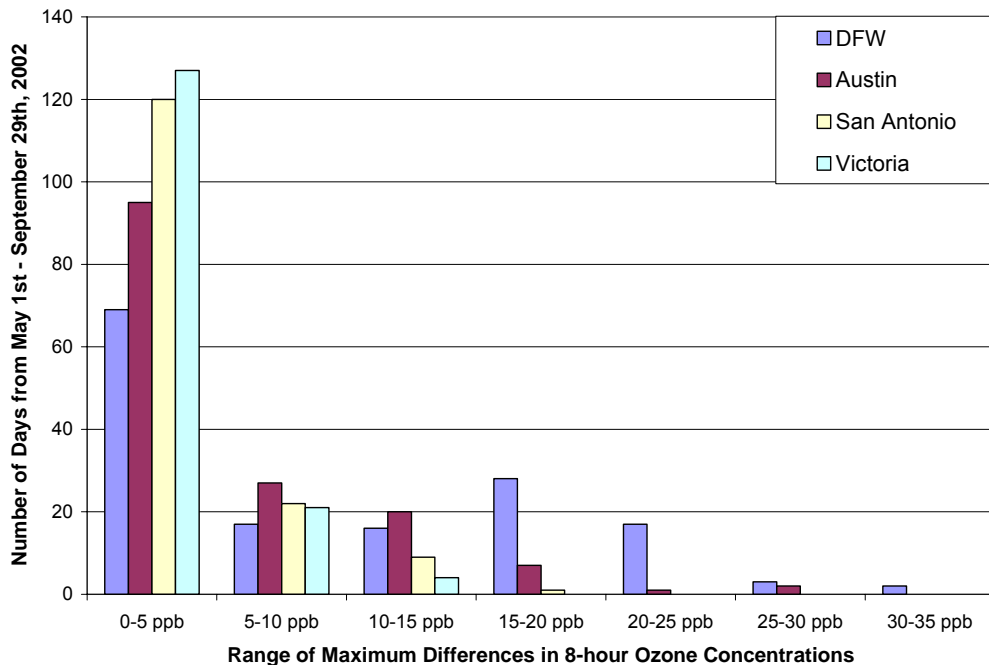


Figure 3-5. Number of days characterized by maximum 8-hour ozone differences between the CAMx base case and zero-out scenario (as calculated by Equation 3.1) within the specified ranges. Results are included for the CAMx modeling period of May 1st-September 29th, 2002.

Table 3-4. Percentage of days with predicted maximum 8-hour ozone differences between the CAMx base case and zero-out scenario (as calculated by Equation 3.1) within the specified ranges. Results are included for 152 days within the CAMx modeling period of May 1st–September 29th, 2002.

Region	0-5 ppb	5-10 ppb	10-15 ppb	15-20 ppb	20-25 ppb	25-30 ppb	30-35 ppb
DFW	45%	11%	11%	18%	11%	2%	1%
Austin	63%	18%	13%	5%	1%	1%	0%
San Antonio	79%	14%	6%	1%	0%	0%	0%
Victoria	84%	14%	3%	0%	0%	0%	0%

For all four regions, the largest number of days experienced maximum differences in modeled 8-hour ozone concentrations ranging from 0-5 ppb. For Austin, San Antonio, and Victoria, as the range of maximum 8-hour ozone differences increases, the number of days included in each range decreases. For DFW, however, there is more variability in the distribution of frequencies. A larger percentage of days within the modeling period are characterized by maximum 8-hour ozone differences ranging from 15-20 ppb and 20-25 ppb than in any other region. Additionally, contributions to 8-hour ozone concentrations in DFW were significantly impacted for longer periods of consecutive days, as shown in Figure 3-4.

The form of the NAAQS influences how these percentages should be interpreted. The National Ambient Air Quality Standard for ozone is based on the four highest ozone concentrations of each season (the highest 3% of the 152 days). Therefore, the fact that transport to Dallas-Fort Worth from Houston contributes more than 20 ppb on 14% of all days is significant when the region seeks to attain a maximum ozone concentration of 60-70 ppb on the days with highest concentration.

To examine regional impacts from HGB during elevated ozone days, the seasonal zero-out data were categorized by ambient 8-hour ozone concentrations. Daily maximum 8-hour ozone concentrations were extracted from the EPA Air Quality System (AQS) database for surface monitors in DFW, Austin, San Antonio, and Victoria with data available during May 1st–September 29th, 2002 (<http://www.epa.gov/ttn/airs/airsaqs>). From these measurements, the highest 8-hour ozone concentration was selected for each day and region.

Table 3-5 presents the distribution of the frequencies of maximum 8-hour ozone differences between the CAMx base case and zero-out scenario for days in this period with ambient 8-hour ozone concentrations above 70 ppb. These days were selected for each region if any monitor located within that region measured an 8-hour ozone concentration above the threshold. Similar to Table 3-4, results are summarized as a percentage of days exceeding the threshold, grouped by ascending ranges of zero-out maximum 8-hour ozone differences. For each region, the total number of days characterized by a local 8-hour ozone measurement above 70 ppb is also shown.

Table 3-5. Percentage of days with predicted maximum 8-hour ozone differences between the CAMx base case and zero-out simulations (as calculated by Equation 3.1) within the specified ranges. Days included for each region (specified as “total days”) are characterized by local surface measurements of 8-hour ozone concentrations above 70 ppb during May 1st–September 29th, 2002.

Region	0-5 ppb	5-10 ppb	10-15 ppb	15-20 ppb	20-25 ppb	25-30 ppb	30-35 ppb
DFW (62 total days)	65%	10%	11%	8%	5%	2%	0%
Austin (19 total days)	32%	26%	21%	16%	5%	0%	0%
San Antonio (37 total days)	57%	32%	8%	3%	0%	0%	0%
Victoria (11 total days)	45%	45%	9%	0%	0%	0%	0%

With the exception of Victoria, the largest number of days with ambient 8-hour ozone concentrations above 70 ppb for each region coincides with maximum zero-out differences in 8-hour ozone concentrations ranging from 0-5 ppb. In comparison to the data shown in Table 3-4, for days with ambient 8-hour ozone concentrations above 70 ppb in DFW, a relatively larger percentage of days are characterized by maximum differences in 8-hour ozone concentrations of 0-5 ppb, and differences of 15-20 ppb and 20-25 ppb are less frequent. This is not the case for the other three regions. Maximum zero-out 8-hour ozone differences ranging from 5-20 ppb occur more frequently during days with ambient 8-hour ozone concentrations above 70 ppb for these areas. For Austin, maximum zero-out ozone differences above 10 ppb resulted for over 40% of these days.

Results were further categorized to compare days with elevated ambient ozone levels and days with large differences in modeled ozone concentrations between the base case and zero-out simulations. Tables 3-6 through 3-9 include ambient and predicted maximum 8-hour ozone concentrations for the four regions, as well as the maximum differences in 8-hour ozone concentrations between the two modeling cases, as calculated by Equation 3.1. Data is shown for the days characterized by the ten highest ambient 8-hour ozone concentrations.

Table 3-6. Ambient and modeled maximum 8-hour ozone concentrations and maximum differences in 8-hour ozone concentrations between the CAMx base case and zero-out case (as calculated by Equation 3.1) for DFW. Results are shown for days with the ten highest ambient 8-hour ozone concentrations during May 1st–September 29th, 2002.

Date	Maximum Difference in O3 (ppb)	CAMx Base Case Max O3 (ppb)	CAMx Zero-Out Case Max O3 (ppb)	Ambient 8-hr Max O3 (ppb)
6/23/2002	0	93	93	114
6/24/2002	3	107	107	122
6/25/2002	13	84	80	99
7/8/2002	0	123	123	114
7/9/2002	12	106	105	113
8/7/2002	0	98	98	106
8/9/2002	23	87	87	127
9/11/2002	0	86	86	105
9/13/2002	1	90	90	101
9/14/2002	4	107	105	99

Table 3-7. Ambient and modeled maximum 8-hour ozone concentrations and maximum differences in 8-hour ozone concentrations between the CAMx base case and zero-out case (as calculated by Equation 3.1) for Austin. Results are shown for days with the ten highest ambient 8-hour ozone concentrations during May 1st–September 29th, 2002.

Date	Maximum Difference in O3 (ppb)	CAMx Base Case Max O3 (ppb)	CAMx Zero-Out Case Max O3 (ppb)	Ambient 8-hr Max O3 (ppb)
6/18/2002	22	86	82	82
6/23/2002	6	82	79	92
6/24/2002	6	92	90	100
6/25/2002	6	65	63	75
8/30/2002	18	90	87	79
9/11/2002	5	82	82	76
9/12/2002	0	112	112	87
9/13/2002	7	97	97	96
9/14/2002	2	76	76	91
9/27/2002	0	71	71	75

Table 3-8. Ambient and modeled maximum 8-hour ozone concentrations and maximum differences in 8-hour ozone concentrations between the CAMx base case and zero-out case (as calculated by Equation 3.1) for San Antonio. Results are shown for days with the ten highest ambient 8-hour ozone concentrations during May 1st–September 29th, 2002.

Date	Maximum Difference in O3 (ppb)	CAMx Base Case Max O3 (ppb)	CAMx Zero-Out Case Max O3 (ppb)	Ambient 8-hr Max O3 (ppb)
6/17/2002	8	70	70	107
6/18/2002	14	76	73	104
6/23/2002	5	78	75	97
6/24/2002	7	89	86	110
6/25/2002	2	69	68	99
8/6/2002	6	96	95	100
8/30/2002	6	83	83	98
8/31/2002	5	88	86	97
9/12/2002	1	112	112	111
9/13/2002	6	98	98	97

Table 3-9. Ambient and modeled maximum 8-hour ozone concentrations and maximum differences in 8-hour ozone concentrations between the CAMx base case and zero-out case (as calculated by Equation 3.1) for Victoria. Results are shown for days with the ten highest ambient 8-hour ozone concentrations during May 1st–September 29th, 2002.

Date	Maximum Difference in O3 (ppb)	CAMx Base Case Max O3 (ppb)	CAMx Zero-Out Case Max O3 (ppb)	Ambient 8-hr Max O3 (ppb)
6/17/2002	6	70	66	73
6/18/2002	4	64	63	74
6/22/2002	2	62	62	78
6/23/2002	1	67	67	74
8/29/2002	9	77	75	71
8/30/2002	13	81	78	80
9/11/2002	7	65	61	73
9/12/2002	6	99	97	86
9/13/2002	8	90	82	93
9/14/2002	1	56	56	75

Tables 3-10 through 3-13 present similar data for the four regions, although results are shown for days with the ten highest 8-hour ozone differences between the base case and zero-out case (as calculated by Equation 3.1). A comparison between both sets of tables shows that days characterized by the highest ambient 8-hour ozone concentrations do not necessarily correspond to large differences in modeled 8-hour ozone concentrations for the zero-out simulation, which is consistent with data shown in Table 3-5. However, there are a number of days with both high contributions from inter-city transport and high total ozone concentrations. This suggests that to reduce all days below 70 ppb (as required by the ozone NAAQS), the role of inter-city transport specifically, and ozone transport over hundreds of kilometers more generally, will need to be understood. Further characterizations of days in this seasonal time period, including examining the relationships between ozone concentrations and predominant meteorological factors, are discussed in Appendix B.

Table 3-10. Ambient and modeled maximum 8-hour ozone concentrations and maximum differences in 8-hour ozone concentrations between the CAMx base case and zero-out case (as calculated by Equation 3.1) for DFW. Results are shown for days with the ten highest 8-hour ozone differences between the base case and zero-out case, during May 1st–September 29th, 2002.

Date	Maximum Difference in O3 (ppb)	CAMx Base Case Max O3 (ppb)	CAMx Zero-Out Case Max O3 (ppb)	Ambient 8-hr Max O3 (ppb)
5/6/2002	24	66	56	45
6/4/2002	25	78	73	50
6/11/2002	25	80	78	41
7/26/2002	32	78	76	63
8/12/2002	29	75	70	71
8/16/2002	25	79	66	49
8/19/2002	33	76	67	48
8/20/2002	28	76	68	44
8/21/2002	24	72	62	44
8/22/2002	24	78	67	54

Table 3-11. Ambient and modeled maximum 8-hour ozone concentrations and maximum differences in 8-hour ozone concentrations between the CAMx base case and zero-out case (as calculated by Equation 3.1) for Austin. Results are shown for days with the ten highest 8-hour ozone differences between the base case and zero-out case, during May 1st–September 29th, 2002.

Date	Maximum Difference in O3 (ppb)	CAMx Base Case Max O3 (ppb)	CAMx Zero-Out Case Max O3 (ppb)	Ambient 8-hr Max O3 (ppb)
6/18/2002	22	86	82	82
6/21/2002	17	74	64	47
6/22/2002	18	80	78	72
7/15/2002	19	56	48	27
7/16/2002	16	48	48	18
8/7/2002	27	98	97	63
8/8/2002	25	95	95	49
8/27/2002	19	63	60	52
8/30/2002	18	90	87	79
8/31/2002	18	100	95	73

Table 3-12. Ambient and modeled maximum 8-hour ozone concentrations and maximum differences in 8-hour ozone concentrations between the CAMx base case and zero-out case (as calculated by Equation 3.1) for San Antonio. Results are shown for days with the ten highest 8-hour ozone differences between the base case and zero-out case, during May 1st–September 29th, 2002.

Date	Maximum Difference in O3 (ppb)	CAMx Base Case Max O3 (ppb)	CAMx Zero-Out Case Max O3 (ppb)	Ambient 8-hr Max O3 (ppb)
6/18/2002	14	76	73	104
7/15/2002	10	49	47	33
7/16/2002	11	44	44	37
8/7/2002	12	103	103	86
8/8/2002	17	74	73	83
8/29/2002	12	80	80	43
9/3/2002	11	65	61	77
9/4/2002	14	57	57	49
9/5/2002	14	59	55	49
9/7/2002	11	58	55	38

Table 3-13. Ambient and modeled maximum 8-hour ozone concentrations and maximum differences in 8-hour ozone concentrations between the CAMx base case and zero-out case (as calculated by Equation 3.1) for Victoria. Results are shown for days with the ten highest 8-hour ozone differences between the base case and zero-out case, during May 1st–September 29th, 2002.

Date	Maximum Difference in O3 (ppb)	CAMx Base Case Max O3 (ppb)	CAMx Zero-Out Case Max O3 (ppb)	Ambient 8-hr O3 (ppb)
5/18/2002	13	54	52	52
5/30/2002	13	71	64	64
5/31/2002	9	64	57	66
8/29/2002	9	77	75	71
8/30/2002	13	81	78	80
9/5/2002	9	54	48	55
9/6/2002	8	53	50	44
9/9/2002	11	60	50	34
9/13/2002	8	90	82	93
9/24/2002	9	62	57	54

3.3.2 Photochemical Modeling Results for 2006

A similar zero-out analysis was performed for the modeling period of August 13th through September 15th, 2006. The TexAQS field programs in 2000 and 2006 provided evidence that significant reductions in highly reactive NO_x and VOC emissions in the

HGB area have been achieved over the past decade. Findings from the TexAQS II study reported indications that ethene (or ethylene, the lightest HRVOC and an important ozone precursor) emissions from industrial sources in the Houston area decreased as much as 40% between 2000 and 2006 (TCEQ, 2009b). Among other TexAQS II findings, inventories for NO_x point sources at petrochemical facilities have suggested that NO_x emissions in the Houston Ship Channel substantially decreased between 2000 and 2006, and measurements from aircraft were qualitatively consistent with these decreases (TCEQ, 2009b). A possible inference from these findings is that, in comparison to the 2002 seasonal results, the predicted impacts to ozone levels for regions in East Texas due to transport from HGB may be less severe and/or less frequent in 2006.

Figure 3-6 below illustrates the maximum 8-hour ozone differences (as calculated by Equation 3.1) that resulted for DFW, Austin, San Antonio, and Victoria when anthropogenic emissions in HGB were eliminated for all days during August 13th-September 14th, 2006. Table 3-14 lists the peak and average of the maximum differences of 8-hour ozone concentrations (as calculated by Equation 3.1), as well as the peak and average values of differences in the maximum 8-hour ozone concentrations (as calculated by Equation 3.2) for both modeling simulations. The results in Table 3-14 were calculated across all days from August 13th-September 14th, 2006. For comparative purposes, Table 3-14 summarizes results for the 2006 period, and also for the same time period in the 2002 simulations.

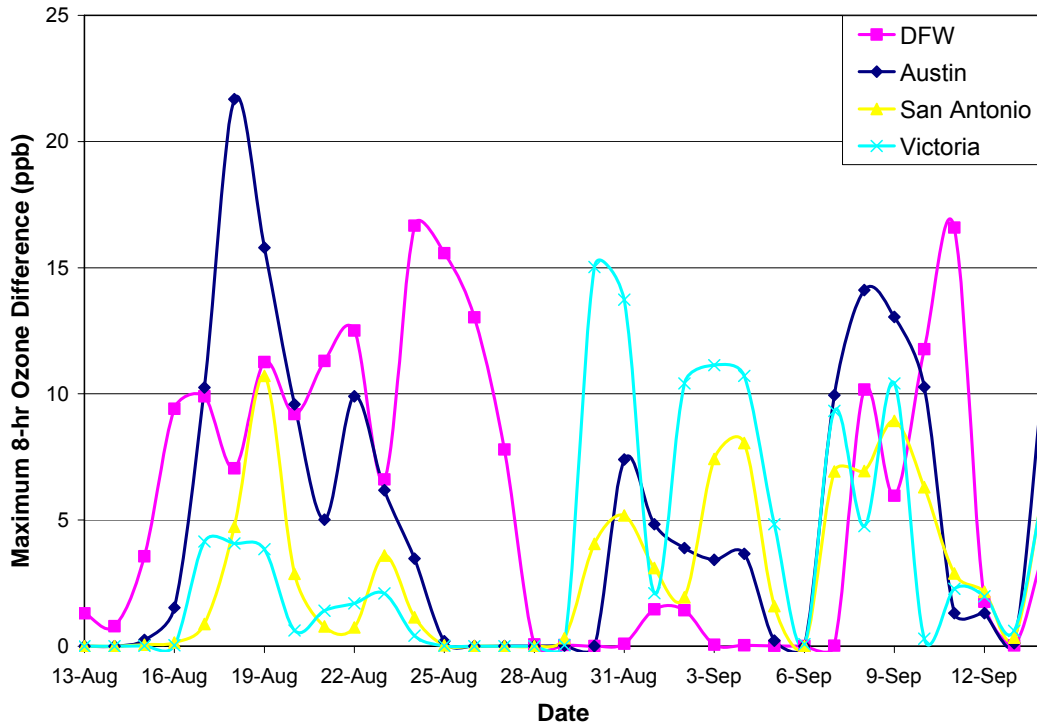


Figure 3-6. Maximum 8-hour ozone differences between the CAMx base case and the zero-out case (as calculated by Equation 3.1) for August 13th-September 14th, 2006.

Table 3-14. Maximum and average values of maximum differences in 8-hour ozone concentrations (as calculated by Equation 3.1) and differences in peak 8-hour ozone concentrations (as calculated by Equation 3.2) between the CAMx base case and zero-out case. Results are based on modeling output from August 13th-September 14th, 2006 and 2002.

Year	Region	Maximum Difference in 8-hr O3 (ppb)	Average Max Difference in O3 (ppb)	Highest Difference in Max 8-hour O3 (ppb)	Average Difference in Max 8-hour O3 (ppb)
2006	DFW	17	6	8	1
	Austin	22	5	11	1
	San Antonio	11	3	2	1
	Victoria	15	4	10	2
2002	DFW	33	10	12	3
	Austin	19	6	5	1
	San Antonio	14	4	5	1
	Victoria	13	4	11	2

As shown in Table 3-14, in comparison to the results from 2002, all values for DFW are lower in 2006, and while average values remain similar for Austin, maximum values are larger in 2006. Correlations of the maximum 8-hour ozone zero-out differences were examined for the 2006 period and the coefficients of correlation are shown in Table 3-15. A notable finding is that the effect on Austin is positively correlated with DFW in 2006, while DFW was negatively correlated with all other regions during the 2002 seasonal period.

Table 3-15. Correlations of CAMx zero-out maximum 8-hour ozone differences for August 13th-September 14th, 2006.

Correlations	Austin	San Antonio	DFW	Victoria
Austin	1			
San Antonio	0.67	1		
DFW	0.26	-0.05	1	
Victoria	0.26	0.64	-0.39	1

The distribution of the frequencies of maximum 8-hour ozone differences for each region that resulted from the zero-out method for the 2006 modeling period (as calculated by Equation 3.1) is shown in Table 3-16, along with results from the 2002 simulations corresponding to the same days. Similar to Table 3-4, results are summarized as the percentage of days within the 33-day period characterized by maximum 8-hour ozone differences falling within the specified ranges.

Table 3-16. Percentage of days with predicted maximum 8-hour ozone differences between the CAMx base case and zero-out simulation (as calculated by Equation 3.1) within the specified ranges. Results are included for 33 days within the CAMx modeling periods of August 13th–September 14th, 2006 and 2002.

Year	Region	0-5 ppb Max O3 Difference	5-10 ppb Max O3 Difference	10-15 ppb Max O3 Difference	15-20 ppb Max O3 Difference	20-25 ppb Max O3 Difference	25-30 ppb Max O3 Difference	30-35 ppb Max O3 Difference
2006	DFW	52%	21%	18%	9%	0%	0%	0%
	Austin	61%	18%	15%	3%	3%	0%	0%
	San Antonio	73%	24%	3%	0%	0%	0%	0%
	Victoria	76%	6%	15%	3%	0%	0%	0%
2002	DFW	55%	6%	6%	9%	15%	6%	3%
	Austin	42%	27%	21%	9%	0%	0%	0%
	San Antonio	64%	21%	15%	0%	0%	0%	0%
	Victoria	64%	30%	6%	0%	0%	0%	0%

Compared to output from 2002, results for DFW show a larger percentage of days in 2006 corresponding to maximum zero-out ozone differences in the 5-15 ppb range, and no differences above 20 ppb. Austin, San Antonio, and Victoria exhibit higher frequencies of days with maximum zero-out differences in the 0-5 ppb range. While differences in HGB emissions and meteorology between the two years likely impacted the variations in frequencies, the results indicate that a substantial percentage of days with significant zero-out contributions to ozone levels from emissions in HGB were predicted for the 2006 period. For DFW, nearly one-third of all days are characterized by maximum zero-out ozone differences in the 10-20 ppb range. Furthermore, similar to results for 2002, half of all days for DFW are characterized by maximum zero-out ozone differences above 5 ppb.

Table 3-17 presents the distribution of the frequencies of maximum 8-hour ozone differences between the CAMx base case and zero-out simulation (as calculated by Equation 3.1) for days with elevated ambient 8-hour ozone concentrations during August 13th-September 14th, 2006 and 2002. These days were selected for each region if any

monitor located within that region measured an 8-hour ozone concentration above a 70 ppb threshold. Similar to Table 3-4, results are summarized as a percentage of days exceeding the threshold, grouped by ascending ranges of maximum zero-out 8-hour ozone differences. For each region, the total number of days characterized by a local 8-hour ozone measurement above 70 ppb is also shown.

Table 3-17. Percentage of days with predicted maximum 8-hour ozone differences between the CAMx base case and zero-out simulation (as calculated by Equation 3.1) within the specified ranges. Days included for each region (specified as “total days”) are characterized by local surface measurements of 8-hour ozone concentrations above 70 ppb during August 13th–September 14th, 2006 and 2002.

Year	Region	0-5 ppb Max O3 Difference	5-10 ppb Max O3 Difference	10-15 ppb Max O3 Difference	15-20 ppb Max O3 Difference	20-25 ppb Max O3 Difference
2006	DFW (16 total days)	38%	25%	31%	6%	0%
	Austin (11 total days)	55%	18%	18%	0%	9%
	San Antonio (8 total days)	63%	38%	0%	0%	0%
	Victoria (3 total days)	33%	0%	33%	33%	0%
2002	DFW (16 total days)	88%	6%	6%	0%	0%
	Austin (6 total days)	33%	33%	0%	33%	0%
	San Antonio (10 total days)	50%	40%	10%	0%	0%
	Victoria (7 total days)	29%	57%	14%	0%	0%

In comparison to 2002, a significantly larger percentage of days for DFW are characterized by higher zero-out ozone differences. This may be due, in part, to meteorological factors; therefore, the predominant wind directions for these days were examined. HYSPLIT 48-hour back trajectories from DFW were generated and qualitatively examined for these days in both 2002 and 2006. These trajectory estimates confirmed that, for the days with ambient 8-hour ozone concentrations above 70 ppb, predominant south/southeasterly winds were more frequent in 2006 (ten days in 2006; five days in 2002). Making direct and conclusive comparisons for the other regions is more difficult due to the difference in total days that had ambient concentrations above 70 ppb. Nevertheless, the results in Table 3-17 suggest that significant zero-out ozone differences frequently resulted on days with elevated ozone concentrations in these areas for 2002 and 2006.

Results were further categorized to compare days in 2006 with elevated ambient ozone levels and days with large differences in modeled ozone concentrations between the base case and zero-out simulation. Tables 3-18 and 3-19 include ambient and predicted maximum 8-hour ozone concentrations for DFW and Austin, respectively, as well as the maximum differences in 8-hour ozone concentrations between the two modeling cases. Data is shown for the days characterized by the ten highest ambient 8-hour ozone concentrations. Tables 3-20 and 3-21 show similar data for days in 2006 characterized by the ten highest zero-out differences in 8-hour ozone for DFW and Austin, respectively.

Table 3-18. Ambient and modeled maximum 8-hour ozone concentrations and maximum differences in 8-hour ozone concentrations between the CAMx base case and zero-out case (as calculated by Equation 3.1) for DFW. Results are shown for days with the ten highest ambient 8-hour ozone concentrations during August 13th–September 14th, 2006.

Date	Maximum Difference in O3 (ppb)	CAMx Base Case Max O3 (ppb)	CAMx Zero-Out Case Max O3 (ppb)	Ambient 8-hr Max O3 (ppb)
8/18/2006	7	97	95	91
8/19/2006	11	94	89	84
8/21/2006	11	108	107	88
8/22/2006	13	130	128	91
8/23/2006	7	132	131	83
8/31/2006	0	109	109	101
9/1/2006	1	124	123	102
9/7/2006	0	82	82	82
9/8/2006	10	92	85	87
9/14/2006	4	78	78	84

Table 3-19. Ambient and modeled maximum 8-hour ozone concentrations and maximum differences in 8-hour ozone concentrations between the CAMx base case and zero-out case (as calculated by Equation 3.1) for Austin. Results are shown for days with the ten highest ambient 8-hour ozone concentrations during August 13th–September 14th, 2006.

Date	Maximum Difference in O3 (ppb)	CAMx Base Case Max O3 (ppb)	CAMx Zero-Out Case Max O3 (ppb)	Ambient 8-hr Max O3 (ppb)
8/18/2006	22	86	76	76
8/31/2006	7	82	81	86
9/1/2006	5	75	74	81
9/2/2006	4	72	72	78
9/3/2006	3	75	74	72
9/4/2006	4	78	78	74
9/6/2006	0	66	66	72
9/7/2006	10	74	74	80
9/8/2006	14	73	67	70
9/14/2006	11	81	78	79

Table 3-20. Ambient and modeled maximum 8-hour ozone concentrations and maximum differences in 8-hour ozone concentrations between the CAMx base case and zero-out case (as calculated by Equation 3.1) for DFW. Results are shown for days with the ten highest 8-hour ozone differences between the base case and zero-out case, during August 13th–September 14th, 2006.

Date	Maximum Difference in O3 (ppb)	CAMx Base Case Max O3 (ppb)	CAMx Zero-Out Case Max O3 (ppb)	Ambient 8-hr Max O3 (ppb)
8/17/2006	10	91	89	75
8/19/2006	11	94	89	84
8/21/2006	11	108	107	88
8/22/2006	13	130	128	91
8/24/2006	17	103	102	78
8/25/2006	16	84	83	66
8/26/2006	13	80	79	58
9/8/2006	10	92	85	87
9/10/2006	12	96	95	72
9/11/2006	17	128	125	64

Table 3-21. Ambient and modeled maximum 8-hour ozone concentrations and maximum differences in 8-hour ozone concentrations between the CAMx base case and zero-out case (as calculated by Equation 3.1) for Austin. Results are shown for days with the ten highest 8-hour ozone differences between the base case and zero-out case, during August 13th–September 14th, 2006.

Date	Maximum Difference in O3 (ppb)	CAMx Base Case Max O3 (ppb)	CAMx Zero-Out Case Max O3 (ppb)	Ambient 8-hr Max O3 (ppb)
8/17/2006	10	68	67	63
8/18/2006	22	86	76	76
8/19/2006	16	68	64	55
8/20/2006	10	58	58	53
8/22/2006	10	72	72	56
9/7/2006	10	74	74	80
9/8/2006	14	73	67	70
9/9/2006	13	71	69	58
9/10/2006	10	81	78	51
9/14/2006	11	81	78	79

The results in Tables 3-18 through 3-21 illustrate the similar finding from the 2002 seasonal data that days with elevated ambient 8-hour ozone concentrations do not necessarily correspond to large predicted zero-out contributions from HGB. Also similar to results from 2002, large zero-out differences in 8-hour ozone concentrations do not necessarily correspond to large decreases in predicted 8-hour maximum ozone concentrations.

To summarize, these findings indicate that, like in 2002, there are a number of days with both high contributions from inter-city transport and high total ozone concentrations. This suggests that to reduce all days below 70 ppb (as required by the ozone NAAQS), the role of inter-city transport will remain important. The results also demonstrate that reductions in the impact of inter-city transport are possible as the emissions from the source region are reduced. Further characterizations of days in this time period, including examining the relationships between ozone concentrations and predominant meteorological factors, are discussed in Appendix C. A detailed case study for August 18th-19th, 2006, is also presented in Appendix C.

3.4 CONCLUSIONS

Despite decreases in HGB emissions from 2002 to 2006, the zero-out results in this Chapter indicate that significantly large impacts to ozone levels in East Texas regions due to anthropogenic emissions in HGB were frequently predicted during August 13th-September 14th, 2006. In comparison to results for the same period in 2002, average maximum zero-out ozone differences were lower in 2006 for all regions with the exception of Victoria, which showed essentially no change. Frequencies of maximum zero-out differences above 5 ppb were lower for Austin, San Antonio, and Victoria in 2006; however, nearly half of all days were characterized by ozone differences above 5 ppb for DFW for both years, although extreme zero-out differences (above 20 ppb) did not occur as frequently in 2006.

Additional factors such as meteorology can have a significant role in the relative impacts of regional transport, as also indicated by results discussed in this Chapter. For example, effects of the zero-out simulations were positively correlated for Austin and DFW in 2006 and negatively correlated in 2002, which is likely due to differences in predominant wind directions for the days included in the analyses. Though examining meteorology can provide valuable information in regards to encompassing trends associated with wind directionality and background ozone levels, as well as frequencies of upwind sources, it is an uncontrollable variable.

As ozone NAAQS are under consideration for a possible decrease to a standard in the range of 60-70 ppb, the results presented in this work provide strong evidence that inter-city regional transport phenomena will become critical in determining whether urban areas in Texas can achieve attainment. Considering that background concentrations of ozone in East Texas can be as large as 50 ppb during summer months, large contributions from HGB ranging from 10-20 ppb, which were frequently predicted by the zero-out simulations in this work, have the potential to elevate ozone concentrations in other regions to levels exceeding the NAAQS without the addition of local contributions.

Though the concept of regional ozone transport in Texas is not a new one, the potential severity of regional impacts from HGB anthropogenic emissions, as well as the frequency of occurrences, had not been well-established on an extensive seasonal basis.

The results in this Chapter show that the magnitude of inter-city contributions in Texas can be quite significant for many days within an ozone season, even when distances between cities are large. While dilution of precursor emissions and/or depletion of ozone formed within plumes originating in HGB may occur to some extent, the plumes are capable of transporting significant amounts of ozone and precursors over large distances, spanning a period of several consecutive days. This justifies the need for further characterization of ozone formation and depletion, as well as the spatial extent of contributions from various emissions sources, within plumes originating from HGB. These topics are investigated in Chapters 5 and 6.

3.5 REFERENCES

- ENVIRON International Corporation (2006), “Seasonal Model of Northeast Texas Ozone”, Final report prepared for the East Texas Council of Governments, Novato, CA, September 2006.
- ENVIRON International Corporation (2009), User’s Guide – Comprehensive Air Quality Model with extensions (CAMx), Version 4.5, Novato, CA, available at <http://www.camx.com>.
- Senff, C., et al. (2007), “Ozone Production and Flux Downwind of Houston and Dallas”, Presentation given at the TexAQS II Principal Findings Data Analysis Workshop, Austin, TX, May 2007, available at http://www.tceq.state.tx.us/assets/public/implementation/air/texaqs/workshop/20070529/2007.05.30/Afternoon-1/1-O3_Production+Flux_Downwind-Senff.pdf.
- Texas Commission on Environmental Quality (2009a), “Protocol for Eight-Hour Ozone Modeling of the Houston/Galveston/Brazoria Area”, Revised report prepared by the Air Modeling and Data Analysis Section, July 2009, available at http://www.tceq.state.tx.us/assets/public/implementation/air/am/modeling/hgb8h2/doc/HGB8H2_Protocol_20090715.pdf.
- Texas Commission on Environmental Quality (2009b), “Houston-Galveston-Brazoria Nonattainment Area Ozone Conceptual Model”, Draft report prepared by the TCEQ Data Analysis Team, May 2009, available at http://www.tceq.state.tx.us/assets/public/implementation/air/am/modeling/hgb8h2/doc/HGB8H2_Conceptual_Model_20090519.pdf.
- Texas Commission on Environmental Quality, photochemical modeling website reference, available at <http://www.tceq.state.tx.us/implementation/air/airmod/overview>, accessed March 2010.
- U.S. Environmental Protection Agency, Air Quality System website reference, available at <http://www.epa.gov/ttn/airs/airsaqs>, accessed February 2010.
- Webb, A.M., C. Durrenberger, G. McGaughey, D.T. Allen, and E.C. McDonald (2007), “Comparison of Source Apportionment and Source Sensitivity Approaches for an Air Quality Analysis in Central and Southeast Texas”, The University of Texas at Austin, Austin, TX, 2007.

Chapter 4: Use of a Rural Monitoring Network and Photochemical Modeling to Characterize Regional Ozone Concentrations

4.1 INTRODUCTION

As described in Chapter 3, photochemical modeling indicates that regional ozone transport plays an important role in the attainment of National Ambient Air Quality Standards (NAAQS) in Texas. This Chapter will examine observational evidence characterizing ozone transport that has emerged from air quality field studies.

The State of Texas has invested in several research studies to develop the science of ozone formation and accumulation. In particular, the Texas Commission on Environmental Quality (TCEQ, previously known as the Texas Natural Resource Conservation Commission) conducted the Coastal Oxidant Assessment for Southeast Texas (COAST) in 1993 (Lawson et al., 1995), using emerging photochemical air monitoring station (PAMS) technology, an augmented surface and tall-building monitoring network, and airborne monitors. Results of that study were used in the late 1990s to develop a State Implementation Plan (SIP) to meet Houston's "severe" ozone classification deadline (TCEQ, 2008a). In 1996, the TCEQ carried out a mini-intensive study in the DFW area to develop the SIP for that region. In 1999, the U.S. Environmental Protection Agency (EPA) initiated a series of particulate matter "Super Site" projects to study aerosol behavior and available monitoring technology, one of which was conducted in Houston in 2000-2001 (Allen and Fraser, 2006). In 1999, the National Park Service worked with TCEQ on a haze study for Big Bend National Park and the West Texas Region, called the Big Bend Regional Aerosol and Visibility Observational, or BRAVO (Schichtel et al., 2004).

More recently, the State conducted a large-scale follow-up field assessment to the COAST study, called the Texas Air Quality Study, or TexAQS, in August-September 2000 (Daum et al., 2002; Allen and Olaguer, 2004). This study was designed to address the persistent ozone issues associated with the chemical and petrochemical industries, port and surface transportation, and large population within the Houston area. Participants in TexAQS included the National Oceanic and Atmospheric Administration (NOAA), Department of Energy (DOE), and numerous universities. TexAQS was

coupled with the Houston Particulate Matter Super Site project to generate a highly detailed characterization of air pollution chemistry for that area.

A missing component in all but the BRAVO study was a concerted effort to study air pollution transport over a regional scale. Additionally, the time scale for earlier studies in eastern Texas had been too short to capture a wide variety of meteorological regimes. In 2002, planning began for a 15-month long 2005-2006 field study, TexAQS II, that would address these two issues and revisit the photochemically-rich Houston air shed to assess changes since 2000 (TCEQ, 2008b). This Chapter presents an overview of findings from a network of rural surface monitors that was operated by the University of Texas as part of the TexAQS II study, including the characterization of air pollutant gradients and other insights revealed by this network. The work presented here combines observational data from this rural monitoring network with comparisons to photochemical modeling, providing evidence that data from rural monitors can significantly benefit the characterization of regional ozone transport within Texas and from exterior sources. Subsequent chapters and analyses will focus to a greater extent on the use of this network to characterize regional air pollutant transport.

4.2 RURAL MONITORING NETWORK

The surface air quality monitoring network in Texas at the initiation of TexAQS II was concentrated in urban areas, particularly those that are in non-attainment of NAAQS. These sites, numbering more than 100, are represented by the triangles in Figure 4-1 (TCEQ, 2008c). Relatively little monitoring data were available for the rural regions in Texas. Therefore, a network of ozone, particulate matter, visibility, surface meteorology, and upper air meteorology monitoring sites was established in the rural areas of East Texas beginning in the summer of 2005 as a preliminary phase of TexAQS II (shown in red in Figure 4-1).

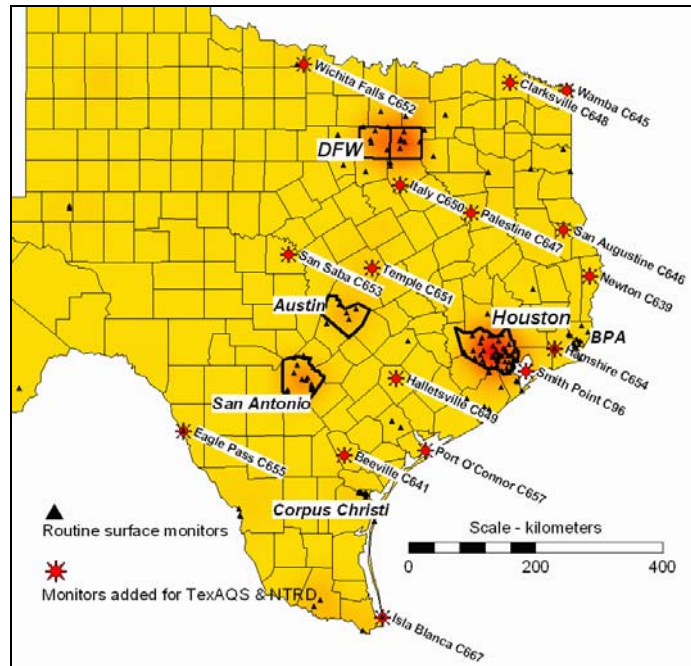


Figure 4-1. Map of Texas showing the locations of routine surface monitors and monitors implemented as part of the TexAQS II field study (TCEQ, 2008c).

This addition of monitors, described in Table 4-1 and mapped in Figure 4-1, presented a unique opportunity to gather data in the rural areas where an absence of surface monitoring data previously existed. Part of this network of rural surface monitoring stations was implemented along the Texas-Louisiana border as shown in Figure 4-2, with the purpose of establishing a “flux line” to quantify the amount of pollutants entering Texas when the origin appears to be from the east and northeast. Another portion of the rural network was established upwind and downwind of urban areas to assess inter-city pollutant transport.

Table 4-1. TexAQS II monitoring sites, locations, and types of measurements collected (TCEQ, 2008c).

CAMS	Site Description	County	Surface Measurements
638	Smith Point Hawkins Camp C96/C638	Chambers	O3, met
639	Newton NTRD C639	Newton	O3, met
645	Wamba NTRD C645	Bowie	O3, met
646	San Augustine Airport NTRD C646	San Augustine	O3, neph, met, 2.5 filter
648	Clarksville NTRD C648	Red River	O3, neph, met, 2.5 filter
641	Beeville Airport C641	Bee	O3, met
649	Hallettsville C649	Lavaca	O3, met
650	Italy High School C650	Ellis	O3, met
651	Temple C651	Bell	O3, met
652	Wichita Falls TEXAQSI C652	Wichita	neph, met, 2.5 filter
653	Millpond Park San Saba C653	San Saba	neph, met, 2.5 filter
654	Hamshire C64/C654	Jefferson	O3, neph, NOx, 2.5 teom, met
655	Eagle Pass C319/C655	Maverick	neph, 2.5 teom, met
647	Palestine C647	Anderson	O3, met
657	Port O Connor C657	Calhoun	O3, 2.5 teom, met
667	Isla Blanca C667/C323	Cameron	O3, neph, met

Table 4-1 Key
CAMS = Continuous Ambient Monitoring Station; abbreviated C. “600” series are non-TCEQ sites.
O3 = Ozone (13 sites)
NOx = Oxides of nitrogen, ozone precursor
2.5 teom = Continuous measurements of PM _{2.5} using tapered element oscillating microbalance (3 sites)
2.5 filter = Daily 24-hour mass, with periodic speciation (4 sites)
met = 10 meter meteorological measurements of wind speed & direction, temperature, relative humidity (16 sites)
neph = Nephelometer back scatter extinction coefficient, for visibility & particulates (7 sites)

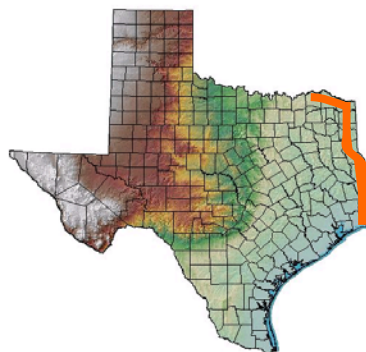


Figure 4-2. “Flux Line” established by the locations of TexAQS II monitoring sites implemented on the Texas-Louisiana border (Allen and Olaguer, 2004).

The continuous surface pollution and meteorological data were reported through the TCEQ Leading Environmental Analysis and Display System (LEADS) and the EPA AIRNow web-accessible data system (TCEQ, 2008c; U.S. EPA, 2008). Ozone monitoring was performed using the ultraviolet photometry method with data continuously reported every five minutes. Monitoring of nitrogen oxide (NO), nitrogen dioxide (NO₂) and total oxides of nitrogen (NO_x) was performed using the chemiluminescent method, with continuous data recorded at the same time resolution. Filter-based PM_{2.5} sampling was performed with the Federal Reference Method. Speciation analysis of filters for elements was performed with X-ray fluorescence for elements, ion chromatography for ions, and with controlled combustion for elemental and organic carbon. Continuous PM_{2.5} measurements were also collected at a five-minute time resolution with tapered element oscillating microbalance (TEOM). Nephelometry was performed using light back-scatter extinction coefficient measurements.

4.3 OBSERVED REGIONAL OZONE CONCENTRATION GRADIENTS

One result from the rural monitoring network implemented as part of TexAQS II was a confirmation of an earlier hypotheses that an ozone gradient exists from relatively low values in the south of Texas to higher values in the north, and that a substantial portion of background contamination enters the state from the Northeast (Sullivan et al., 2006). To qualitatively represent the distribution of observed regional ozone concentrations within Texas, ozone contour plots were generated using a grid-based graphics program, Surfer by Golden Software. When creating a grid from the ambient data, the Surfer program interpolates between the locations of these monitoring stations to create the contouring map in areas where ambient data are not available (Surfer software website, <http://www.goldensoftware.com/products/surfer/surfer.shtml>). The contours included in this Chapter implemented a simple point Kriging interpolation method, which uses an inverse distance weighting algorithm that considers the distances and directions of the surface monitors.

The region of interest for the contour plots runs north-south from the Texas-Oklahoma border at about 34 degrees north latitude to the Corpus Christi area at 28 degrees north latitude, and east-west from east of the Sabine River around 93 degrees west longitude to west of the Austin area at 99 degrees west longitude. As expected, the large population centers of the State tend to have the highest ozone concentrations. However, the focus of this Chapter is on the rural measurements taken during the TexAQS II campaign.

Figure 4-3 illustrates the ozone contour of the 75th percentile eight-hour ozone daily maximum for rural sites in eastern Texas (urban sites were not included in the contouring) during the months of August through October of 2005 and 2006. The 75th percentile was used to characterize the typical background concentrations on high ozone days. As previously mentioned, this contour plot confirms the notion of the existence of a regional gradient with ozone concentrations increasing from the southeast of Texas to the northwest. Similar contour plots generated for the median and 90th percentile days for the same time period show similar south-to-north gradients. During this period, most sites were active, with the exception of several days in September-October, 2005 (9/21-10/8), when monitoring at several sites was suspended due to Hurricane Rita. In creating these maps, sites located in or near large cities were excluded, the exception being the CAMS 56 site in mixed rural/suburban Denton County, just north of Fort Worth and on the prevailing downwind side of DFW, which was used to provide a data point in the northwest corner of the domain. It should also be noted that data from C602 and C657 were not available in 2005. Additionally, overall concentrations were lower in the late summer of 2006 in comparison to 2005.

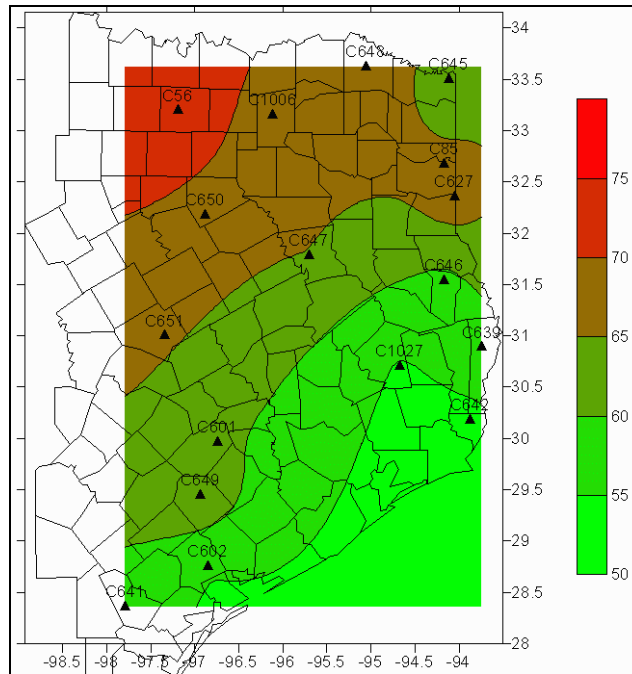


Figure 4-3. Surfer rural ozone contour plot showing the 75th percentile daily 8-hour maximum ozone concentrations. Locations of rural monitoring stations are also shown (Sullivan et al., 2006).

While Figure 4-3 represents the general spatial distribution of rural ozone concentrations in the rural regions of eastern Texas on days with high ozone concentrations (75th percentile), the highest observed concentrations can be spatially isolated due to the effects of urban plumes (Sullivan et al., 2006). For example, the Italy C650 site in rural southern Ellis County experienced an ozone exceedance on Sept. 26th, 2005 that was due to the DFW urban plume. The 115 ppb 1-hour maximum recorded at the site was the State’s highest for that day, and the 90 ppb 8-hour average was the State’s second highest for that day.

The background meteorology reveals that a flow reversal occurred in the DFW area, causing a build-up of pollutants. This reversal was then followed by transport to the southeast, affecting the rural Italy C650 site southeast of Fort Worth, and the rural/suburban Kaufman C71 site located to the southeast of Dallas. The following day, the rural Temple C651 site (located farther south) experienced a 1-hour maximum of 88 ppb, and an 8-hour maximum of 82 ppb. A contour of the ozone concentrations at 14:30 CST on Sept. 26th, 2005 is illustrated in Figure 4-4. This case study provides further

evidence that the presence of the rural sites implemented during TexAQS II has the potential to significantly reduce the uncertainty associated with contouring pollution levels and characterizing urban plumes.

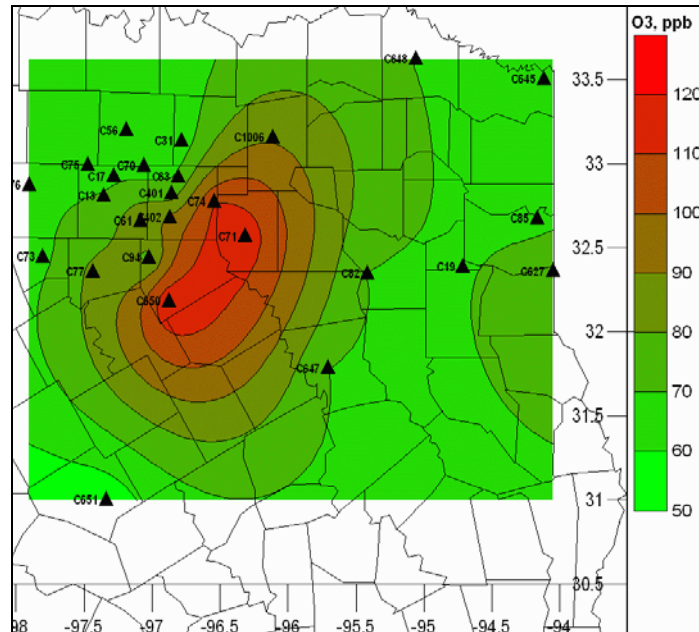


Figure 4-4. Contour plot of ozone concentrations at 14:30 CST on September 26th, 2005.

A second case occurred on Oct. 17th, 2005, when high regional ozone levels and exceedances were recorded in Houston and San Antonio, and 8-hour average concentrations at 90 percent of the NAAQS occurred in Austin and DFW. The boundary layer meteorology on this day indicates that upper air fetches in the Fort Worth area originated from the west and southwest (as shown in Figure 4-5). Regional contour plots of ozone concentrations extracted from the EPA AIRNow and TCEQ databases were generated by Surfer, illustrated in Figure 4-6. Two cases are illustrated in the figure: one plot includes data from all surface monitors available prior to 2005 and from five TexAQS II monitors, and the other excludes data from the TexAQS II monitors. As the figure shows, without the data from the TexAQS II monitors, the presence of a ridge of high ozone concentrations observed along the southeast central portion of the State are not accurately represented.

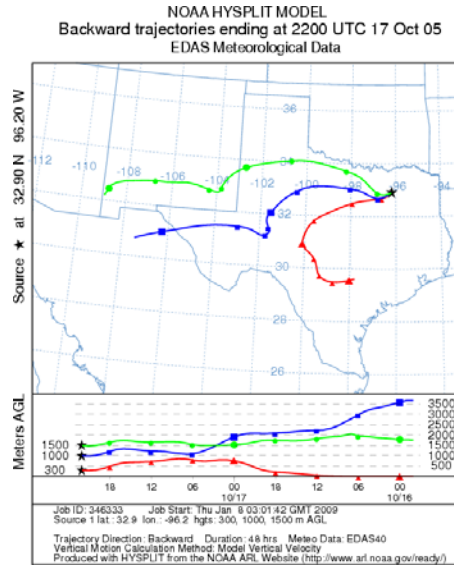


Figure 4-5. HYSPLIT 48-hour back-trajectories for 16:00 CST on October 17th, 2005, from the Dallas-Fort Worth area at elevations of 300, 1000, and 1500 meters.

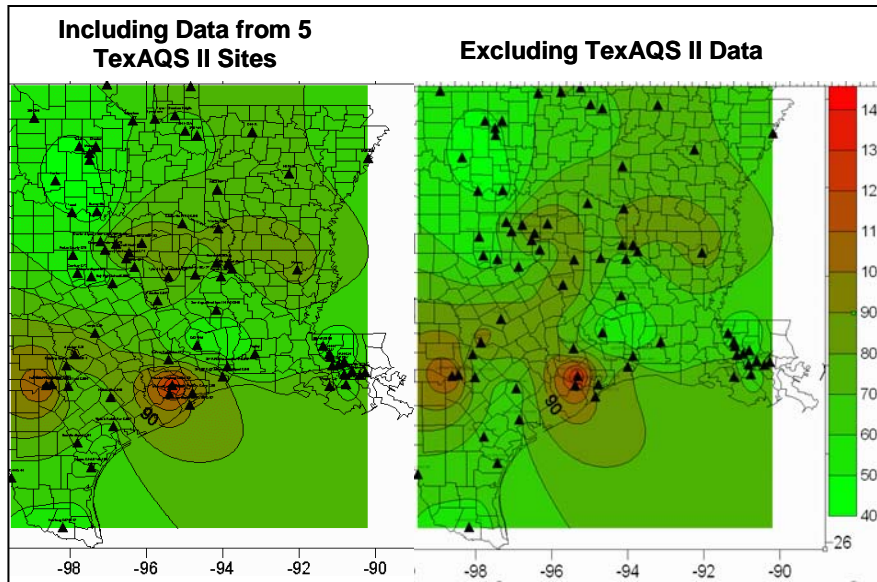


Figure 4-6. Regional contour plot of ozone concentrations on Oct. 17th, 2005, 16:00 CST, with and without TexAQS II monitoring sites.

More detailed analyses of ozone transport case studies will be described in Chapter 5. The remainder of this Chapter will examine the information that the rural monitoring network provides on emissions, in addition to ozone transport.

4.4 DIURNAL PATTERNS OF RURAL OZONE CONCENTRATIONS

As mentioned in Chapter 2 and illustrated in Figure 2-1, the typical diurnal pattern of ozone levels in urban areas includes a peak in ozone concentrations between late morning and early afternoon, with levels often diminishing to near zero overnight. This pattern results from several factors. The temporal pattern in precursor emissions (including NO and hydrocarbon emissions) increases sharply during morning rush hour. Solar energy drives chemical reactions that increase to a midday maximum, decreasing as the day wears on. In addition, mixing heights increase throughout the day (hence no peak following the afternoon rush hour, as mixing heights are high at that time). Ozone is consumed during night-time hours as it reacts with other pollutants and deposits on surfaces.

The diurnal ozone pattern in rural areas is typically quite different from that in urban areas. While the peak hourly maximum ozone concentration is generally lower than in the urban and near-urban locations, concentrations in rural areas are elevated over much of the day (and even at night). This characteristic rural diurnal pattern may be explained by the combination of continual replenishment of ozone and its precursors by the transport of pollutants from upwind urban regions with relatively lower levels of pollutants (such as NO) that serve as ozone sinks that is observed in rural areas.

The diurnal pattern of summertime rural ozone concentrations, for both surface monitors in East Texas and the surface monitor at Big Bend National Park, are shown in Figure 4-7. The monitor at the Big Bend location is representative of a prototypical rural site, with average minimum night-time ozone concentrations of approximately 40 ppb. A second group of sites in rural Northeast Texas (Palestine, San Augustine, and Clarksville) exhibit average minimum night-time concentrations of 20 ppb, while a third group of monitors (Cypress River, Waskom, Panola, Karnack, and Wamba) experience average minimum night-time ozone concentrations of 5-10 ppb.

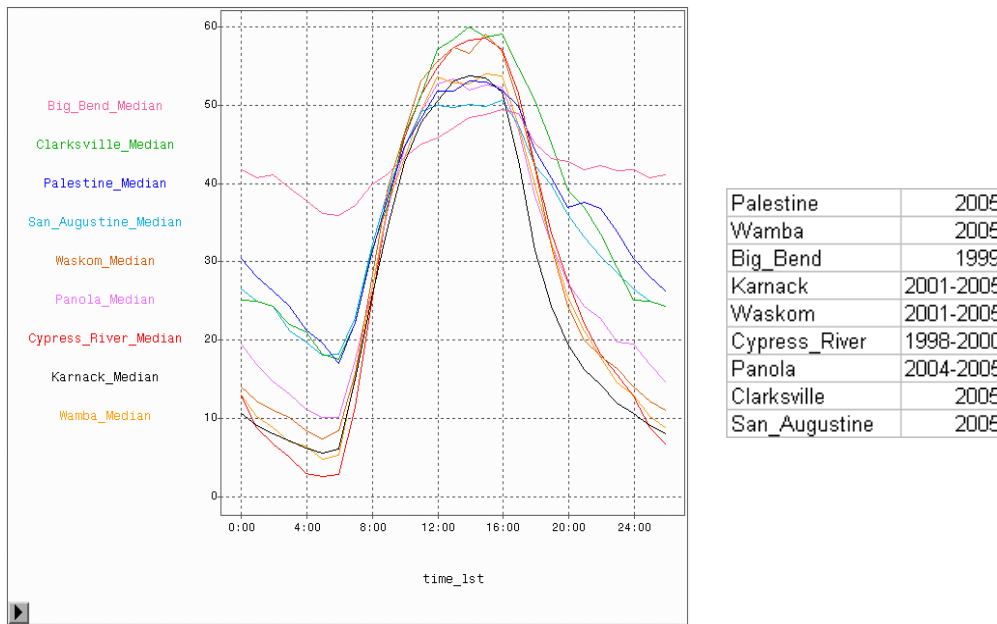


Figure 4-7. Ozone concentration diurnal patterns for rural Northeast Texas monitoring sites and Big Bend.

The monitors exhibiting the lowest minimum night-time ozone concentrations are located in or near Panola County. At 24 tons/day, Panola County has the highest non-road area NO_x emissions in the state due to local natural gas production, including equipment such as pumps, compressors, and steam generation for steam flooding. Freestone County produces the second highest NO_x emissions in Northeast Texas due to natural gas production. Figure 4-8 illustrates natural gas production in relation to surface monitor locations in rural Northeast Texas. The areas of dense gas production are shown in purple and represent natural gas production, pipelines, and compressors located in the area (TCEQ, 2007). The locations of Panola and Freestone counties are also shown. As Figure 4-8 illustrates, the monitors in Figure 4-7 that exhibit average minimum night-time ozone concentrations around 20 ppb (Palestine, Clarksville, San Augustine) are located farther away from Panola county, while the monitors with the lowest average night-time concentrations (Karnack, Cypress River, and Panola) are located within the area of dense natural gas production.

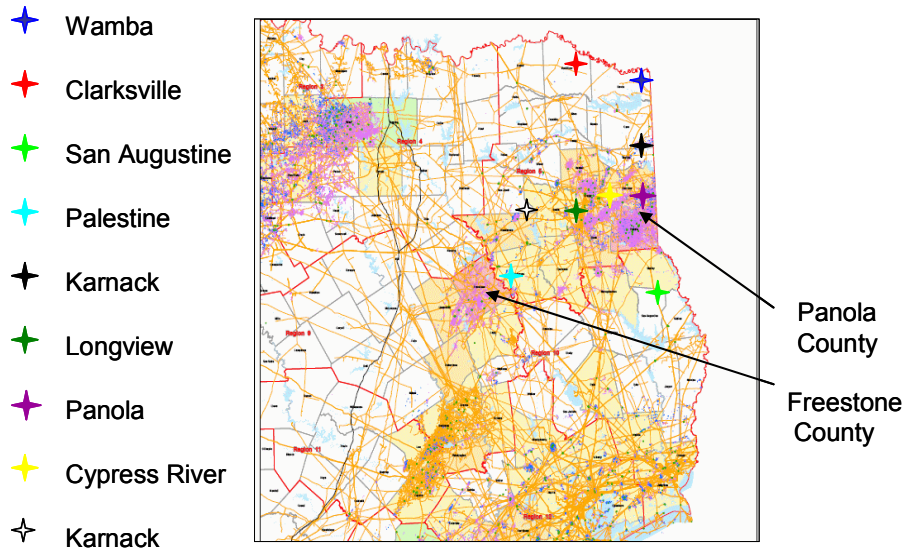


Figure 4-8. Locations of rural Northeast Texas surface monitors in relation to natural gas production density.

4.5 PHOTOCHEMICAL MODEL DESCRIPTION AND INPUTS

The Comprehensive Air Quality Model with Extensions (CAMx) was used to generate predictions of ozone concentrations during a simulated episode from August 13th-22nd, 1999. This CAMx simulation was used by the TCEQ in developing the State Implementation Plan (SIP) for the DFW area (ENVIRON, 2003). As part of the SIP process, the performance of this episode has been evaluated and approved for regulatory purposes.

The CAMx horizontal grid structure, shown in Figure 4-9, includes a 4-km high-resolution grid, covering the DFW non-attainment area and extending north to the Texas/Oklahoma border and south to include the Waco urban area. The 4-km domain is nested within 12-km and 36-km grids covering much of the South, Southeast and Central U.S. The modeling grids are based on a Lambert Conformal Projection (LCP) coordinate system with the central coordinate of the LCP grid at 100°W and 40°N (ENVIRON, 2003). The CAMx vertical grid structure is comprised of 15 layers, as indicated in Table 4-2, with a surface layer depth of approximately 20 meters.

Meteorological inputs were developed with the Fifth-Generation Pennsylvania State University/National Center for Atmospheric Research (PSU/NCAR) Mesoscale Model (MM5, version 3.4) (ENVIRON, 2003). Biogenic emissions were developed using versions 2.2 and 3.1 of Global Biosphere Emissions and Interactions System (GloBEIS) model with landuse/landcover (LULC) data, MM5 temperature data, and GOES satellite data provided by the TCEQ (ENVIRON, 2003). Anthropogenic emissions inventories were processed using the version 2x of the Emissions Processing System (EPS2x) for area, off-road, onroad mobile, and point sources (ENVIRON, 2003). The modeling protocol for this episode, along with files containing emissions inventories and meteorological inputs, are provided by the TCEQ and available at <http://www.tceq.state.tx.us/implementation/air/airmod/data/dfw1.html>.

4.6 COMPARISON OF AMBIENT DATA TO PHOTOCHEMICAL MODELING RESULTS

Photochemical modeling results were compared with ambient observations to evaluate potential causes of low observed night-time ozone concentrations. For August 13th-22nd, 1999, hourly ambient and modeled ozone concentrations for rural monitoring sites in Northeast Texas are shown in Figure 4-10, and the results reveal a discrepancy in night-time ozone concentrations. Ozone concentrations observed by several surface monitors fall to near 0 ppb overnight, while the photochemical model predicts night-time ozone levels near 40 ppb. It should be noted that Figure 4-10 only presents results for rural monitors illustrated in Figure 4-8 that were operational in 1999, and these monitors are located within the East Texas 12-km CAMx domain (Figure 4-9). A variety of hypotheses pertaining to the causes of the discrepancies in modeled and measured night-time ozone concentrations in rural Northeast Texas are investigated in this Chapter.

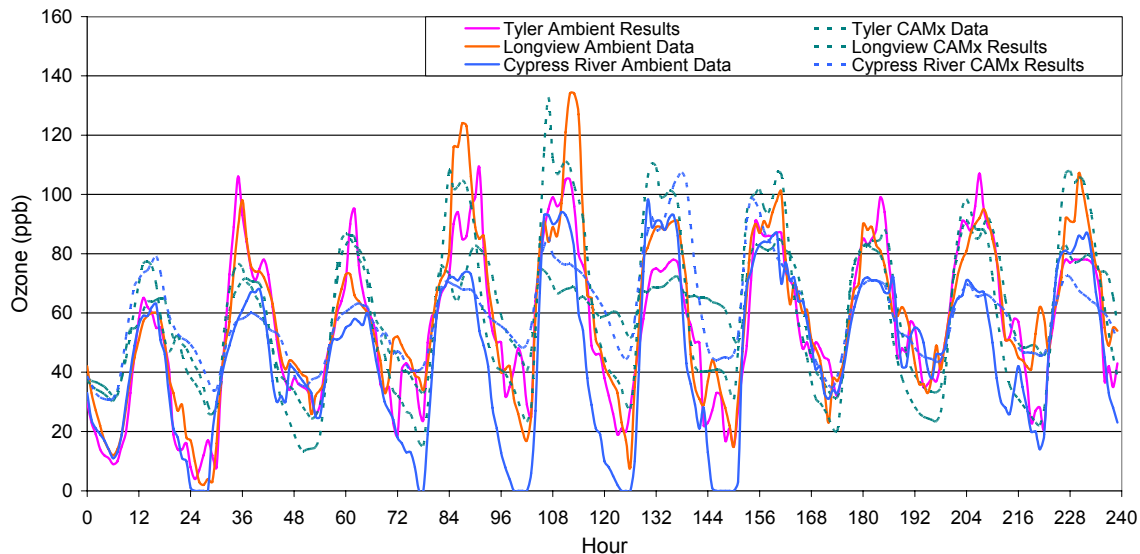


Figure 4-10. Time series of one-hour average ozone concentrations (in ppb) measured by the Tyler, Longview, and Cypress River surface monitors for August 13th-22nd, 1999. Photochemical modeling results are also shown for surface layer grid cells within the CAMx 12-km domain that correspond to the locations of these monitors.

Figures 4-11 and 4-12 show the same time series for Cypress River and Longview monitoring sites, respectively. When examining these figures, it is important to note the locations of each monitor relative to Panola and Freestone counties. The Cypress River monitor is embedded in an area of concentrated natural gas production, and the discrepancy in night-time ozone concentrations between the ambient data and CAMx predictions is quite large, reaching a maximum of 51 ppb in the early morning hours of August 17th, 1999. Ambient night-time ozone concentrations reach a minimum of 0 ppb on August 14th and August 16th-19th; however, the photochemical model predicts minimum night-time ozone concentrations near 40 ppb throughout the episode, similar to diurnal pattern for the Big Bend rural site (refer to Figure 4-7).

In comparison to Cypress River, the Longview surface monitor is located farther from Panola and Freestone counties. As Figure 4-12 illustrates, the model performs relatively well in predicting both daytime and night-time ozone concentrations at this monitor. Furthermore, CAMx night-time ozone concentrations are underestimated for August 14th, 15th, 21st, and 22nd. The results shown in Figures 4-11 and 4-12 suggest the hypothesis that underestimated NO_x emissions in rural Northeast Texas due to oil and

natural gas production is a probable factor impacting the overestimated night-time ozone concentrations predicted by the CAMx model.

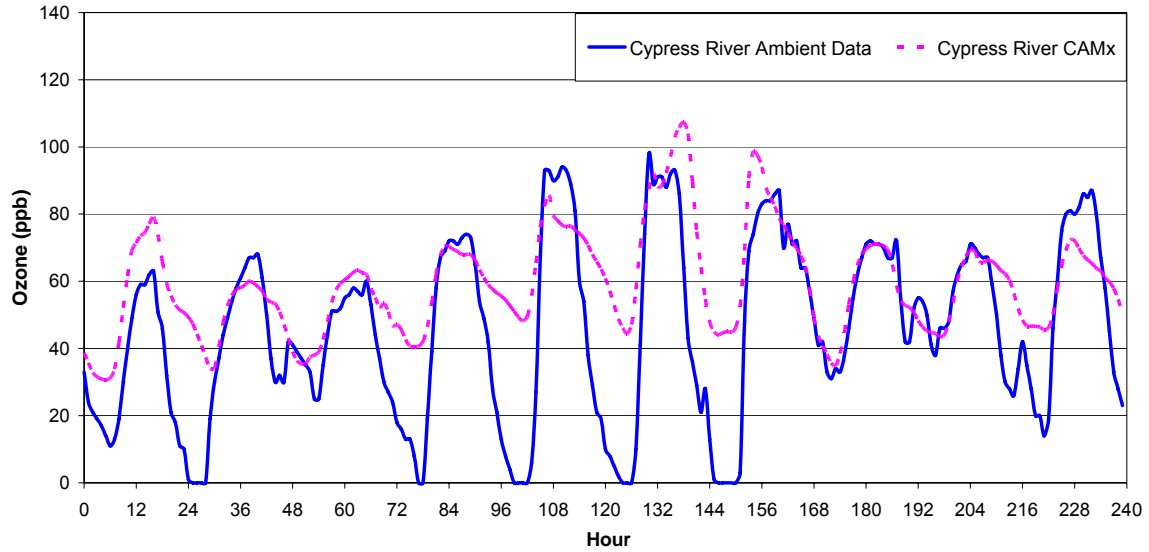


Figure 4-11. Hourly ambient surface monitor ozone concentrations and corresponding CAMx photochemical modeling predictions (in ppb) for the Cypress River monitoring site during August 13th-22nd, 1999.

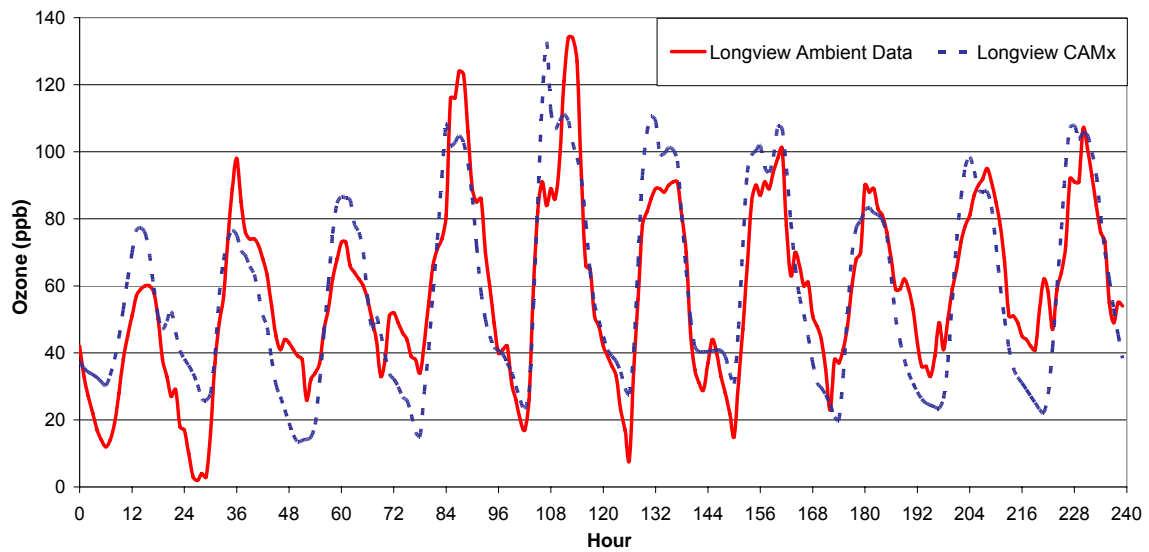


Figure 4-12. Hourly ambient surface monitor ozone concentrations and corresponding CAMx photochemical modeling predictions (in ppb) for the Longview monitoring site during August 13th-22nd, 1999.

The chemical depletion of ozone after sunset primarily occurs through a reaction with NO, as discussed in Chapter 2. Therefore, if NO_x emissions in Northeast Texas are underestimated by the CAMx photochemical model, night-time ozone will not be depleted to the concentrations that are observed during this modeled period. To further probe this hypothesis, additional comparisons between modeled and observed measurements were performed, and a series of model sensitivity analyses were conducted.

Figures 4-13 and 4-14 show the ambient and CAMx-predicted concentrations of NO at the Cypress River and Longview monitoring sites for August 13th-22nd, 1999. Similar to the trends observed in Figures 4-11 and 4-12, NO peak concentrations at the Cypress River monitor are underestimated by CAMx, with the primary discrepancies occurring on August 14th and August 16th-19th, the same days that experience large errors in ozone concentration predictions. For the Longview monitor, with the exception of August 18th, modeled NO concentrations are overestimated during the late morning hours (note the different concentration scales for the two time series in Figure 4-14). The difference in peak NO concentrations at the Cypress River monitor reach levels as high as 30 ppb, while the maximum difference in NO concentrations at the Longview monitor is approximately 7 ppb.

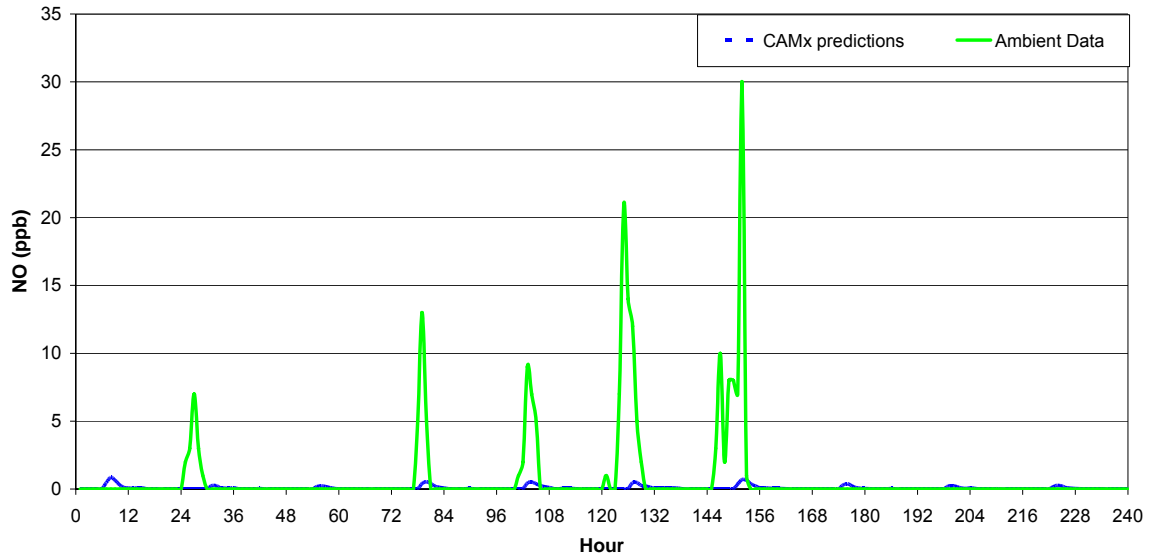


Figure 4-13. Hourly ambient surface monitor NO concentrations and corresponding CAMx photochemical modeling predictions (in ppb) for the Cypress River monitor during August 13th-22nd, 1999.

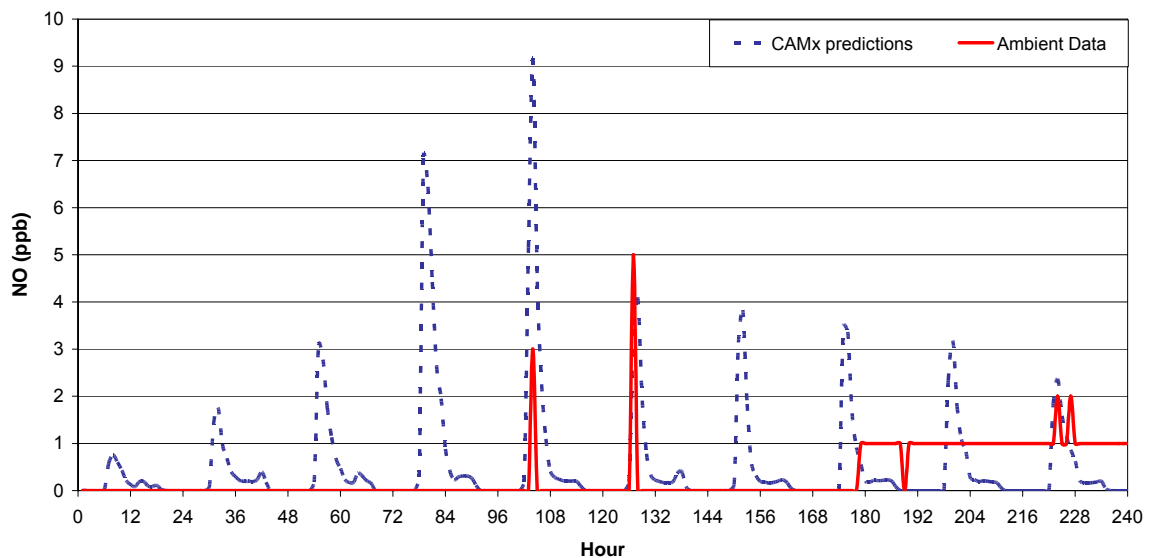


Figure 4-14. Hourly ambient surface monitor NO concentrations and corresponding CAMx photochemical modeling predictions (in ppb) for the Longview monitor during August 13th-22nd, 1999.

The severe under-prediction of night-time NO and over-prediction of night-time ozone may be due to under-prediction of emissions from oil and gas operations. The distribution of modeled NO_x emissions input into CAMx for 10:00 CST on August 17th, 1999, is shown in Figure 4-15 alongside the natural gas production map that was also

presented in Figure 4-8, illustrating that NO_x emissions due to natural gas production in Panola and Freestone counties may not have been accurately represented in the emissions inventory used for this photochemical model simulation.

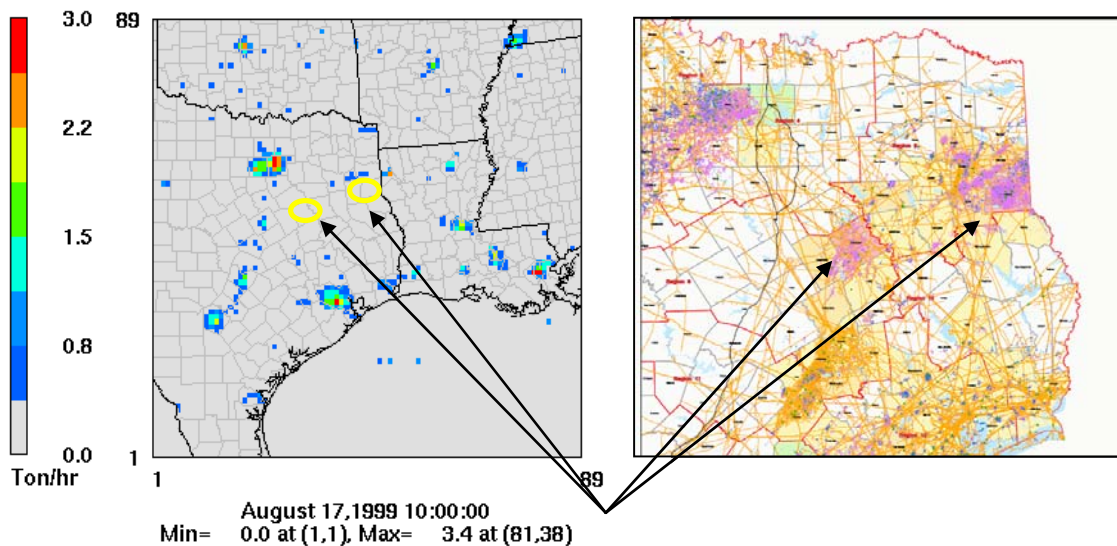


Figure 4-15. Comparison of CAMx modeled NO_x emission levels in tons per hour at 10:00 CST on August 17th, 1999, to locations of dense natural gas production levels in Northeast Texas.

4.7 PHOTOCHEMICAL MODELING NO_x EMISSIONS SENSITIVITY ANALYSES

A series of sensitivity analyses were performed with CAMx to assess the sensitivity of rural night-time ozone and NO_x concentrations to rural NO_x emissions. Low-level NO_x emissions were increased by a factor of 2 and a factor of 10 for Panola and Freestone counties. In a separate sensitivity analysis, low-level NO_x emissions were increased by a factor of 2 and a factor of 10 for East Texas counties excluding the urban Houston, Beaumont/Port Arthur and DFW regions. Figures 4-16 and 4-17 illustrate the counties with altered emissions for the two simulations involving a 2-fold increase in NO_x. The configurations for the simulations involving a 10-fold increase in NO_x emissions are geographically identical.

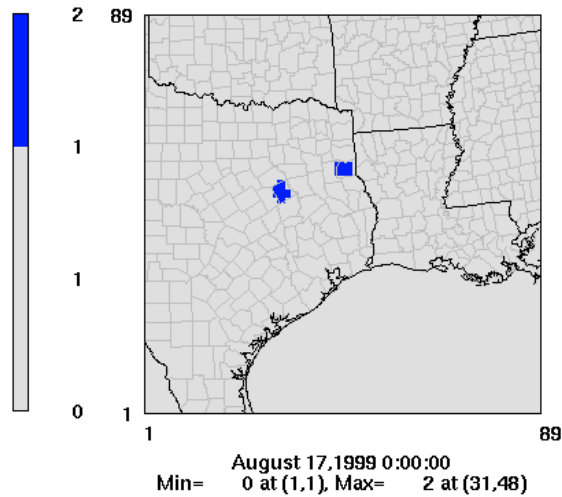


Figure 4-16. CAMx surface layer 12-km domain for simulations involving an increase in NO_x emissions in Panola and Freestone counties. Results are shown for August 17th, 1999.

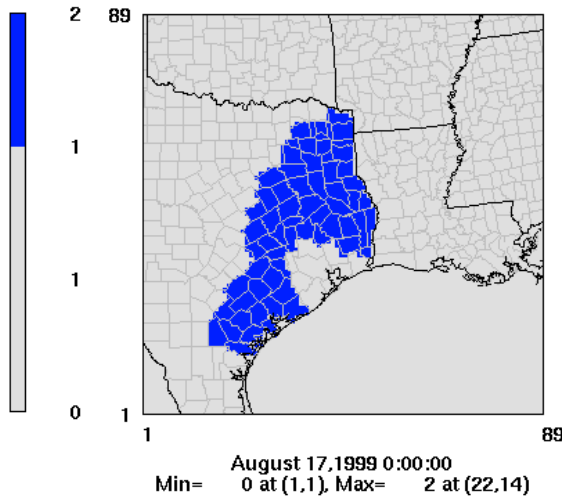


Figure 4-17. CAMx surface layer 12-km domain for simulations involving an increase in NO_x emissions in East Texas counties (excluding the Houston and DFW urban areas). Results are shown for August 17th, 1999.

A time series of ambient and modeled NO concentrations (in ppb) for these sensitivity assessments is shown in Figure 4-18 for the Cypress River monitoring site from August 13th-22nd, 1999. The maximum hourly increase in modeled NO_x emissions (in tons/hr) on August 17th, 1999 is shown for each sensitivity simulation (relative to the

base case simulation) in Figures 4-19 through 4-22, which occurs at 16:00 CST for each case study. The modeled hourly ozone concentrations that resulted from the sensitivity studies for the Cypress River monitoring site, located within the CAMx 12-km domain, are presented in Figure 4-23 for all days in the episode. The results indicate that it is necessary to increase the NO_x emissions by a factor of 10 over a wide area in order to replicate observed night-time ozone and NO concentrations for the Cypress River monitoring site, however, this order of magnitude increase in NO_x emissions results in an over-prediction of day-time ozone concentrations, not only at Cypress River, but also over a broad region of eastern Texas (discussed in further detail below).

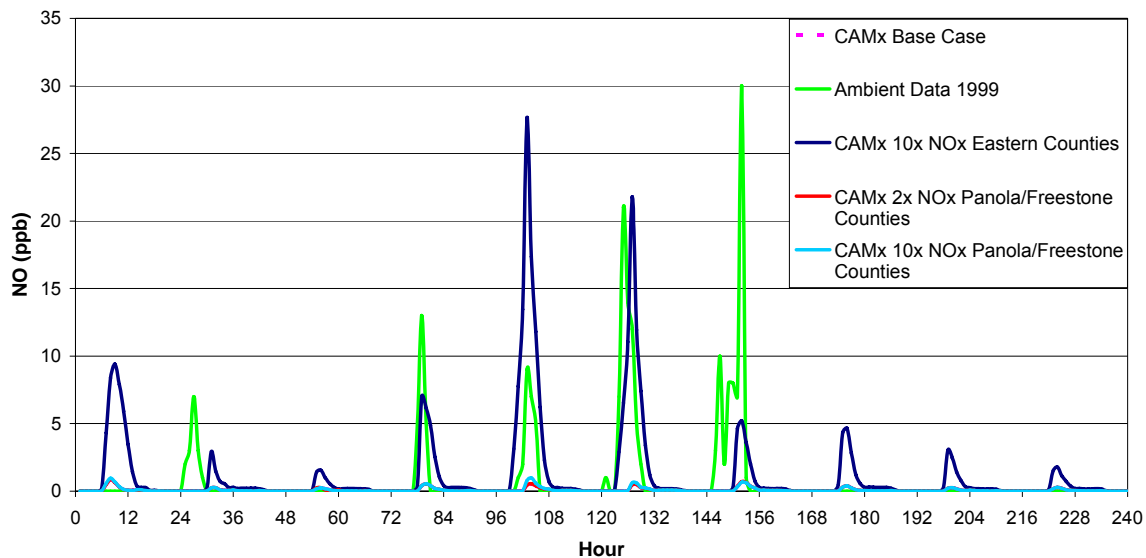


Figure 4-18. Hourly ambient surface monitor NO concentrations and corresponding CAMx photochemical modeling predictions (in ppb) for NO_x sensitivity studies for the Cypress River monitoring site during August 13th-22nd, 1999.

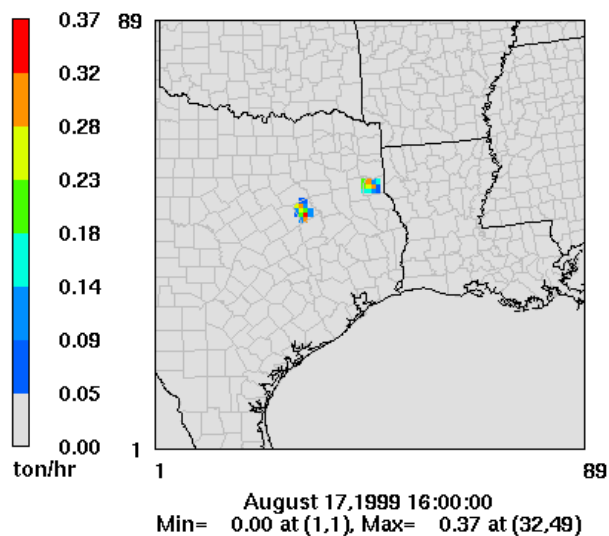


Figure 4-19. Difference between hourly surface layer NO_x emissions (ton/hr) for the CAMx 12-km domain associated with a 2-fold increase in low-level NO_x emissions in Panola and Freestone counties versus the base case. Results are presented for the hour with the maximum difference in NO_x emissions on August 17th, 1999.

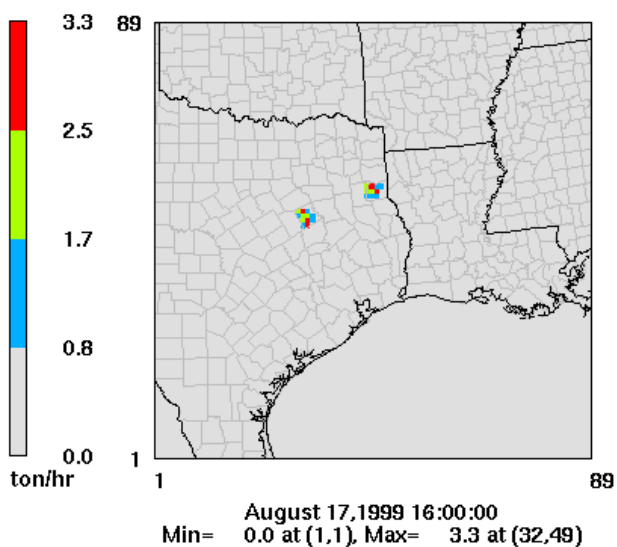


Figure 4-20. Difference between hourly surface layer NO_x emissions (ton/hr) for the CAMx 12-km domain associated with a 10-fold increase in low-level NO_x emissions in Panola and Freestone counties versus the base case. Results are presented for the hour with the maximum difference in NO_x emissions on August 17th, 1999.

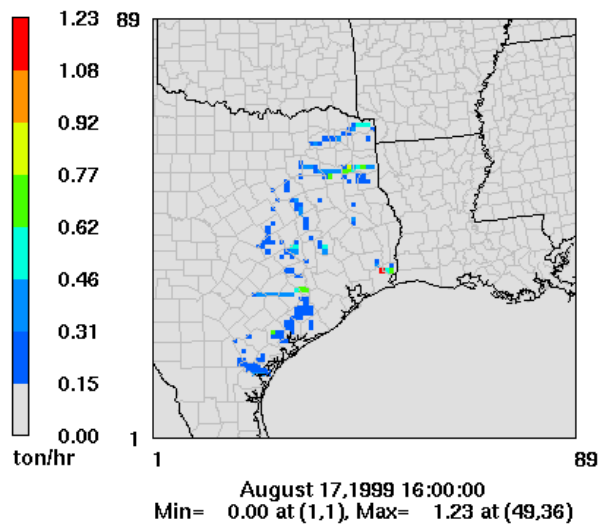


Figure 4-21. Difference between hourly surface layer NO_x emissions (ton/hr) for the CAMx 12-km domain associated with a 2-fold increase in low-level NO_x emissions in Eastern Texas counties (excluding the Houston and Dallas urban areas) versus the base case. Results are presented for the hour with the maximum difference in NO_x emissions on August 17th, 1999.

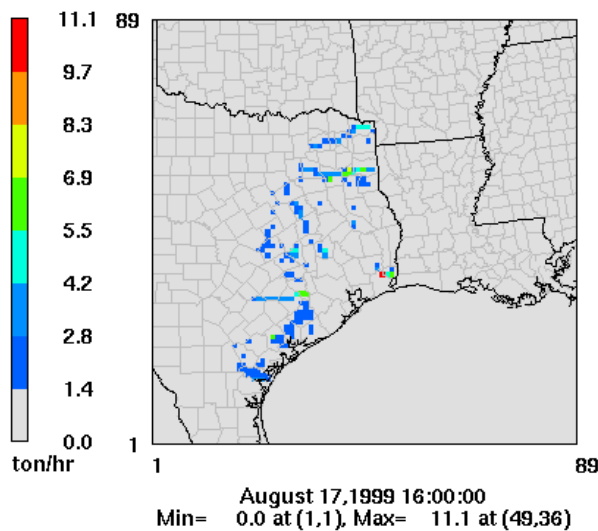


Figure 4-22. Difference between hourly surface layer NO_x emissions (ton/hr) for the CAMx 12-km domain associated with a 10-fold increase in low-level NO_x emissions in Eastern Texas counties (excluding the Houston and Dallas urban areas) versus the base case. Results are presented for the hour with the maximum difference in NO_x emissions on August 17th, 1999.

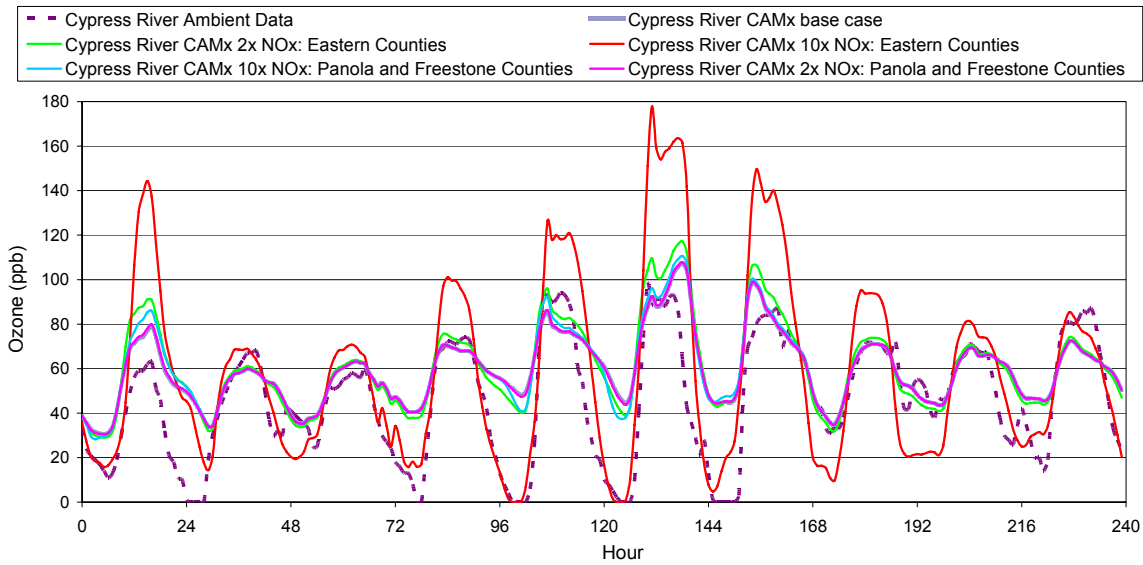


Figure 4-23. Hourly ambient surface monitor ozone concentrations and corresponding CAMx photochemical modeling predictions (in ppb) for the Cypress River monitoring site during August 13th-22nd, 1999.

The sensitivity studies were initially performed by exclusively increasing local levels of NO_x to improve the performance of the photochemical model during night-time hours while maintaining the ability of the model to accurately capture the ambient daytime ozone behavior. However, it was expected that increasing NO_x levels would have an impact on the daytime ozone concentrations within the 12-km domain, and all case studies resulted in a significant difference in hourly afternoon ozone concentrations in the DFW urban area in comparison to the base case. The maximum differences in CAMx-predicted ozone concentrations between two case studies and the base case for August 17th, which is the day with the highest observed 1-hour ambient ozone concentration in the DFW area, are shown in Figures 4-24 and 4-25. For the simulation involving a 2-fold increase of NO_x emissions in Panola and Freestone counties, Figure 4-24 shows a maximum increase in hourly ozone concentrations near DFW of 14.3 ppb at 14:00 CST in comparison to the base case. For the simulation involving a 10-fold increase of NO_x emissions in the East Texas counties, Figure 4-25 shows a maximum increase in hourly ozone concentrations near DFW of 77.4 ppb at 15:00 CST.

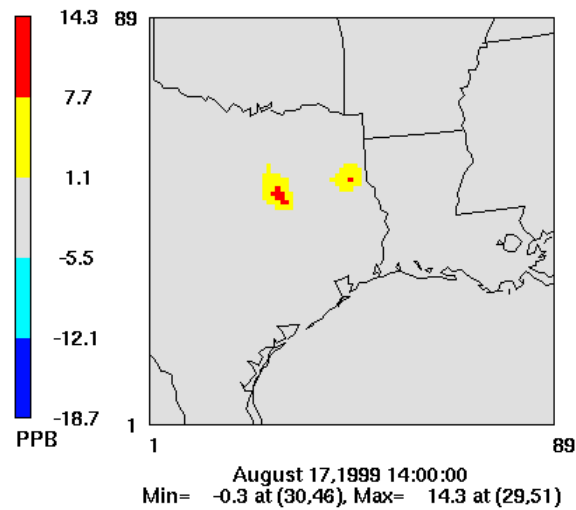


Figure 4-24. Difference in hourly surface layer ozone concentrations (ppb) for grid cells within the CAMx 12-km domain resulting from a 2-fold increase in low-level NO_x emissions in Panola and Freestone counties, relative to the base case. Results are shown for 14:00 CST on August 17th, 1999.

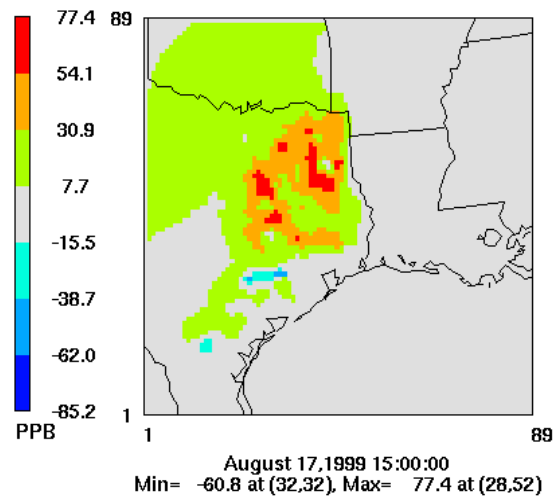


Figure 4-25. Decrease in hourly surface layer ozone concentrations (ppb) for grid cells within the CAMx 12-km domain resulting from a 10-fold increase in low-level NO_x emissions in Eastern Texas counties, relative to the base case (excluding the Houston and Dallas urban areas). Results are shown for 15:00 CST on August 17th, 1999.

4.7.1 CAMx Process Analysis Methodology

To direct additional sensitivity analyses, a more in-depth modeling analysis was done to examine the processes that may have contributed to low night-time ozone concentrations. CAMx includes a probing tool called Process Analysis (PA) which is primarily used as an explanatory tool to gain an understanding of the chemical reactions and physical transport processes at a specified location in the photochemical modeling domain. The technique generates mass budgets of several compounds such as HO_x, NO_y, and ozone. Furthermore, PA provides information regarding how the specific model predictions were obtained, which can be interpreted to improve model performance and/or inform control strategy decisions (ENVIRON, 2004).

PA includes the Integrated Process Rate Analysis (IPR) and the Integrated Reaction Rate Analysis (IRR). The IRR method provides detailed reaction rate information for all reactions within the chemical mechanism for selected grid cells. The IRR output data can be analyzed to determine how chemical changes occurring in the model are related to chemical mechanisms. The IPR method provides detailed rate information for the primary chemical and physical transport processes such as diffusion, advection, and deposition. Outputs can be analyzed to determine what processes governed the model-predicted concentrations of a species at any time and location (ENVIRON, 2004). More specifically, this information provides a complete description of how the modeled concentration of a species varies across the output time interval, as well as the magnitudes of the processes that contribute to these variations (ENVIRON, 2004).

The specific processes that are reported by IPR are summarized in Table 4-3. For most of the process rates listed in Table 4-3, the interpretation is straightforward: the rate is simply the concentration change caused by the named process across the output time interval, and the sign convention is such that a positive flux always tends to increase the cell concentration (ENVIRON, 2004). This IPR output information is often plotted as a time series of process contributions for specific cells or groups of cells, and they have also been used to check the mass balance in the host model, i.e., to determine whether

model concentrations are fully explained by the diagnosed process information or whether unexpected artifacts are occurring (ENVIRON, 2004).

Table 4-3. Process information reported by the IPR option (ENVIRON, 2004).

IPR Parameter	Process Information	Units ^a
1	Initial concentration	$\mu\text{mole}/\text{m}^3$ ($\mu\text{g}/\text{m}^3$)
2	Gas phase chemistry	$\mu\text{mole}/\text{m}^3$ ($\mu\text{g}/\text{m}^3$)
3	Gridded emissions	$\mu\text{mole}/\text{m}^3$ ($\mu\text{g}/\text{m}^3$)
4	Point source emissions	$\mu\text{mole}/\text{m}^3$ ($\mu\text{g}/\text{m}^3$)
5	Plume-in-Grid change	$\mu\text{mole}/\text{m}^3$ ($\mu\text{g}/\text{m}^3$)
6	West boundary advection	$\mu\text{mole}/\text{m}^3$ ($\mu\text{g}/\text{m}^3$)
7	East boundary advection	$\mu\text{mole}/\text{m}^3$ ($\mu\text{g}/\text{m}^3$)
8	South boundary advection	$\mu\text{mole}/\text{m}^3$ ($\mu\text{g}/\text{m}^3$)
9	North boundary advection	$\mu\text{mole}/\text{m}^3$ ($\mu\text{g}/\text{m}^3$)
10	Bottom boundary advection	$\mu\text{mole}/\text{m}^3$ ($\mu\text{g}/\text{m}^3$)
11	Top boundary advection	$\mu\text{mole}/\text{m}^3$ ($\mu\text{g}/\text{m}^3$)
12	Dilution in the vertical	$\mu\text{mole}/\text{m}^3$ ($\mu\text{g}/\text{m}^3$)
13	West boundary diffusion	$\mu\text{mole}/\text{m}^3$ ($\mu\text{g}/\text{m}^3$)
14	East boundary diffusion	$\mu\text{mole}/\text{m}^3$ ($\mu\text{g}/\text{m}^3$)
15	South boundary diffusion	$\mu\text{mole}/\text{m}^3$ ($\mu\text{g}/\text{m}^3$)
16	North boundary diffusion	$\mu\text{mole}/\text{m}^3$ ($\mu\text{g}/\text{m}^3$)
17	Bottom boundary diffusion	$\mu\text{mole}/\text{m}^3$ ($\mu\text{g}/\text{m}^3$)
18	Top boundary diffusion	$\mu\text{mole}/\text{m}^3$ ($\mu\text{g}/\text{m}^3$)
19	Dry deposition	$\mu\text{mole}/\text{m}^3$ ($\mu\text{g}/\text{m}^3$)
20	Wet deposition	$\mu\text{mole}/\text{m}^3$ ($\mu\text{g}/\text{m}^3$)
21	Inorganic aerosol chemistry	$\mu\text{mole}/\text{m}^3$ ($\mu\text{g}/\text{m}^3$)
22	Organic aerosol chemistry	$\mu\text{mole}/\text{m}^3$ ($\mu\text{g}/\text{m}^3$)
23	Aqueous aerosol chemistry	$\mu\text{mole}/\text{m}^3$ ($\mu\text{g}/\text{m}^3$)
24	Final concentration	$\mu\text{mole}/\text{m}^3$ ($\mu\text{g}/\text{m}^3$)
25	Units conversion	$\text{ppm}/(\mu\text{mole}/\text{m}^3)$ (N/A) ^b
26	Average cell volume	m^3

^a Units in the parentheses are for PM species.

^b Unit conversion factor for PM species is always 1.

The PA tool with IPR Analysis was used within the CAMx 12-km domain to investigate what (and to what extent) chemical and physical processes contribute to ozone, NO, and NO₂ formation and depletion during night-time hours for the grid cells corresponding to the Cypress River and Longview surface monitors. The days selected for PA analysis were August 16th-19th, 1999, which are the days corresponding to the large discrepancies in ambient and modeled night-time ozone concentrations at the Cypress River monitor, and the days associated with 1-hour exceedances in ozone

concentrations in DFW. During this period, ambient wind speeds are seen to be very low and are inversely related to the peak 1-hour and 8-hour ozone concentrations (ENVIRON, 2002). Conversely, during the beginning and end of the episode, surface wind speeds are considerably higher, with correspondingly lower ozone concentrations (ENVIRON, 2002). Throughout the episode, long range transport is seen to shift from the north to northeast and southeast, reflecting the wind directions, and considerable subsidence occurred during the period, which suppresses mixing and encourages accumulation of local emissions (ENVIRON, 2002).

Table 4-4 shows the night-time wind speeds (in mph) extracted from the CAMx surface layer for the Cypress River and Longview monitoring sites, averaged from 10:00 pm-6:00 am. As shown in Table 4-4, CAMx surface layer winds during these night-time hours are relatively and consistently light throughout the episode, similar to the observed ambient wind speeds.

Table 4-4. CAMx predictions of surface layer night-time (averaged from 10:00 pm-6:00 am) wind speeds (in mph) for grid cells corresponding to the Cypress River and Longview monitoring sites. Results are shown for August 13th-22nd, 1999.

Date in August, 1999	Cypress River Wind Speed (mph)	Longview Wind Speed (mph)
13	5.0	5.4
14	1.9	2.8
15	3.6	4.0
16	3.3	4.1
17	1.8	4.0
18	1.8	3.9
19	2.6	2.4
20	3.7	4.6
21	3.0	3.5
22	2.8	4.1

The HYSPLIT 48-hour back trajectories for August 17th and 19th are presented in Figures 4-26 and 4-27, respectively. For August 17th, back trajectory fetches are comparably longer and originate from the northeast, reflecting the impact of long range transport to background ozone concentrations affecting levels in DFW. For August 19th, the fetches are shorter and seem to show that winds originated and circulated within Texas. This evidence of a lack of ventilation undoubtedly coincided with the subsidence

described in the meteorology during this episode, contributing to the higher observed 1-hour average ozone concentrations on August 17th-19th.

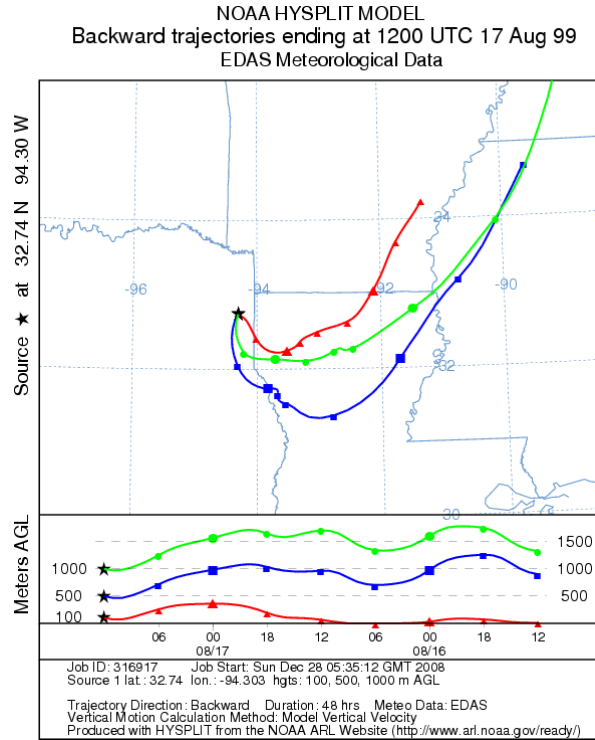


Figure 4-26. HYSPLIT 48-hour back trajectories from the Cypress River surface monitor at initial altitudes of 100, 500, and 1000 meters for 12:00 UTC on August 17th, 1999.

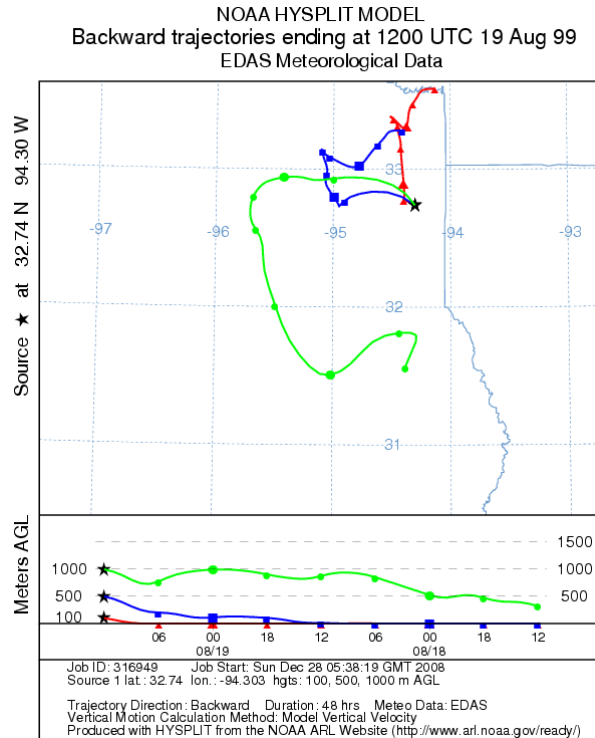


Figure 4-27. HYSPLIT 48-hour back trajectories from the Cypress River surface monitor at initial altitudes of 100, 500, and 1000 meters for 12:00 UTC on August 19th, 1999.

4.7.2 CAMx Process Analysis Results

Hourly total ozone concentrations (in ppb) and formation/depletion rates (in ppb/hr) output by the PA IPR analysis tool are shown for August 16th-19th in Figures 4-28 through 4-31. These results represent an average for the first three vertical layers in CAMx (97.3 magl in altitude) for the Cypress River location. Tables 4-5 and 4-6 present the total depletion/formation ozone contributions (a negative sign indicates ozone is being depleted) for the night-time hours of August 16th-17th and 18th-19th at the Cypress River and Longview sites, respectively. It should be noted that the night-time period analyzed for each day includes the hours of 10:00 pm-11:00 pm on that day and 12:00 am-6:00 am on the following morning.

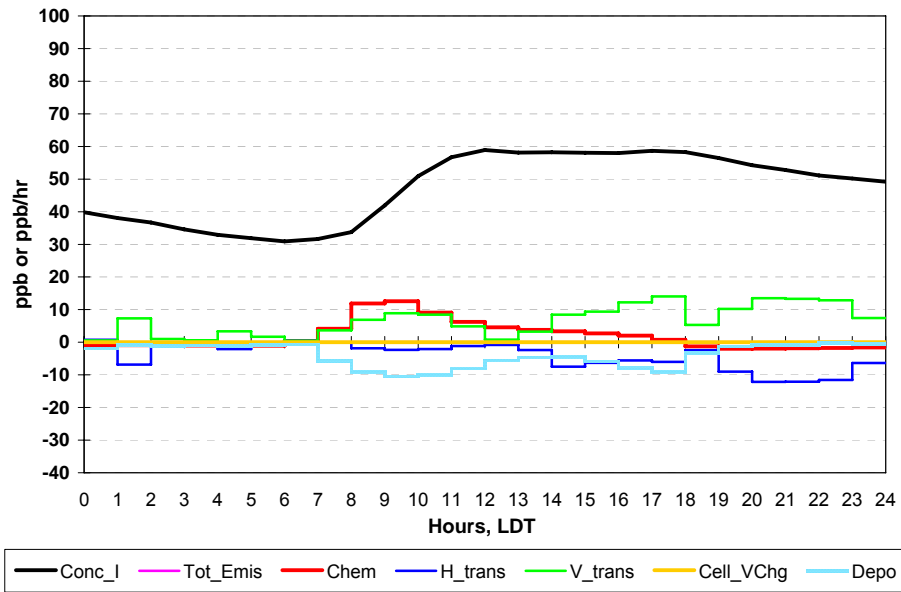


Figure 4-28. CAMx 12-km domain PA results for the Cypress River monitoring site on August 16th, 1999. Total ozone concentrations (ppb) and rates of formation/depletion (ppb/hr) are shown.

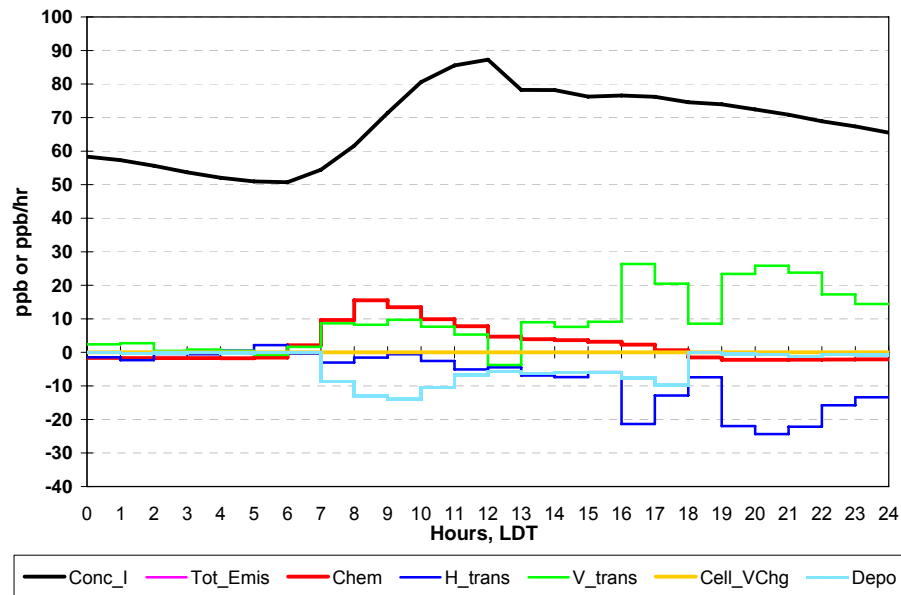


Figure 4-29. CAMx 12-km domain PA results for the Cypress River monitoring site on August 17th, 1999. Total ozone concentrations (ppb) and rates of formation/depletion (ppb/hr) are shown.

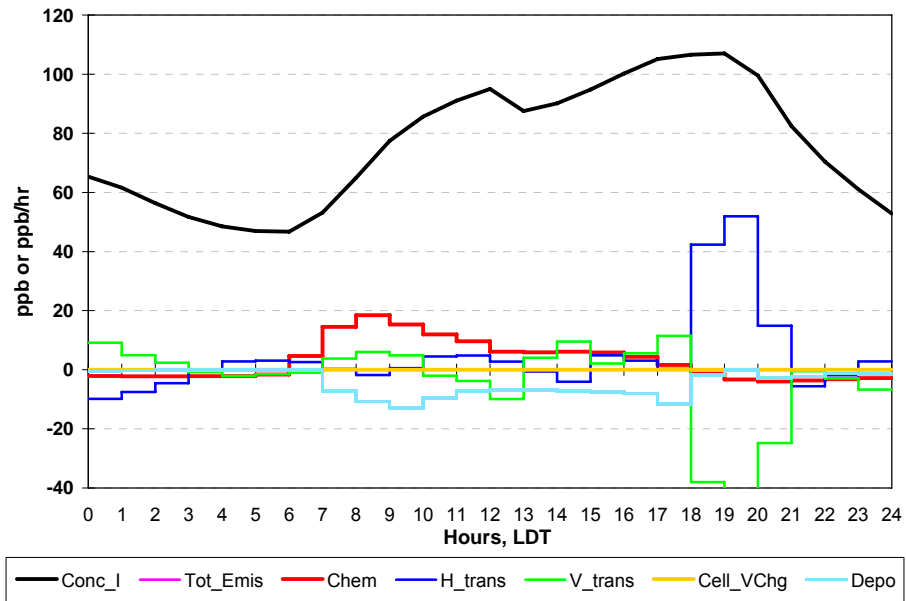


Figure 4-30. CAMx 12-km domain PA results for the Cypress River monitoring site on August 18th, 1999. Total ozone concentrations (ppb) and rates of formation/depletion (ppb/hr) are shown.

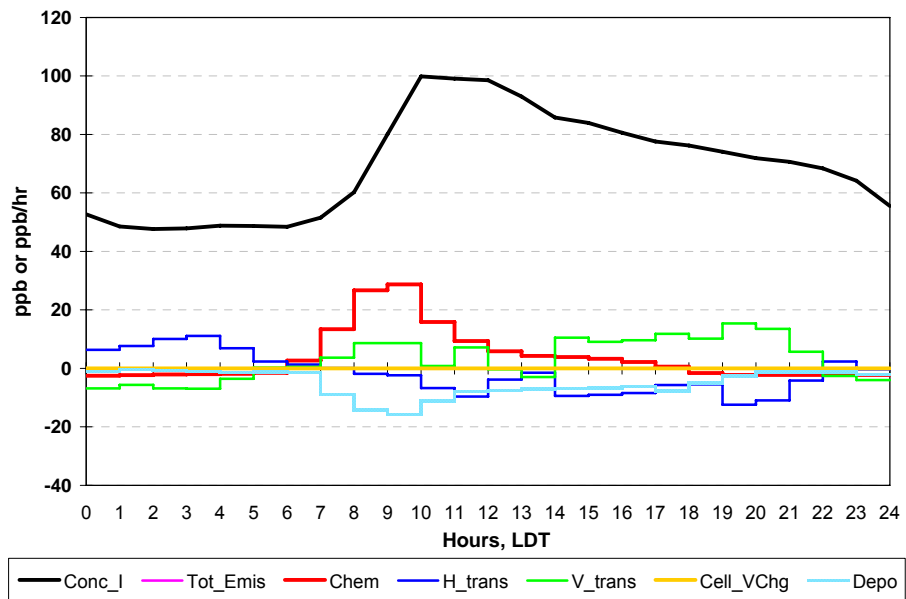


Figure 4-31. CAMx 12-km domain PA results for the Cypress River monitoring site on August 19th, 1999. Total ozone concentrations (ppb) and rates of formation/depletion (ppb/hr) are shown.

Table 4-5. CAMx initial and final total ozone concentrations (ppb) and total formation/depletion contributions (ppb) for 10:00 pm-6:00 am on August 16th-17th and 18th-19th, 1999. Results are shown for the Cypress River monitoring site, averaged over the first three vertical layers in the CAMx 12-km modeling domain.

	C,initial (ppb)	C,final (ppb)	Chemistry	Horiz. Advection	Horiz. Diffusion	Horiz. Transport	Vertical Diffusion	Vertical Advection	Vertical Transport	Deposition
Aug 16-17	51.1	54.2	-11.2	-18.0	-2.3	-20.3	11.1	17.0	28.1	-1.6
Aug 18-19	70.5	51.4	-15.8	47.8	-1.2	46.6	14.5	-53.3	-38.8	-10.3

Table 4-6. CAMx initial and final total ozone concentrations (ppb) and total formation/depletion contributions (ppb) for 10:00 pm-6:00 am on August 16th-17th and 18th-19th, 1999. Results are shown for the Longview monitoring site, averaged over the first three vertical layers in the CAMx 12-km modeling domain.

	C,initial (ppb)	C,final (ppb)	Chemistry	Horiz. Advection	Horiz. Diffusion	Horiz. Transport	Vertical Diffusion	Vertical Advection	Vertical Transport	Deposition
Aug 16-17	47.9	37.7	-56.9	-6.8	9	2.2	25.9	14	39.9	-3.2
Aug 18-19	49.4	46.1	-48.9	79.6	-9.2	70.5	24	-37.5	-13.5	-10.6

As shown in Tables 4-5 and 4-6, the process analysis results indicated that vertical mixing significantly impacting ozone concentrations. According to Table 4-5, for the night-time hours of August 16th-17th at the Cypress River location, ozone is generated by vertical transport and primarily consumed by horizontal transport, with additional losses due to chemistry and minor losses due to deposition. For the night-time hours of August 18th-19th, ozone is generated by horizontal advection and vertical diffusion. It is primarily consumed by vertical advection, with additional losses due to chemistry and deposition. It is interesting to note that deposition losses are larger for the night-time of August 18th-19th at the same location, since the land cover basis is the same for both evenings.

The data presented in Table 4-6 for the Longview monitoring site show similar trends in ozone production/loss processes, although horizontal transport is a source of ozone generation on both nights. This is due to the positive horizontal diffusion contribution during the night-time hours of August 16th-17th, which is a loss term for the same night at the Cypress River monitor. Additionally, the chemical contributions to ozone depletion are greater than those for Cypress River, which is expected from the

ozone and NO night-time concentration differences shown in Figures 4-11 through 4-14. Similar to the results shown for Cypress River, the vertical advection term becomes a source of ozone depletion on the night of August 18th-19th, resulting in an overall depletion of ozone due to vertical transport.

The HYSPLIT back trajectories shown in Figures 4-26 and 4-27 illustrate the primary difference between the processes governing ozone formation and depletion on these two nights. The long fetches in Figure 4-26 are indicative of dilution by horizontal advection; thus, it is expected that horizontal transport would be a primary source for ozone removal from the area. The short, circulating fetches shown in Figure 4-27, in addition to the subsidence experienced in the DFW region, are indicative of inhibited vertical mixing and little ventilation by horizontal advection.

The results shown in Tables 4-5 and 4-6 for the night-time hours of August 18th-19th may be explained by these meteorological results. Locally generated or previously transported ozone appears to be circulating within the area, and, since vertical mixing is inhibited, ozone from aloft is prevented from mixing with the air mass included within the area specified for the PA analysis. A previous meteorological analysis of this photochemical modeling episode concluded that the extreme concentrations experienced in DFW may be due to areas of near-zero winds superimposed upon a broader area of weak winds, which appear to arise from deformed flows near stationary fronts and diffluent zones associated with mesoscale high-pressure systems (McNider, 2005). These fronts and small high-pressure systems reduce horizontal dilution and may limit mixing heights, which is an explanation for the difference in the governing processes for ozone generation and depletion predicted by the CAMx PA tool for the two nights represented in Tables 4-5 and 4-6.

Ozone depletion due to chemistry does not vary much between the two night-time cases presented in Table 4-5. The PA results showing total concentrations and generation/depletion processes for NO are presented in Figure 4-32 below for August 17th for the Cypress River location. The trends observed here are identical for the days included in the PA analysis: NO is generated by emissions and consumed by chemistry during night-time hours.

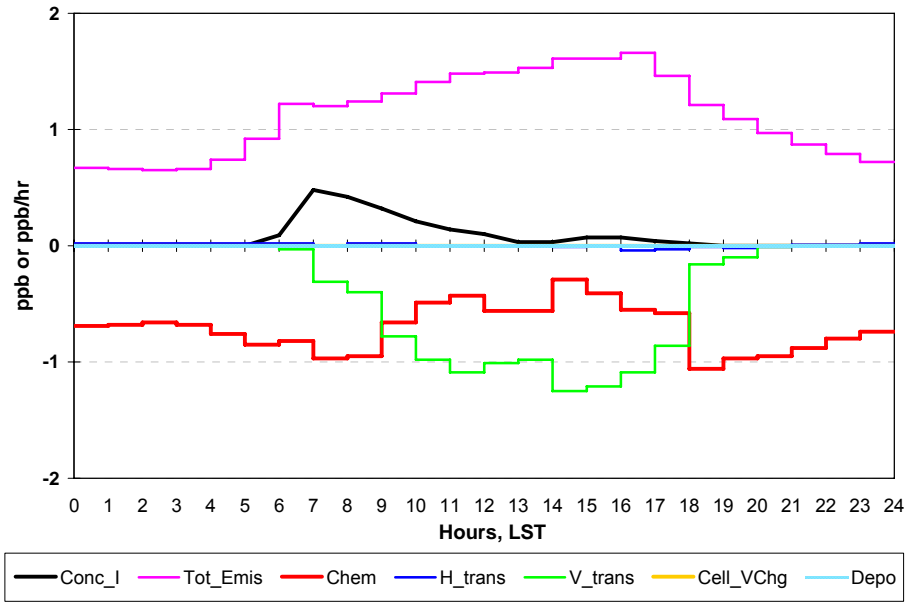


Figure 4-32. CAMx 12-km domain PA results for the Cypress River monitoring site on August 17th, 1999. Total NO concentrations (ppb) and rates of formation/depletion (ppb/hr) are shown.

Similar to the results in Figures 4-28 through 4-31, CAMx PA results are shown in Figures 4-33 through 4-36 for the Cypress River location for the sensitivity study involving a 10-fold increase in NO_x concentrations in all eastern Texas rural counties. From the results of the sensitivity studies summarized in Figure 4-23, only this simulation replicated similar CAMx night-time ozone concentrations at the Cypress River monitor to what is observed in the ambient data for this episode; however, increasing NO_x emissions by a factor of 10 resulted in substantial increases in daytime ozone concentrations (refer to Figure 4-25). When comparing these results to Figures 4-28 through 4-31, it is clear that the chemical contribution to ozone depletion is significantly larger for this case study.

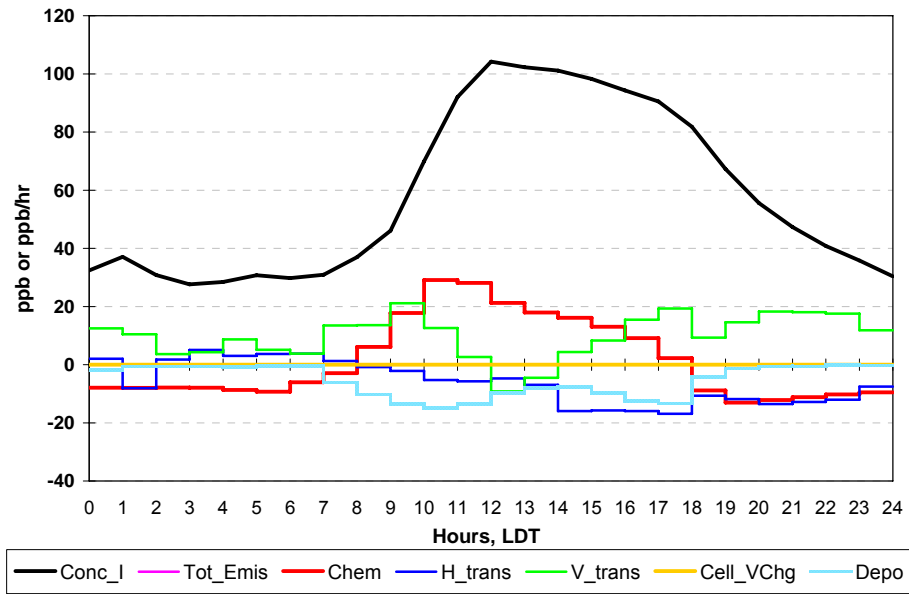


Figure 4-33. CAMx 12-km domain PA results for the Cypress River monitoring site on August 16th, 1999, for the case involving a 10-fold increase in NO_x emissions in rural East Texas counties. Total ozone concentrations (ppb) and rates of formation/depletion (ppb/hr) are shown.

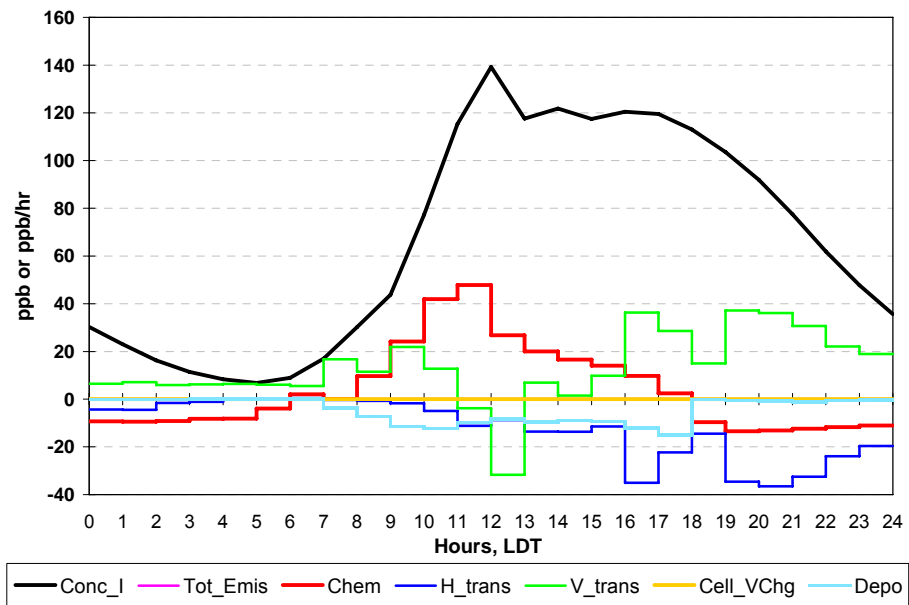


Figure 4-34. CAMx 12-km domain PA results for the Cypress River monitoring site on August 17th, 1999, for the case involving a 10-fold increase in NO_x emissions in rural East Texas counties. Total ozone concentrations (ppb) and rates of formation/depletion (ppb/hr) are shown.

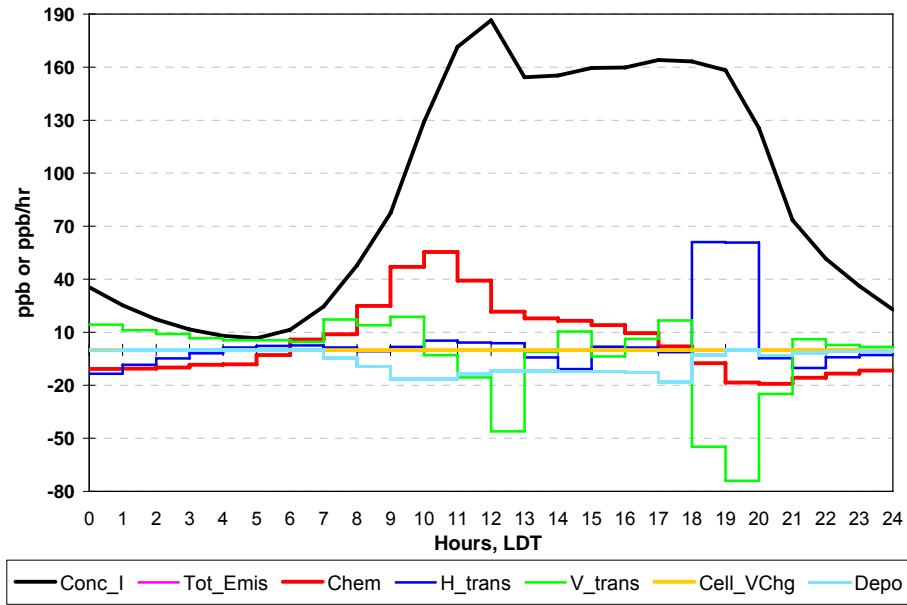


Figure 4-35. CAMx 12-km domain PA results for the Cypress River monitoring site on August 18th, 1999, for the case involving a 10-fold increase in NO_x emissions in rural East Texas counties. Total ozone concentrations (ppb) and rates of formation/depletion (ppb/hr) are shown.

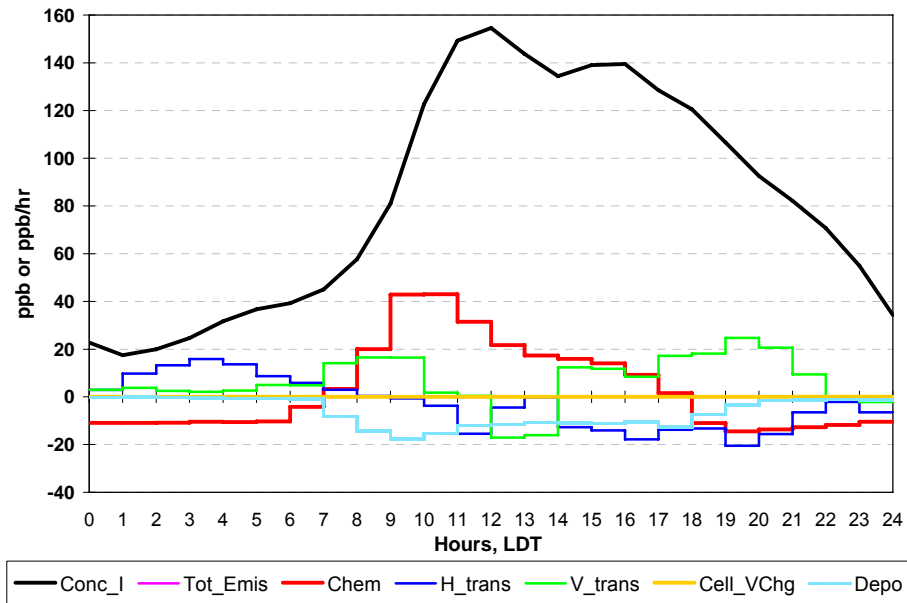


Figure 4-36. CAMx 12-km domain PA results for the Cypress River monitoring site on August 19th, 1999, for the case involving a 10-fold increase in NO_x emissions in rural East Texas counties. Total ozone concentrations (ppb) and rates of formation/depletion (ppb/hr) are shown.

Similar to the data in Tables 4-5 and 4-6, Tables 4-7 and 4-8 summarize the results of this sensitivity simulation for the CAMx 12-km grid cells corresponding to the Cypress River and Longview surface monitors, respectively. In comparison to the base case, results for both night-time periods show a decrease in deposition rates and increases in magnitudes of chemical depletion, horizontal transport, and vertical diffusion rates.

Table 4-7. CAMx initial and final total ozone concentrations (ppb) and total formation/depletion contributions (ppb) for 10:00 pm-6:00 am on August 16th-17th and 18th-19th, 1999. Results are shown for the Cypress River monitoring site, averaged over the first three vertical layers in the CAMx 12-km domain, for the case study involving a 10-fold increase in NO_x emissions in rural East Texas counties.

	C,initial (ppb)	C,final (ppb)	Chemistry	Horiz. Advection	Horiz. Diffusion	Horiz. Transport	Vertical Diffusion	Vertical Advection	Vertical Transport	Deposition
Aug 16-17	40.8	17	-65.9	-35.7	5.3	-30.5	51.8	21.6	73.4	-0.5
Aug 18-19	51.7	44.9	-93.2	54.3	8.7	63	62.9	-34.4	28.5	-4.6

Table 4-8. CAMx initial and final total ozone concentrations (ppb) and total formation/depletion contributions (ppb) for 10:00 pm-6:00 am on August 16th-17th and 18th-19th, 1999. Results are shown for the Longview monitoring site, averaged over the first three vertical layers in the CAMx 12-km domain, for the case study involving a 10-fold increase in NO_x emissions in rural East Texas counties.

	C,initial (ppb)	C,final (ppb)	Chemistry	Horiz. Advection	Horiz. Diffusion	Horiz. Transport	Vertical Diffusion	Vertical Advection	Vertical Transport	Deposition
Aug 16-17	11.1	4.2	-141.6	31.1	10.5	41.6	77.7	15.6	93.2	0
Aug 18-19	51.7	44.9	-266.6	163.3	21.7	184.9	104.2	-25.8	78.4	-0.9

During the night-time hours of August 16th-17th, ozone losses due to chemistry increased by 54.7 ppb at the Cypress River location and 84.7 ppb at the Longview location. The final concentration of ozone at 6:00 am for both sites on August 17th is significantly lower than the base case. For this overnight period, the primary methods of ozone depletion are chemistry and horizontal transport at the Cypress River location, while ozone is consumed solely due to chemistry at the Longview location. For both monitors, vertical transport (vertical diffusion) is the predominant method of ozone

generation. The primary discrepancy in results for both monitoring sites on this night is the horizontal advection term, which is similar in magnitude but negative (an ozone depletion term) at the Longview site.

For the night-time hours of August 18th-19th, the differences between the base case and this sensitivity case are more substantial. Ozone losses due to chemistry increased by 77.4 ppb at the Cypress River location and 217.8 ppb at the Longview location. Horizontal transport by means of advection is consistently the largest contributor to ozone generation on this night, and overnight ozone concentrations do not decrease to same extent as on August 16th-17th. While vertical diffusion rates significantly increased for both night-time periods in comparison to the base case, the magnitude of vertical advection rates decreased for the August 18th-19th overnight period at both locations. The positive vertical diffusion rate dominates in this sensitivity case study, resulting in an overall generation of ozone due to vertical transport, compared to ozone depletion for the base case. It is important to note that this result is inconsistent with the previously discussed meteorological events that occurred during the episode at this time, which support the base case result of ozone depletion by vertical transport during the night of August 18th-19th.

4.8 IMPLICATIONS OF DIURNAL PATTERNS OF RURAL OZONE CONCENTRATIONS

Several factors are likely contributing to the discrepancy between modeled and observed night-time ozone and NO_x concentrations in rural East Texas. The combination of under-prediction of NO_x and over-prediction of ozone at night exclusively in rural areas characterized by extensive oil and gas production strongly suggests that NO_x emissions due to oil and gas production are underestimated. The extent of the under-estimation of these emissions is made unclear by uncertainties in the meteorology. Vertical mixing plays a critical role in determining ozone concentrations under episodic conditions. Studies have shown that, in rural areas beyond the impact of urban pollutant plumes, the vertical mixing process may be the dominant mechanism for the buildup of ozone near the surface (Zhang et al., 1999). Furthermore, results from the PA analyses indicate that examining the vertical mixing parameterization in the model may have a

significant impact on the sensitivity of the model to changes in NO_x emissions. Based on these findings, one hypothesis is that the model may be overestimating vertical mixing, and NO_x emissions may be mixing aloft to layers above the first three vertical layers in CAMx, rather than titrating ozone near the surface.

The planetary boundary layer (PBL) depth, or atmospheric mixing height, is a useful and straightforward indication of the extent of vertical mixing. The PBL determines the depth through which the precursors emitted near the ground level are mixed and influences the amount of ozone that can be mixed downward to the ground (Zhang et al., 1999). Instead of directly using the mixing height or planetary boundary layer depth, advanced photochemical models such as CAMx use the turbulent vertical exchange coefficient predicted by the meteorological model, K_v , to describe vertical mixing and the vertical layer structure within the model.

Previous CAMx modeling results of the DFW SIP episode included in this work have suggested that low-level mixing problems may contribute to low ozone production in the urban core. In particular, the vertical mixing within the lowest layers of the model appeared to be weak, trapping the emissions in the lowest layers of the model (ENVIRON, 2003). A vertical mixing adjustment (called “Kv100”) was applied in post-processing, which increased the mixing in the first three layers to match the mixing at 100 meters. More specifically, all vertical diffusivity fields were “patched” such that in each column, the largest diffusivity value in the lowest 100 meters was used for every layer below 100 meters. This adjustment improved CAMx ozone predictions in the urban core by producing more ozone in areas with strong NO_x emissions that had previously experienced low ozone production (ENVIRON, 2003).

To test the hypothesis that altering the vertical mixing may effectively titrate CAMx night-time ozone concentrations in rural East Texas to near-ambient levels, a sensitivity study was performed by decreasing the K_v values input into CAMx for Panola and Freestone counties to one half of the original values. The K_v values were decreased for the first three vertical layers (approximately 100 meters), similar to the methodology used in Kv100. The resulting time series of modeled hourly ozone concentrations at the Cypress River and Longview sites are presented in Figures 4-37 and 4-38, as well as

observed 1-hour average ozone concentrations at both surface monitors. In comparison to the CAMx base case, decreasing K_v values by this magnitude produced minimal changes in surface level ozone concentrations at both locations.

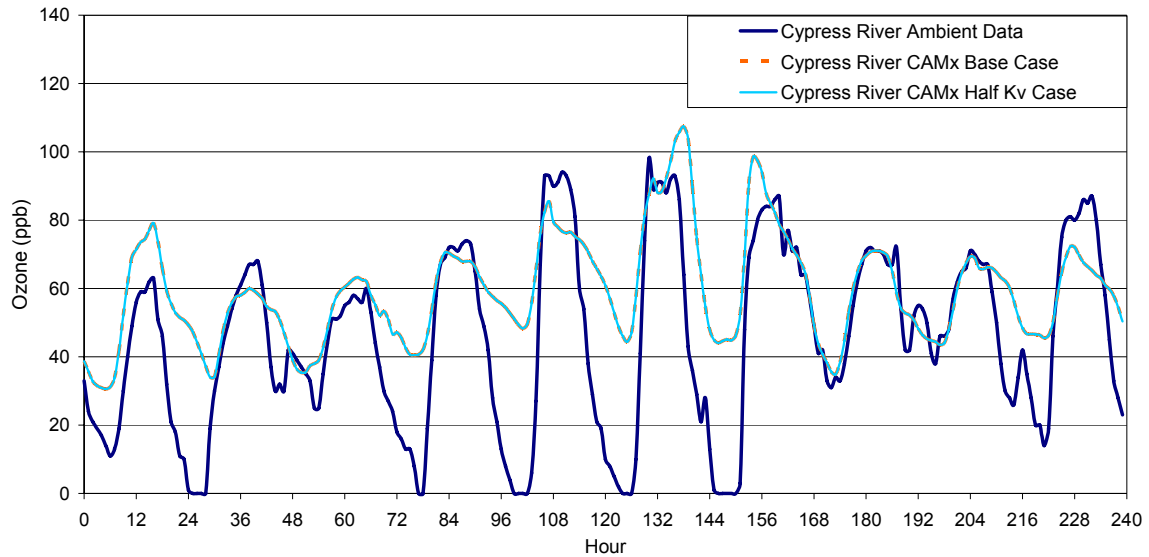


Figure 4-37. Hourly ambient and CAMx-predicted ozone concentrations (in ppb) for the Cypress River monitor during August 13th-22nd, 1999. Modeled results are shown for the CAMx base case and for the sensitivity study involving decreased K_v values at Panola and Freestone counties within the first three vertical layers in the CAMx 12-km domain.

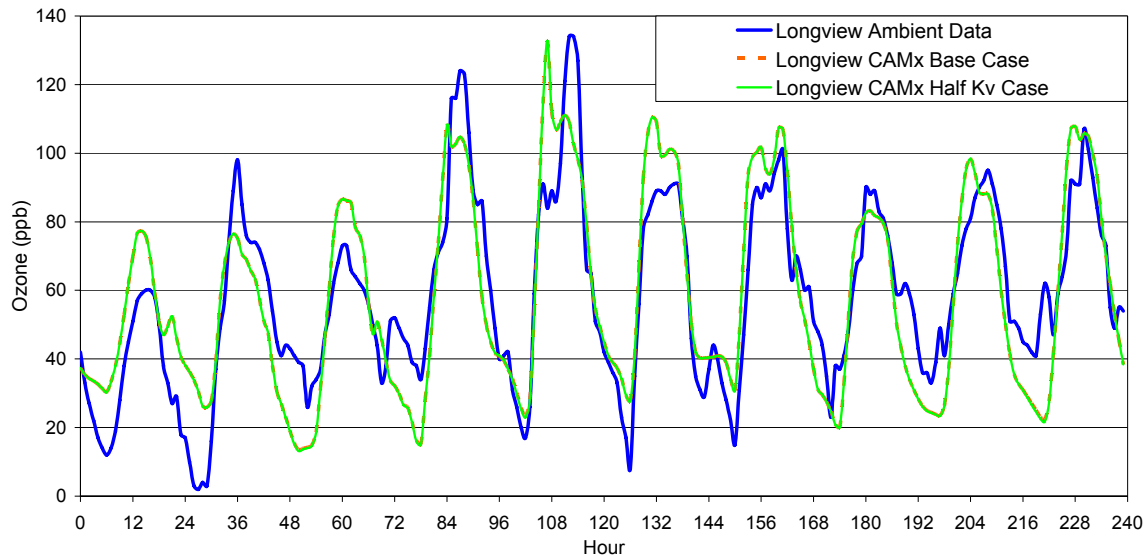


Figure 4-38. Hourly ambient and CAMx-predicted ozone concentrations (in ppb) for the Longview monitor during August 13th-22nd, 1999. Modeled results are shown for the CAMx base case and for the sensitivity study involving decreased K_v values at Panola and Freestone counties within the first three vertical layers in the CAMx 12-km domain.

4.9 CONCLUSIONS

Results from this Chapter include findings from a network of monitoring sites that were established in the rural areas of East Texas as part of the TexAQS II study. The data from this network indicate that a substantial component of background ozone is transported into the State under air flow from the northeast and east, and baseline gradients in background ozone levels can be observed to extend from lower in the south to higher in the north. The rural surface monitoring network also indicates the presence of substantial urban plumes.

Comparisons of measurements made by this network to results from photochemical modeling indicate a significant discrepancy between modeled and observed night-time rural ozone concentrations. At some, but not all, rural monitoring sites, measured night-time ozone concentrations are substantially lower than modeled values. The data concerning diurnal patterns of ozone and NO_x concentrations and emissions from rural surface monitors, coupled with the locations of the monitors, suggest that estimates of emissions from oil and natural gas production operations in rural

Northeast Texas may be underestimated. Until better data are available in regards to night-time rural vertical advection and mixing, it may be difficult to precisely quantify the extent to which rural NO_x emissions are underestimated.

Surface mobile monitoring is an effective method for collecting air quality data over large geographic regions between surface monitoring stations (Northeast Texas Air Care, or NETAC, 2010). This involves measurements from instruments that are installed in a vehicle that is driven along roads to conduct concentration surveys. The University of Texas, in conjunction with work proposed by ENVIRON to NETAC, collected surface mobile samples in rural Northeast Texas areas to investigate the spatial distribution and magnitude of VOC and NO_x emissions from oil and gas production activities (NETAC, 2010) . Emissions inventories have been updated to integrate these measurements and to reflect increases in NO_x from drill rigs in Northeast Texas and satellite fire emissions data for the Eastern U.S. (NETAC, 2010). The effects of these more recent inventories on modeled ozone concentrations in Northeast Texas have shown enhancements in the CAMx model performance, though mostly in relation to capturing maximum ozone concentrations, which typically occur during daytime hours (ENVIRON, 2009).

4.10 REFERENCES

- Allen, D., and J. Olaguer (2004), “State of the Science of Air Quality in Eastern Texas: Major Scientific Findings and Recommendations”, Report for the Texas Environmental Research Consortium, July 31, 2004, available at <http://files.harc.edu/Projects/AirQuality/Projects/H030.2004/H30FinalReport.pdf>.
- Allen, D. T., and M.P. Fraser (2006), “An Overview of the Gulf Coast Aerosol Research and Characterization Study: The Houston Fine Particulate Matter Supersite”, *Journal of the Air and Waste Management Association*, 56, 456-466.
- Daum, P., J. Meagher, D. Allen, and C. Durrenberger (2002), “Accelerated Science Evaluation of Ozone Formation in the Houston/Galveston Area: Summary”, Report to the Texas Natural Resources Conservation Commission, Austin, TX, November 13, 2002, available at <http://www.utexas.edu/research/ceer/texaqsarchive/accelerated.htm>.
- Draxler, R.R. and G.D. Rolph (2003), HYSPLIT (HYbrid Single-Particle Lagrangian Integrated Trajectory), NOAA Air Resources Laboratory, Silver Spring, MD, Model access via the NOAA ARL READY website, available at <http://www.arl.noaa.gov/ready/hysplit4.html>, accessed March 2010.
- ENVIRON International Corporation (2002), “Conceptual Model of Ozone Formation in the Dallas/Fort Worth Ozone Non-Attainment Area”, Final report, Novato, CA, October 2002.
- ENVIRON International Corporation (2003), “Development of Base Case Photochemical Modeling to Address 1-Hour and 8-Hour Ozone Attainment in the Dallas/Fort Worth Area”, Final report prepared by Mansell, G., G. Yarwood, M. Jimenez, and T. Dinh for the Texas Commission on Environmental Quality, Novato, CA, August 2003.
- ENVIRON International Corporation (2004), User’s Guide – Comprehensive Air Quality Model with extensions (CAMx), Version 4.00, Novato, CA, available at <http://www.camx.com>.
- ENVIRON International Corporation (2009), “Recent Improvements to the 2005 Ozone Model”, Presentation given to the Northeast Texas Air Care (NETAC) Technical Committee, Novato, CA, April 2009, available at http://etcog.sitestreet.com/UserFiles/File/NETAC/pdf/reports/air%20quality/2009/Enclosure_TC3.pdf.
- Golden Software, Surfer product description, available at <http://www.goldensoftware.com/products/surfer/surfer.shtml>, accessed March 2010.

- Lawson, D.R., N.F. Robinson, S. Diaz, J.G. Watson, E.M. Fujita, and P.T. Roberts (1995), "Coastal Oxidant Assessment for Southeast Texas (COAST) Project", Final Report submitted to the Texas Natural Resource Conservation Commission, August 1995.
- Northeast Texas Air Care (NETAC) (2010), "Summary of 2009 NETAC Air Quality Planning Activities", Final Report, March 2010.
- Schichtel, B.A., K.A. Gebhart, M.G. Barna, W.C. Malm, D.E. Day, S. Kreidenweis, and J. Collett, Jr. (2004), "Big Bend Regional Aerosol and Visibility Observational (BRAVO) Study Results: Air Quality Data and Source Attribution Analyses Results from the National Park Service/Cooperative Institute for Research in the Atmosphere", Final report prepared by the Cooperative Institute for Research in the Atmosphere, Colorado State University, Ft. Collins, CO, 2004, available at http://vista.cira.colostate.edu/improve/Studies/BRAVO/reports/FinalReport/bravofinalreport_CIRA.htm.
- Sullivan, D.W., V.M. Torres, and M.C. Dionisio (2006), "Early Findings from a Regional Ozone and PM_{2.5} Field Study in Texas", Extended abstract #06-A-354-AWMA, submitted to the Air and Waste Management Association.
- Texas Commission on Environmental Quality (2007), personal communication, Office of the Chief Engineer.
- Texas Commission on Environmental Quality (2008a), State Implementation Plan website reference, available at <http://www.tceq.state.tx.us/nav/eq/sip.html>, accessed December 2008.
- Texas Commission on Environmental Quality, Monitoring Operations (2008b), TexAQS II reference, available at <http://www.tceq.state.tx.us/nav/eq/texaqsII.html>, accessed December 2008.
- Texas Commission on Environmental Quality, Monitoring Operations (2008c), Air pollution and meteorological data, available at http://www.tceq.state.tx.us/nav/data/air_met_data.html, accessed December 2008.
- Texas Commission on Environmental Quality, 1999 Dallas-Fort Worth ozone SIP modeling reference, available at <http://www.tceq.state.tx.us/implementation/air/airmod/data/dfw1.html>, accessed April 2010.
- U.S. Environmental Protection Agency, AIRNow website reference, available at www.airnow.gov, accessed December, 2008.

Zhang, J., and S. T. Rao (1999), "The role of vertical mixing in the temporal evolution of ground-level ozone concentrations," *Journal of Applied Meteorology*, 38, 12, 1674–1691.

Chapter 5: Intercomparison of Ambient Data and Photochemical Modeling to Characterize Pollutant Transport in Plumes

5.1 INTRODUCTION

As discussed in previous chapters, ambient measurements and modeling tools have been used for the characterization of ozone transport over regional scales. In this Chapter, data from surface monitoring stations will be coupled with aircraft LIDAR measurements to obtain quantitative estimates of ozone fluxes upwind and downwind of urban areas. These calculated fluxes will be compared to photochemical model predictions to evaluate the performance of the model, and the model will then be used to evaluate source contributions (discussed in Chapter 6).

The observational datasets that will be used in this work include data from two urban areas with very different emission profiles: Dallas-Fort Worth (DFW) and Houston. The DFW area is largely dominated by vehicular emission sources, while the Houston area has substantial emissions from both typical urban sources and petrochemical industry sources (Kemball-Cook et al., 2009). In particular, for Houston, the urban plumes encounter different conditions as they move downwind, providing robust evaluation possibilities for the ability of photochemical models to predict the extent of regional ozone transport.

Ozone flux calculations were performed using surface monitoring data for six case studies in which aircraft LIDAR data were available for similar calculations, incorporating measurements collected during the TexAQS field studies in 2000 and 2006. The availability of observational data from these large field studies allows for quantitative comparisons of regional ozone transport from the Houston area for years in which substantial reductions in Houston emissions have been achieved. The work presented in Chapter 3 used photochemical modeling to quantitatively characterize regional impacts of the transport of ozone and ozone precursors. Results provided strong evidence that anthropogenic emissions originating in Houston can have significant impacts on ozone concentrations in other cities within the State, and suggested a need for additional characterizations of regional ozone transport in Texas. The remainder of this Chapter will describe complimentary methods using ambient data to provide quantitative

estimates of ozone levels transported in urban plumes within Texas, as well as preliminary comparisons between the results obtained with observational data and photochemical modeling.

5.2 OBSERVATIONAL CHARACTERIZATIONS OF OZONE TRANSPORT: DATA FROM AIRBORNE LIDAR AND SURFACE MONITORS

During the TexAQS I (2000) and the TexAQS II (2006) field campaigns, the National Oceanic and Atmospheric Administration (NOAA) measured ozone concentrations using a LIDAR (Light Detection and Ranging) sensor mounted on an aircraft. LIDAR is an optical remote sensing technology, which Chapter 2 described in more detail. Coupled analysis of the aerosol backscatter and ozone absorbing wavelengths incorporated in LIDAR measurements provides vertical profiles of pollutant concentrations. These measurements may be collected along horizontal flight paths to generate map pollutant concentrations along a pre-defined 2-dimensional flight path, often with the purpose of characterizing the formation and pollutant transport in plumes. Based on these measurements, quantitative estimates of regional transport of ozone have been derived from the average ozone measured during flight transects downwind of an urban area (Senff et al., 2007). As an additional method of quantifying ozone transport, the horizontal flux is defined as the mass of ozone transported across a boundary per unit time, divided by the area over which the ozone is transported.

Observational airborne LIDAR data collected during TexAQS I and II were used to compute the total horizontal flux of ozone emitted by Houston and DFW for several days in August and September of 2000 and 2006 (Senff et al., 2007). On these days, LIDAR observations provided vertical profiles of ozone concentrations, extending from the surface to approximately 2500 meters above mean sea level (mMSL), at a vertical and temporal resolution of 90 meters and 10 seconds, respectively. As described in Chapter 2, the LIDAR-derived vertically averaged excess ozone (plume ozone minus background ozone) was integrated across the entire area between the surface and the top of the planetary boundary layer (PBL) and within horizontal plume boundaries. For each transect, the excess ozone resulting from this integration (divided by the duration time of

the flight transect, t) was then multiplied by the average wind speed, \bar{u} (obtained from nearby wind profilers), and the area of the plume, A , to compute the total horizontal ozone flux according to Equation 5.1:

$$Ozone\ Flux = \left(\frac{1}{t}\right) \left[\int_0^t (Plume\ O_3 - Background\ O_3) dt \right] * \bar{u} * A \quad (\text{Equation 5.1})$$

Figure 5-1 illustrates the LIDAR data collected by Senff et al. (2007) from a NOAA Twin Otter flight during TexAQS II on August 14th, 2006. Ozone contours are shown for the entire flight track along each transect, vertically averaged over 200-1000 mMSL, along with an image of ozone concentrations recorded as a function of altitude for one flight transect. For this transect, the background and plume ozone levels are clearly distinguishable. The boundary layer height, which is easily interpreted from the LIDAR backscatter, is also estimated from these LIDAR time series plots. The horizontal extent of the plume (plume width) is calculated by multiplying the amount of time the plane observed these elevated ozone levels by the average aircraft speed of 60 meters per second.

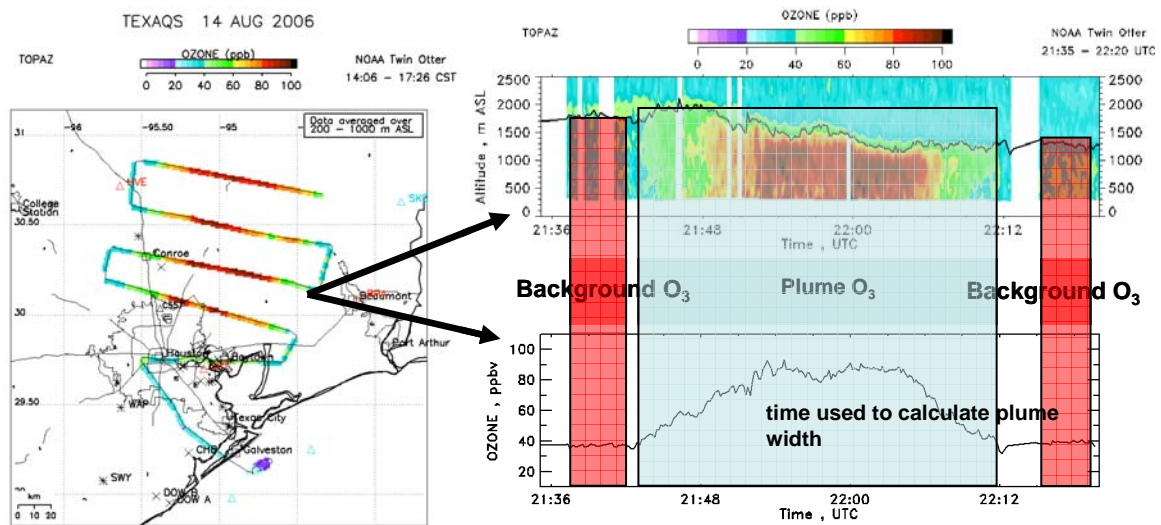


Figure 5-1. LIDAR data collected by the NOAA Twin Otter for the second flight transect on August 14th, 2006 (Senff et al., 2007).

While the aircraft data are a valuable and relatively accurate source for the data used for air pollutant flux calculations, the inherent scarcity of such data indicates a need for performing similar calculations with other data that is more readily and frequently available. To assess whether surface monitoring data may achieve this, an inter-comparison was performed between flux estimates based on surface data and airborne plume flux calculations. Comparisons between the aircraft LIDAR data and photochemical modeling estimates will also be presented later in this Chapter.

Ozone flux calculations were performed using surface monitoring data for six case studies in which aircraft LIDAR data had previously been used for similar calculations. Five of the case studies are focused on the Houston urban region and one of the case studies is focused on the DFW urban region. Of the six case studies, four incorporated surface monitoring data collected during the TexAQS II field study during 2006. The remaining two case studies used surface data collected during the first TexAQS field study in 2000. Flux calculations were also performed for the two episode days in 2000 using the results of a photochemical modeling simulation from August 22nd– September 6th, 2000.

5.2.1 Ozone Flux Calculation Method with Surface Monitor Data

The total amount of ozone passing through a boundary is calculated as the product of the average ozone concentration along that boundary multiplied by the wind speed perpendicular to the boundary and the mixing height. Results are represented as a flux which is defined as the mass of ozone entering the boundary per unit time, divided by the area for ozone transport. This flux is strictly a component of horizontal bulk transport by advection, and transport by diffusion is not included in the analysis. In addition to quantifying ozone transport in terms of flux, these calculations were used to quantify the amount of ozone generated by an urban area. This is done by implementing a box model analysis and a basic mass balance approach (defining a “box” around an urban area), as shown in Figure 5-2.

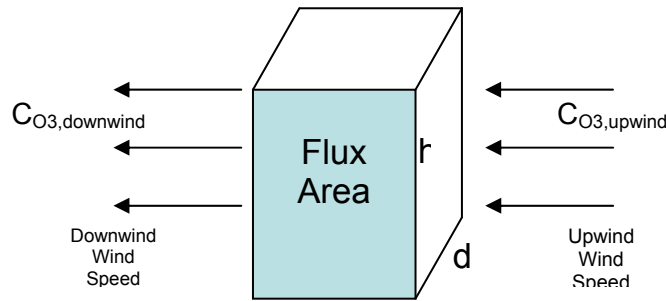


Figure 5-2. Illustration of the “box” model for ozone flux calculations with surface monitor data.

Using ozone concentrations obtained from surface monitors and wind speed data at the upwind and downwind boundaries of the urban area, it is possible to estimate the total amount of ozone generated by this urban “box” by implementing the calculation methods discussed above, according to Equation 5.2:

$$Ozone\ Flux = [C_{O_3,downwind} - C_{O_3,upwind}] * \bar{u} * A \quad (\text{Equation 5.2})$$

where \bar{u} represents the mean wind speed, averaged at the upwind and downwind locations, C_{O_3} is the concentration of ozone, and A is the area of transport. For the “box” model described above, the area (A) would be the height of the PBL, h , multiplied by the length of the horizontal boundary of interest, d . For ozone flux calculations in plumes, the area of interest would be the height of the PBL multiplied by the horizontal extent of the plume. The assumption of a well-mixed PBL is also implemented.

Observational surface measurements include 1-hour average ozone concentrations and wind speeds (averaged from measurements collected in 5-minute intervals), as recorded by the upwind and downwind monitors for the hour most closely corresponding to the flight transect associated with the highest LIDAR-derived ozone flux. These surface measurements were obtained from the TCEQ online database, available at http://www.tceq.state.tx.us/cgi-bin/compliance/monops/daily_average.pl. The average upwind ozone concentration, or background ozone concentration, is background only in a local spatial and short-term temporal sense and does not refer to a continental-scale background (Kemball-Cook et al., 2009). These concentrations are likely influenced by

urban plumes from other nearby and distant cities, or even recirculation of ozone produced from the same city on an earlier day (Kemball-Cook et al., 2009).

5.2.2 Estimation of the Planetary Boundary Layer Height

The height of the planetary boundary layer (PBL, also referred to as the convective boundary layer or vertical mixing height) is a basic scaling parameter that is required for pollutant flux calculations. PBL height measurements with boundary layer wind profilers are now a common part of many field campaigns addressing air quality (Nielsen-Gammon et al., 2008). The PBL height can be detected as an enhancement in the radar reflectivity due to strong humidity gradients and turbulence. Figure 5-3 shows the results of an analysis performed as part of TexAQS II that used wind profilers located in various geographic regions of Texas to approximate vertical mixing heights (Wilczak et al., 2007). The results show the diurnal variations and statistical distributions of PBL heights and illustrate that the average hourly mixing height (as well as diurnal variability) can vary significantly depending on location and the meteorology associated with the days that were included in the analysis. Figure 5-4 shows the geographical locations of the wind profilers used in this assessment (Wilczak et al., 2007).

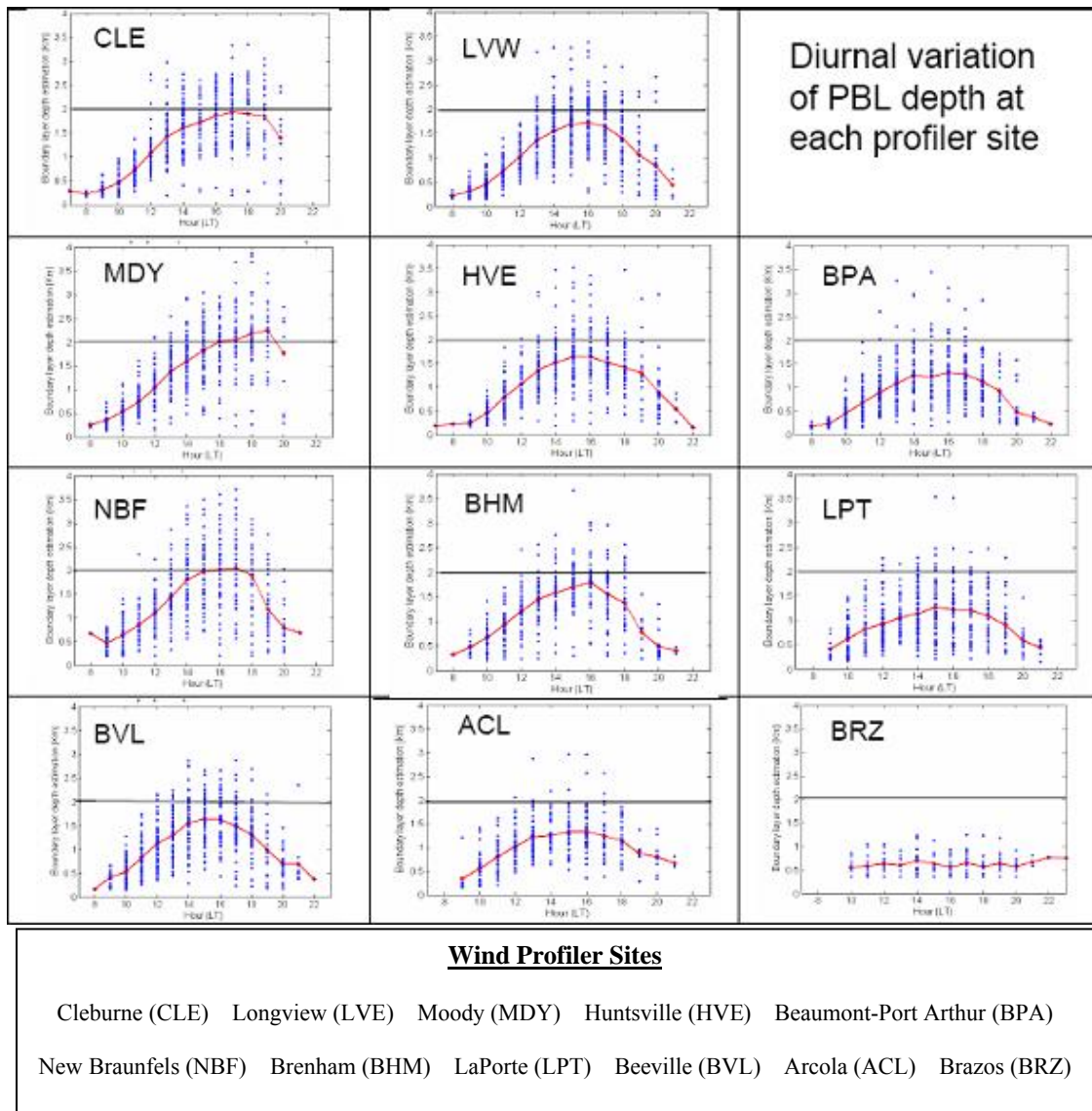


Figure 5-3. Radar profiler summaries of planetary boundary layer diurnal patterns during TexAQS II (Wilczak et al., 2007).

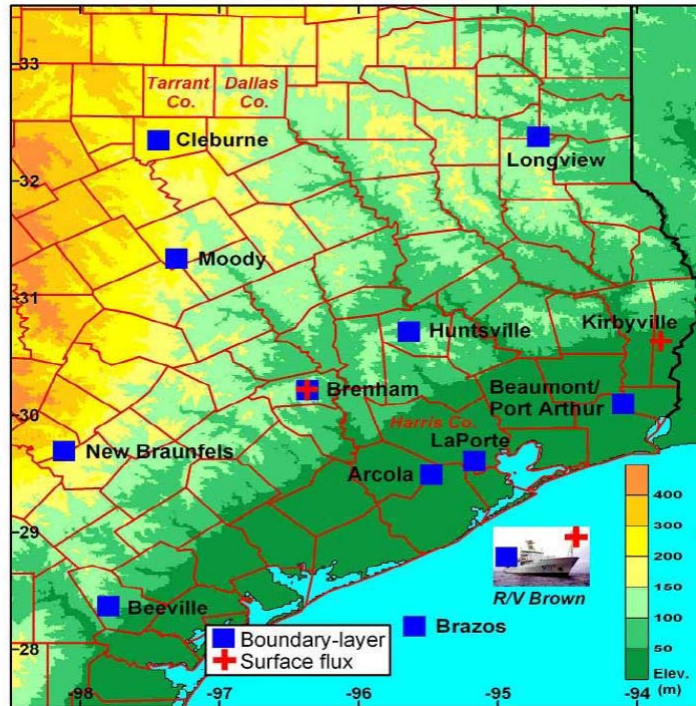


Figure 5-4. Geographical locations of radar profilers used in the TexAQS II analysis of diurnal patterns of average PBL heights (Wilczak et al., 2007).

With the exception of the Brazos (BRZ) wind profiler located offshore, the diurnal patterns show a common trend of hourly increases in the average mixing height (indicated by the red line in Figure 5-3) until a maximum is reached during the afternoon hours (typically between 15:00-17:00 CST), followed by hourly decreases in the average mixing height. A general observation based on this data is that locations closer to the coastline experience lower mixing heights compared with results for wind profilers located farther inland. For example, the average maximum mixing heights at LaPorte and Brazoria are around 1100 meters and 500 meters, respectively; however maximum average mixing heights observed at wind profilers near Dallas can reach an average of 2000 meters (e.g., refer to the Cleburne wind profiler site (CLE)).

For case study days characterized by winds from the south transporting urban plumes to the north of the Houston region, the vertical mixing height was estimated to be 1500 meters. This average mixing height was selected based on the maximum average mixing heights measured at wind profiler stations located farther inland from the coast, including Huntsville (HVE) and Brenham (BHM). For August 30th, 2006, which was a

case study day with an urban plume advecting south from Houston and over the Gulf of Mexico, a lower estimated vertical mixing height of 1000 meters was used in calculations, based on the average maximum mixing heights experienced at wind profilers closer to the coast, such as LaPorte (LPT). For September 13th, 2006, the case study day characterizing the Dallas urban plume, the vertical mixing height was estimated to be around 2000 meters. This estimate was based on the maximum average mixing heights estimated for wind profiler locations to the south of Dallas, including the Cleburne (CLE) and Moody (MDY) profilers.

Table 5-1 summarizes the mixing height approximations used in ozone flux calculations as estimated from the wind profiler data, as well as those computed with aircraft LIDAR measurements (Senff et al., 2007). LIDAR-derived mixing heights were computed based on data collected along each flight transect; therefore, the LIDAR results in Table 5-1 are listed as a range of mixing heights for each day. Additionally, mixing heights were averaged over each individual flight transect and in some cases, such as August 12th and 14th, 2006, mixing heights measured by the LIDAR varied significantly (by a factor of 2 or so) along the plume transects (Senff et al., 2007).

Table 5-1. Approximations of PBL depth used in ozone flux calculations as estimated from wind profiler data, as well as those computed with aircraft LIDAR measurements (Senff et al., 2007).

Urban Region	Date	Wind Direction	LIDAR Data (m)	Wind Profiler Average Estimate (m)
Houston	8/12/2006	S	1303-1499	1500
Houston	8/14/2006	S	1517-1552	1500
Houston	8/30/2006	N	1173-1418	1000
Houston	8/28/2000	S	1601-2582	1500
Houston	9/6/2000	NE	771-2005	1500
Dallas-Ft. Worth	9/13/2006	N	1001-1246	2000

As discussed in Section 5.2.2, the PBL height for the Dallas area was based on estimates of the maximum mixing height achieved at a nearby wind profiler (Cleburne). As Table 5-1 shows, this estimate is significantly different in comparison to the range of LIDAR measurements on September 13th, 2006. The PBL height can vary significantly

with location and meteorology, and the mixing height observed on this day may not be indicative of the average mixing height for the DFW area.

5.2.3 Estimation of the Horizontal Extent of the Urban Plume

The University of Houston Institute for Multi-dimensional Air Quality Studies (IMAQS) has developed an air quality forecasting (AQF) system for East Texas to provide air quality data and to further facilitate increased understanding of ozone episodes and emissions within the region. The daily AQF system provides two-day forecast photochemical modeling simulations showing both 1-hour and 8-hour daily maximum ozone concentrations throughout the East Texas regional domain at a 12-km resolution, and at a 4-km resolution for the Houston-Galveston domain (available at http://www.imaqs.uh.edu/ftp/AQF_usa/). Simulations of the 1-hour daily maximum ozone concentration for the days with available aircraft data for flux calculation comparison purposes were used to qualitatively characterize the urban plume and estimate its width. Average plume width was estimated by identifying monitors on each side of the plume approximately at its average width, and the latitude and longitude coordinates of these two monitors were then used to calculate the distance between those two locations. Figure 5-5 below illustrates the AQF map for August 12th, 2006. Surface monitor locations are indicated by the small green circular symbols, and the numbers near each surface monitor represent the 1-hour daily maximum observed ozone concentration for that monitor.

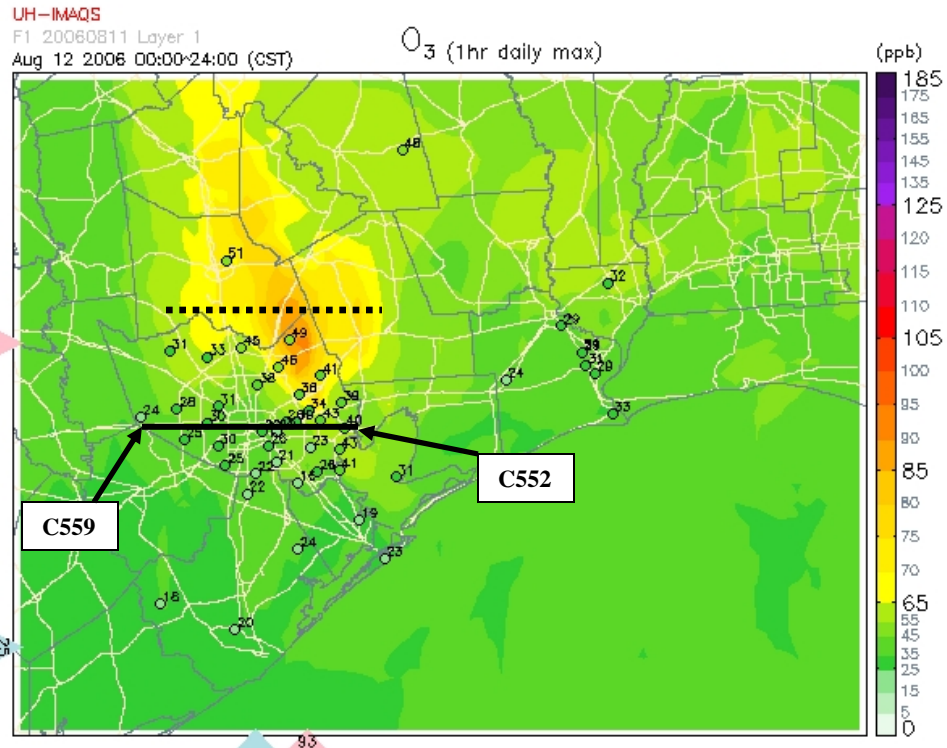


Figure 5-5. Air Quality Forecast 1-hour daily maximum ozone concentrations for the Houston-Galveston 4-km modeling domain on August 12th, 2006. The surface monitors used to approximate the width of the plume (C559 and C552) are indicated.

On this particular day, the urban plume moving north from the Houston region is well-defined by the model. The average width of the plume was calculated from the locations of the Katy Park (C559) and Baytown Wetlands (C552) monitoring stations. The distance between the two points (indicated by the thick black line in Figure 5-5) is approximately 80 km. Table 5-2 summarizes the horizontal urban plume widths for the case study days as estimated using the University of Houston AQF model results versus those calculated from the aircraft LIDAR measurements as reported by Senff et al. (2007). The surface monitors used to estimate these widths are presented in Appendix F. Based on these results, the estimates using the AQF model generally show good agreement with those calculated by the LIDAR measurements for all days with the exception of August 12th, 2006. On this day, it appears the AQF model was not capable of accurately simulating the horizontal distribution of the urban plume.

Table 5-2. Comparison of horizontal extent of the urban plume estimated from the AQF modeling results versus estimates obtained from aircraft LIDAR measurements calculated by Senff et al. (2007).

Urban Region	Date	Wind Direction	LIDAR Data (km)	University of Houston AQF model estimate (km)
Houston	8/12/2006	S	122-133	80
Houston	8/14/2006	S	97-108	106
Houston	8/30/2006	N	83-108	95
Houston	8/28/2000	S	43-72	72
Houston	9/6/2000	NE	61-108	85
Dallas-Ft. Worth	9/13/2006	N	144-162	139

Results from the University of Houston AQF model were not available for days in 2000; therefore, the CAMx photochemical model was similarly used to approximate the plume widths on August 28th and September 6th, 2000. Specifications regarding the datasets and modeling domains used in this CAMx simulation will be described in Section 5.4. Figure 5-6 shows contours of ozone concentrations that were extracted for surface layer grid cells within the CAMx 4-km modeling domain for 13:00 CST on September 6th, 2000, as well as the NOAA DC-3 flight track for this day.

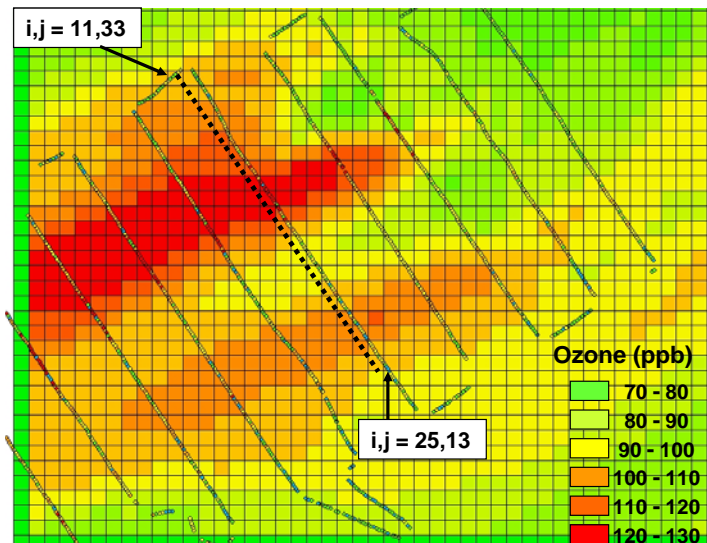


Figure 5-6. CAMx-predicted 1-hour surface layer ozone concentrations for the 4-km domain at 13:00 CST on September 6th, 2000. The CAMx i and j coordinates for two grid cells that were selected to estimate the horizontal extent of the plume are indicated, and the NOAA DC-3 flight track for this day is also shown.

Two grid cells were selected within the 4-km domain that correspond to approximate endpoints of the horizontal extent of the plume, encompassing grid cells characterized by ozone concentrations above 100 ppb. The locations of these endpoints are indicated in Figure 5-6, and the distance between these two grid cells corresponds to an estimated plume width of 85 km, as shown in Table 5-2. A similar approximation of plume width using CAMx predictions was performed for August 28th, 2000 and is presented in Appendix F.

5.2.4 Estimation of Wind Speeds

Wind trajectory results were used to estimate wind direction and speed, and to determine the locations of monitoring stations upwind and downwind of the plume. Trajectories are estimates of the hypothetical path an air parcel takes prior to arriving or after leaving a specific place and time. One tool that has been frequently used for trajectory analyses (discussed in Chapter 2) is the HYbrid Single-Particle Lagrangian Integrated Trajectory (HYSPLIT) application based on archived meteorological wind data (Draxler et al., 2003). The application is capable of calculating trajectories either forward or backward in time, and hourly trajectories are generated using a three-dimensional meteorological data set. Documentation of the calculation methods used by HYSPLIT can be accessed from the HYSPLIT website (www.arl.noaa.gov/read.html). For the case studies analyzed in 2006, HYSPLIT data are available on a 40-km scaled grid. For the case studies analyzed prior to 2004, data are available at an 80-km resolution. Figure 5-7 illustrates HYSPLIT forward trajectory estimates for August 12th, 2006 from an origin near the Houston urban region. The results are generally consistent with the predominant direction of the plume advection as predicted by the AQF model on this day (illustrated in Figure 5-5).

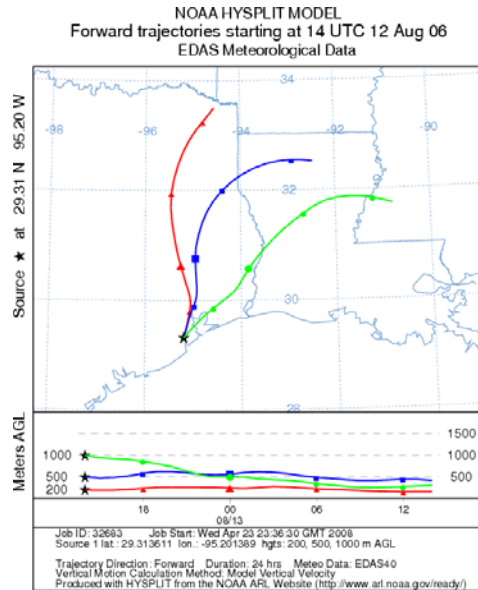


Figure 5-7. HYSPLIT 24-hour forward wind trajectory estimates from the Houston region beginning at 14:00 UTC on August 12th, 2006. Trajectories are estimated at initial heights of 200, 500, and 1000 meters.

For each case study, the wind speed was initially estimated as the mean of upwind and downwind 1-hour average wind speeds recorded by the selected surface monitors; however, these surface measurements were discernibly lower in comparison to wind speeds measured aloft. As mentioned in Section 5.2, the flux calculations using LIDAR data incorporated vertically averaged wind speeds obtained from nearby wind profilers. The HYSPLIT application was used to provide estimates of vertically averaged afternoon wind speeds for comparison purposes.

HYSPLIT also has the capability to generate an endpoints file with each hourly latitude and longitude position of the theoretical air parcel being traced. From the endpoints file, the distance the air parcel traveled within a time period of one hour (averaged over 5 hours) was used to calculate an approximate average afternoon wind speed. HYSPLIT results were used to calculate a 5-hour vertically averaged mean wind speed (the average of results from 5 endpoints) from 14:00-19:00 CST, vertically averaged over altitudes of 200, 500, and 1000 meters above ground level. It should be noted that, although the input specification for the HYSPLIT program is for a specific altitude, there are variations in altitude for each time step due to vertical motion of the

hypothetical air parcel being tracked by the program. In other words, at each endpoint, the altitude of the hypothetical air parcel does not remain constant, as illustrated in Figures 5-7 through 5-10.

For case studies involving flux from the Houston area when winds are coming from the south, such as on August 12th, 2006, the point of origin used was the Mustang Bayou surface monitor (C619), indicated by the black star in Figure 5-7. For days with northerly winds, such as August 30th, 2006, the origin of the trajectories used was the Manvel Croix surface monitor (C84), indicated by the black star in Figure 5-8. For the Dallas case study day, September 13th, 2006, the Pilot Point surface monitor site (C1032) was used, as shown in Figure 5-9. September 6th, 2000, is characterized by winds originating from the northeast of Houston. The surface monitor location used for this case study as the origin of the HYSPLIT wind speed analysis was the Mont Belvieu site (C610), as shown in Figure 5-10.

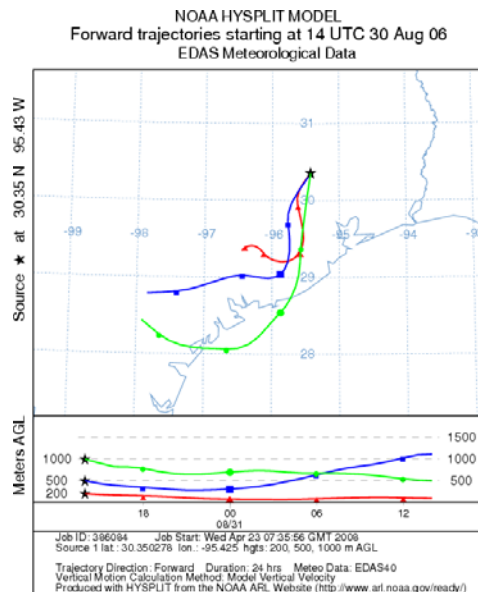


Figure 5-8. HYSPLIT 24-hour forward wind trajectory estimates from the Houston region beginning at 14:00 UTC on August 30th, 2006. Trajectories are estimated at initial heights of 200, 500, and 1000 meters.

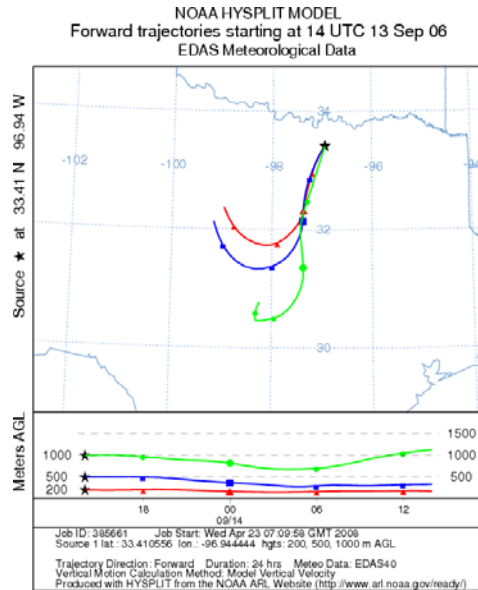


Figure 5-9. HYSPLIT 24-hour forward wind trajectory estimates from the Dallas region beginning at 14:00 UTC on September 13th, 2006. Trajectories are estimated at initial heights of 200, 500, and 1000 meters.

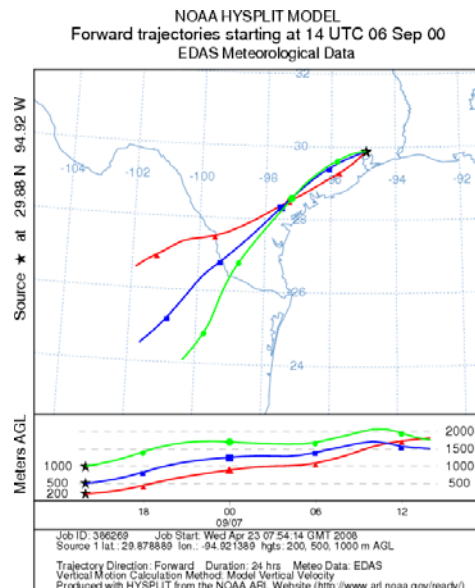


Figure 5-10. HYSPLIT 24-hour forward wind trajectory estimates from the Houston region beginning at 14:00 UTC on September 6th, 2000. Trajectories are estimated at initial heights of 200, 500, and 1000 meters.

Table 5-3 lists wind speeds (in m/s) estimated from the radar wind profilers (used in the LIDAR-based flux calculations by Senff et al., 2007), surface monitors, and

HYSPLIT application. In comparison to the wind profiler data, the surface monitors consistently underestimated wind speeds, while the HYSPLIT application underestimated wind speeds on days when winds originate from the south of Houston and overestimated wind speeds on the other case study days.

Table 5-3. Wind speeds (in m/s) implemented in computations of ozone flux, as approximated by wind profilers, surface monitors, and the HYSPLIT application.

Urban Region	Date	Wind Direction	Wind Profiler Estimates Used for LIDAR Results (m/s)	Surface Monitors (m/s)	HYSPLIT (m/s)
Houston	8/12/2006	S	7.3	4.3	4.7
Houston	8/14/2006	S	4.5	3.5	4.1
Houston	8/30/2006	N	3.8	2.1	5.4
Houston	8/28/2000	S	4.2	3.7	3.1
Houston	9/6/2000	NE	5.2	2.9	7.3
Dallas-Ft. Worth	9/13/2006	N	4.6	2.6	5.2

All three estimation methods experience variations as the wind speeds vary hourly and at each location selected for analysis. Additionally, while the HYSPLIT model has the benefit of providing wind speed estimates at various elevations, the grid resolution (especially for the case studies in 2000) used in the model is an inherent disadvantage. Surface monitor measurements and HYSPLIT estimates of wind speeds were both implemented in computations of ozone flux.

5.2.5 Estimation of Background and Downwind Ozone

In order to calculate the ozone generated by an urban area or within a plume according to Equation 5.2, the difference between the upwind and downwind ozone concentrations must be estimated. Once the predominant afternoon wind direction and approximate plume dimensions were established using the HYSPLIT and AQF results, the appropriate surface monitors located upwind and downwind of the urban region of interest were identified. For the hour most closely corresponding to the flight transect associated with the maximum LIDAR-derived ozone flux, the upwind and downwind 1-

hour average ozone concentrations were extracted from the TCEQ online database, and the difference between the two was calculated. This calculation conceptually implies that the excess ozone locally produced by a region is equal to the downwind ozone concentration minus the background ozone concentration. This excess ozone concentration was then multiplied by the average wind speed and the approximate cross-sectional area of transport (plume width by vertical mixing height) in order to obtain the ozone flux result in units of molecules per second.

5.3 OZONE FLUX CALCULATION RESULTS

As previously mentioned, the inherent scarcity of aircraft data suggests a need for calculating pollutant fluxes using alternative techniques that have more frequently available data. Section 5.3.1 presents a sample ozone flux calculation using ground-based monitoring data for August 12th, 2006. A summary of the ozone flux results for each of the six case study days is presented in Section 5.3.2. Section 5.3.3 provides ozone flux calculations using the estimates from photochemical modeling for August 28th and September 6th, 2000.

5.3.1 Example of Ozone Flux Calculation with Data from Surface Monitors

A detailed example of the ozone flux calculation method using data collected by surface monitors will now be described for the case study of August 12th, 2006, for the Houston region. The NOAA Twin Otter flight track and ozone concentrations (vertically averaged over a depth of 200-1000 mMSL) captured by the aircraft LIDAR on this day are presented in Figure 5-11, as well as the locations of the surface monitors selected for ozone flux computations.

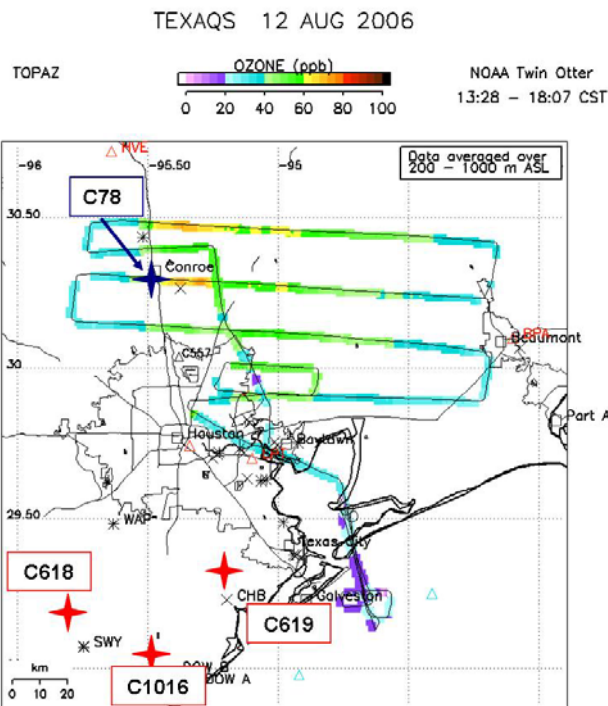


Figure 5-11. Ozone concentrations from the NOAA Twin Otter flight on August 12th, 2006 (Senff et al., 2007). The locations of the upwind and downwind surface monitors used to calculate ozone flux are also shown in red and blue, respectively.

As Figure 5-11 illustrates, predominant winds transported an urban plume to the north/northeast of the Houston region on this day. Figure 5-7 illustrates the HYSPLIT forward trajectory predictions from an origin near the Houston urban region, the Mustang Bayou C619 surface monitor. An average wind speed of 4.7 m/s was calculated using the HYSPLIT forward trajectory endpoints file.

Figure 5-12 shows the locations of the operational surface monitors available on this day. Based on the predominant wind direction predicted by the HYSPLIT trajectories, upwind and downwind surface monitors were selected in the outlying regions of the southwest and northeast areas of the urban Houston region, respectively. The upwind monitors used to estimate background ozone concentrations were the Danciger monitor (C618), the Mustang Bayou monitor (C619), and the Lake Jackson monitor (C1016). The NOAA aircraft tracked the plume during the late afternoon from 15:39-17:34 CST, and the maximum ozone flux was calculated with LIDAR measurements

average ozone concentration at this site was 51 ppb at 17:00 CST. The ozone difference (excess ozone generated by sources in the Houston area), as calculated by subtracting the average background ozone from this value at 17:00 CST, is 34 ppb. This mixing ratio was then converted to a concentration in terms of molecules per cubic meter using the assumption of standard temperature and atmospheric pressure conditions ($8.3E17$ molecules/ m^3). For 17:00 CST, the mean of 1-hour average wind speeds measured by the selected upwind and downwind surface monitors was calculated as approximately 4.3 m/s.

The horizontal extent of the plume was estimated by the methods described in Section 4.2, using the AQF system developed by the University of Houston Studies IMAQS. Figure 5-5 illustrated the AQF map for August 12th, 2006. As previously described, the average width of the plume was approximated by the two surface monitors indicated in Figure 5-5 as the Katy Park site (C559), located at 29.8° latitude and -95.8° longitude, and the Baytown Wetlands site (C552), located at 29.7° latitude and -95.0° longitude. The distance between the two points is indicated by the thick black line in Figure 5-5, and was calculated to be approximately 80 km.

The PBL or vertical mixing height for this case study was estimated according to the methods discussed in Section 5.2.1. As previously mentioned, PBL height measurements using radar wind profilers are now a common part of many field campaigns addressing air quality, and Figure 5-3 shows the results from an analysis that was performed in support of TexAQS II. For case studies such as August 12th, 2006, characterized by winds originating from the south and transporting urban plumes north from the Houston region, the vertical mixing height was estimated to be 1500 meters. This average mixing height was selected based on the maximum average mixing heights experienced at the wind profilers located inland from the coast, such as Huntsville (HVE) and Brenham (BHM).

The horizontal ozone flux was then calculated according to Equation 5.2 as the product of the vertical mixing height (1500 m) multiplied by the horizontal extent of the plume (80,000 m), the average wind speed (4.3 m/s), and the ozone concentration differential ($8.7E17$ molecules/ m^3) to obtain a result of $4.3E26$ molecules of ozone per

second. Implementing the HYSPLIT wind speed estimate (4.7 m/s) results in an ozone flux of $4.7E26$ molecules per second. Table 5-4 summarizes the estimated parameters that were used in the ozone flux computations with Equation 5.2 for all days in this assessment, along with estimates of similar parameters based on LIDAR and wind profiler measurements (provided by Senff et al., 2007).

Table 5-4. Surface monitor estimates of ozone concentrations, wind speed, and plume dimensions implemented in ozone flux computations with Equation 5.2. Estimates of similar parameters based on LIDAR and wind profiler measurements (provided by Senff et al., 2007) that were implemented in ozone flux computations with LIDAR data (using Equation 5.1) are also shown.

Date/ Urban Region		Background O3 (ppb)	Downwind/Plume O3 (ppb)	O3 Enhancement (ppb)	Wind Speed (m/s)	Plume Width (km)	Mixing Height (km)
8/12/2006 Houston	Surface Monitor Estimates	17	51	34	4.3	80	1500*
	LIDAR Estimates	29	68	39	7.3*	122-133	1303-1499
8/14/2006 Houston	Surface Monitor Estimates	16	61	45	3.5	106	1500*
	LIDAR Estimates	34	89	55	4.5*	97-108	1517-1552
8/30/2006 Houston	Surface Monitor Estimates	61	85	24	2.2	95	1000*
	LIDAR Estimates	59	111	52	3.8*	83-108	1173-1418
9/13/2006 DFW	Surface Monitor Estimates	59	68	9	2.7	139	2000*
	LIDAR Estimates	57	75	18	4.6*	144-162	1001-1246
8/28/2000 Houston	Surface Monitor Estimates	23	87	64	3.7	72	1500*
	LIDAR Estimates	53	105	52	4.2*	43-72	1601-2582
9/06/2000 Houston	Surface Monitor Estimates	71	115	44	2.2	85	1500*
	LIDAR Estimates	69	115	46	3.8*	61-108	771-2005

*Estimate obtained from wind profiler data

The one-hour average measurements from surface monitors that was used to approximate the background and downwind ozone concentrations listed in Table 5-4, as

well as the average wind speeds shown in the table, are presented in Appendix F. Discrepancies in estimates of wind speed and plume dimensions with measurements from surface monitors, wind profilers, and LIDAR were previously addressed in this Chapter.

With the exception of August 30th, 2006, the ozone enhancement terms based on data from surface monitors and LIDAR are comparable, with a maximum difference of 12 ppb on August 28th, 2000. For days characterized by southerly winds (August 12th and 14th, 2006 and August 28th, 2000), the surface monitors underestimated background and downwind ozone levels in comparison to the LIDAR-derived estimates; however, the ozone enhancement terms associated with both types of measurements are in reasonable agreement. On August 30th, 2006, predominant winds transported an urban plume to the south of the Houston region. The NOAA Twin Otter flight track and ozone concentrations (vertically averaged over a depth of 200-1000 mMSL) collected by the aircraft LIDAR on this day are presented in Figure 5-13, along with the locations of the surface monitors used in ozone flux computations.

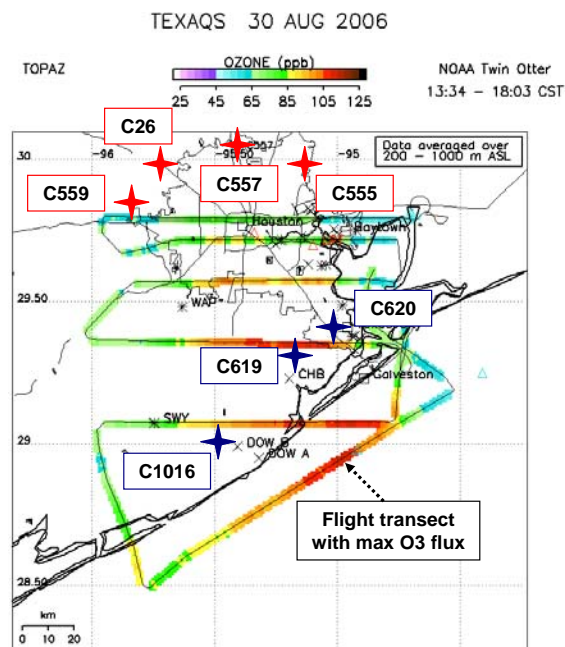


Figure 5-13. Ozone concentrations from the NOAA Twin Otter flight on August 30th, 2006 (Senff et al., 2007). The locations of the upwind and downwind surface monitors used to calculate ozone flux are also shown in red and blue, respectively.

LIDAR data collected over the Gulf of Mexico along the final transect, corresponding to a flight time of 17:10-17:43 CST, result in the maximum ozone flux calculated for this day. As shown in Table 5-4, measurements of ozone concentrations from the upwind surface monitors are consistent with the background ozone approximated with LIDAR data; however, the selected downwind monitors do not capture the elevated ozone observed by the LIDAR. While the LIDAR measured plume ozone concentrations in excess of 100 ppb above land prior to 17:00 CST, the 1-hour average data from the surface monitors in Table 5-4 correspond to the hour of 17:00-18:00 CST. The LIDAR observations in Figure 5-13 suggest that elevated ozone within the plume has been transported over open water at this time, and the resulting decrease in depositional losses at the surface may explain the relatively higher LIDAR measurements of downwind ozone levels aloft.

5.3.2 Results of Ozone Flux Calculations Using Data from Surface Monitors and LIDAR

The results of ozone flux calculations based on data from surface monitors are summarized in Table 5-5 for six case studies: five for the Houston urban region and one for the DFW urban region. Four of the case studies include datasets from the TexAQS II field study in 2006, and the remaining two case studies include data collected during the first TexAQS field study in 2000. For comparison, ozone flux results based on airborne LIDAR measurements, calculated by Senff et al. (2007), are also presented in Table 5-5. The LIDAR-derived values for each flight were calculated for data collected along multiple flight transects; therefore, a range of ozone flux results are presented for each day. Ozone flux results based on 1-hour average measurements from surface monitors were calculated for the hour of the flight transect corresponding to the upper bound of these ranges, shown in boldface type in Table 5-5.

Table 5-5. Ozone flux (in molecules of ozone per second) computed with ambient measurements from airborne LIDAR (according to Equation 5.1) and surface monitors (according to Equation 5.2).

Urban Region	Date	Wind Direction	O3 Flux: LIDAR Results (molec O3/s)	O3 Flux: Surface Monitor Results (molec O3/s)
Houston	8/12/2006	S	3.9E26 - 5.0E26	4.3E26
Houston	8/14/2006	S	4.1E26 - 5.0E26	6.1E26
Houston	8/30/2006	N	1.4E26 - 3.2E26	3.0E26
Houston	8/28/2000	S	0.9E26 - 6.0E26	6.2E26
Houston	9/6/2000	NE	0.7E26 - 3.6E26	4.0E26
Dallas-Ft. Worth	9/13/2006	N	1.4E26 - 1.7E26	1.6E26

The results in Table 5-5 show that the ozone flux values calculated with surface monitor and aircraft LIDAR data are in good agreement, despite differences in the spatial and temporal resolutions associated with both types of measurements. Variations in these measurements are addressed in Appendix E, which assesses the degree to which data collected at the surface may be considered representative of ozone levels in the well-developed mixed layer. The results in Table 5-5 also suggest the surprising finding that the excess ozone emitted by the Houston area does not vary much during the days with available LIDAR data. In another interesting finding, results for 2006 are comparable with those from 2000, despite substantial emission reductions in the Houston urban area between 2000 and 2006. Additionally, while the DFW area emitted less excess ozone in comparison to Houston for the days in this study, the ozone flux remains on the same order of magnitude as Houston flux values.

These results indicate that extensive datasets available from surface monitors, coupled with routinely available estimates of wind speeds and mixing heights, can be used to generate pollutant flux estimates. As a next step, these flux measurements will be compared to predictions by the photochemical models.

5.4 PHOTOCHEMICAL MODELING DATASETS

In order to attribute ozone formation in urban plumes to specific sources, photochemical modeling will be required, and this is the focus of Chapter 6. However,

before employing photochemical models for source attribution, it is useful to compare overall fluxes in urban plumes predicted by the photochemical model to aircraft data and surface data.

The model configuration used for flux calculations incorporating CAMx data is based on the August 22nd–September 6th, 2000 photochemical modeling episode for the TCEQ ozone SIP mid-course review developed in support of the 1-hour ozone standard (McGaughey et al., 2005). Aircraft LIDAR data are available for several days during this time period. The hybrid base case for 2000 combined two meteorological characterizations: MM5-GOES for the period of August 22nd–September 1st and MM5-ATMET for September 2nd–6th (McGaughey et al., 2005). Output files from the August 22nd–September 6th, 2000 CAMx photochemical modeling episode have been used by the State of Texas for air quality planning in the HGB area and were downloaded from the TCEQ website, available at

ftp://ftp.tceq.state.tx.us/pub/OEPAA/TAD/Modeling/HGMCR/CAMx/output/camx403_base5b.psito2n2/atmetnoapbl/. CAMx predictions of hourly ozone concentrations and wind speeds were extracted for the 4-km grid domain for August 28th, 2000, and September 6th, 2000, for the surface layer and for the vertical layers that correspond to the altitude of the aircraft measurements for these two case study days.

Figure 5-14 illustrates the CAMx modeling domains and vertical grid structure for the simulation used in this work, obtained from the TCEQ website at http://www.tceq.state.tx.us/implementation/air/airmod/data/hgbmcr/hgb1_camx_domain.html#layer. The horizontal modeling domain structure consists of a regional 36-km resolution coarse grid domain and three nested fine grid sub-domains: East Texas 12-km resolution sub-domain, Houston-Galveston-Brazoria—Beaumont-Port Arthur (HGBPA) 4-km resolution sub-domain, and the optional Houston-Galveston Bay (HGB) and Beaumont-Port Arthur (BPA) 1-km resolution sub-domains. It should be noted that the optional 1-km sub-domains are not shown in Figure 5-14. The vertical layer structure in CAMx for the 4-km HGBPA domain, also illustrated in Figure 5-14, consists of 24 layers and extends to 5385.9 meters above ground level.

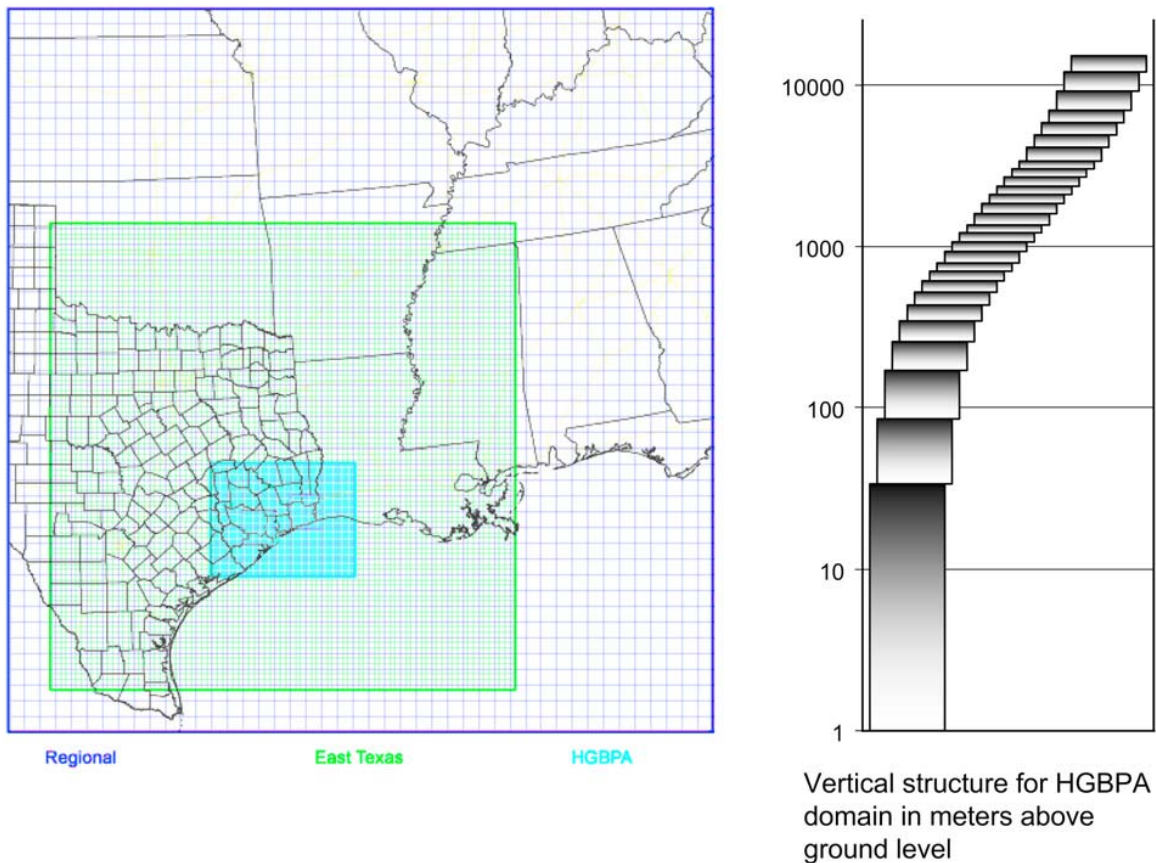


Figure 5-14. CAMx photochemical modeling horizontal domains and vertical layer structure for the August 22nd–September 6th, 2000 episode.

5.4.1 Ozone Flux Calculations with Photochemical Modeling Data

Similar flux calculations were performed using data obtained from photochemical modeling analyses for August 28th and September 6th, 2000. Hourly ozone concentrations and wind speeds were extracted for the 4-km grid cells in CAMx that correspond to the latitude and longitude coordinates of upwind and downwind surface monitors in order to directly compare flux calculation results with data collected by the monitors.

CAMx has the option of specifying the output of ozone concentrations and wind speeds either at the surface level or at additional vertical levels in order to calculate vertically averaged parameters. For the grid cells corresponding to the locations of the selected surface monitors used in the previous ozone flux analysis for these two days

(results were shown in Table 5-5), both the surface layer and vertically averaged hourly ozone concentrations and wind speeds were extracted from CAMx and used to compute ozone flux according to Equation 5.2. These ozone concentrations and wind speeds are listed in Appendix F.

The flight track and ozone concentrations captured by the NOAA DC-3 aircraft on these two days are presented in Figure 5-15. The predominant wind direction and average wind speed from nearby wind profilers used in the LIDAR-based ozone flux calculations are also superimposed onto the figures, and the flight transect associated with the maximum ozone flux is indicated.

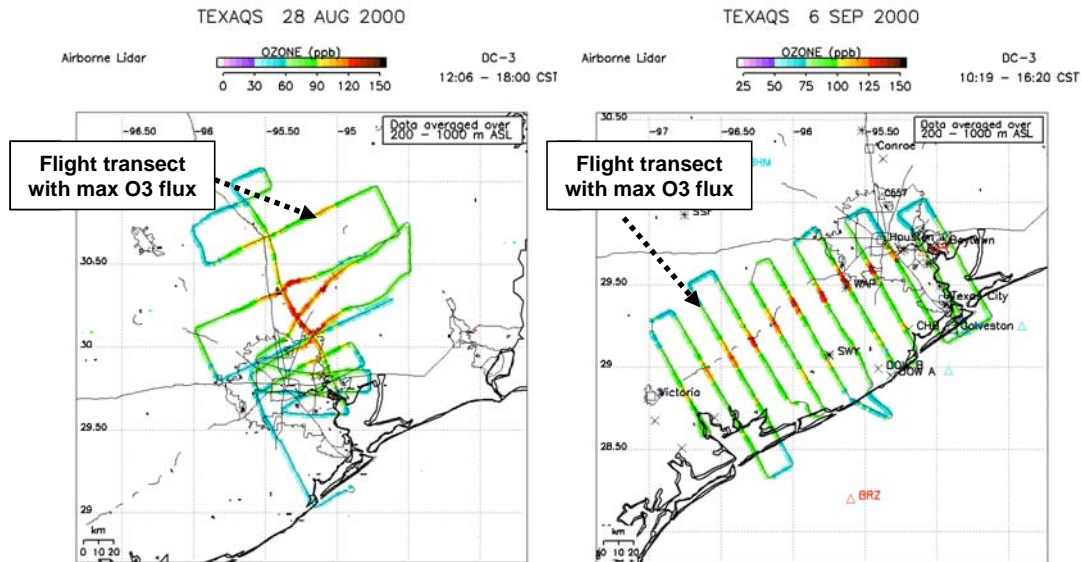


Figure 5-15. Ozone concentrations from the NOAA DC-3 flights on August 28th and September 6th, 2000 (Senff et al., 2007).

The HYSPLIT forward wind trajectories were generated for both days in order to identify the appropriate upwind and downwind surface monitors to use in the flux calculations. The locations of the monitors used in these two case studies are shown in Figure 5-16, which illustrates the locations of all surface monitors in the HGB area that were operational in 2000.

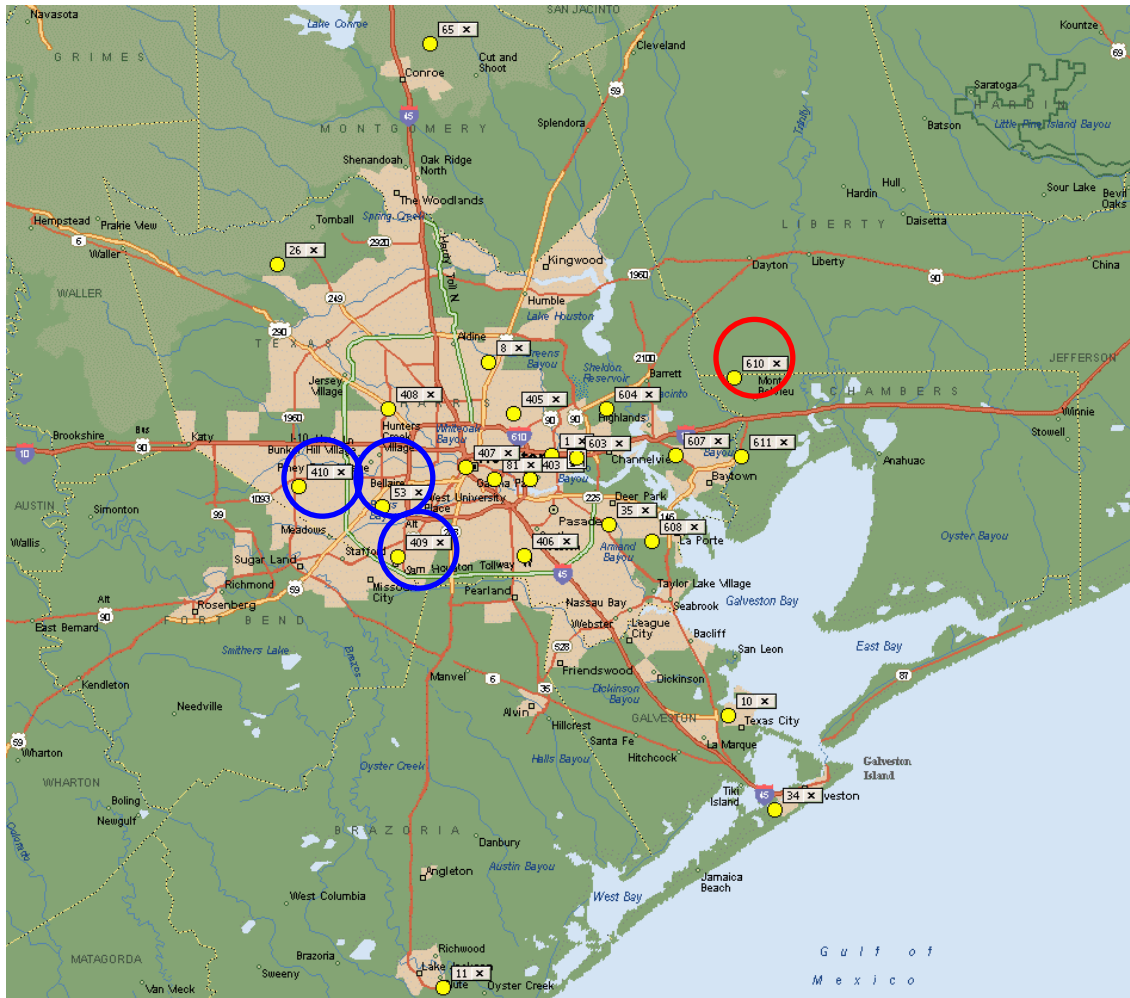


Figure 5-16. Surface monitoring stations in the HGB area that were operational during 2000 (CAPCO et al., 2004). The locations of the upwind and downwind surface monitors used to calculate ozone flux on September 6th, 2000, are circled in red and blue, respectively.

On September 6th, 2000, afternoon winds were northeasterly across Houston. Figure 5-10 showed the HYSPLIT forward trajectory for this day, initiated at the location of the upwind C610 Mont Belvieu surface monitor. The downwind monitors on the southwest side of Houston were chosen as the Houston Westhollow monitor (C410), the Houston Croquet monitor (C409), and the Houston Bayland Park monitor (C53). Figure 5-17 shows the HYSPLIT forward trajectory for August 28th, 2000, originating from the Clute surface monitor (C11). Additional monitors on the south side of Houston include the Galveston Airport monitor (C34) and the Texas City monitor (C10). The downwind

monitor selected on the northwest side of Houston for August 28th, 2000 was chosen as the Northwest Harris Country monitor (C26). It should be noted that C26 was the only surface monitor sufficiently downwind of the Houston urban region on this day.

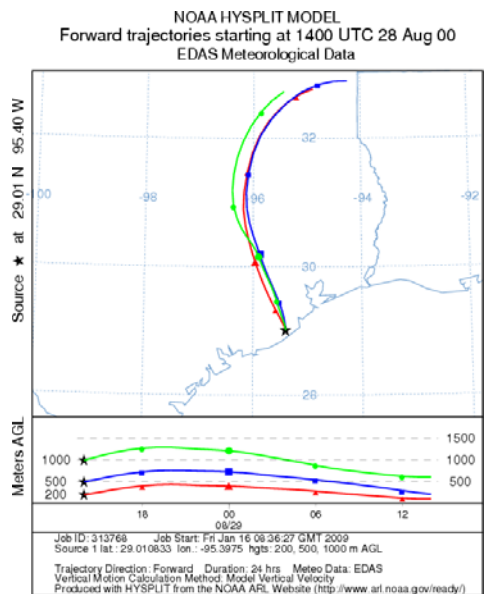


Figure 5-17. HYSPLIT 24-hour forward wind trajectory estimates from the Houston region beginning at 14:00 UTC on August 28th, 2000. Trajectories are estimated at initial heights of 200, 500, and 1000 meters.

Results of the ozone flux calculations for August 28th and September 6th, 2000 are summarized in Table 5-6. Results associated with LIDAR data are shown in Table 5-6 for the maximum flux on each respective flight day (shown in boldface type in Table 5-5), computed with measurements collected along the DC-3 flight transects indicated in Figure 5-15. CAMx results are presented for data from surface layer grid cells, as well as for data that were vertically averaged over the CAMx layers that correspond to the altitudes of airborne LIDAR observations. LIDAR measurements were recorded from the surface to an altitude of approximately 2600 mMSL (meters above mean sea level). The vertical structure of the CAMx 4-km HGBPA grid domain for this modeling episode reveals that the center of layer 20 is at an altitude of 2858.3 magl (meters above ground level); therefore, CAMx predictions were averaged over layers 1-20. It should be noted that the discrepancy between the sea level and ground level altitudes for the LIDAR and

CAMx data, respectively, is negligible. The elevations of surface monitors to the southwest of Houston are near sea level, with elevations ranging from 0-24 mMSL.

Table 5-6. Ozone flux (in molecules of ozone per second) computed with modeled CAMx predictions and ambient measurements from airborne LIDAR and surface monitors. Calculations with data from surface monitors and CAMx were performed according to Equation 5.2, and LIDAR-derived results were computed based on Equation 5.1.

Urban Region	Date	O3 Flux: LIDAR Results (molec O3/s)	O3 Flux: Surface Monitor Results (molec O3/s)	O3 Flux: CAMx Surface Layer Results (molec O3/s)	O3 Flux: CAMx Vertically Averaged Results (molec O3/s)
Houston	8/28/2000	0.9E26 - 6.0E26	6.2E26	7.7E26	6.0E26
Houston	9/6/2000	0.7E26 - 3.6E26	3.8E26	3.4E26	3.5E26

As shown in Table 5-6, values of ozone flux calculated with CAMx predictions for surface layer grid cells are comparable to results obtained from the vertically averaged CAMx data. The ozone flux based on CAMx surface layer data for August 28th, 2000 is higher than values calculated by the other methods on this day, due to a larger predicted difference in upwind and downwind concentrations. Nonetheless, the results show that values of ozone flux computed with photochemical modeling data are in good agreement with those based on observational measurements from surface monitors and airborne LIDAR.

For September 6th, 2000, CAMx model predictions were also matched in time and space with the LIDAR data and ozone flux was calculated according to Equation 5.1 for a direct comparison with LIDAR-based ozone flux computations. Specifically, the Alpine Geophysics Flying Data Grabber (FDG) software package was used to match LIDAR observations and CAMx predictions in time and space for altitudes ranging from approximately 200-1000 mMSL, corresponding to layers 1-13 in CAMx (McGaughey et al., 2005). For each observation time, the average of the instantaneous LIDAR ozone measurements collected in an individual CAMx grid cell was calculated, and a two-point linear interpolation in time was used to calculate the corresponding one-hour average CAMx predictions of ozone and wind speed (McGaughey et al., 2005).

Figure 5-18 provides a contour plot of the vertically averaged (200-1000 mMSL) ozone concentrations observed by the NOAA DC-3 LIDAR on September 6th, 2000 for the portion of the flight that occurred within the CAMx 4-km HGBPA grid domain (refer to Figure 5-14). Note that data collected during the final three transects of the DC-3 flight (visible in Figure 5-15) are not included in Figure 5-18 since these observations were collected beyond the CAMx 4-km grid domain. Figure 5-19 shows a time series of vertically averaged ozone concentrations measured by the LIDAR, as well as the comparable CAMx predictions, for the transect corresponding to a flight time of 12:14-12:39 CST (indicated in Figure 5-18).

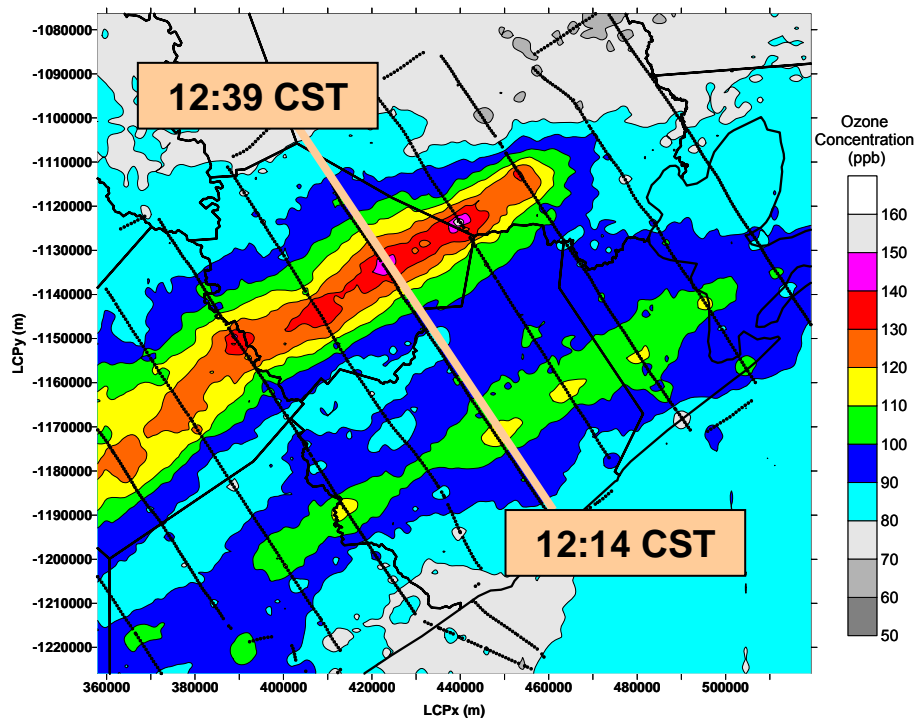


Figure 5-18. Ozone concentrations (vertically averaged over 200-1000 mMSL) from the NOAA DC-3 LIDAR on September 6th, 2000. The figure illustrates average concentrations from 10-second sampling within the 4-km HGBPA CAMx grid domain. The DC-3 flight track is provided for reference (McGaughey et al., 2005).

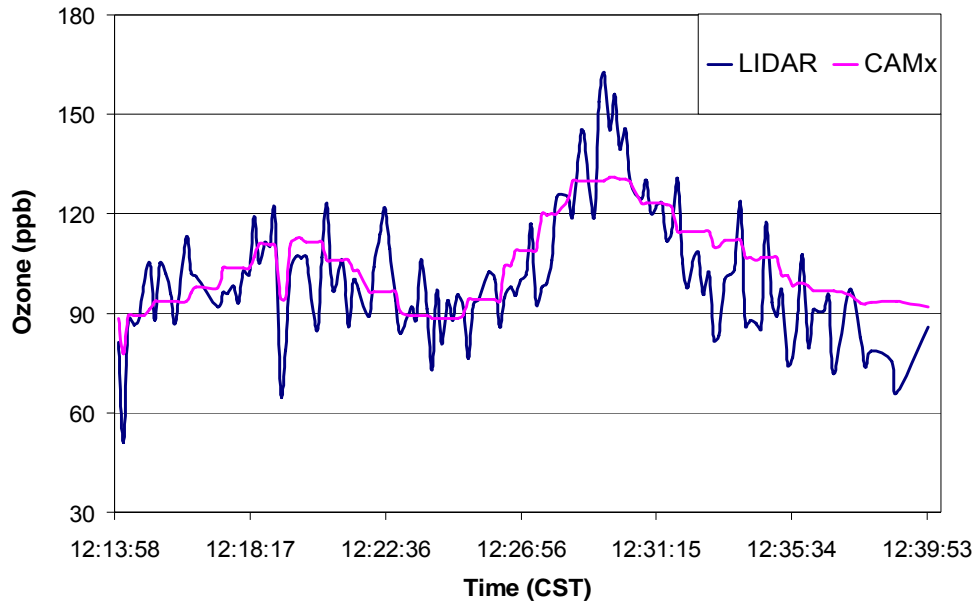


Figure 5-19. Ozone concentrations (vertically averaged over 200-1000 mMSL) observed by the NOAA DC-3 LIDAR and predicted by CAMx on September 6th, 2000. Results are shown for the DC-3 flight transect corresponding to a flight time of approximately 12:14-12:39 CST.

From the results in Figure 5-19, the background ozone concentration derived from CAMx predictions was estimated as 85 ppb, comparable to 72 ppb estimated with LIDAR data by Senff et al. (2007). While the excess ozone computed by Equation 5.1 is represented as an integral, the integral may be approximated as a summation of the discrete measurements taken over finite 10-second intervals (as opposed to a continuous function over infinitely small intervals). For each 10-second interval, the 85 ppb background ozone was subtracted from the vertically averaged CAMx ozone prediction, and this excess ozone term was multiplied by the 10-second interval time (dt), according to Equation 5.1. These terms were summed over the horizontal extent of the plume along this transect, which is essentially a summation across the flight time from 12:14-12:39 CST, and this summation value was then divided by the total time of 1500 seconds to yield the integrated excess ozone term in Equation 5.1.

Along with ozone concentrations, modeled wind speeds were extracted and vertically averaged (from 200-1000 mMSL) for the CAMx grid cells that were matched in time and space with LIDAR measurements. A mean of these vertically averaged

modeled wind speeds was computed for the flight transect. As described in Section 5.2.3 and shown in Figure 5-6, the plume width was computed as the distance between two CAMx grid cells that correspond to approximate endpoints of the horizontal plume extent, which is approximately 85 km. Figure 5-20 illustrates a vertical contour plot of ozone concentrations predicted by CAMx along the majority of the flight transect indicated in Figure 5-18 (from 12:14:25-12:36:55 CST) (McGaughey et al., 2005). A PBL height of 1200 meters was estimated from these CAMx predictions, indicated by the dashed line in Figure 5-20.

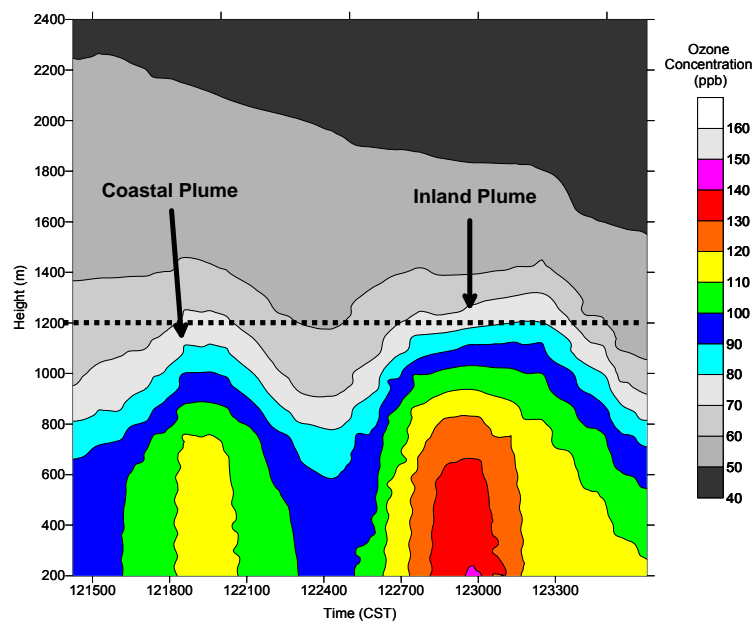


Figure 5-20. Vertical contour plot of modeled one-hour average ozone concentrations on the 4-km HGBPA CAMx grid domain, corresponding to the NOAA DC-3 flight transect indicated in Figure 5-18 (McGaughey et al., 2005).

For the flight transect indicated in Figure F-18, ozone flux was computed according to Equation 5.1 by multiplying the integrated excess ozone with the average wind speed, plume width, and PBL height to yield a result of $2.9E26$ molecules of ozone per second. Table 5-7 summarizes the parameters, based on CAMx predictions and LIDAR measurements, that were implemented to compute ozone flux with Equation 5.1 for this transect. Results of ozone flux in molecules per second are also shown. It should be noted that the LIDAR-derived ozone flux is not the same result shown in Table 5-6;

the result in Table 5-6 corresponds to the flight transect associated with the maximum computed ozone flux (refer to Figure 5-15), for LIDAR measurements collected from 14:13-14:23 CST.

Table 5-7. Ozone flux (in molecules of ozone per second) computed with CAMx predictions and airborne LIDAR measurements according to Equation 5.1. Results are shown for September 6th, 2000, for the NOAA DC-3 flight transect indicated in Figure 5-18.

	Integrated Excess Ozone (ppb)	Wind Speed (m/s)	Plume Width (km)	PBL Height (m)	Ozone Flux (molecules/s)
LIDAR	26	5.2	90	1150	3.4E+26
CAMx	18	6.5	85	1200	2.9E+26

The excess ozone was calculated with LIDAR observations relative to a background ozone level of 72 ppb, as estimated by Senff et al. (2007). The plume width, mixing height, and average wind speed shown in Table 5-7 for the LIDAR data were reported by Senff et al. (2007), and the average wind speed was derived based on measurements from nearby wind profilers. The results in Table 5-7 suggest that the photochemical model is clearly capable of providing accurate estimates of ozone flux in comparison to computations based on LIDAR observations.

5.5 CONCLUSIONS

In this Chapter, data from surface monitoring stations were coupled with aircraft LIDAR measurements to obtain quantitative estimates of ozone fluxes upwind and downwind of the DFW and Houston urban areas. These calculated fluxes were then compared to photochemical model predictions to evaluate the performance of the model. Results showed very good agreement between aircraft and surface monitoring data, and consequently, this validates the use of surface monitoring in future work to provide quantitative estimates of urban plume magnitudes. Agreement is reasonable between photochemical modeling predictions in comparison with results from observational data, with some underestimation of ozone flux in the model. This suggests that the modeled

impact of inter-city ozone transport described in Chapter 3 may represent lower bound estimates of the significance of regional transport.

5.6 REFERENCES

- Draxler, R.R. and G.D. Rolph (2003), HYSPLIT (HYbrid Single-Particle Lagrangian Integrated Trajectory), NOAA Air Resources Laboratory, Silver Spring, MD, Model access via the NOAA ARL READY website, available at <http://www.arl.noaa.gov/ready/hysplit4.html>, accessed March 2010.
- ENVIRON International Corporation (2004), User's Guide – Comprehensive Air Quality Model with extensions (CAMx), Version 4.00, Novato, CA, available at <http://www.camx.com>.
- Kemball-Cook, S., D. Parrish, T. Ryerson, U. Nopmongcol, J. Johnson, E. Tai, and G. Yarwood (2009), “Contributions of regional transport and local sources to ozone exceedances in Houston and Dallas: Comparison of results from a photochemical grid model to aircraft and surface measurements”, *Journal of Geophysical Research*, 114, D00F02, doi: 10.1029/2008JD010248.
- McGaughey G., C. Durrenberger, E.C. McDonald-Buller, and D.T. Allen (2005), “Assessing the Performance of the CAMx Photochemical Model: A Qualitative Comparison of Observed and Simulated Ozone Plumes on September 6, 2000 within the 4-km HGA Grid Domain”, Report prepared for the City of Victoria, The University of Texas at Austin Center for Energy and Environmental Resources, Austin, TX, April 2005.
- Nielsen-Gammon, J.W., C.L. Powell, M.J. Mahoney, W.M. Angevine, C. Senff, A. White, C. Berkowitz, C. Doran, and K. Knuff (2008), “Multisensor estimation of mixing heights over a coastal city”, *Journal of Applied Meteorology and Climatology*, 47, pp. 27-43, January 2008.
- Senff, C., et al. (2007), “Ozone Production and Flux Downwind of Houston and Dallas”, Presentation given at the TexAQS II Principal Findings Data Analysis Workshop, Austin, TX, May 2007, available at http://www.tceq.state.tx.us/assets/public/implementation/air/texaqs/workshop/20070529/2007.05.30/Afternoon-1/1-O3_Production+Flux_Downwind-Senff.pdf.
- Texas Commission on Environmental Quality website reference for hourly data retrievals, available at http://www.tceq.state.tx.us/cgi-bin/compliance/monops/daily_average.pl, accessed March 2010.
- Texas Commission on Environmental Quality website reference for Figures 5-14 and 5-15, available at http://www.tceq.state.tx.us/implementation/air/airmod/data/hgb1_camx_domain.html#layer, accessed February 2008.

The Capital Area Planning Council (CAPCO), the University of Texas at Austin, and ENVIRON International Corporation (2004), “Development of the September 13-20, 1999 Base Case Photochemical Model for Austin’s Early Action Compact”, Submitted to the United States Environmental Protection Agency and the Texas Commission on Environmental Quality, September 2004.

The University of Houston Institute for Multi-dimensional Air Quality Studies (IMAQS) Air Quality Forecast Model database, available at http://www.imaqs.uh.edu/ftp/AQF_usa/, accessed February 2007.

Wilczak J., I. Djalalova, S. McKeen, and L. Bianco (2007), “Evaluation of NMM-CMAQ and WRF-Chem during High Ozone Episodes in TexAQS-II”, Presentation given at the TexAQS II Principal Findings Data Analysis Workshop, Austin, TX, May 2007, available at <http://www.tceq.state.tx.us/assets/public/implementation/air/texaqs/workshop/20070529/2007.05.31/Afternoon/2-NMM-CMAQ+WRF-Chem-Wilczak.pdf>.

Chapter 6: Reconciling Modeling Approaches for Apportioning Regional Sources with Ambient Data

6.1 INTRODUCTION

As discussed in other chapters, plumes from urban areas in Texas such as the Houston/Galveston/Brazoria (HGB) ozone non-attainment region can make substantial contributions to the ozone and ozone precursor concentrations in other urban and rural regions of the State. For example, the conceptual model of ozone formation in Victoria, located approximately 150 kilometers to the southwest of Houston, concluded that emissions from HGB sources likely had a greater impact on peak 8-hour ozone levels than local emissions during some episodes (University of Texas at Austin, 2004). Long-range back trajectories from Victoria prior to high ozone episodes often indicate transport of ozone and ozone precursors via urban and industrial plumes originating from the HGB non-attainment area (University of Texas at Austin, 2004). As discussed in Chapter 3, emissions from HGB can significantly impact other cities in Texas, as far away as Dallas. More specifically, the results of the work presented in Chapter 3 provided strong evidence for the necessity to further assess the advection of urban plumes originating in HGB, including the characterization of ozone formation and accumulation within these plumes.

In Chapter 5, comparisons of aircraft, surface monitor and model predictions of ozone transport were compared, and the results indicated that, in general, the three approaches yielded consistent quantitative predictions of ozone transport. This suggests that more detailed analyses of the chemical and physical processes occurring in these plumes using photochemical models is appropriate. In this Chapter, transport of ozone from the HGB area will be characterized using both ambient measurements and photochemical modeling source apportionment and process analysis tools. The HGB area was selected for this analysis because of the magnitude and variety of its emissions sources, because of its position along the Gulf Coast, and because of the heterogeneity of downwind land coverage.

6.2 OZONE FORMATION AND PLUME CHARACTERIZATION IN HOUSTON

While the focus of this Chapter, Houston is not the only city to generate significant urban plumes. Modeling analyses (McDonald et al., 2000; Webb et al., 2002) have indicated that urban plumes from every city in the eastern half of Texas affect ozone concentrations in at least one other city. However, the HGB area presents an interesting case study as it is unusual in comparison to other urban areas within Texas and the U.S. in various aspects. While the basic factors that contribute to ozone formation are present in HGB, it is unique by virtue of its large population, extensive petrochemical industry, major port facilities, subtropical coastal meteorology, and topography (TCEQ, 2009).

The rate of ozone production and accumulation in and around the industrial areas in Houston can be very high; ozone formation rates ranging between 50 ppb/hr and 150 ppb/hr were measured on multiple days during the month-long TexAQS I (2000) study (Allen et al., 2007). These rates of ozone production are much higher than those observed in other urban areas, which are almost always less than 40 ppb/hr (Allen et al., 2007). In addition, the efficiency of ozone production in and downwind of the industrial source dominated areas in Houston can be very high, ranging from 10-20 molecules of ozone per molecule of reacted NO_x (Allen et al., 2007). These efficiencies of ozone formation are significantly higher than those observed in other urban areas (typically 3-5), those observed in the Houston urban plume (approximately 5), or those observed in the plume of an isolated power plant in the region (approximately 2) (Allen et al., 2007). For all of these reasons, the HGB area presents a unique situation with regard to its emissions source areas, and significant effort during the TexAQS I field campaign was given to obtaining measurements that would elucidate the processes contributing to ozone formation and accumulation in the unique industrial plumes and surrounding areas of the Houston-Galveston region (Allen et al., 2007).

One conclusion from the TexAQS I analyses is that high rates and high efficiencies of ozone production in the industrial plumes originating in Houston are driven by high concentrations of reactive hydrocarbons in the presence of NO_x (Allen et al., 2007). Additionally, the industrial plumes exhibiting rapid and efficient ozone

formation also tend to exhibit a complex spatial and temporal structure (Allen et al., 2007).

The geographic distribution of VOC reactivity, its very high magnitude in comparison with other less industrial urban regions, and its high fraction of olefins indicate that industrial emissions are large contributors to elevated ozone concentrations in Houston (Allen et al., 2007). Ozone production rates were calculated based on aircraft measurements for five major U.S. cities (Houston, Nashville, New York, Phoenix, and Philadelphia); 90% of the measurements made in the HGB area were similar to other cities with regard to NO_x concentrations, VOC reactivity, and ozone production rate. However, 10% of Houston is very different, with high anthropogenic VOC reactivity and high ozone production rates (Allen et al., 2007). Samples with high ozone production rates had high concentrations of ethene, propene, and/or butenes, butanes, and aromatics and were in areas near industrial sources (Allen et al., 2007).

These features result in urban plumes originating from Houston that are chemically distinct and separable from background concentrations. Specifically, the Houston area has two distinct source regions. The eastern portion of the region, bordering Galveston Bay, contains a high density of petrochemical facilities, while the western portion of the region is a more typical urban area. When winds are from the south, two chemically distinct plumes advect from Houston: a plume containing typical urban emissions is found to the west of an industrial plume containing NO_x and highly reactive hydrocarbons, especially low molecular weight alkenes such as ethylene and propylene. These plumes, often separable, advect over forested areas to the north of the city, which release large quantities of isoprene and other biogenic emissions. When winds are from the east or northeast, the urban plume from Houston is a mixture of these two sources and advects over a region downwind that has much lower biogenic emissions. Thus, examination of the Houston urban plume offers the opportunity to probe a variety of plume types, which in some cases, occur on the same day.

Airborne LIDAR data collected on September 6th, 2000 by the National Oceanic and Atmospheric Administration (NOAA) DC-3 aircraft illustrate a case of regional transport of ozone into Victoria from the HGB region. The aircraft flight track and ozone

concentrations collected by the LIDAR on this day are presented in Figure 6-1. Two distinct plumes of high ozone concentrations that originated from industrial facilities located in the Houston Ship Channel and Texas City were clearly mapped during the flight. On this day, steady winds from the northeast, parallel to the coast, transported these plumes over distances of more than 100 kilometers from the urban area (as a mixed urban and industrial plume) and from a separate, isolated industrial area. This case study, and other case studies examined in this work, characterizes plumes from distinctly different urban and industrial source regions, advecting over rural regions with different levels of biogenic emissions. Moreover, this work compares how the plumes chemically evolve and the effect of the chemistry on the extent of regional ozone transport.

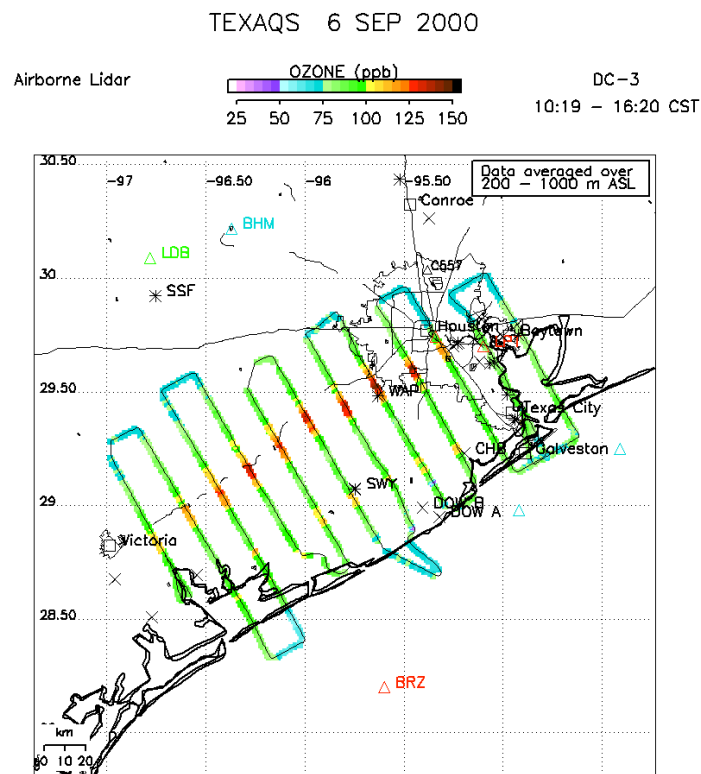


Figure 6-1. Measurements of ozone concentrations collected by the LIDAR during the NOAA DC-3 flight on September 6th, 2000 (Senff et al., 2007). The contours represent ozone concentrations vertically averaged over an approximate depth of 200-1000 meters above mean sea level.

The September 6th case study provides an excellent example of regional transport observed by aircraft measurements, as high ozone concentrations were likely transported from the HGB area southwestward into Victoria by prevailing winds. Figure 6-2 illustrates the one-hour average ozone concentrations measured on September 6th, 2000, at all HGB surface monitors and at the CAMS 87 monitor in Victoria (McGaughey et al., 2005). Although Victoria is located approximately 40 miles to the south outside of the CAMx 4-km modeling domain, the orientations of the plumes strongly suggest their extension into the Victoria area (McGaughey et al., 2005). The maximum HGB one-hour average concentration of 156 ppb was measured at 13:00 CST at the Croquet surface monitor (CAMS 409). In Victoria, a daily maximum one-hour average concentration of 94 ppb was measured at 16:00 CST, suggesting that the plume extended into the Victoria region approximately three hours after its effects were seen in HGB (McGaughey et al., 2005).

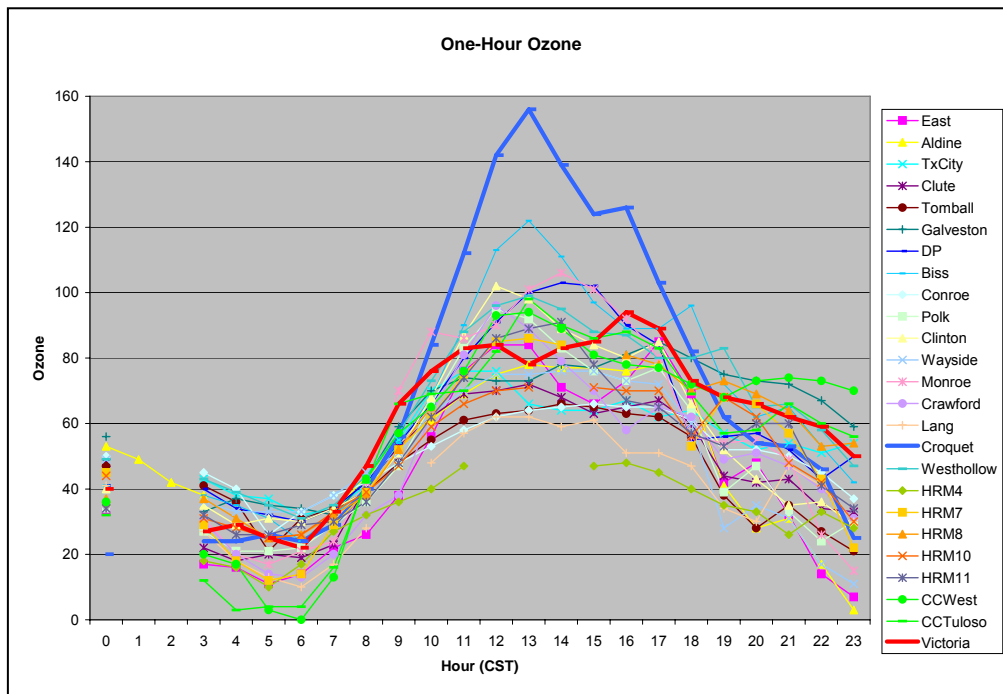


Figure 6-2. One-hour average ozone concentrations measured by surface monitors in the HGB area and the CAMS 87 monitor in Victoria (McGaughey et al., 2005).

One of the preliminary issues to be addressed when assessing pollutant transport is the identification of the major source or sources of these pollutants, as well as the relative importance of these varying source regions. For the plumes examined in this work, extensive ambient data (aircraft and surface monitoring data) are available from the TexAQS I study. In addition to analyses of the observational data, a variety of photochemical modeling source apportionment and probing tools have the ability to assess the contributions of precursor emissions and transported ozone from different source regions. These tools provide valuable and complimentary information regarding the major processes contributing to ozone formation and depletion within the plume, as well as source apportionment. The observational data will be qualitatively and quantitatively compared to photochemical modeling results. Specifically, the results from CAMx OSAT and APCA source apportionment tools and Process Analysis (PA) will be compared to the aircraft LIDAR data.

6.3 PHOTOCHEMICAL MODEL DESCRIPTION AND INPUTS

Details for the CAMx photochemical modeling run for this case study were described in Chapter 5 but will be briefly revisited here. The configuration is based on the August 22nd–September 6th, 2000 photochemical modeling episode for the TCEQ ozone SIP mid-course review (TCEQ, 2004) developed in support of the 1-hour ozone standard (McGaughey et al., 2005). The hybrid base case for 2000 combined two meteorological characterizations: MM5-GOES for the period of August 22nd–September 1st and MM5-ATMET for September 2nd–6th. Output files from the August 22nd-September 6th, 2000 CAMx photochemical modeling episode have been used by the State of Texas for air quality planning in the HGB area were downloaded from the TCEQ website, available at (<ftp://ftp.tceq.state.tx.us/pub/OEPAA/TAD/Modeling/HGMCR/CAMx/output/camx403.ase5b.psito2n2/atmetnoapbl/>).

Figure 6-3 illustrates the CAMx horizontal grid structure for the modeling episode used in this work as obtained from the TCEQ website, available at http://www.tceq.state.tx.us/implementation/air/airmod/data/hgbmcr/hgb1_camx_domain.html#layer. The horizontal modeling domain structure consists of a 36-km resolution

coarse grid regional domain and nested fine grid sub-domains: East Texas 12-km resolution sub-domain, Houston-Galveston-Brazoria—Beaumont-Port Arthur (HGBPA) 4-km resolution sub-domain and the optional Houston-Galveston Bay (HGB) and Beaumont-Port Arthur (BPA) 1-km resolution sub-domains. The location of the plumes evaluated in the source apportionment and PA assessments lie within the 4-km resolution HGBPA domain.

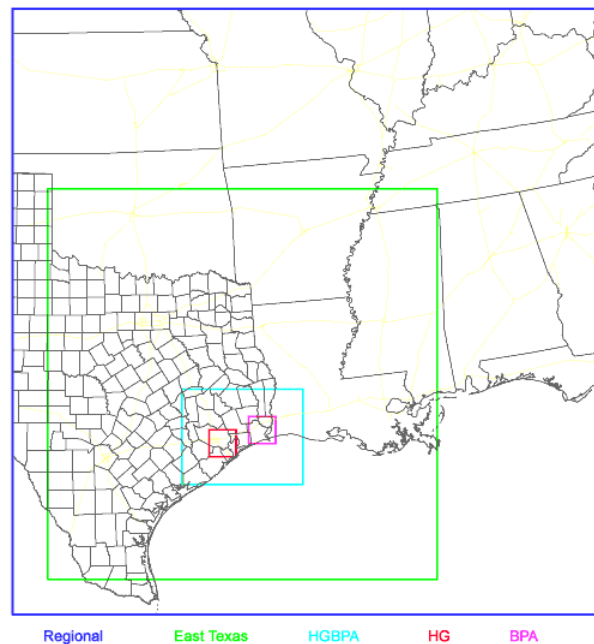


Figure 6-3. CAMx photochemical modeling horizontal domains for the August 22nd–September 6th, 2000 episode.

6.4 AIRCRAFT LIDAR DATASETS

Data from aircraft flights that determine the horizontal and vertical distributions of pollutants is a source of observational data (introduced in Chapter 2) that was used to characterize the pollutant plumes in this analysis. LIDAR data were collected on September 6th, 2000 by the NOAA DC-3 aircraft and were obtained from the NOAA Environmental Technology Laboratory website, available at http://www.etl.noaa.gov/et2/data/data_pages/texaqs/air_ozone.html.

The flight track for this day was shown in Figure 6-1. The dynamic and chemical evolution of the plumes were tracked by the DC-3 aircraft by performing ten crosswind transects, oriented along north-northwest to south-southwest axes, within the mixed layer at successive distances downwind of the HGB source region. LIDAR measurements were recorded in 10-second intervals, beginning at approximately 10:20 CST and ending at 16:20 CST. It should be noted that measurements were taken at times of day when mixing was most rapid, ensuring that compounds emitted from the source regions were extensively mixed within the boundary layer. The elevation of the recorded measurements spans from the surface to an altitude of nearly 2600 meters above sea level (masl), and a vertical average of each 10-second ozone concentration was calculated for the purposes of this analysis. Observational data are provided in ASCII text files consisting of 50 columns: time in decimal hours Universal Time (UTC), aircraft altitude in masl, latitude, longitude, LIDAR beam elevation angle, LIDAR beam azimuth angle, and ozone mixing ratio in ppbv for each range gate.

6.5 CAMx SOURCE APPORTIONMENT METHODOLOGY

Due to the nonlinearity of the chemical mechanisms involved in ozone formation, as well as the fact that ozone formation involves the interaction between emissions that most likely come from varying sources, e.g., anthropogenic NO_x interacting with biogenic VOC, there is no single “correct” source apportionment analysis method. Ozone Source Appointment Technology (OSAT) and the Anthropogenic Precursor Culpability Assessment (APCA) are source apportionment tools available in CAMx that were used in this work, and were discussed in further detail in Chapter 2. Both of these methods are capable of estimating contributions to ozone concentrations from multiple source groups within and outside of a region of interest. Source groups may be defined in terms of geographic areas and/or emission categories. Ozone and precursors originating from the model boundary and initial concentrations are also tracked as separate source groupings. The output for OSAT and APCA analyses are summarized as contributions to ozone formation (source apportionments) of biogenic and anthropogenic NO_x and VOC for the various selected receptor regions. It is important to note that the mass of NO_x or VOC

from a given source area that may be present at a given receptor at a selected hour is often not particularly relevant to the amount of ozone present there at that time. Rather, it is the contribution to ozone formation activity of the NO_x and VOC emissions en-route to a receptor that is important.

Figure 6-4 illustrates the locations of the source and receptor regions for the September 6th, 2000 case study on a portion of the CAMx 4-km domain. For this case study, two geographic areas were selected as the primary industrial plume sources: the Houston Ship Channel region and the Texas City industrial region. Five additional source regions were selected downwind of each of these primary source groupings, and a final source region (Source 8) encompasses emissions in the remaining area of the 4-km grid that is not explicitly listed as a source region, including emission sources in the Gulf of Mexico.

The receptor regions were selected by examining the observed LIDAR ozone concentrations along the flight transects. Receptor grid cells were selected in CAMx that correspond to the aircraft coordinates at the centerline of the plume for each flight transect downwind from the source regions. The selected centerline receptor grid cells are characterized by a threshold of observed elevated ozone levels above 90 ppb. The CAMx-predicted 1-hour surface layer ozone concentrations for 13:00 CST on this day are shown for the entire 4-km domain, and the NOAA DC-3 aircraft flight path, along with the LIDAR-measured concentrations, are matched in space and superimposed on the CAMx 4-km grid. The plume originating from the Ship Channel region is denoted as Plume A, and the plume originating from the Texas City region is denoted as Plume B. Receptor sites are labeled with “a” and “b” followed by a number, and they are numbered in the order of proximity to the source regions (i.e., a1 is located closest to the source regions). As shown in Figure 6-4, there are eight source regions that could potentially contribute emissions that lead to ozone formation. The anthropogenic and biogenic VOC and NO_x emissions input into the CAMx model for September 6th, 2000 were extracted for all source regions and are presented in Table 6-1 below and illustrated in Figure 6-5.

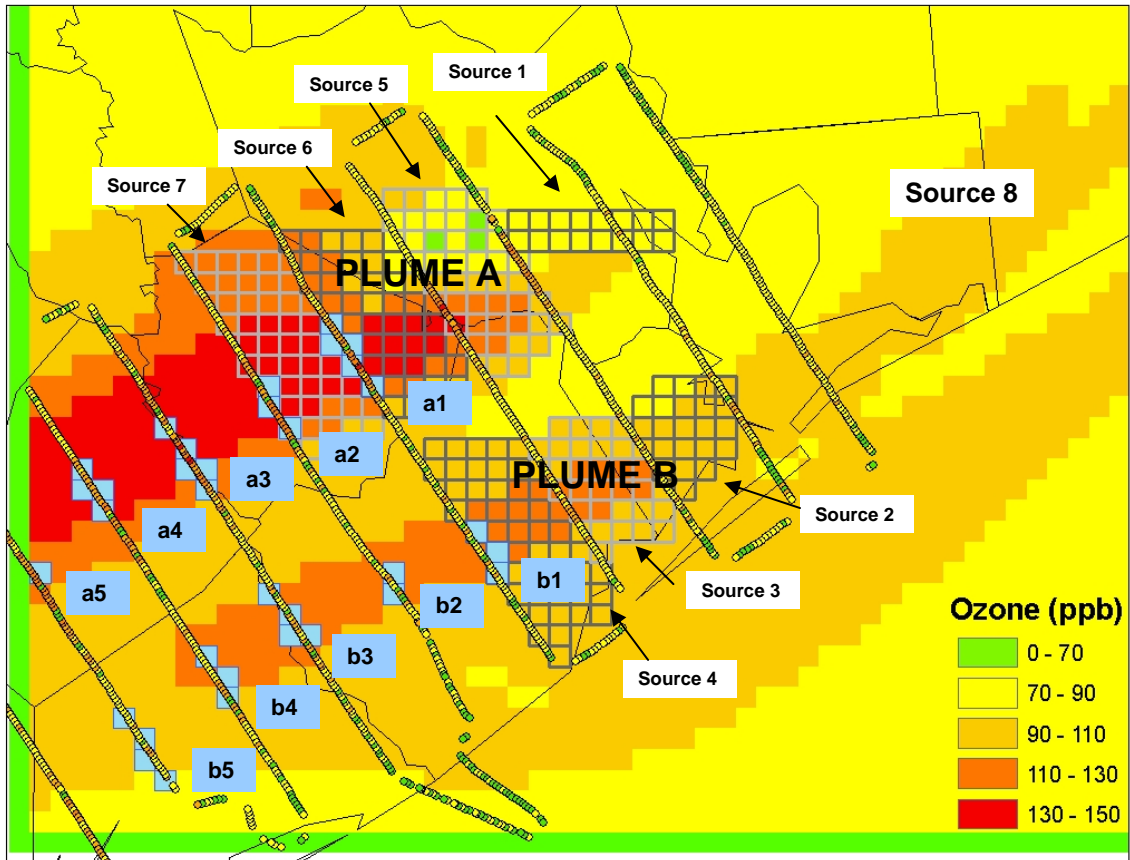


Figure 6-4. CAMx-predicted 1-hour surface layer ozone concentrations for the 4-km domain at 13:00 CST on September 6th, 2000. The locations of the selected source and receptor regions used for the source apportionment study are also shown, as well as the NOAA DC-3 aircraft flight track for this day.

Table 6-1. Summary of anthropogenic and biogenic VOC and NO_x emissions in tons per day for all source regions on September 6th, 2000.

	Biogenic VOC Emissions (tons/day)	Anthropogenic VOC Emissions (tons/day)	Biogenic NO _x emissions (tons/day)	Anthropogenic NO _x emissions (tons/day)
Source 1	4.9	175.8	0.1	134.8
Source 2	6.2	52.4	0.1	51.9
Source 3	12.2	19.4	0.3	6.4
Source 4	21.5	9.4	0.5	8.9
Source 5	21.1	70.8	0.4	111.9
Source 6	30.3	36.2	1.7	45.5
Source 7	31.0	7.8	3.9	96.0
Source 8	77467.4	15287.8	3035.6	26870.6

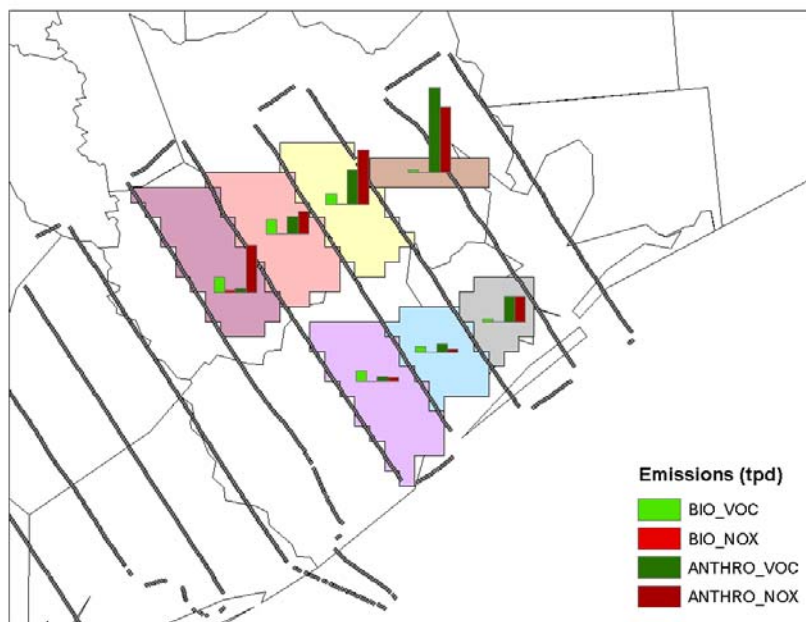


Figure 6-5. Relative anthropogenic and biogenic VOC and NO_x emissions in tons per day for all source regions on September 6th, 2000, superimposed on the CAMx 4-km domain. The NOAA DC-3 aircraft flight track for this day is also shown.

According to Table 6-1 and Figure 6-5, excluding Source 8, the Ship Channel region (Source 1) has the highest anthropogenic and VOC and NO_x emissions, followed by the source region encompassing the Houston urban region (Source 5). As these sources have the highest precursor emission levels, it was therefore expected that these sources would be the largest contributors to the downwind receptor sites.

6.6 CAMx PROCESS ANALYSIS METHODOLOGY

In addition to source apportionment tools, the CAMx photochemical model also features a probing tool called Process Analysis (PA) which is primarily used as an explanatory tool to characterize the physical and chemical processes incorporated in CAMx. The technique generates mass budgets of several compounds such as HO_x, NO_y, and ozone. Additionally, it includes the Integrated Process Rate Analysis (IPR), which provides detailed process rate information for key chemical and physical processes such

as diffusion, advection, and deposition. A detailed description of the PA tool and available output options was discussed in Chapter 4.

Process analysis will be used in conjunction with source apportionment tools to investigate which (and to what extent) chemical and physical processes are contributing to both ozone formation and depletion along the path of the plumes observed on September 6th, 2000. Additionally, this work includes PA post-processing with the IPR output data.

6.7 PROCESS ANALYSIS RESULTS AND DISCUSSION

Figure 6-6 illustrates vertically averaged total ozone concentrations at the receptor regions downwind of both plumes. The receptor regions are designated as “a” and “b” followed by the number on the x-axis of Figure 6-6, and the locations of these regions are shown in Figure 6-4 (i.e., data for site a1 is represented by the “Plume A” curves and by the “1” on the x-axis). As previously mentioned, the groups of receptor cells were selected along the flight track within the 4-km CAMx domain at the centerlines of the plumes that were characterized by LIDAR-observed ozone concentrations greater than 90 ppb. CAMx predictions were matched in time and space (within the 4-km domain) with the vertically averaged aircraft observations for a direct comparison. However, it should be noted that CAMx results are 1-hour averages, as opposed to the 10-second measurements collected by the aircraft LIDAR. For example, a LIDAR measurement at 13:05 CST would be compared to a CAMx prediction at the same location at 13:00 CST.

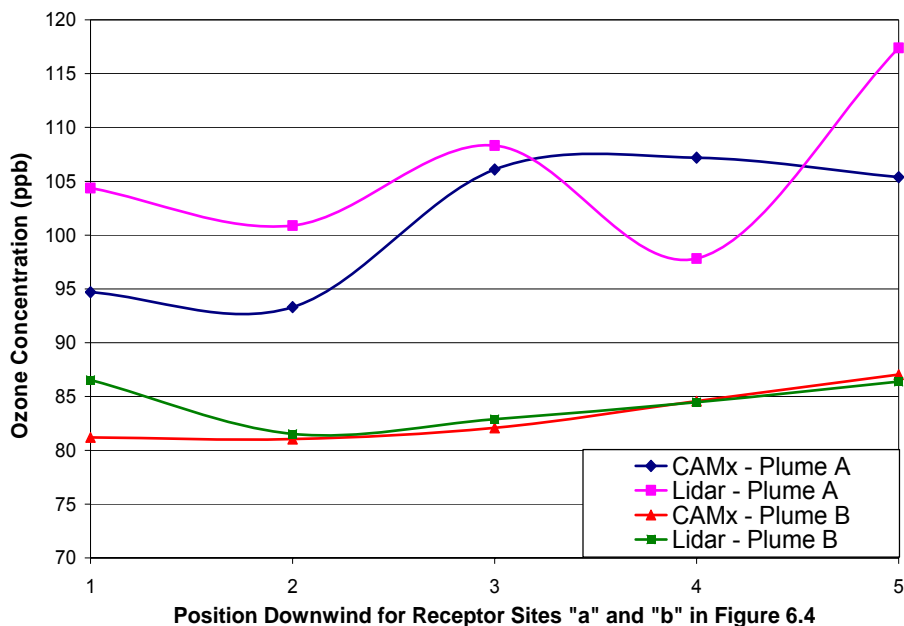


Figure 6-6. Average CAMx and LIDAR vertically averaged total ozone concentrations at the receptor regions selected in the centerline of Plume A (Houston Ship Channel source) and Plume B (Texas City source).

The results shown in Figure 6-6 reinforce the previous conclusion (from Chapter 5) that the CAMx model was able to predict ozone concentrations relatively well in comparison with the observed LIDAR concentrations. It was initially expected that the rapid formation of ozone would occur near the source regions, and that total ozone concentrations would decrease at receptor locations downwind of the plume. However, as illustrated in Figure 6-6, observed and predicted total ozone concentrations remain relatively constant for Plume B, ranging from about 80 ppb to 87 ppb. The LIDAR observations for Plume B show that the total ozone concentration initially decreases from approximately 87 ppb to 81 ppb, followed by gradual slight increases of about 2 ppb at each receptor site. For Plume A, the CAMx-predicted ozone concentrations increase from approximately 95 ppb to 107 ppb, remaining nearly constant at the last three receptor regions. The LIDAR observations for Plume A suggest that total ozone concentrations alternately increase and decrease at the downwind receptor regions, ranging from 105 ppb to 117 ppb.

In order to investigate the causes of this nearly zero-order decay of downwind ozone concentrations observed in both plumes, the CAMx PA tool was used to examine the chemical and physical processes that account for the changes in ozone concentrations at the receptor locations. It should be noted that results were generated for the first vertical layer of the CAMx grid structure, which covers the first 34 meters above ground level (magl), as opposed to the vertically averaged results shown in Figure 6-6. Therefore, results should be largely interpreted as a qualitative characterization of the dominating ozone formation and consumption processes near the surface, as opposed to a direct quantitative comparison to the LIDAR data. Additionally, the PA output results are specific to the receptor regions selected along the centerline of the plume.

6.7.1 Results for the Houston Ship Channel plume (Plume A)

Figure 6-7 illustrates a time series of all sources and sinks analyzed with the PA tool for a1, the receptor site immediately downwind of the Houston Ship Channel plume (Plume A) closest to the source regions. Results are shown as hourly ozone concentrations in ppb and ozone production and loss rates in ppb per hour, for the grid cells at the surface layer, highlighted for receptor site “a1” in Figure 6-4. The complete tabular results of each of the processes contributing to the sources and sinks of ozone for the hours corresponding to the flight time for all receptor regions are presented in Appendix D.

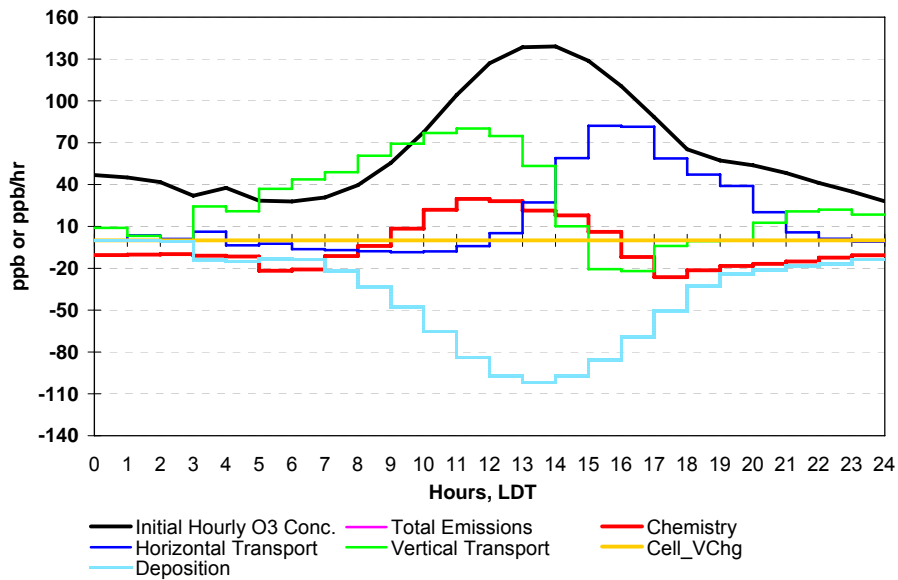


Figure 6-7. CAMx PA results for September 6th, 2000, for Plume A at receptor location a1. Results show hourly ozone concentrations in ppb and ozone production and loss rates in ppb/hr.

The total ozone concentrations at the beginning of each hour are represented by the solid black curve, with a maximum ozone concentration of around 140 ppb at approximately 14:00 CST. During the hours of the aircraft flight (approximately 10:00–16:00 CST), ozone generation is initially attributed to vertical transport and chemistry, with maximum generation rates of approximately 80 ppb/hr and 30 ppb/hr at 11:00 CST, respectively, followed by horizontal transport later in the afternoon, with a maximum contribution of 82 ppb/hr at 15:00 CST. Potential causes of the predominant source of ozone generation changing from vertical to horizontal transport will be discussed further, although an initial explanation may be that upwind ozone generated at the source regions is being transported downwind and does not affect this receptor region until the later afternoon hours.

At the time when the maximum total ozone concentration is achieved (14:00 CST for this receptor site), the primary methods of ozone generation are vertical transport, horizontal transport, and chemistry. The dominant source of ozone depletion is deposition, with a maximum loss rate of 102 ppb/hr at 13:00 CST. Ozone depletion due

to vertical transport and chemistry begins at around 15:00 CST, with maximum loss rates of 21 ppb/hr at 15:00 CST and 12 ppb/hr at 16:00 CST, respectively.

Figures 6-8 to 6-11 present similar results for receptor locations a2 through a5. All receptor sites associated with Plume A experience predicted maximum surface ozone concentrations ranging from 125-143 ppb occurring around 14:00-15:00 CST, with similar characteristics of ozone generation occurring primarily by vertical transport and chemistry in the early afternoon hours, shifting to horizontal transport in the later afternoon hours. For all of the “a” receptor sites, ozone production rates by vertical transport and chemistry increase in the early hours of the flight, with the maximum production rates reached at around 10:00-13:00 CST, followed by hourly decreases that occur simultaneously with hourly increases in horizontal transport production rates. Horizontal transport then becomes the dominant method of ozone production in the later afternoon hours of 14:00-16:00 CST.

Maximum chemical ozone production rates range from about 13 ppb/hr at the most rural receptor region (a5) to approximately 40 ppb/hr at receptor sites closer to the dense urban region of Houston (a2 and a3). Maximum ozone generation within the surface layer due to vertical transport ranges from 56 ppb/hr at site a5 to 114 ppb/hr at site a2. Ozone is predominantly consumed by deposition for all receptor sites, with maximum ozone consumption rates occurring at 13:00-14:00 CST and ranging from 93 ppb/hr at receptor site a5 to 136 ppb/hr at receptor site a2. Differences in deposition losses are likely due to the altering land coverage characteristics of each receptor site. Ozone is also depleted to a lesser extent by horizontal transport, vertical transport, and chemistry.

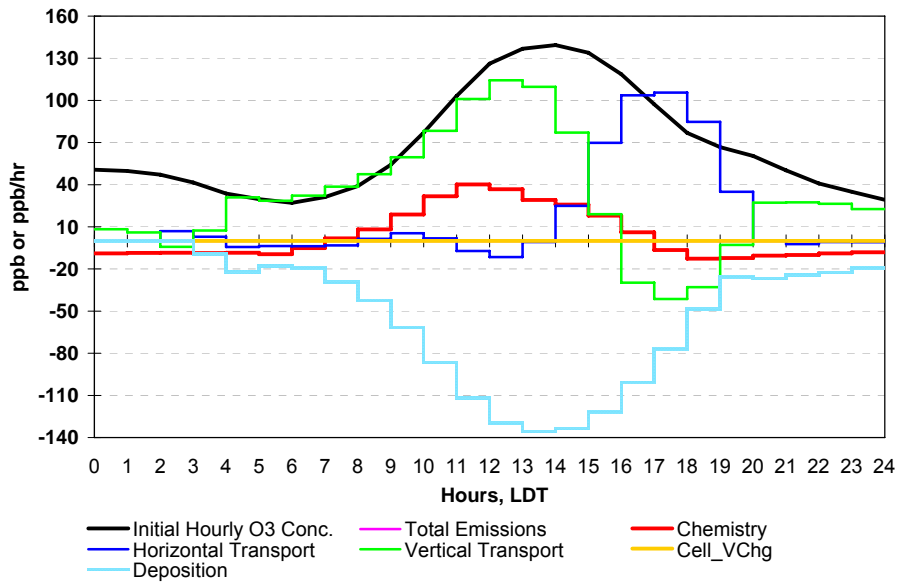


Figure 6-8. CAMx PA results for September 6th, 2000, for Plume A at receptor location a2. Results show hourly ozone concentrations in ppb and ozone production and loss rates in ppb/hr.

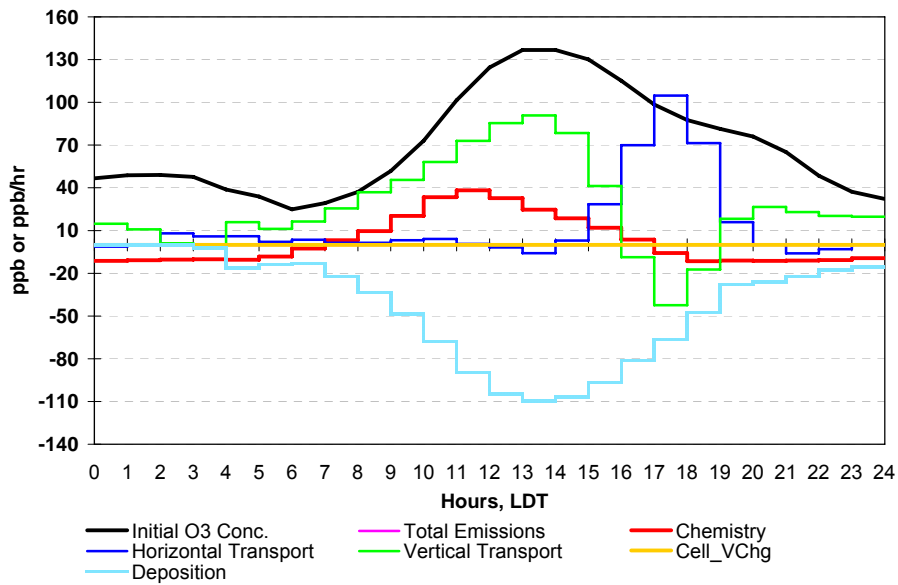


Figure 6-9. CAMx PA results for September 6th, 2000, for Plume A at receptor location a3. Results show hourly ozone concentrations in ppb and ozone production and loss rates in ppb/hr.

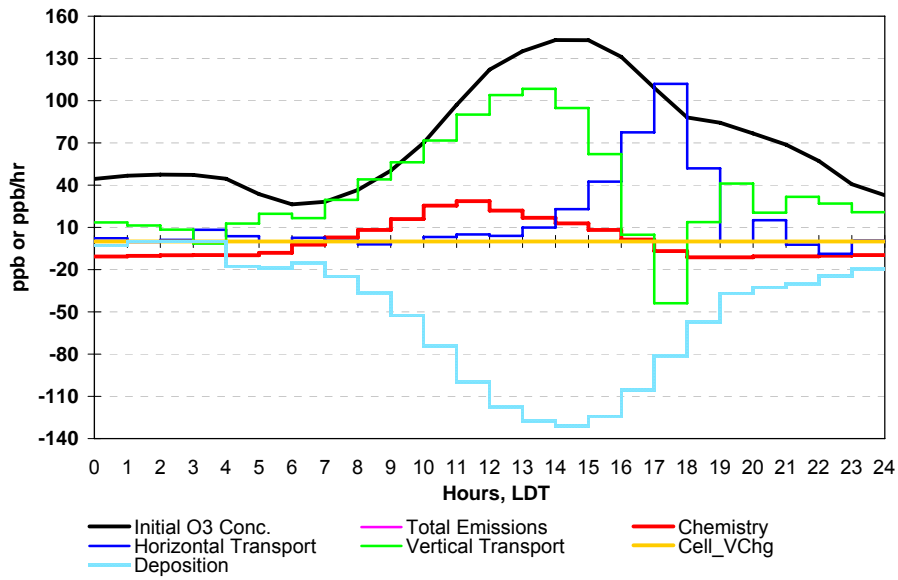


Figure 6-10. CAMx PA results for September 6th, 2000, for Plume A at receptor location a4. Results show hourly ozone concentrations in ppb and ozone production and loss rates in ppb/hr.

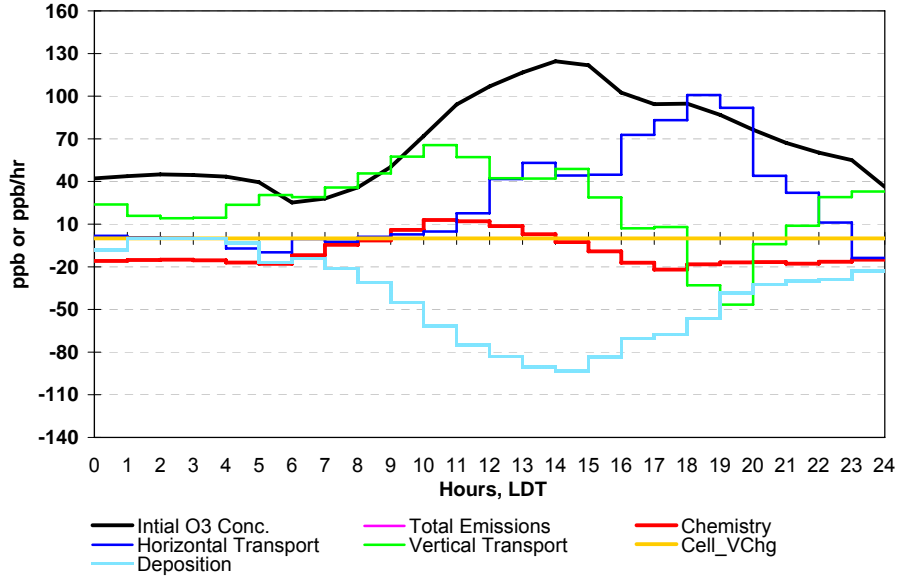


Figure 6-11. CAMx PA results for September 6th, 2000, for Plume A at receptor location a5. Results show hourly ozone concentrations in ppb and ozone production and loss rates in ppb/hr.

For receptor site a5, located farthest downwind of the source regions, and consequently, closest to the Victoria area, the maximum hourly surface level ozone concentration reaches roughly 125 ppb at around 14:00 CST, approximately 15 ppb less than the maximum hourly ozone concentration at receptor site a1. This can be contrasted with the vertically-integrated CAMx and LIDAR results shown in Figure 6-6, which show lower total ozone concentrations at both receptor sites, as well as an increase in ozone concentrations from approximately 105 ppb at receptor site a1 to 117 ppb at receptor a5. This is likely due to vertical mixing and, consequently, differences that result in the CAMx-predicted ozone concentrations throughout the planetary boundary layer at the various downwind locations within the plume.

Similar to the results for receptor site a1, vertical transport and chemistry are the predominant sources for ozone production in the early afternoon hours at a5, followed by horizontal transport in the late afternoon. Vertical transport and chemical processes generate maximum contribution rates of 66 ppb/hr at 12:00 CST and 12 ppb/hr at 10:00 CST, respectively. At the hour during which the maximum 1-hour total ozone concentration is at its peak (14:00 CST), ozone is primarily generated by vertical and horizontal transport, as opposed to receptor site a1, which included relatively higher contributions from chemistry. In comparison to the generation rates from chemical processes at receptor site a1, chemistry accounts for relatively less of the ozone produced in the early afternoon at this receptor site. The maximum ozone production rate due to chemistry for receptor site a1 is nearly 30 ppb/hr at 11:00 CST, more than double the maximum rate (12 ppb/hr) predicted at site a5. This may be a direct effect of the proximity difference of these receptor regions to the source regions. Receptor site a1 is located closer to the sources near the ship channel industrial and primary Houston urban regions, which has higher levels of anthropogenic VOC and NO_x emissions that contribute to the chemical formation of ozone. Receptor site a5, on the contrary, is located farther downwind from these areas and located in a more rural region with relatively lower VOC and NO_x emissions (refer to Table 6-1).

At the a5 receptor location, ozone production due to horizontal transport increases to levels of approximately 40-50 ppb/hr at 12:00 CST, with rates nearly identical to those

due to vertical transport from 12:00 CST to 14:00 CST. After 14:00 CST, the predominant source of ozone formation shifts to horizontal transport for the late afternoon hours, as was observed for site a1. This likely indicates that ozone generated in earlier hours upwind of this region was transported downwind, and its effects are only seen on this receptor region during the late afternoon hours. While the shift from vertical transport to horizontal transport as the primary source of ozone generation is shared by the two receptor sites, the generation rate due to horizontal transport is significantly higher for receptor region a5. It is possible that this difference is because receptor region a5 experiences the effects of horizontal transport from the primary source region in addition to ozone formed by chemical processes in the urban regions located between a1 and a5; whereas receptor region a1 does not have the same quantity of upwind emission sources. It should also be noted that receptor region a5 is closer to the Victoria region. These results for a5 (located immediately upwind of Victoria) imply that, at the hours of peak ozone production, transport is the primary source of ozone generation.

At both the a1 and a5 receptor locations, deposition is the predominant source of ozone depletion, with a maximum consumption rate of 93 ppb/hr occurring at 14:00 CST at a5, only 9 ppb/hr less than the maximum deposition loss rate at site a1. Additionally, at a5, losses due to chemistry begin at 13:00 CST with a maximum loss rate of 17 ppb/hr at 16:00 CST, which is comparable to the maximum chemical depletion rate of 12 ppb/hr at site a1. However, during the afternoon hours at a5 there are no losses due to vertical transport as was experienced at receptor site a1.

It should also be noted that the receptor sites that experience increased ozone consumption by deposition (such as receptor sites a2 and a4) are also characterized by increased ozone production in comparison to the other receptor sites. For example, receptor site a2 experiences the maximum ozone depletion due to deposition of 140 ppb/hr at 13:00 CST. However, this site also experiences the largest ozone production levels due to chemistry and vertical transport at 11:00 CST and 12:00 CST, respectively. Similarly, the receptor sites with lower ozone depletion rates experience lower ozone generation rates, such as receptor site a5. This essentially explains the zero-order decay observed in Plume A as shown in Figure 6-6.

6.7.2 Results for the Texas City Plume (Plume B)

Figure 6-12 illustrates a time series plot of all sources and sinks of ozone for the b1 receptor region, which is the receptor site of nearest proximity to Texas City (Source 2). CAMx predicts a maximum ozone concentration within the surface layer of approximately 115 ppb at 13:00 CST. The results show that, for the first hour of the flight (10:00 CST), ozone is primarily created by vertical transport with a 34 ppb/hr generation rate, followed by horizontal transport and chemistry, with production rates of 21 ppb/hr and 25 ppb/hr, respectively. For the remaining hours of the flight (11:00–16:00 CST), the contributions from vertical transport and chemistry decrease, and the source of ozone generation is primarily attributed to horizontal transport with a maximum production rate of 67 ppb/hr at 13:00 CST. At the hour when the maximum total hourly ozone concentration is reached, the primary source of ozone generation is horizontal transport, with a small contribution due to chemistry. For comparison purposes, receptor site a1 attributed ozone generation primarily to vertical transport and chemistry during the hour with the peak hourly ozone concentration. Ozone is almost exclusively consumed by deposition, with a maximum loss rate of 79 ppb/hr at 13:00 CST. Significantly lower depletion rates due to horizontal transport and chemistry occurs at around 16:00 CST, with loss rates of 6 ppb/hr and 4 ppb/hr, respectively.

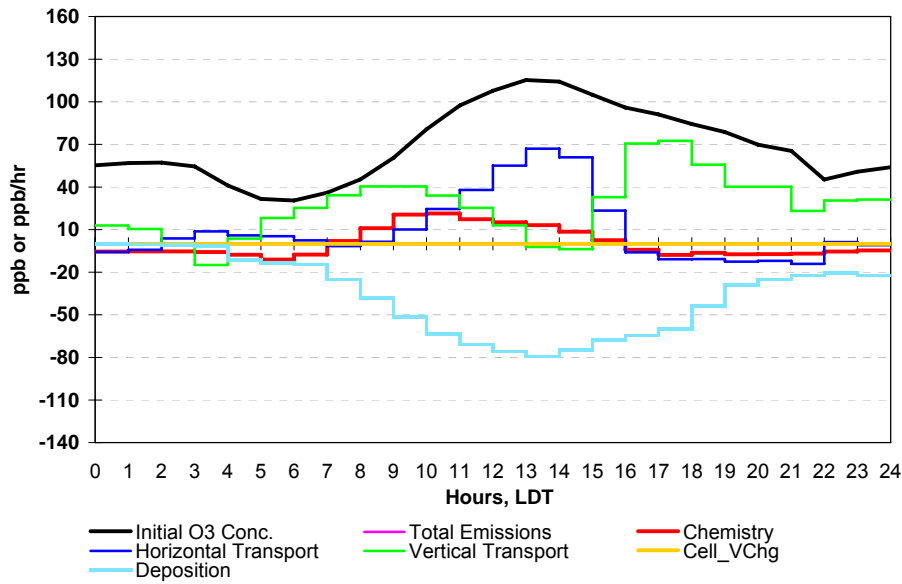


Figure 6-12. CAMx PA results for September 6th, 2000, for Plume B at receptor location b1. Results show hourly ozone concentrations in ppb and ozone production and loss rates in ppb/hr.

The corresponding graphical results for the other receptor regions (b2 through b5) are presented in Figures 6-13 to 6-16. All receptor locations associated with Plume B experience similar maximum ozone concentrations ranging from 114-118 ppb occurring around 13:00-15:00 CST, with the exception of receptor site b5, which reaches a maximum of 99 ppb at 14:00 CST. These maximum total surface ozone concentrations at the surface are 7-44 ppb less than those experienced at the receptor sites for Plume A. Consistent with the PA results for Plume A, the maximum total ozone concentrations are similar for all receptor sites with the exception of the site farthest from the source regions, b5. This can be contrasted with the results shown for the vertically averaged ozone concentrations in Figure 6-6, which show that ozone concentrations increase from about 81 ppb to 87 ppb from receptor site b1 to b5. As previously mentioned, this is likely due to the difference in the CAMx prediction of total ozone within the surface layer versus the vertically averaged total ozone concentration.

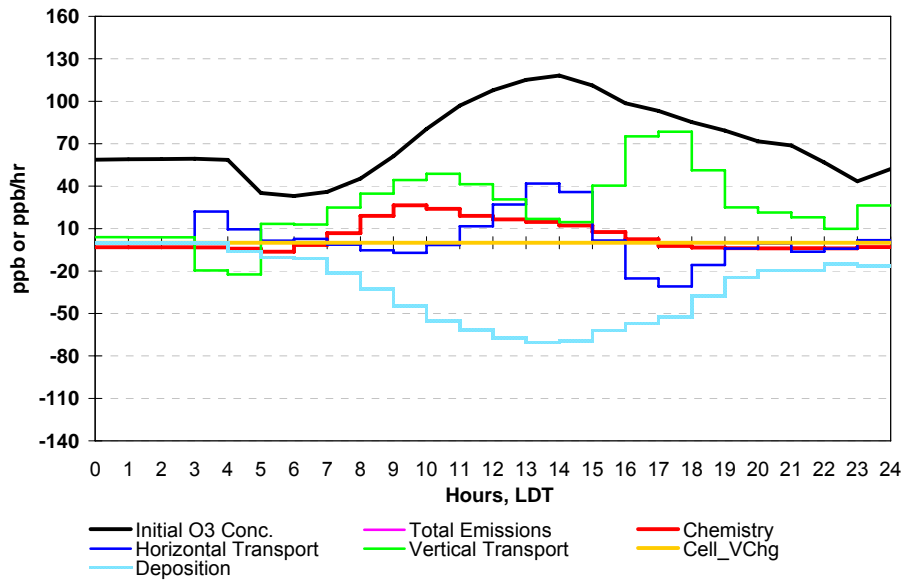


Figure 6-13. CAMx PA results for September 6th, 2000, for Plume B at receptor location b2. Results show hourly ozone concentrations in ppb and ozone production and loss rates in ppb/hr.

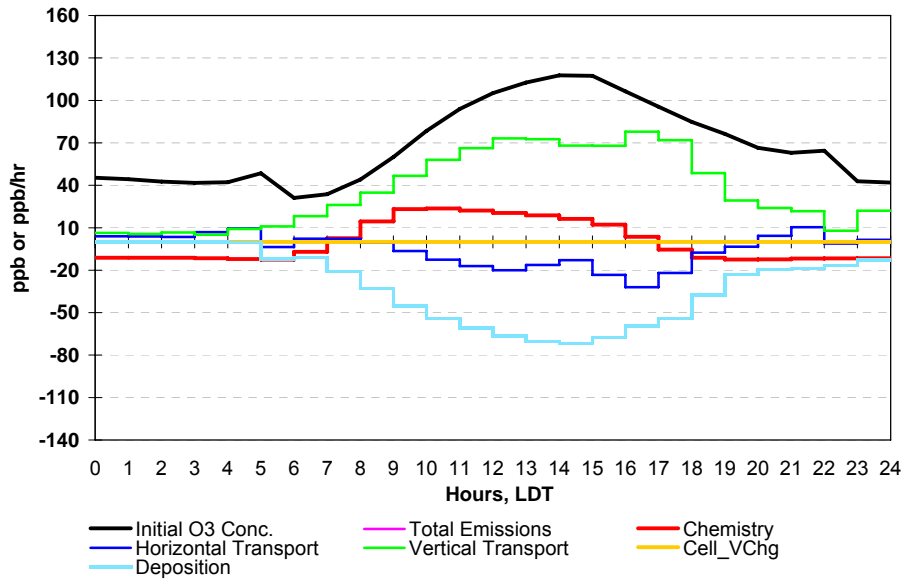


Figure 6-14. CAMx PA results for September 6th, 2000, for Plume B at receptor location b3. Results show hourly ozone concentrations in ppb and ozone production and loss rates in ppb/hr.

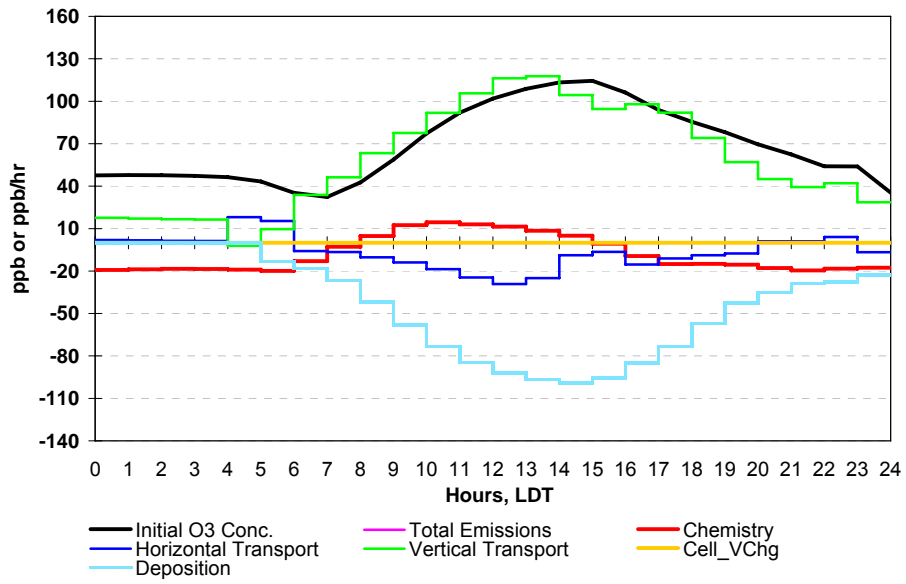


Figure 6-15. CAMx PA results for September 6th, 2000, for Plume B at receptor location b4. Results show hourly ozone concentrations in ppb and ozone production and loss rates in ppb/hr.

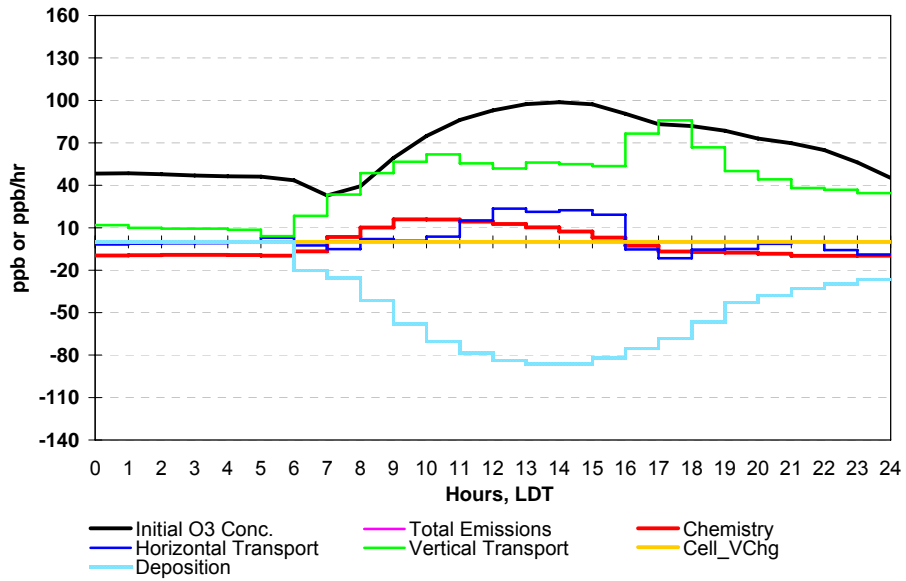


Figure 6-16. CAMx PA results for September 6th, 2000, for Plume B at receptor location b5. Results show hourly ozone concentrations in ppb and ozone production and loss rates in ppb/hr.

Receptor sites b1 and b2 are qualitatively similar with respect to sources and sinks of ozone concentrations. For receptor site b2, ozone generation occurs primarily by vertical transport and chemistry in the early hours of the flight, with maximum generation rates of around 24 ppb/hr and 49 ppb/hr at 10:00 CST, respectively. Ozone generation rates due to chemistry and vertical transport then decline each hour thereafter until 16:00 CST, when vertical transport increases to become the predominant form of ozone generation. The contribution due to horizontal transport increases steadily from 11:00-13:00 CST and becomes the primary source of ozone generation with a maximum generation rate of 42 ppb/hr. During the hours when the peak hourly ozone concentrations occur, horizontal transport is the largest contributor to ozone generation, with smaller (but nearly equal) contributions due to chemistry and vertical transport. The primary method of ozone depletion is deposition with a maximum loss rate of 70 ppb/hr, with some losses due to horizontal transport during the last hour of the flight. These results are similar to those for b1; however, ozone generation due to horizontal transport is significantly greater at site b1, with a maximum difference of approximately 30 ppb.

Unlike the results for the other receptor sites, ozone is not generated by horizontal transport at sites b3 and b4, and site b5 has a relatively smaller production rate (maximum of 23 ppb/hr) due to horizontal transport in comparison to the other receptor sites. Ozone production at receptor sites b3, b4, and b5 are all dominated by vertical transport, with secondary contributions due to chemistry that reach a maximum of 14-24 ppb/hr at around 10:00 CST and steadily decline each hour thereafter. For receptor site b4, ozone is almost exclusively generated by vertical transport and largely consumed by deposition; however, receptor sites b3 and b4 experience significant ozone depletion due to horizontal transport (up to 28 ppb for receptor site b4). This source of ozone depletion is uncharacteristic of all other receptor sites and may be due to a shift in the wind direction at this location. The total losses and gains of ozone concentrations during the hours of the flight are similar for receptor sites b1, b2, and b3; however, receptor site b4 is characterized by a larger deposition loss, and consequently higher generation levels due to vertical transport. This result is similar to that for Plume A, supporting the zero-

order decay of the vertically averaged total ozone concentrations within Plume B that were observed by the aircraft LIDAR and predicted by CAMx (refer to Figure 6-6).

As previously mentioned, receptor site b5 experiences ozone generation primarily by vertical transport during the hours of peak hourly ozone concentrations, with smaller contributions due to horizontal transport (~20 ppb) and chemistry (<10 ppb). In comparison, results for receptor site a5 show nearly equal contributions from vertical and horizontal transport during the hours of peak ozone concentrations, with a negligible contribution due to chemistry. Both receptor regions a5 and b5 (farthest from the source regions and closest to the Victoria area) are associated with ozone generation primarily by vertical and horizontal transport during the early afternoon hours associated with maximum ozone concentrations. This result further emphasizes the critical role that the transport of upwind emissions can potentially have on ozone concentrations in the Victoria region.

The process analysis results for the “b” receptor sites closer to the more urban regions of Houston (b1 and b2) are qualitatively similar to the receptor sites closer to urban Houston for Plume A (a1, a2, and a3). For these receptor sites, ozone is primarily generated by vertical transport with a secondary contribution due to chemistry, followed by a shift to horizontal transport in the later afternoon hours. Similarly, the receptor sites for both plumes that are located farther downwind of the dense urban region in more rural locations (a4, a5, b4, and b5) experience a similar process analysis trend of relatively lower ozone generation contributions due to chemistry due to the lower anthropogenic emissions in the more rural areas. For all of the receptor regions for both plumes, ozone generation rates due to chemistry reach a maximum in the late morning hours of 10:00–11:00 CST, and decrease steadily each hour after the maximum is reached. This is a typical characteristic of the diurnal pattern of chemical generation of ozone, as discussed in more detail in Chapters 2 and 4, with the dominant chemical reactions that produce ozone primarily taking place during the late morning and early afternoon hours. Additionally, in comparison to the receptor sites for Plume A, contributions due to chemistry are lower at all “b” receptor sites, which may be due to lower emission levels associated with the more rural region encompassed by Plume B.

6.7.3 Analysis of Zero-order Decay

The CAMx PA results provide supportive evidence of the zero-order decay observed by the vertically averaged aircraft LIDAR measurements and CAMx predictions along the downwind receptor locations at the centerlines of both plumes. Figures 6-17 and 6-18 below depict CAMx PA results of total ozone production rates versus total ozone loss rates per flight hour (10:00-16:00 CST) for each receptor site in Plume A and Plume B, respectively. A linear regression was performed for each hourly set of data points, with the equations for the linear trend line for all hourly datasets displayed on each figure. Additionally, the R^2 coefficient of determination, or the statistical measure of how well the regression line approximates the real data points (an R^2 of 1.0 indicates that the regression line perfectly fits the data) is also displayed.

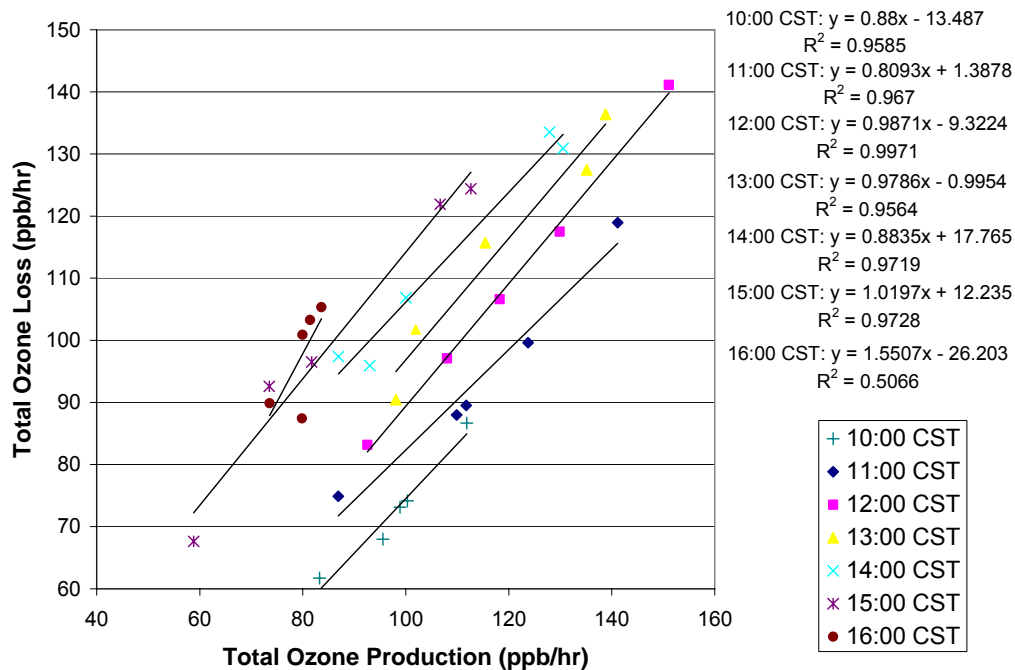


Figure 6-17. CAMx surface layer PA results of total ozone production rates vs. loss rates for all Plume A receptor sites during the NOAA DC-3 flight hours of 10:00–16:00 CST on September 6th, 2000. A linear regression was performed for the data at each hour.

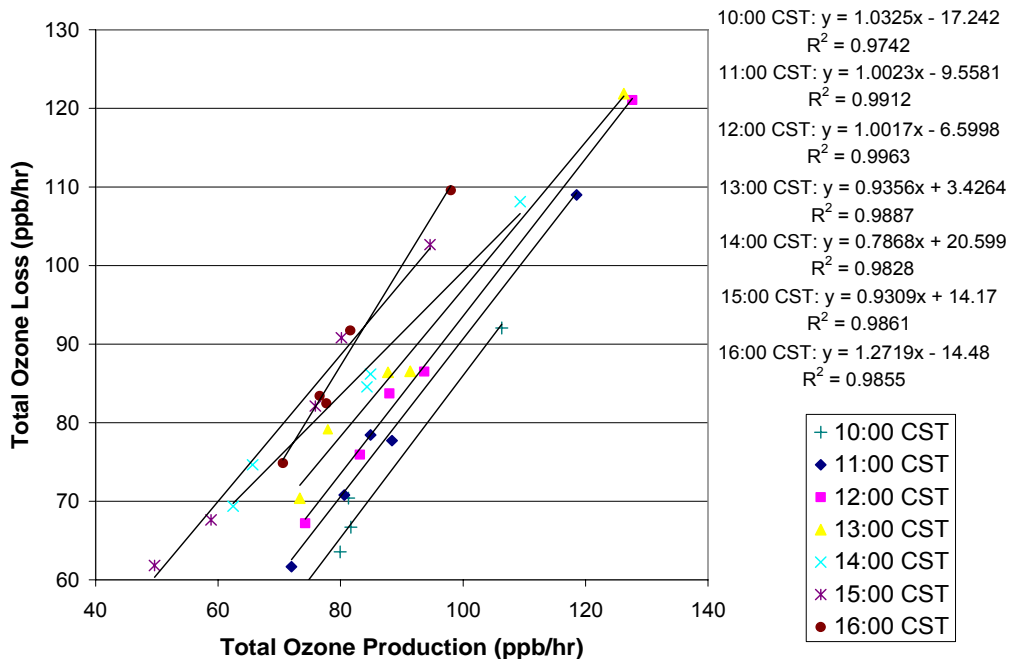


Figure 6-18. CAMx surface layer PA results of total ozone production rates vs. loss rates for all Plume B receptor sites during the NOAA DC-3 flight hours of 10:00–16:00 CST on September 6th, 2000. A linear regression was performed for the data at each hour.

For the data presented in Figures 6-17 and 6-18, the receptor sites in Plume A and Plume B exhibit results that correlate well with the linear regression approximation for all hours (with the exception of 16:00 CST for Plume A), with R^2 values ranging from 0.956 to 0.997 and slopes near unity, ranging from 0.81-1.27. This is an indication that the ratio of the ozone production rate to the ozone depletion rate at the surface of each receptor site remains relatively constant in both plumes, and that ozone is being consumed at the surface as quickly as it is being formed. This consequently results in the total surface ozone concentrations also remaining nearly constant, explaining the zero-order decay in total ozone concentrations observed at the receptor sites in the centerlines of both plumes.

Maximum hourly percent differences and standard deviations in surface layer production/loss rate ratios for the data shown in Figures 6-17 and 6-18 were calculated. Results for the flight hours of 10:00-16:00 CST for Plume A and Plume B are shown in Tables 6-2 and 6-3 below. These results support the conclusion that, while the ozone production and consumption rates change at each receptor site downwind from the

sources, the ratio of the ozone production to consumption rates in each plume remains relatively constant.

Table 6-2. Maximum hourly percent difference and standard deviations for total ozone production/loss ratios at all receptor sites for Plume A.

Hour	Maximum Percent Difference	Maximum Standard Deviation
10	8.5%	4.1%
11	7.3%	4.1%
12	3.5%	1.8%
13	8.3%	3.8%
14	11.1%	3.9%
15	13.2%	4.3%
16	14.2%	5.3%

Table 6-3. Maximum hourly percent difference and standard deviations for total ozone production/loss ratios at all receptor sites for Plume B.

Hour	Maximum Percent Difference	Maximum Standard Deviation
10	10.5%	6.1%
11	7.5%	3.8%
12	4.6%	2.5%
13	7.0%	3.0%
14	13.9%	6.1%
15	13.8%	4.9%
16	5.2%	2.5%

In the CAMx PA algorithm, the governing three-dimensional equation for the change in concentration of a species with time, including all ozone production and loss terms, is:

$$\frac{\partial c_i}{\partial t} = \underbrace{\left(\frac{\partial (uc_i)}{\partial x} + \frac{\partial (vc_i)}{\partial y} + \frac{\partial (wc_i)}{\partial z} \right)}_{\text{Bulk Advection}} + \underbrace{\frac{\partial}{\partial x} \left(K_H \frac{\partial c_i}{\partial x} \right) + \frac{\partial}{\partial y} \left(K_H \frac{\partial c_i}{\partial y} \right) + \frac{\partial}{\partial z} \left(K_V \frac{\partial c_i}{\partial z} \right)}_{\text{Turbulent Diffusion}} + \underbrace{\text{Ri}}_{\text{Chemical Reaction}} + \underbrace{\text{Si}}_{\text{Emissions}} + \underbrace{\text{Li}}_{\text{Surface Removal (Deposition)}}$$

where u, v, and w represent wind speeds in the x, y, and z directions, respectively, c represents the concentration of a species, and K_v is the turbulent mass transfer diffusion coefficient (ENVIRON, 2004). In order to explain the shift in contribution from vertical to horizontal transport predicted by CAMx at all of the receptor regions for Plume A and at the receptor regions b1, b2, and b3, the horizontal and vertical components of transport

rates were examined for both plumes at each hour (tables shown in Appendix D). For Plume A, the horizontal diffusion terms are negative and remain relatively low (0 to -7.4 ppb); however, the horizontal advection term increases each hour, with significant increases in the later flight hours of 13:00-16:00 CST. The horizontal diffusion terms for the receptor sites for Plume B are also small, negative numbers ranging from -0.1 ppb/hr to -3.1 ppb/hr. For receptor sites b1, b2, and b5, an increase in horizontal advection is observed similar to that for Plume A receptor sites; however, the larger increases occur earlier in the afternoon, and large decreases occur from 14:00-16:00 CST, with negative values at 16:00 CST. For receptor sites b3 and b4, the horizontal diffusion terms remain small and negative in value, and the horizontal advection terms are also negative loss terms but with larger absolute values.

According to the CAMx PA algorithm, for the bulk advection term, increased wind speeds in the x-direction would result in increases in horizontal advection terms. An initial hypothesis was that the increase in horizontal transport may be due to increased predicted wind speeds. Therefore, hourly wind speeds from the CAMx meteorological input files were extracted for each hour of the NOAA DC-3 flight, from 10:00-16:00 CST. Tables 6-4 and 6-5 below list the hourly wind speeds extracted from the CAMx meteorological input files for the surface layer, averaged for the cells at each receptor site for Plume A and Plume B.

Table 6-4. CAMx hourly surface layer wind speeds (m/s) at the receptor sites for Plume A from 10:00-16:00 CST on September 6th, 2000.

Receptor Site	10:00 CST	11:00 CST	12:00 CST	13:00 CST	14:00 CST	15:00 CST	16:00 CST
a1	5.1	4.7	4.7	4.7	4.7	4.9	5.3
a2	5.0	4.8	4.8	4.9	5.0	4.8	5.0
a3	4.5	4.4	4.7	5.0	5.2	5.1	5.1
a4	4.7	4.4	4.8	5.1	5.4	5.5	5.4
a5	4.1	3.7	3.7	4.1	4.9	5.2	5.3

Table 6-5. CAMx hourly surface layer wind speeds (m/s) at the receptor sites for Plume B from 10:00-16:00 CST on September 6th, 2000.

Receptor Site	10:00 CST	11:00 CST	12:00 CST	13:00 CST	14:00 CST	15:00 CST	16:00 CST
b1	4.8	4.7	4.6	4.8	4.9	5.3	5.8
b2	4.7	4.6	4.4	4.4	4.6	4.9	5.8
b3	4.4	4.2	4.0	3.9	4.0	4.5	5.0
b4	4.4	4.2	4.1	4.1	4.2	4.8	5.3
b5	4.4	4.2	4.2	4.2	4.4	5.1	5.9

Wind speeds remain nearly constant with only slight increases from 14:00-16:00 CST, and these results do not seem to adequately explain the observed shift in the predominant ozone production rates from vertical transport to horizontal transport experienced at many receptor locations. Increases or decreases in advection may also be due to the relative x and y directional components of the wind velocity terms. For example, the negative horizontal advection values observed at sites b3 and b4 are likely due to a change in wind direction for those hours.

A similar analysis was performed to explain the fluctuations in ozone production rates due to vertical transport. Hourly ozone production rates by vertical diffusion and losses by vertical advection for all receptor sites in Plume A and Plume B are illustrated in Figure 6-19 and Figure 6-20, respectively. The results for both plumes show an increase in vertical diffusion rates that reach maximum values at 14:00-15:00 CST.

Vertical advection depletion rates for Plume A increase in magnitude hourly, with the exception of receptor location a1 which reaches a maximum depletion rate at 15:00 CST. Vertical advection rates at receptor sites for Plume B show significant variation. For receptor sites b1, b2, and b5 hourly loss rates increase in magnitude until about 13:00 CST, followed by hourly decreases in magnitude. Receptor sites b3 and b4, however, experience ozone production gains by vertical advection for every hour, with a maximum production rate at 12:00 CST and a minimum at 14:00-15:00 CST.

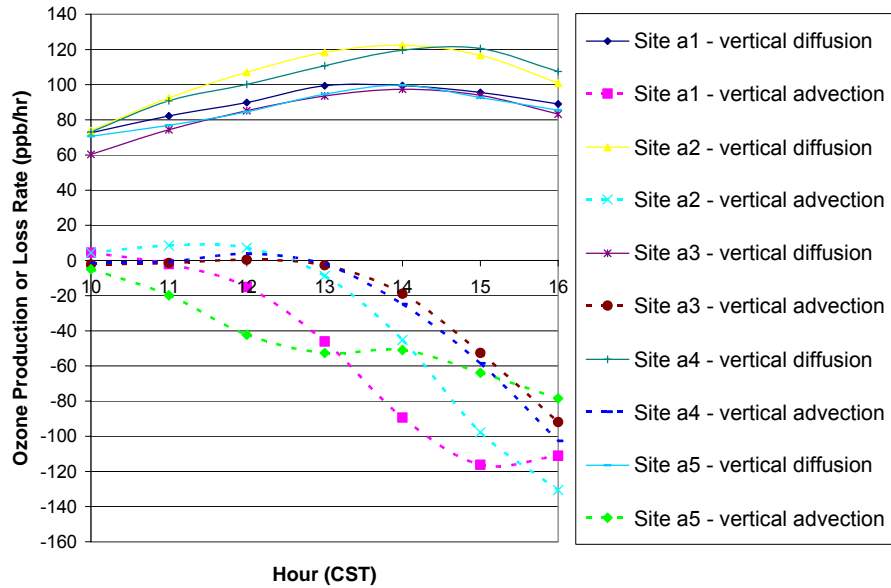


Figure 6-19. CAMx PA hourly ozone production rates from 10:00-16:00 CST by vertical diffusion (solid curves) and losses by vertical advection (dashed curves) for all receptor sites in Plume A, in ppb/hr.

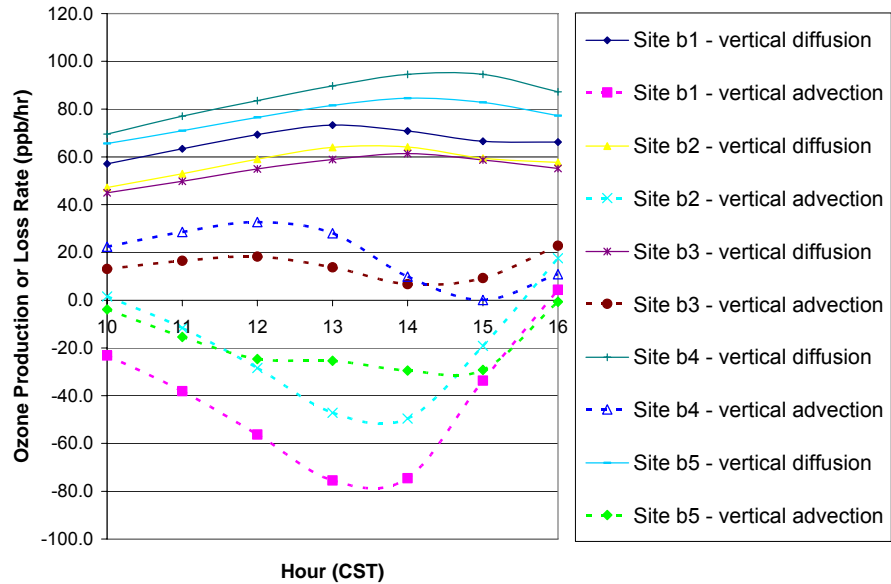
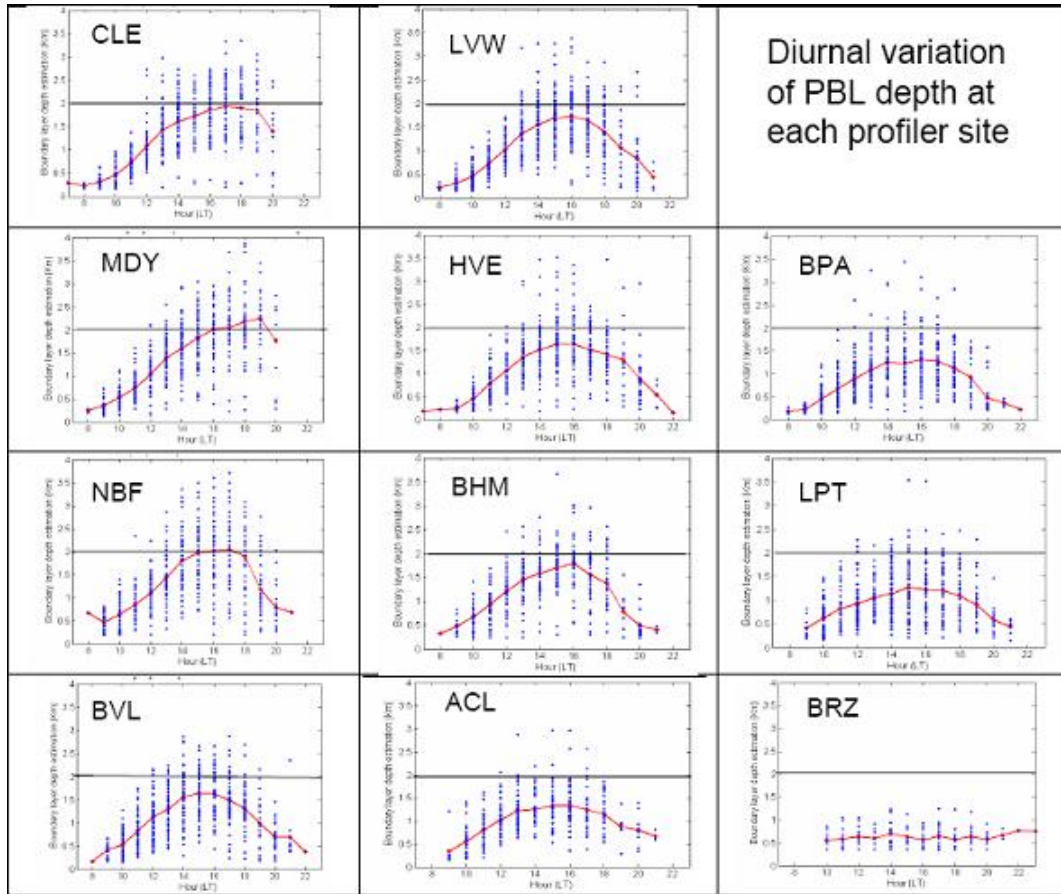


Figure 6-20. CAMx PA hourly ozone production rates from 10:00-16:00 CST by vertical diffusion (solid curves) and losses by vertical advection (dashed curves) for all receptor sites in Plume B, in ppb/hr.

The results for vertical advection losses for Plume A may be related to the diurnal pattern of the planetary boundary layer (PBL) at locations near the “a” receptor sites. The

results for wind profilers located in various geographic regions of Texas for an analysis that was performed as part of the TexAQS II campaign in 2006 (as shown in Chapter 5) is shown in Figure 6-21, and their locations are shown in Figure 6-22.



Wind Profiler Sites

Cleburne (CLE) Longview (LVE) Moody (MDY) Huntsville (HVE) Beaumont-Port Arthur (BPA)
 New Braunfels (NBF) Brenham (BHM) LaPorte (LPT) Beeville (BVL) Arcola (ACL) Brazos (BRZ)

Figure 6-21. Radar profiler summaries of planetary boundary layer diurnal patterns during TexAQS II (Wilczak et al., 2007).

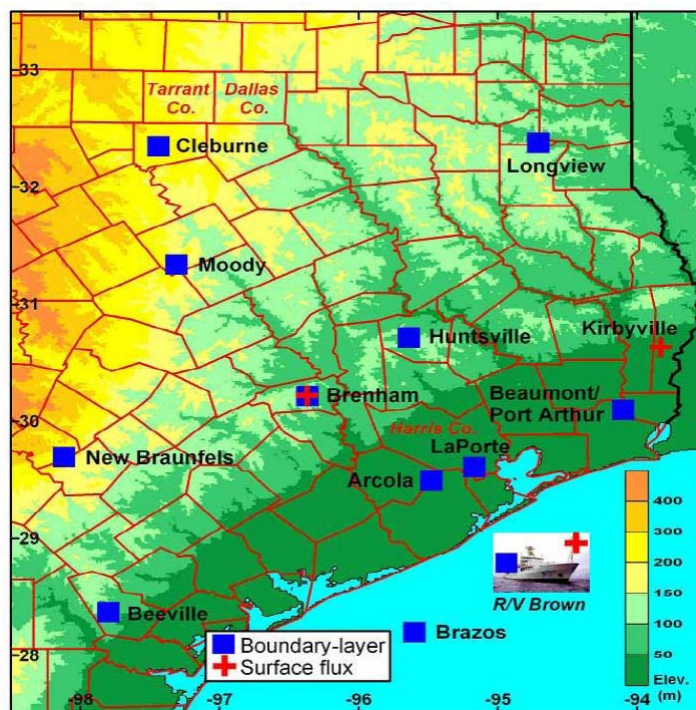


Figure 6-22. Geographical locations of radar profilers used in the TexAQS II analysis of diurnal patterns of average PBL heights (Wilczak et al., 2007).

Figure 6-21 illustrates that the mixing height can vary significantly depending on location. A likely indication of the vertical development of the PBL height is the vertical transport of pollutants that have been trapped in lower atmospheric layers. For the wind profilers closer to the receptor locations in this study, such as Beeville (BVL), Arcola (ACL), and LaPorte (LPT), the PBL height increases hourly until a maximum is reached at around 15:00-16:00 CST. This diurnal pattern correlates well with the hourly increases in vertical advection losses experienced at the receptor sites for Plume A.

The receptor sites for Plume B are located closer to the coast than those for Plume A. As Figure 6-21 illustrates, wind profilers located closer to the coast, such as LaPorte (LPT) and Arcola (ACL), experience a maximum PBL height earlier in the day than profilers located further inland. This may explain why the maximum losses due to vertical advection are experienced at earlier hours for receptor sites b1, b2, and b5 in relation to receptor sites for Plume A.

6.8 SOURCE APPORTIONMENT RESULTS AND DISCUSSION

For Plume A and Plume B, the contributions of each of the source regions to ozone concentrations at the ten receptor sites (a1-a5 and b1-b5) were estimated using the photochemical modeling source apportionment tools described in Section 6.5. Tables 6-6 through 6-9 summarize the results for the OSAT and APCA source apportionment analyses for the plumes observed on September 6th, 2000. The results in these tables represent the total ozone (combined NO_x and VOC biogenic and anthropogenic contributions) that each source region contributes to each receptor site as predicted by CAMx at 13:00 CST. Additionally, relative source contributions are ranked for each receptor site.

Table 6-6. OSAT ozone contributions to Plume A for 13:00 CST on September 6th, 2000. All contributions are in ppb of ozone. Relative source rankings are also listed next to each value in parenthesis.

Receptor Site	Source 1	Source 2	Source 3	Source 4	Source 5	Source 6	Source 7	Source 8	Boundary Conditions
a1	8.40 (3)	0.03 (7)	0.01 (8)	0.00 (9)	7.57 (4)	7.20 (5)	0.51 (6)	78.75 (1)	37.05 (2)
a2	8.51 (3)	0.14 (7)	0.05 (8)	0.04 (9)	6.49 (6)	6.50 (5)	6.79 (4)	73.51 (1)	36.23 (2)
a3	7.02 (4)	0.36 (7)	0.15 (9)	0.21 (8)	5.01 (6)	5.71 (5)	9.28 (3)	71.93 (1)	35.47 (2)
a4	6.77 (4)	0.22 (7)	0.09 (9)	0.14 (8)	5.81 (6)	6.21 (5)	11.09 (3)	73.81 (1)	35.18 (2)
a5	4.46 (4)	1.00 (7)	0.39 (9)	0.56 (8)	3.04 (6)	3.30 (5)	7.83 (3)	68.58 (1)	31.54 (2)

Table 6-7. APCA ozone contributions to Plume A for 13:00 CST on September 6th, 2000. All contributions are in ppb of ozone. Relative source rankings are also listed next to each value in parenthesis.

Receptor Site	Source 1	Source 2	Source 3	Source 4	Source 5	Source 6	Source 7	Source 8	Boundary Conditions
a1	18.10 (3)	0.04 (7)	0.01 (8)	0.00 (9)	13.87 (4)	5.69 (5)	0.39 (6)	64.08 (1)	37.34 (2)
a2	16.55 (3)	0.17 (7)	0.04 (8)	0.03 (9)	10.38 (4)	5.03 (6)	7.41 (5)	62.11 (1)	36.53 (2)
a3	13.56 (3)	0.47 (7)	0.12 (9)	0.17 (8)	8.55 (5)	4.30 (6)	12.41 (4)	59.78 (1)	35.78 (2)
a4	13.68 (4)	0.31 (7)	0.07 (9)	0.10 (8)	10.89 (5)	5.26 (6)	14.37 (3)	59.13 (1)	35.50 (2)
a5	8.88 (4)	1.56 (7)	0.33 (9)	0.44 (8)	5.41 (5)	2.69 (6)	10.78 (3)	58.77 (1)	31.84 (2)

Table 6-8. OSAT ozone contributions to Plume B for 13:00 CST on September 6th, 2000. All contributions are in ppb of ozone. Relative source rankings are also listed next to each value in parenthesis.

Receptor Site	Source 1	Source 2	Source 3	Source 4	Source 5	Source 6	Source 7	Source 8	Boundary Conditions
b1	0.09 (6)	6.56 (3)	2.87 (4)	2.79 (5)	0.01 (7)	0.00	0.00	69.07 (1)	34.95 (2)
b2	0.25 (6)	6.83 (3)	2.54 (5)	3.11 (4)	0.06 (7)	0.01 (8)	0.00 (9)	69.28 (1)	34.20 (2)
b3	0.29 (6)	5.85 (3)	2.04 (5)	2.72 (4)	0.09 (7)	0.04 (8)	0.02 (9)	70.95 (1)	32.83 (2)
b4	0.18 (6)	4.81 (3)	1.61 (5)	2.21 (4)	0.06 (7)	0.03 (8)	0.02 (9)	72.20 (1)	31.36 (2)
b5	0.15 (6)	3.97 (3)	1.22 (5)	1.78 (4)	0.05 (7)	0.03 (8)	0.03 (9)	69.69 (1)	29.42 (2)

Table 6-9. APCA ozone contributions to Plume B for 13:00 CST on September 6th, 2000. All contributions are in ppb of ozone. Relative source rankings are also listed next to each value in parenthesis.

Receptor Site	Source 1	Source 2	Source 3	Source 4	Source 5	Source 6	Source 7	Source 8	Boundary Conditions
b1	0.09 (6)	7.99 (3)	2.13 (5)	2.83 (4)	0.00	0.00	0.00	66.76 (1)	35.08 (2)
b2	0.22 (6)	8.93 (3)	2.07 (5)	3.20 (4)	0.03 (6)	0.00	0.00	67.84 (1)	34.51 (2)
b3	0.46 (6)	8.22 (3)	1.71 (5)	2.72 (4)	0.09 (7)	0.03 (8)	0.02 (9)	68.43 (1)	33.14 (2)
b4	0.24 (6)	6.59 (3)	1.20 (5)	1.94 (4)	0.05 (7)	0.02 (8)	0.01 (9)	69.07 (1)	31.48 (2)
b5	0.09 (6)	3.79 (3)	0.59 (5)	0.97 (4)	0.02 (7)	0.01	0.01	62.65 (1)	29.98 (2)

For both plumes, the largest ozone contributions to all of the receptor regions comes from Source 8, which is the area of the 4-km grid that was not encompassed by Sources 1-7. For the Ship Channel plume (Plume A), APCA predicted that 45.2% of the total ozone was contributed by Source 8, averaged over all receptor regions. OSAT predicted this average percentage as 54.5%. For the Texas City plume (Plume B), APCA predicted that 60.4% of the total ozone was contributed by Source 8, averaged over all receptor regions. OSAT predicted this averaged percentage as 62.2%. The second largest contribution comes from the CAMx boundary conditions, or sources that lie beyond the 4-km grid domain, which are representative of the continental ozone background levels. For Plume A, APCA predicted that 26.3% of the total ozone was contributed by boundary conditions, averaged over all receptor regions. OSAT predicted this average percentage as 26.1%. For the Plume B, APCA predicted that 29.3% of the total ozone was contributed by boundary conditions, averaged over all receptor regions. OSAT predicted this average percentage as 29.6%.

On average, the third largest contributions to the receptor regions for the Plume A come from Source 1, which includes the majority of industrial sources in the Houston Ship Channel region, followed by Sources 5, 6, and 7 (not necessarily in this order), which are downwind of Source 1 and include anthropogenic NO_x sources in the Houston urban region. APCA predicted that 10.4%, 7.2%, 3.4%, and 6.8% of the total ozone was contributed by Source 1, 5, 6, and 7, respectively, averaged over all receptor regions. OSAT predicted these averaged percentages as 5.2%, 4.1%, 4.3% and 5.3%, respectively. APCA attributes larger contributions to Sources 1, 5, and 7 in comparison to OSAT, likely because these source regions are also characterized by relatively large anthropogenic NO_x emissions, which is weighed more heavily by the APCA method.

Additionally, for receptor sites farther downwind from the Ship Channel (a3, a4, and a5), OSAT predicts that Source 7 ranks as the third largest contributor to ozone concentrations. APCA predicts a similar ranking for Source 7 with receptor sites a4 and a5. Source 7 does not rank highest in emissions from these sources; therefore, this may indicate that the proximity of a receptor site to the source region in the Houston Ship Channel area may take precedence over levels of emissions, depending on meteorological conditions.

On average, the third largest contributions to the receptor regions for Plume B come from Source 2, which includes the majority of industrial sources within the immediate Texas City region, followed by Sources 4 and 3, which are located downwind of Source 2. APCA predicted that 6.3%, 1.4%, and 2.1% of the total ozone was contributed by Sources 2, 3, and 4, respectively, averaged over all receptor regions. OSAT predicted these average percentages as 4.6%, 1.6%, and 2.1%, respectively.

Figures 6-23 and 6-24 below illustrate the primary difference between APCA and OSAT predicted ozone contributions, which is that APCA attributes more ozone production to anthropogenic NO_x in comparison to the OSAT results. This is a fundamental difference between the APCA and OSAT methods that was discussed in detail in Chapter 2. Results are shown for Plume A at 13:00 CST on September 6th, 2000 for the first receptor site a1, though the distributions are relevant to the other receptor sites. Additionally, the figures illustrate the previously discussed result that is

characteristic for all other receptor sites: Source 8 was predicted to be the primary contributor to ozone concentrations by both OSAT and APCA methods.

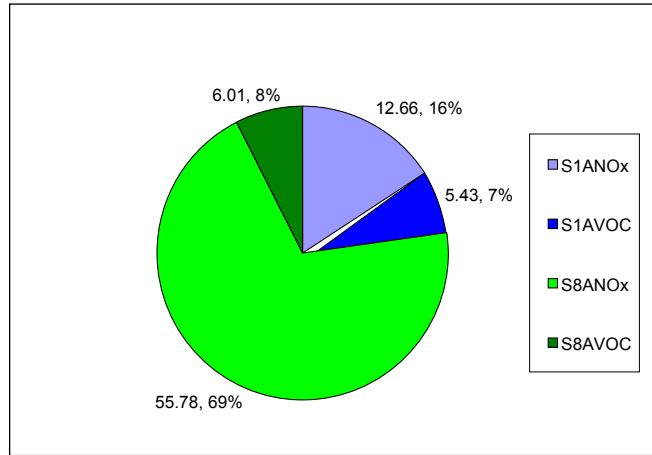


Figure 6-23. APCA contributions (in ppb and percentage) from anthropogenic NO_x and VOC for Sources 1 and 8. Results are shown for receptor site a1 at 13:00 CST on September 6th, 2000.

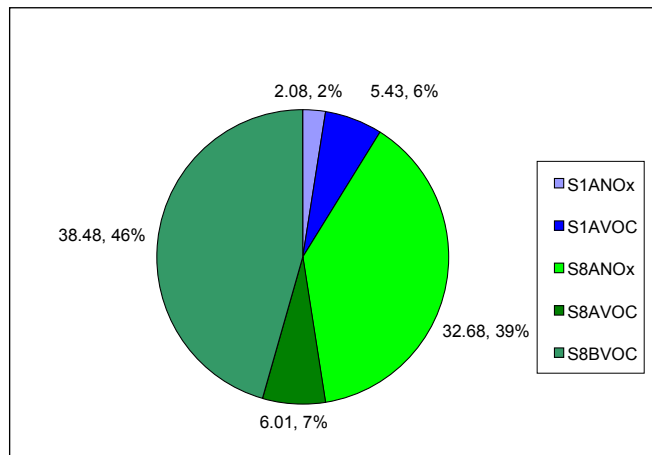


Figure 6-24. OSAT contributions (in ppb and percentage) from anthropogenic NO_x and VOC, and biogenic VOC, for Sources 1 and 8. Results are shown for receptor site a1 at 13:00 CST on September 6th, 2000.

Because Sources 1 and 2 included the Ship Channel and Texas City primary industrial emissions regions, respectively, the contributions of these sources were examined in further detail. Figure 6-25 shows the biogenic and anthropogenic NO_x and

VOC contributions from Source 1 for all “a” receptor regions at 13:00 CST on September 6th, 2000. Contributions are shown in ppb of ozone for the APCA and OSAT methods.

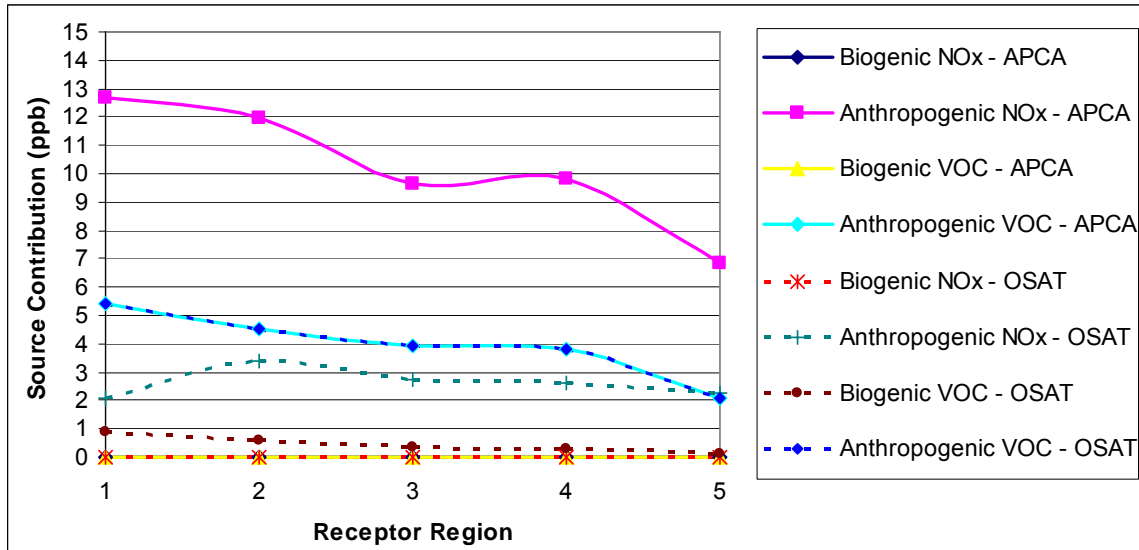


Figure 6-25. Plume A APCA and OSAT contributions in (ppb of ozone) from Source 1 (Ship Channel) for all “a” receptor regions. Results are shown for 13:00 CST on September 6th, 2000.

For Plume A, the largest contribution from Source 1 estimated by APCA is due to anthropogenic NO_x for all receptor sites. The APCA results show a gradual decrease in the contribution from anthropogenic NO_x as the locations of the receptor regions move farther downwind from the source. The contribution reaches a maximum of nearly 13 ppb at the receptor site nearest to the source, decreasing to a minimum contribution of approximately 7 ppb at the receptor site located farthest downwind from Source 1. The predicted APCA contributions from biogenic NO_x are relatively negligible, ranging between 0-1 ppb. The second largest contribution predicted by APCA is due to anthropogenic VOC, which also shows a gradual (although less significant) decrease as the receptor region locations increase in distance from the sources from a maximum of contribution of about 5.5 ppb to a minimum of about 2 ppb.

For all “a” receptor sites, the largest contribution from Source 1 estimated by OSAT is due to anthropogenic VOC, and the contributions for each receptor site are identical to the anthropogenic VOC contributions predicted by APCA. This result is

expected, as the difference between APCA and OSAT methods are related to the allocation of biogenic emissions. OSAT also predicts that anthropogenic NO_x and biogenic NO_x and VOC contributions remain relatively constant at about 2-3 ppb and 0-1 ppb for all receptor sites, respectively.

The anthropogenic NO_x contribution predicted by APCA is intuitively greater than the contributions predicted by OSAT. As previously mentioned, the APCA method characterizes biogenic emissions as uncontrollable, and it therefore attributes more ozone formation to anthropogenic sources relative to biogenic sources. It is also expected that anthropogenic contributions are dominant due to the industrial location of Source 1, which is characterized by the largest anthropogenic and biogenic emissions when compared to the other sources (excluding Source 8), as shown in Table 6-1.

Similar results for Source 2 (the Texas City industrial region) are shown in Figure 6-26. APCA results are similar to those for Plume A, although anthropogenic NO_x contributions are lower and range from about 8.5 ppb to 6 ppb, with the maximum contribution occurring at the second receptor site. This is likely due to lower anthropogenic NO_x emissions in the Texas City region in comparison to the Ship Channel region, as shown in Table 6-1. The predicted APCA contributions for biogenic NO_x and all VOC remain relatively negligible, ranging between 0-1 ppb. Additionally, consistent with the results for Plume A, the anthropogenic VOC contributions predicted by APCA and OSAT are identical for the Texas City region.

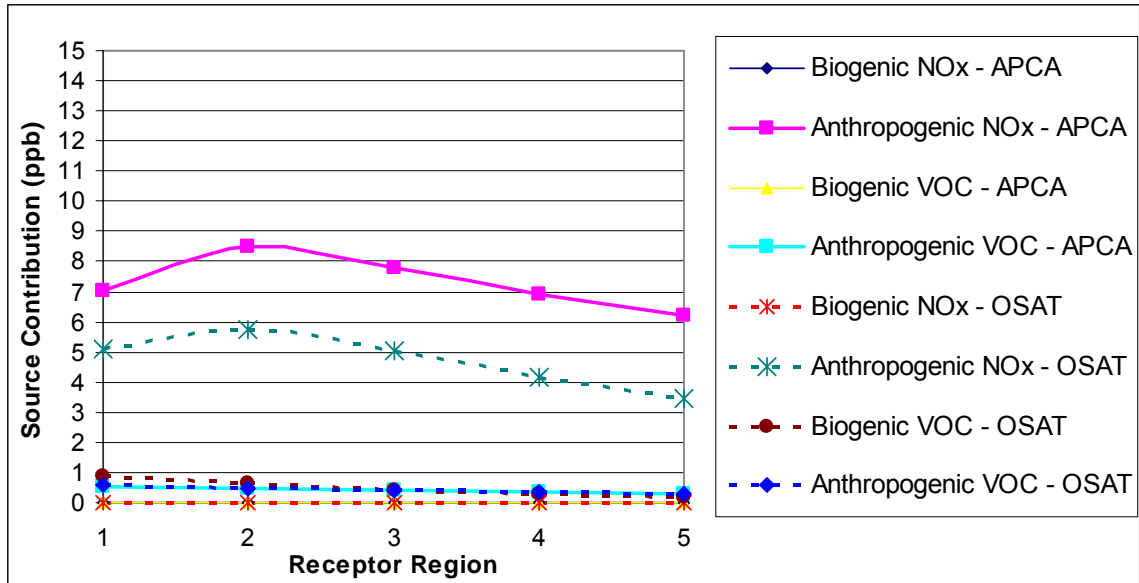


Figure 6-26. Plume B APCA and OSAT contributions in (ppb of ozone) from Source 2 (Texas City) for all “b” receptor regions. Results are shown for 13:00 CST on September 6th, 2000.

OSAT estimates lower contributions due to anthropogenic VOC in comparison to results for Plume A (less than 1 ppb for all receptor sites). Similar to the APCA results, these lower contribution OSAT estimates for the Texas City source region are likely due to the lower anthropogenic VOC emission levels in this area in comparison to emissions in the Ship Channel area. However, OSAT estimates higher anthropogenic NO_x contributions in comparison to results for Plume A, ranging from about 3.5 ppb to 5.8 ppb. This was somewhat unexpected due to the comparatively lower emissions of anthropogenic NO_x in the Texas City region (refer to Table 6-1). However, as mentioned in Section 6.5, it is the source contribution to ozone formation activity of the NO_x and VOC emissions en-route to a receptor that is important. Furthermore, the anthropogenic VOC to NO_x ratio for this region differs from the Ship Channel, which also has an impact on ozone formation (discussed in Chapter 2).

6.9 CONCLUSIONS

In this work, OSAT, APCA, and PA tools were implemented in CAMx to characterize, in great detail, two distinct plumes originating from the Houston Ship Channel and Texas City industrial areas on September 6th, 2000, which were then transported over urban and rural regions with varying levels of anthropogenic and biogenic emissions. The results reveal several interesting phenomena. The predicted CAMx total ozone concentrations were generally in good agreement with aircraft LIDAR observations collected on that day. It was initially expected that ozone concentrations would decrease at receptor sites located at successive distances downwind from the source regions. However, vertically integrated modeled and measured ozone concentrations indicated roughly no decay in the total amount of ozone transported over distances of over 100 km over the course of one day.

Results from photochemical modeling at the surface layer did show decay in concentrations downwind of the source regions. CAMx PA results reveal that this difference is due to vertical mixing, surface losses, and production of ozone aloft. While the ozone production and consumption rates change at each receptor site downwind from the sources, the ratio of the ozone production to consumption rates in each plume remains relatively constant. Deposition losses at the surface are balanced by horizontal and vertical transport, and to a lesser extent, by chemical production. While the photochemical modeling portion of this work was focused on comparisons at the surface layer, results indicate vertical mixing from a regional ozone reservoir aloft can be a dominant process contributing to ozone formation and depletion in plumes originating in Houston. Source apportionment analyses indicate that contributions from surface sources decay as the plume advects downwind, suggesting that ozone stored aloft is a predominant contributor to regional transport.

6.10 REFERENCES

- Allen, D., and J. Olaguer (2004), “State of the Science of Air Quality in Eastern Texas: Major Scientific Findings and Recommendations”, Report for the Texas Environmental Research Consortium, July 31, 2004, available at <http://files.harc.edu/Projects/AirQuality/Projects/H030.2004/H30FinalReport.pdf>.
- Draxler, R.R. and G.D. Rolph (2003), HYSPLIT (HYbrid Single-Particle Lagrangian Integrated Trajectory), NOAA Air Resources Laboratory, Silver Spring, MD, Model access via the NOAA ARL READY website, available at <http://www.arl.noaa.gov/ready/hysplit4.html>, accessed March 2010.
- ENVIRON International Corporation (2004), User’s Guide – Comprehensive Air Quality Model with extensions (CAMx), Version 4.00, Novato, CA, available at <http://www.camx.com>.
- McDonald-Buller, E.C., A.A. Eusebi, Y. Kimura, M.M. Russell, and D.T. Allen (2000), “Impacts of Regional Control Strategies on Air Quality in Eastern and Central Texas: Zeroing Out Emissions in Each of the Non-Attainment and Near Non-Attainment Regions”, Report submitted to the Texas Natural Resource Conservation Commission, January 2000.
- McGaughey G., C. Durrenberger, E.C. McDonald-Buller, and D.T. Allen (2005), “Assessing the Performance of the CAMx Photochemical Model: A Qualitative Comparison of Observed and Simulated Ozone Plumes on September 6, 2000 within the 4-km HGA Grid Domain”, Report prepared for the City of Victoria, The University of Texas at Austin Center for Energy and Environmental Resources, Austin, TX, April 2005.
- Senff, C., et al. (2007), “Ozone Production and Flux Downwind of Houston and Dallas”, Presentation given at the TexAQS II Principal Findings Data Analysis Workshop, Austin, TX, May 2007, available at http://www.tceq.state.tx.us/assets/public/implementation/air/texaqs/workshop/20070529/2007.05.30/Afternoon-1/1-O3_Production+Flux_Downwind-Senff.pdf.
- Texas Commission on Environmental Quality website reference for Figure 6-3, available at http://www.tceq.state.tx.us/implementation/air/airmod/data/hgb1_camx_domain.html#layer, accessed February 2008.

Texas Commission on Environmental Quality (2009), “Houston-Galveston-Brazoria Nonattainment Area Ozone Conceptual Model”, Draft report prepared by the TCEQ Data Analysis Team, May 2009, available at http://www.tceq.state.tx.us/assets/public/implementation/air/am/modeling/hgb8h2/doc/HGB8H2_Conceptual_Model_20090519.pdf.

The University of Texas at Austin (2004), “Development of an Ozone Conceptual Model for Victoria”, Report prepared by The University of Texas at Austin Center for Energy and Environmental Resources, Austin, TX, June 2004.

Webb, A.M., C. Durrenberger, E.C. McDonald-Buller, and D.T. Allen (2002), “Texas Non-Attainment and Near Non-Attainment Zero-Out Modeling Runs for the July 7-12, 1995 episode”, Report submitted to the Capital Area Planning Council and the Texas Natural Resource Conservation Commission, August 2002.

Wilczak J., I. Djalalova, S. McKeen, and L. Bianco (2007), “Evaluation of NMM-CMAQ and WRF-Chem during High Ozone Episodes in TexAQS-II”, Presentation given at the TexAQS II Principal Findings Data Analysis Workshop, Austin, TX, May 2007, available at <http://www.tceq.state.tx.us/assets/public/implementation/air/texaqs/workshop/20070529/2007.05.31/Afternoon/2-NMM-CMAQ+WRF-Chem-Wilczak.pdf>.

Chapter 7: Recommendations for Future Work

7.1 INTRODUCTION

Despite the generally recognized importance of regional transport in contributing to urban air pollution, there have been very few large scale air quality studies that have rigorously tested photochemical models that characterize regional air pollutant transport. The recent Texas Air Quality Study performed in 2006 (TexAQS II) was specifically designed to collect data to assess regional transport of air pollutants. Part of this effort involved the establishment of a network of pollutant monitoring sites in the rural areas of East Texas, where an absence of surface monitoring data previously existed. The observational data available through the Texas Air Quality Studies provided a unique opportunity to develop, evaluate, and improve methods for characterizing regional air pollutant transport.

The primary objectives of this dissertation include the development and evaluation of methods that incorporate modeling and ambient measurements in an integrated, systematic approach to characterize regional ozone transport. To date, most analyses of regional transport have focused only on short duration episodes, or semi-quantitative assessments. The work presented in this dissertation includes the first detailed quantitative assessment of regional ozone transport over the course of an entire ozone season, based on photochemical modeling calculations and observational data.

Collectively, the results presented in this dissertation provide strong evidence that provisions for regional transport in air quality planning are critical to maintain areas in accordance with the NAAQS. In contrast to the increasingly regional nature of air pollution and non-attainment regions, air quality planning and implementation of emission control programs have historically focused on metropolitan areas, and integrated regional and local strategies have only recently become a focal point. The methodologies described in this dissertation are significantly relevant to policy implications and will continue to be relevant in formulating effective air quality strategies that consider the potential effects of regional transport.

This Chapter summarizes key findings and recommendations, organized by topics discussed in previous chapters.

7.2 FUTURE WORK RECOMMENDATIONS FOR THE USE OF AMBIENT DATA AND PHOTOCHEMICAL MODELING TO CHARACTERIZE REGIONAL OZONE CONCENTRATIONS

A major conclusion from Chapter 4 was that rural oil and gas emissions in Northeast Texas may be significantly underestimated, and that these rural emissions may lead to substantial ozone formation and transport into urban areas. Comparisons of measurements from rural surface monitors in Northeast Texas to results from photochemical modeling indicated a significant discrepancy between modeled and observed night-time rural ozone concentrations. Emissions inventories for Northeast Texas have undergone significant revisions to integrate recent measurements that reflect increases in previously under-estimated NO_x from oil and gas production activities, as well as decreases in emissions due to implementations of regional regulatory controls. As discussed in Chapter 4, the effects of these updated inventories on modeled ozone concentrations in Northeast Texas have shown enhancements in model performance, though mostly pertaining to peak daytime ozone levels. An examination of these effects on modeled night-time ozone concentrations in rural Northeast Texas is recommended for future studies.

7.3 FUTURE WORK RECOMMENDATIONS FOR THE USE OF SURFACE MONITORS AND PHOTOCHEMICAL MODELING TO CHARACTERIZE POLLUTANT TRANSPORT IN PLUMES

The key finding from Chapter 5 was that for the limited number of airborne LIDAR measurements available, the surface monitoring network and the photochemical model provided consistent estimates of the magnitude of ozone transport. While the days examined in Chapter 5 indicated a surprising consistency of ozone transport in plumes, these days were selected for measurements because they were characterized by relatively high ozone concentrations. The zero-out analyses performed on a seasonal basis in

Chapter 3 suggested that magnitudes of regional transport in East Texas can vary, depending on meteorological conditions. However, while significant reductions in Houston emissions have been achieved over the last decade, results from 2002 and 2006 indicated that significantly large impacts to ozone levels in East Texas due to anthropogenic emissions in Houston were frequently predicted during both seasonal periods. In light of these results, future studies implementing the surface monitoring network and photochemical models to assess ozone transport in urban plumes on a seasonal basis is recommended.

Specifically, the average ozone flux emitted from Houston as predicted by aircraft LIDAR measurements is sufficient to produce a 4 ppb increase in ozone over an area encompassing DFW, which is comparable with the seasonal average contributions predicted by the CAMx zero-out analyses. While these average values are consistent, future work is recommended to further compare the results from Chapter 3 to magnitudes of ozone transport using measurements from the 2006 ozone season, when TexAQS II rural monitoring stations were operational. Results should be compared to estimates from aircraft LIDAR measurements when available. The TCEQ has also developed modeling simulations for additional days from May-August in 2005 and May-September in 2006, and these days should be included in future assessments.

Results from Chapter 3 are consistent with previous findings that elevated ozone concentrations in East Texas can be a combined result of emissions originating from multiple sources, depending on meteorology. Additional quantitative statistical analyses investigating the relationships between large modeled impacts from Houston to ozone levels in East Texas and predominant meteorological factors is recommended for future work. Such studies may provide more substantive evidence of the probability and frequency of large regional contributions from Houston emissions on an extensive seasonal basis. When TexAQS II rural monitoring stations were operational, further verification of modeling results should be done by comparing large predicted enhancements in ozone levels in East Texas regions to ambient background ozone levels as measured by rural upwind surface monitors. Furthermore, results should be compared

for simulations that span ozone seasons during several years to examine year-to-year variability, along with the effects of emissions reductions in Houston.

In Chapter 5, vertically averaged ozone concentrations and wind speeds predicted by CAMx were matched in time and space with aircraft LIDAR observations along a plume transect on September 6th, 2000. These CAMx predictions were used to calculate the total horizontal ozone flux by integrating the excess plume ozone (according to Equation 5.1), and results showed good agreement with similar computations performed with LIDAR observations. These ozone flux calculations should be repeated with photochemical modeling data for the days in 2006 with available airborne LIDAR measurements, and results should be compared to ozone flux computed with data from surface monitors on these days.

The major topic addressed in Chapter 6 was the detailed modeling of an urban plume for which aircraft data were available, and results indicated a combination of processes that influenced ozone concentrations within this plume. While dilution of precursor emissions due to vertical mixing and/or depletion of ozone formed within plumes originating in Houston may occur to some extent, the work in Chapter 3 demonstrated that the plumes are capable of transporting significant amounts of ozone and precursors over large distances, spanning a period of several consecutive days. For the case study on September 6th, 2000, vertically-integrated modeled and measured results indicated essentially no decay in the total amount of ozone transported across distances of over 100 km on that day. Process Analysis (PA) results suggested that this was due to chemical formation of ozone within the plume occurring at nearly the same rates as deposition losses.

The analyses described in Chapter 6 should be repeated for selected urban plumes that encounter significantly different types of photochemical conditions, with a focus on examining the effects of variations in downwind land coverage and emissions sources to ozone losses and chemical production rates. The goal of this future work will be to explain differences observed in the behavior of major categories of urban plumes identified in the seasonal characterizations described in Chapter 3. More specifically, in-depth analyses of processes within a plume originating in Houston that is capable of

significantly impacting ozone levels in Austin and Dallas over the course of several days, such as the case study on August 18th-19th, 2006, would be of interest for future work.

Expanding on this, the PA method in Chapter 6 was applied in the conventional Eulerian framework of CAMx, which incorporates a “box-model” within the modeling domain. A limitation of this method is the inability to track temporal chemical evolution within a moving plume. A Lagrangian PA tool has recently been developed that allows for calculations to be performed on a moving air mass, which is a more accurate representation of actual conditions. Future studies examining ozone formation and depletion within urban plumes should incorporate this Lagrangian approach.

7.4 FUTURE WORK RECOMMENDATIONS FOR RECONCILING MODELING APPROACHES FOR APPORTIONING REGIONAL SOURCES WITH AMBIENT DATA

Another topic of Chapter 6 was the evaluation of source apportionment methods as applied to urban plumes. In addition to ozone formation and depletion, the spatial extent of contributions from various emissions sources within plumes originating in Houston, under various meteorological and photochemical conditions, should also be examined. Analyses involving photochemical modeling source apportionment tools should be performed for additional case studies in which airborne monitoring data is available, with the goal of complementing the modeling work that was performed to understand the physical and chemical processes occurring within the plumes.

The work in Chapter 3 identified an extensive number of days characterized by various indications of regional ozone transport resulting from Houston emissions. The source apportionment techniques implemented in Chapter 6 should be applied to these days with the goal of identifying the relative importance of emissions sources within the Houston area throughout a seasonal period. Future work is also recommended to determine the potential impacts of incremental reductions in local Houston emissions, including projected future emissions, to regional ozone levels in East Texas.

7.5 REFERENCES

Senff, C., et al. (2007), “Ozone Production and Flux Downwind of Houston and Dallas”, Presentation given at the TexAQS II Principal Findings Data Analysis Workshop, Austin, TX, May 2007, available at http://www.tceq.state.tx.us/assets/public/implementation/air/texaqs/workshop/20070529/2007.05.30/Afternoon-1/1-O3_Production+Flux_Downwind-Senff.pdf.

Appendix A: Vertical Grid Structures for CAMx 2002 and 2006 Simulations

Table A-1. MM5 and CAMx vertical grid structures based on 28 sigma-p levels. Heights are in meters above ground level (agl) according to a standard atmosphere; pressure is in millibars (ENVIRON, 2006). This vertical grid structure was used for the modeling period of May 1st- September 30th, 2002, and results were discussed in Chapter 3.

Layer	sigma	pressure	height	thickness	CAMx Layers
28	0.0000	50.00	18874.41	1706.76	
27	0.0250	73.75	17167.65	1362.47	
----- CAMx Top -----					
26	0.0500	97.50	15805.17	2133.42	--20---
25	0.1000	145.00	13671.75	1664.35	--19---
24	0.1500	192.50	12007.40	1376.75	
23	0.2000	240.00	10630.65	1180.35	--18---
22	0.2500	287.50	9450.30	1036.79	
21	0.3000	335.00	8413.52	926.80	--17---
20	0.3500	382.50	7486.72	839.57	
19	0.4000	430.00	6647.15	768.53	
18	0.4500	477.50	5878.62	709.45	--16---
17	0.5000	525.00	5169.17	659.47	
16	0.5500	572.50	4509.70	616.58	
15	0.6000	620.00	3893.12	579.34	--15---
14	0.6500	667.50	3313.78	546.67	--14---
13	0.7000	715.00	2767.11	517.77	--13---
12	0.7500	762.50	2249.35	491.99	--12---
11	0.8000	810.00	1757.36	376.81	--11---
10	0.8400	848.00	1380.55	273.60	--10---
9	0.8700	876.50	1106.95	266.37	---9---
8	0.9000	905.00	840.58	259.54	---8---
7	0.9300	933.50	581.04	169.41	---7---
6	0.9500	952.50	411.63	166.65	---6---
5	0.9700	971.50	244.98	82.31	---5---
4	0.9800	981.00	162.67	65.38	---4---
3	0.9880	988.60	97.29	56.87	---3---
2	0.9950	995.25	40.43	20.23	---2---
1	0.9975	997.62	20.19	20.19	---1---
0	1.0000	1000.00	0.00	=====	Surface =====

Table A-2. MM5 and CAMx vertical grid structures. Heights are in meters above ground level (agl) according to a standard atmosphere (ENVIRON, 2006). This vertical grid structure was used for the modeling period of August 13th-September 15th, 2006, and results were discussed in Chapter 3.

MM5 Layer	Layer Top (m AGL)	East US and East Texas Domains			HGB/BPA and HG Domains		
		CAMx Layer	Center (m AGL)	Thickness (m)	CAMx Layer	Center (m AGL)	Thickness (m)
38	15179.1	17	12172.9	6012.5	28	13637.9	3082.5
36	12096.6				27	10631.6	2930.0
32	9166.6	16	7501.3	3330.7	26	8063.8	2205.7
29	6960.9				25	6398.4	1125.0
27	5835.9	15	4970.9	1730.0	24	5367.0	937.9
25	4898.0				23	4502.2	791.6
23	4106.4	14	3565.9	1080.0	22	3739.9	733.0
21	3373.5				21	3199.9	347.2
20	3026.3	13	2564.5	922.9	20	2858.3	335.9
19	2690.4				19	2528.3	324.3
18	2366.1				18	2234.7	262.8
17	2103.3	12	1728.1	749.8	17	1975.2	256.2
16	1847.2				16	1722.2	249.9
15	1597.3				15	1475.3	243.9
14	1353.4	11	1210.6	285.2	14	1281.6	143.6
13	1209.8				13	1139.0	141.6
12	1068.2	10	929.3	277.5	12	998.3	139.7
11	928.5				11	859.5	137.8
10	790.6	9	700.0	181.0	10	745.2	90.9
9	699.7				9	654.7	90.1
8	609.7	8	564.9	89.3	8	565.0	89.3
7	520.3	7	476.0	88.5	7	476.1	88.5
6	431.8	6	387.8	87.8	6	387.9	87.8
5	344.0	5	300.4	87.0	5	300.5	87.1
4	256.9	4	213.7	86.3	4	213.8	86.3
3	170.6	3	127.7	85.6	3	127.8	85.6
2	85.0	2	59.4	51.0	2	59.4	51.0
1	33.9	1	16.9	33.9	1	17.0	33.9

A.1 REFERENCES

ENVIRON International Corporation (2006), "Seasonal Model of Northeast Texas Ozone", Final report prepared for the East Texas Council of Governments, Novato, CA, September 2006.

Appendix B: Continued Analysis of Photochemical Modeling Results for May 1st - September 30th, 2002

This Appendix includes a continued analysis of the discussion in Section 3.2.1.

From a regulatory perspective, the NAAQS for ozone are based the fourth highest observed 8-hour ozone concentrations. Table B-1 below shows the fourth highest predicted 8-hour ozone concentrations for both the base case and the zero-out case. While the NAAQS criteria are based on the fourth highest day during a 1-year period (then averaged over 3 years), this analysis was performed to examine any effects of eliminating HGB anthropogenic emissions on the fourth highest 8-hour ozone concentrations for the 5-month period.

Table B-1. For each region, the fourth highest predicted 8-hour ozone concentrations are listed for May 1st-September 29th, 2002. These concentrations are ranked by CAMx output from the base case and zero-out case.

Region	Date	4th Highest CAMx Base Case Max O3 (ppb)	4th Highest CAMx Zero-Out Case Max O3 (ppb)	Ranked by
DFW	9/14/2002	107	105	Base Case
	6/24/2002	107	107	Zero-Out Case
Austin	9/12/2002	112	112	Base Case
	9/12/2002	112	112	Zero-Out Case
San Antonio	9/13/2002	98	98	Base Case
	7/8/2002	100	98	Zero-Out Case
Victoria	8/29/2002	77	75	Base Case
	8/30/2002	77	75	Zero-Out Case

For all regions, the fourth highest 8-hour ozone concentrations for these days did not decrease as a result of eliminating anthropogenic emissions from HGB, with one exception of a 2 ppb decrease on September 14th, 2002, for DFW. Based on the finding that predicted decreases in maximum ozone concentrations are not consistently related to zero-out contributions from HGB, it would be difficult to predict whether reductions in HGB anthropogenic emissions would have a significant impact on this value.

From these collective results, it is important to note that, while significant reductions in ozone concentrations may be achieved in other regions in Texas by

reducing anthropogenic emissions in HGB, there will be some days when other sources cause ozone levels to exceed the NAAQS. To further illustrate this finding, Figure B-1 shows the maximum differences in predicted 8-hour ozone concentrations between the base case and the zero-out case, as well as maximum ambient and modeled 8-hour ozone concentrations for DFW during the entire modeling period.

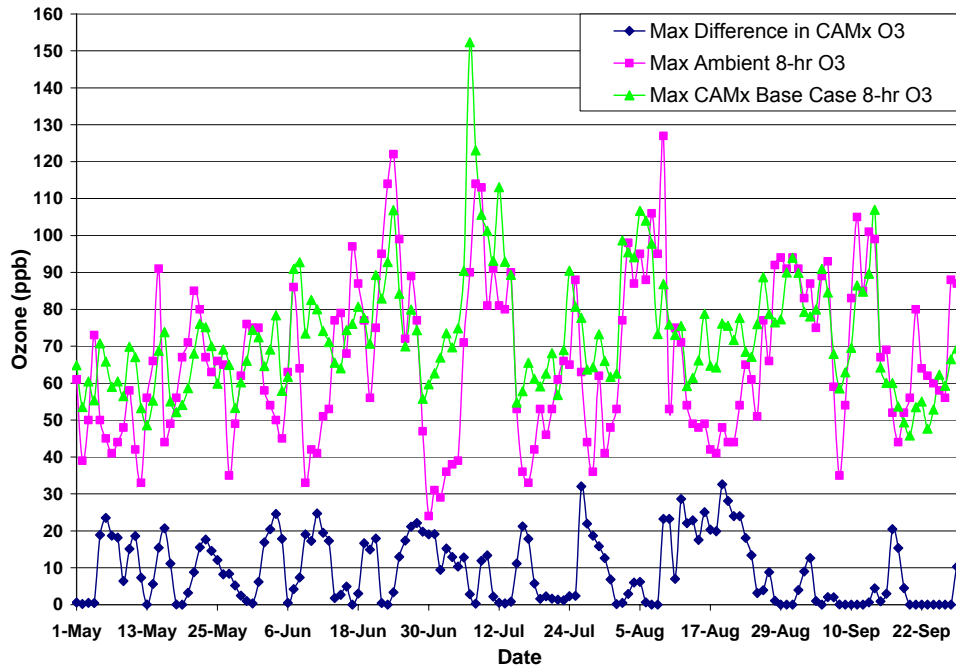


Figure B-1. Maximum ambient and modeled (base case) 8-hour ozone concentrations are shown for DFW for May 1st-September 29th, 2002. The maximum difference between modeled base case and zero-out case 8-hour ozone concentrations (as calculated by Equation 3.1) for DFW are also shown.

The figure shows that both modeled and observed elevated ozone concentrations in DFW do not always correspond to large predicted contributions from HGB emissions. For example, on June 23rd, 2002, the maximum ambient and CAMx base case 8-hour ozone concentrations in the DFW area were 114 ppb and 93 ppb, respectively; however, the modeling results indicate no difference in 8-hour ozone concentrations when anthropogenic emissions from HGB were eliminated. On the other hand, Figure B-1 also illustrates that there are days during this period that exhibit relatively low ozone levels in DFW and large predicted zero-out ozone contributions. On August 13th, the peak ambient

and CAMx base case 8-hour ozone concentrations in DFW were 54 ppb and 59 ppb, respectively, and the maximum zero-out difference in ozone concentrations was 22 ppb. These findings are not exclusive to DFW, as the results for all regions shown in Table 3-5 indicated that days with ambient 8-hour ozone concentrations above 70 ppb most frequently coincided with zero-out ozone differences in the lowest range of 0-5 ppb.

Figure B-1 shows large discrepancies in 8-hour maximum ozone values (as large as 62 ppb on July 7th) that frequently correspond to sharp increases or drops in ozone levels. Overpredictions of maximum ozone largely occur during periods characterized by relatively high contributions from the zero-out case. However, it is difficult to make substantial conclusions regarding model performance from these results because the ambient data and model predictions are not matched in time and space. It is also important to note that performance evaluations have shown that the model has adequate resolution for characterizing regional contributions to ozone but lacks the fine resolution necessary to accurately represent local ozone contributions (ENVIRON, 2006).

Significant inaccuracies of the model predictions are also associated with extreme maximum and minimum ozone concentrations. Therefore, predicted differences between the base case and zero-out maximum ozone, as well as comparisons between predicted and ambient 8-hour maximum ozone, may not be entirely accurate. The ambient maximum ozone values were generally not used as comparative measure of model performance, but rather as an applicable way to group the extensive dataset into categories that are relevant to regulatory standards. Additionally, significant findings of this work are not exclusive to these specific numerical outputs from CAMx, but rather also include the associated trends, frequency of occurrences, and potential regional impacts of HGB anthropogenic emissions on a seasonal basis.

As stated in previous chapters, background ozone concentrations can account for a significant fraction of total ozone concentrations. Figure 1-3 showed that, for the six years of surface monitoring data averaged in that study, the local contribution is the smaller component of the 8-hour peak ozone concentrations in DFW, contributing to less than one-third of the total observed ozone (Nielsen-Gammon et al., 2005). Wind direction may be interpreted as a qualitative indication of upwind sources contributing to

background ozone concentrations transported by bulk advection. For all receptor regions in this study, wind directions for three categories of days occurring throughout the seasonal period were examined:

1. Days with elevated ambient 8-hour peak ozone concentrations, but relatively low predicted differences in 8-hour ozone concentrations resulting from the zero-out scenario.
2. Days with low ambient 8-hour peak ozone concentrations, but relatively large predicted differences in 8-hour ozone concentrations resulting from the zero-out scenario.
3. Days with elevated ambient 8-hour peak ozone concentrations, and relatively large predicted differences in 8-hour ozone concentrations resulting from the zero-out scenario.

Similar to the ambient 8-hour ozone data, measurements of wind directions from surface monitors are available on the EPA AQS website. However, for the purposes of this work, wind directionality over larger scales and at various altitudes provide more accurate representations of winds associated with bulk advection. As a qualitative characterization of these prevailing winds, a meteorological modeling application was used to generate back trajectories of winds at various elevations. As discussed in Chapter 2, one tool that has been readily used for trajectory analyses is the HYbrid Single-Particle Lagrangian Integrated Trajectory (HYSPLIT) application based on archived meteorological wind data, capable of estimating trajectories either forward or backward in time. The back trajectory estimates represent the hypothetical path of an air parcel for a number of previous hours at various elevations. HYSPLIT 48-hour back trajectories were generated for the days and regions listed in Tables 3-6 through 3-13 for 22:00 UTC and an initial altitude of 500 meters above ground level (magl). An ensemble of trajectories from the same point of origin is shown, illustrating vertical variations in winds.

Four of the ten days shown in Table 3-6 for DFW were characterized by elevated ambient 8-hour ozone levels and no predicted impacts on 8-hour ozone concentrations from anthropogenic emissions in HGB, thus corresponding to the first category of days as

defined above. HYSPLIT back trajectories were qualitatively examined for these days, and an example is presented for August 7th, 2002. On this day, the observed peak 8-hour ozone concentration in DFW was 114 ppb. As shown in Figure B-2, predominant winds for DFW on this day are characterized by longer trajectories, or fetches, originating from the northeast and extending as far as the central/Midwestern U.S.

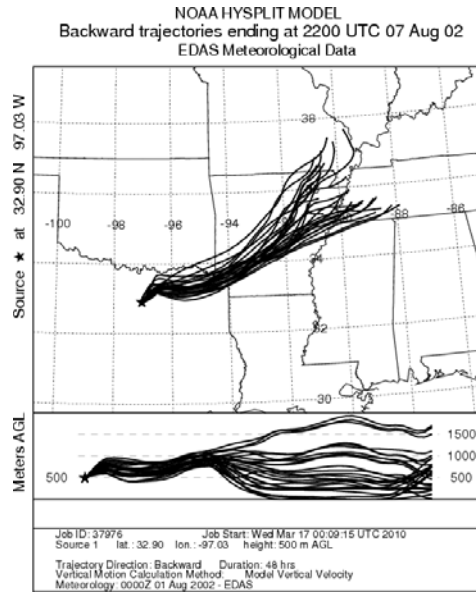


Figure B-2. HYSPLIT 48-hour back trajectories for winds arriving in DFW at 22:00 UTC and 500 magl for August 7th, 2002.

Table 3-10 showed, for DFW, the days characterized by large predicted impacts on 8-hour ozone concentrations from anthropogenic emissions in HGB. These days also experienced relatively low ambient 8-hour peak ozone concentrations, all below the NAAQS, thus corresponding to the second category of days as defined above. An example is presented for August 19th, 2002. On this day, the observed peak 8-hour ozone concentration in DFW was 48 ppb, and the maximum 8-hour ozone difference resulting from the zero-out method was 33 ppb. As shown in Figure B-3, predominant winds for DFW on this day are characterized by longer trajectories, or fetches, originating from the south/southeast over the Gulf of Mexico.

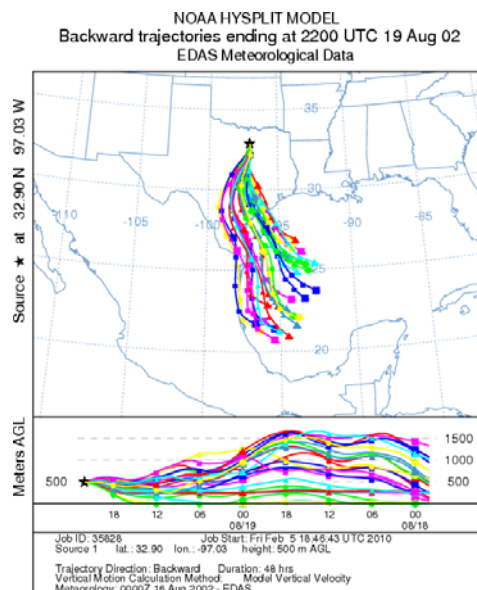


Figure B-3. HYSPLIT 48-hour back trajectories for winds arriving in DFW at 22:00 UTC and 500 magl for August 19th, 2002.

For these two categories (1 and 2), back trajectories for days in each category were qualitatively similar. As discussed in Chapter 2, studies of HYSPLIT back trajectories from areas in East Texas (ENVIRON, 2004; Nielsen-Gammon et al., 2005; McGaughey et al., 2006; Sullivan, 2009) have shown that low ozone days frequently correspond to the long-range transport of relatively clean maritime air westward over the Gulf of Mexico. Results from these studies also suggested that elevated ozone concentrations in East Texas are frequently correlated with predominant northeasterly winds, which are capable of substantial long-range transport of background ozone levels from the continental U.S.

Taken collectively, the results of the seasonal zero-out analysis, back trajectory estimates, and ambient measurements are generally consistent with these findings. These results suggest that contributions to DFW background ozone levels on days characterized by relatively low zero-out differences and elevated ambient ozone levels were likely impacted by long-range continental transport. For days characterized by low ambient 8-hour ozone concentrations coinciding with large predicted zero-out ozone differences, non-local contributions to ozone levels in DFW were likely dominated by emissions from the HGB region.

Tables 3-6 and 3-10 also included days within category (3) for DFW, such as August 9th, 2002. On this day, the observed peak 8-hour ozone concentration in DFW was 127 ppb, and the maximum zero-out 8-hour ozone difference was 23 ppb. While results showed that days characterized by predominant northeasterly winds were generally not associated with large zero-out contributions from HGB, there were also days that experienced winds from multiple directions at various altitudes, including fetches passing over HGB and from origins to the east/northeast of the State. Local and background contributions on these days are not easily correlated with wind direction, as back trajectories show that both the lengths of fetches (indicative of wind speed) and wind origins vary significantly. These results were similar for Austin, San Antonio, and Victoria.

Photochemical modeling results showed that, for DFW, nearly half of all days from May 1st-September 29th, 2002, are characterized by contributions to 8-hour ozone concentrations from HGB anthropogenic emissions ranging from 10-30 ppb. For days in this period with ambient 8-hour ozone concentrations above 70 ppb, one-fourth were characterized by these zero-out differences in the range of 10-30 ppb for DFW, and nearly half of these days in Austin corresponded to zero-out ozone differences within 10-25 ppb. However, even smaller contributions from HGB can exacerbate existing elevated ozone concentrations due to local emissions. Additional conclusions based on the findings of this work were discussed in Section 3.3.

B.1 REFERENCES

- Draxler, R.R. and G.D. Rolph (2003), HYSPLIT (HYbrid Single-Particle Lagrangian Integrated Trajectory), NOAA Air Resources Laboratory, Silver Spring, MD, Model access via the NOAA ARL READY website, available at <http://www.arl.noaa.gov/ready/hysplit4.html>, accessed March 2010.
- ENVIRON International Corporation (2006), “Seasonal Model of Northeast Texas Ozone”, Final report prepared for the East Texas Council of Governments, Novato, CA, September 2006.
- ENVIRON International Corporation (2004), “Dallas-Fort Worth Transport Project”, Final report prepared for the Houston Advanced Research Center (HARC), Novato, CA, April 2004.
- McGaughey, G., C. Durrenberger, E.C. McDonald-Buller, and D.T. Allen (2006), “Monthly Back-Trajectory Analyses on High and Low Ozone Days for the Texas Near Nonattainment Areas for the Years 2001 through 2005”, Report prepared for the City of Victoria, The University of Texas at Austin Center for Energy and Environmental Resources, Austin, TX, August 2006.
- Neilsen-Gammon, J., J. Tobin, and A. McNiel (2005), “A Conceptual Model for Eight-Hour Ozone Exceedances in Houston Texas: Part I: Background Ozone Levels in East Texas”, Final report for HARC project H-12, January 2005.
- Sullivan, D. (2009), “Effects of Meteorology on Pollutant Trends”, Final report to the Texas Commission on Environmental Quality, grant activities No. 582-5-86245-FY08-01, The University of Texas at Austin Center for Energy and Environmental Resources, Austin, TX, March 2009.
- U.S. Environmental Protection Agency, AIRNow website reference, available at www.airnow.gov, accessed December 2008.

Appendix C: Further Analysis of Photochemical Modeling Results for August 13th-September 15th, 2006

This Appendix includes a continued analysis of the discussion in Section 3.2.2.

One notable difference from the 2002 seasonal results is that, as confirmed by examining Figure 3-6 and the correlations in Table 3-15, DFW and Austin experienced significantly large predicted zero-out ozone differences for several of the same days (and consecutive days) in this 2006 period, indicating a more widespread impact from HGB emissions. When results are ranked by the ten highest zero-out ozone differences during August 13th-September 14th, 2006, there are no days that coincide for the DFW and Austin regions (five days coincide in Tables 3-20 and 3-21 for 2006). This finding is in agreement with the increased frequency of south/southeasterly winds on days with elevated ambient ozone concentrations during this 2006 period in comparison to 2002, as verified by the HYSPLIT back trajectories that were generated for the days included in Table 3-17. Similar to the results in Figure 3-6 for 2006, Figure C-1 shows maximum zero-out differences in 8-hour ozone concentrations for this 2006 period for the DFW and Austin regions. As illustrated in Figure C-1, zero-out differences in ozone concentrations affected both regions on several of the same days during this period in 2006, though to a lesser extent.

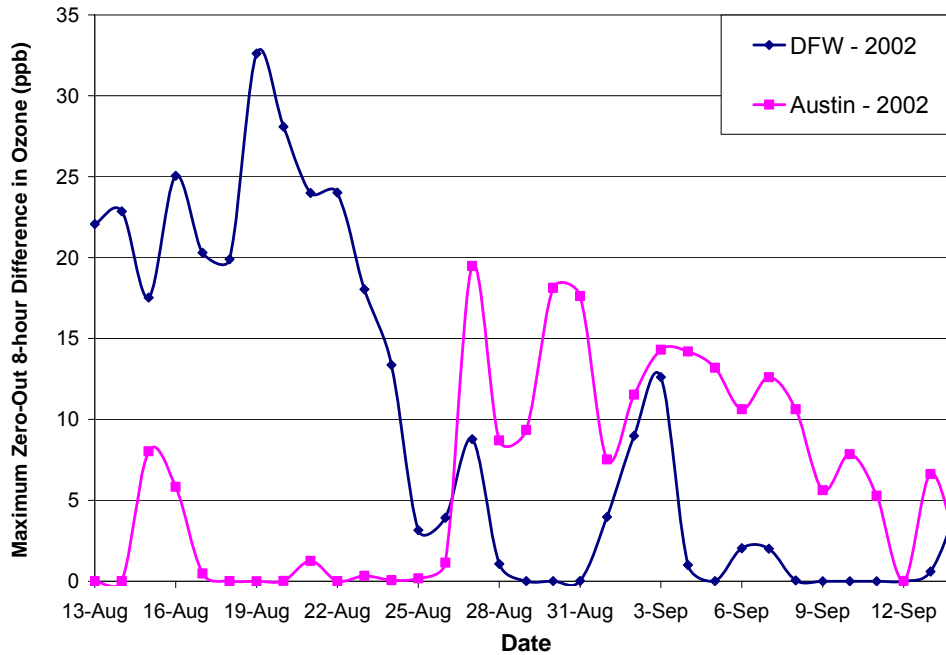


Figure C-1. Maximum 8-hour ozone differences between the CAMx base case and the zero-out case (as calculated by Equation 3.1) for August 13th-September 14th, 2002, for the DFW and Austin regions.

This also implies that, depending on meteorology, potentially large impacts from HGB emissions affecting ozone levels in Austin may or may not result in elevated 8-hour ozone measurements for that day; however, the addition of contributions from HGB and Austin may have a large combined effect on ambient ozone concentrations in DFW later that day or on the following day. The remainder of this Appendix examines a detailed case study of these phenomena during August 18th-19th, 2006.

August 18th, 2006, was characterized by the largest zero-out difference in 8-hour ozone concentrations for the Austin region (22 ppb). Ambient and modeled (base case) maximum 8-hour ozone levels in Austin were relatively high, with concentrations of 86 ppb and 76 ppb, respectively. On the following day, the maximum zero-out difference in the DFW region was 11 ppb, and ambient and modeled (base case) peak 8-hour ozone concentrations were 94 ppb and 84 ppb, respectively.

Figure C-2 shows 24-hour HYSPLIT back trajectories from Austin on August 18th, 2006. These trajectories estimate that winds arriving in Austin at 22:00 UTC at 500

magl originated from the southeast and east, qualitatively suggesting that HGB was a likely source region for pollutants transported by advection into Austin, in addition to possible contributions from long-range transport from the east/northeast. However, the longer fetches are primarily associated with winds at higher elevations, and it would therefore be expected that predominant advection near the surface is characterized by a winds from the southeast.

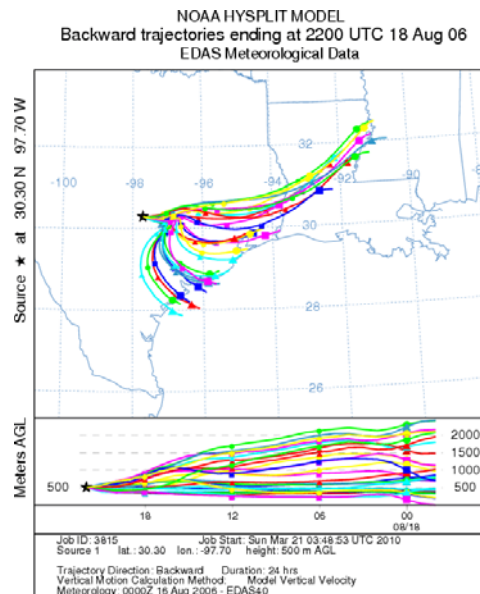


Figure C-2. HYSPLIT 24-hour back trajectories for winds arriving in Austin at 22:00 UTC and 500 magl for August 18th, 2006.

Similar HYSPLIT 24-hour back trajectories were generated for DFW on August 19th, 2006, for winds arriving at 22:00 UTC and 500 magl. As shown in Figure C-3, back trajectory estimates suggest that winds arriving in DFW on this day were predominantly from the south and southeast.

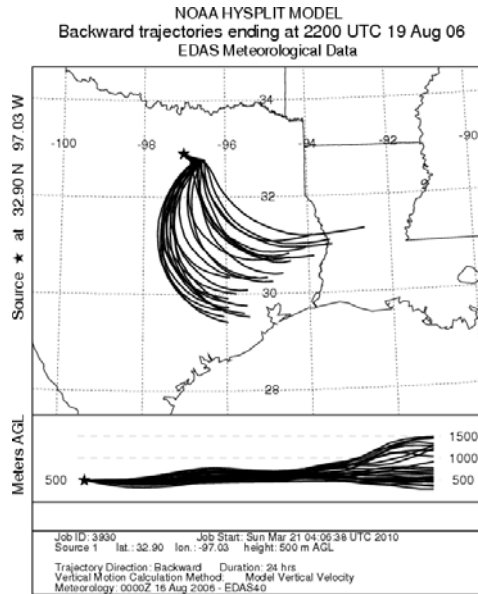


Figure C-3. HYSPLIT 24-hour back trajectories for winds arriving in DFW at 22:00 UTC and 500 magl for August 19th, 2006.

The results presented in Sections 3.2.1 and 3.2.2 of this work were predominantly focused on the maximum zero-out differences in ozone concentrations and peak ozone concentrations. Both of these measures, while valuable in identifying and characterizing trends, as well as selecting days for further analysis, are limited to the hour and grid cell (and/or surface monitor) in which these maxima occur. Furthermore, while the back trajectories presented here are qualitatively suggestive of potential sources of regional ozone transport, they are not indicative of quantitative estimates of this transport. Therefore, examining zero-out ozone differences across larger spatial and temporal scales would provide additional valuable information to assess ozone transport that occurred on these days.

Commonly available graphical and animation software can be used to view CAMx average output and/or input files. A flexible graphics visualization application that is compatible with multivariate gridded CAMx data is called the Package for Analysis and Visualization of Environmental data (PAVE). PAVE Version 2.3.2 was used to generate hourly graphics for differences in 1-hour ozone concentrations between the base case and the zero-out case for the CAMx 12-km grid domain. While these illustrations show results based on 1-hour ozone concentrations as opposed to ozone concentrations

averaged over eight hours, the spatial and temporal trends are qualitatively similar, though 1-hour results are generally larger in magnitude. Results are presented in Figures C-4 through C-6 for August 18th, 2006, at 12:00 CST, 16:00 CST, and 20:00 CST, respectively.

Base Case - Zero Out Case

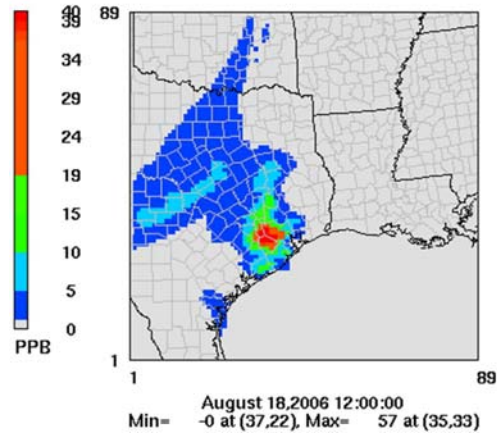


Figure C-4. CAMx differences in 1-hour ozone concentrations between the base case and zero-out case. Results are shown for the 12-km grid domain, at 12:00 CST on August 18th, 2006.

Base Case - Zero Out Case

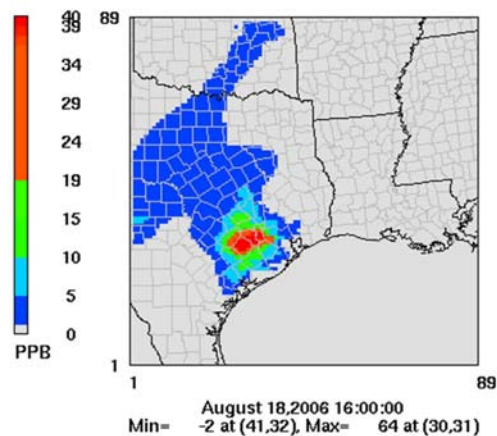


Figure C-5. CAMx differences in 1-hour ozone concentrations between the base case and zero-out case. Results are shown for the 12-km grid domain, at 16:00 CST on August 18th, 2006.

Base Case - Zero Out Case

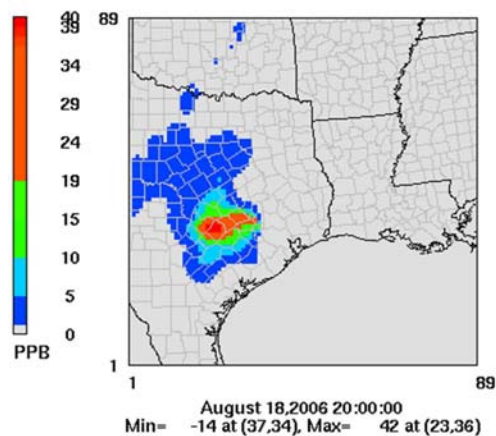


Figure C-6. CAMx differences in 1-hour ozone concentrations between the base case and zero-out case. Results are shown for the 12-km grid domain, at 20:00 CST on August 18th, 2006.

The modeled impacts of the urban plume originating in the HGB area are clearly tracked, illustrating advective transport from Houston, affecting ozone concentrations in Austin during the evening hours. This is consistent with the ambient data for this day, which will be discussed further. Figures C-7 through C-9 are similar zero-out ozone difference plots for August 19th, 2002, tracking the modeled impacts of the same plume into the DFW area during the early morning hours of 0:00 CST, 4:00 CST, and 7:00 CST, respectively.

Base Case - Zero Out Case

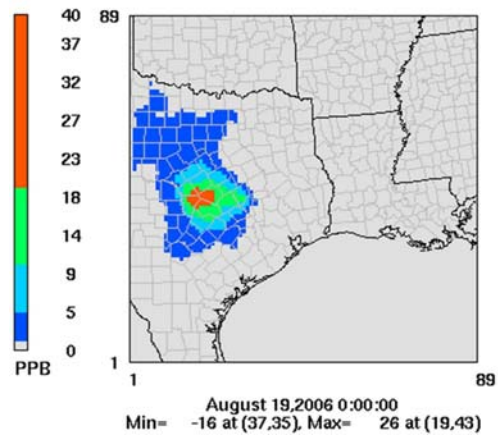


Figure C-7. CAMx differences in 1-hour ozone concentrations between the base case and zero-out case. Results are shown for the 12-km grid domain, at 0:00 CST on August 19th, 2006.

Base Case - Zero Out Case

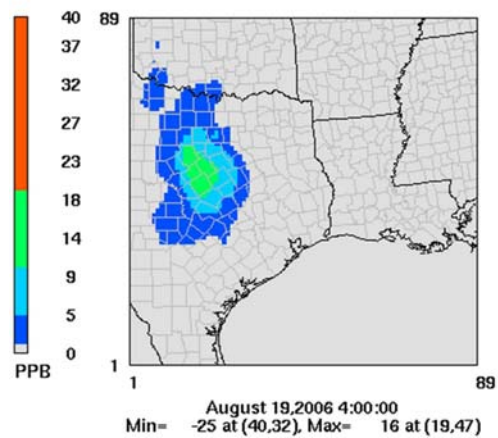


Figure C-8. CAMx differences in 1-hour ozone concentrations between the base case and zero-out case. Results are shown for the 12-km grid domain, at 4:00 CST on August 19th, 2006.

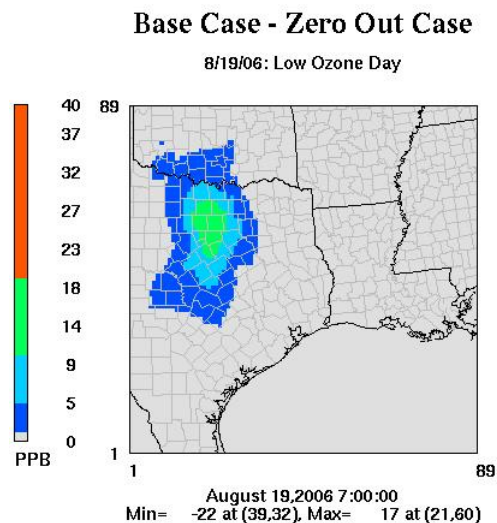


Figure C-9. CAMx differences in 1-hour ozone concentrations between the base case and zero-out case. Results are shown for the 12-km grid domain, at 7:00 CST on August 19th, 2006.

According to the modeling protocol for this episode, the TCEQ will submit a SIP revision based on this simulation to EPA by April 15th, 2010, to satisfy EPA requirements for an 8-hour ozone attainment demonstration (TCEQ, 2009). The TCEQ has completed a performance evaluation of this simulation for the 2-km HG domain, and model predictions fall within acceptable EPA standards (supporting files for this performance evaluation are provided by the TCEQ and available on their website, <http://www.tceq.state.tx.us/implementation/air/airmod/data/hgb8h2/hgb8h2.html>). The zero-out results are based on impacts to regions in East Texas that lie within the 12-km domain; therefore, the model may not perform at the same level of accuracy at this resolution in comparison to the finer 2-km domain.

As shown in Figure C-10, with the exception of September 10th-11th, while the model has a tendency to overestimate maximum ozone concentrations, it captures the variations in these maxima relatively well. One statistical measure of model performance is unpaired peak accuracy (UPA), which was examined for the 2002 seasonal model and shown in Figure B-1. This statistic compares the difference between the maximum modeled ozone concentration and the highest monitored ozone concentration over all hours and over all monitoring stations for each day in the simulation. For August 18th and

19th, the UPA values are 6% and 11% for DFW, and 12% and 20% for Austin, respectively. In the past, the EPA has recommended an acceptable range for the UPA of 15-20% for 1-hour average ozone concentrations, although there have been no recommendations for corresponding ozone concentrations averaged over eight hours (TCEQ, 2009).

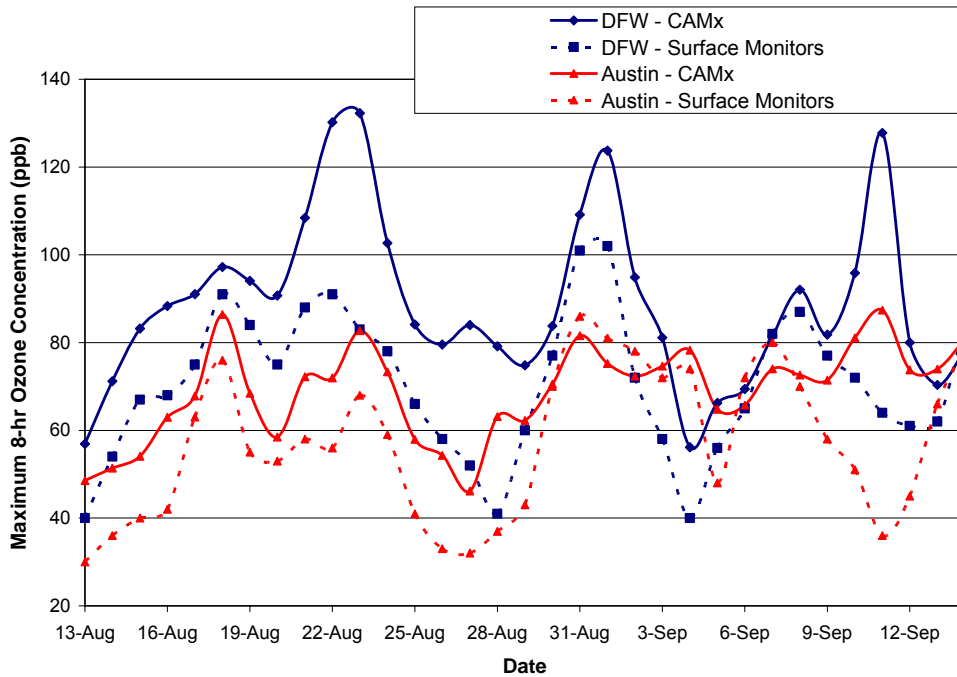


Figure C-10. Modeled and ambient surface monitor maximum 8-hour ozone concentrations for DFW and Austin from August 13th-September 14th, 2006. CAMx modeling results are shown for the base case.

As stated in Appendix B (in relation to results in Section 3.2.1), observational ozone concentrations were primarily used as a measure of categorize the zero-out modeling results and to assess general trends for high and low ozone days, rather than as a comparative measure of model performance. The remainder of this Appendix compares photochemical modeling results with ambient data, and while these results are largely qualitative, the model showed relatively good agreement with the ambient maximum 8-hour ozone concentrations on this day.

Ambient 1-hour average ozone concentrations were extracted from the TCEQ online database for August 18th and 19th, 2006 (<http://www.tceq.state.tx.us/cgi->

[bin/compliance/monops/daily_average.pl](#)). Elevated ozone levels were measured on the west side of the Houston area on August 18th. The highest ambient 1-hour average ozone concentration was 106 ppb, as measured by the Katy Park Continuous Ambient Monitoring Site (CAMS) 559 at 14:00 CST.

High ozone was measured in Austin during the late afternoon and evening hours of the same day. Figure C-11 illustrates the geographic locations of surface monitors in the city of Austin and surrounding areas, obtained from the TCEQ website <http://www.tceq.state.tx.us/assets/public/compliance/monops/graphics/clickable/region11.gif>. Elevated 1-hour average ozone concentrations include 97 ppb at 16:00 CST and 17:00 CST, and 103 ppb at 18:00 CST. These measurements were recorded by the Fayette County CAMS 601, which is located in a relatively rural area between Austin and Houston (indicated in Figure C-11). At 20:00 CST, 1-hour average ozone concentrations of 94 ppb and 98 ppb were measured at the Pflugerville CAMS 613 and Austin Northwest CAMS 3 locations, respectively. At 21:00 CST, a 1-hour ozone concentration of 93 ppb was measured at the CAPCOG Round Rock CAMS 674. Diurnally, elevated ozone concentrations from local emissions typically occur in the afternoon hours, as discussed in Chapter 2. These elevated ozone concentrations in Austin during late evening hours are indicative of a secondary impact, likely due to advective transport of pollutants into the region.

Table C-1. Ambient 1-hour ozone concentrations are shown for Italy High School CAMS 650, averaged from August 13th-September 15th, 2006. The ambient 1-hour ozone concentrations for CAMS 650 are also shown for August 19th, 2006.

Hour	CAMS 650 Average 1-hour O3 (ppb)	CAMS 650 1-hour O3 (ppb) on 8/19/2006
Midnight	32	43
1:00	31	42
2:00	27	40
3:00	25	37
4:00	23	35
5:00	20	30
6:00	19	24
7:00	24	35
8:00	33	53
9:00	40	60
10:00	46	60
11:00	50	60
12:00	52	59
13:00	55	61
14:00	56	69
15:00	58	68
16:00	59	66
17:00	59	63
18:00	56	63
19:00	51	55
20:00	45	46
21:00	40	40
22:00	37	37
23:00	34	41

Ozone contour plots were generated using a grid-based graphics program, Surfer by Golden Software (<http://www.goldensoftware.com/products/surfer/surfer.shtml>). When creating a grid from surface monitoring data, Surfer interpolates between these monitoring stations to create the contouring map in areas where ambient data are not available. Consequently, values for locations farther away from the monitoring stations may not be accurate representations of ambient measurements. Several interpolation schemes are available in Surfer, the differences between them being mathematical algorithms used to compute the weights during grid node interpolations. Each method may result in a different representation of the data. Example methods include Kriging, Modified Shepard's Method, Natural Neighbor, Nearest Neighbor, and Moving Average. The contours included in this Chapter used a simple point Kriging interpolation method.

Figures C-13 and C-14 illustrate ozone contour plots created for August 18th and 19th, 2006, respectively, using data from all available surface monitors in Texas, Oklahoma, Arkansas, and Louisiana from the EPA AIRNow database. HYSPLIT 72-hour back trajectories were created for the same days to show wind origins from six points in East Texas at 18:00 UTC and an altitude of 300 magl. These back trajectories are superimposed onto the ozone isopleths, and 1-hour time steps are displayed. In comparison to the modeled results in Figures C-4 through C-9, the contour plots of the ambient data also suggest advection of elevated ozone concentrations from HGB into the Austin region on August 18th, and elevated ozone concentrations in DFW on the following day.

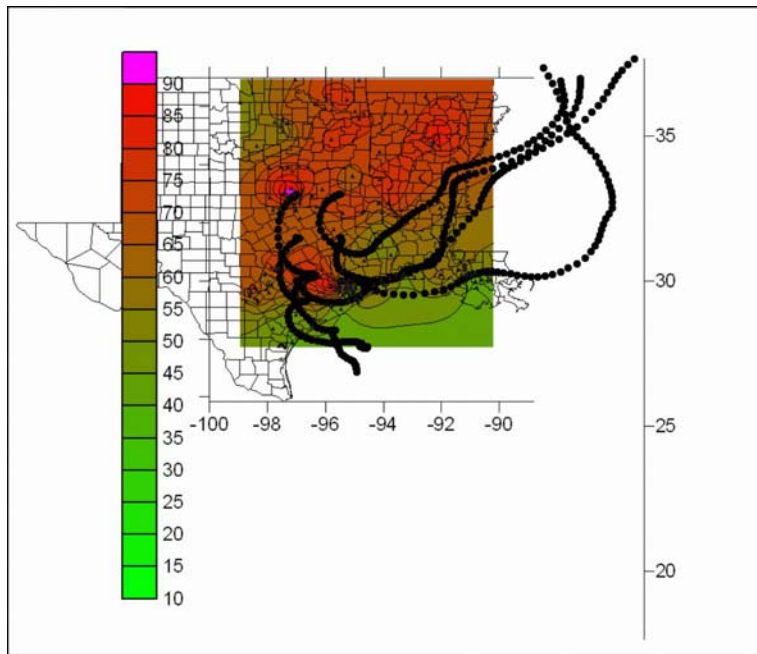


Figure C-13. Surfer contour plot of interpolated ambient 8-hour maximum ozone concentrations for August 18th, 2006. HYSPLIT 72-hour back trajectories are also shown for six origins in East Texas, at 18:00 UTC and an altitude of 300 magl.

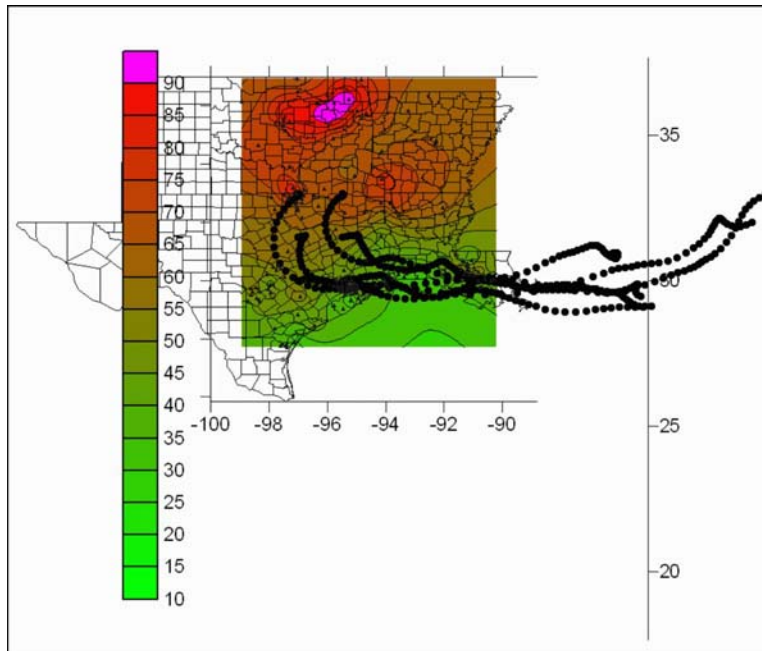


Figure C-14. Surfer contour plot of interpolated ambient 8-hour maximum ozone concentrations for August 19th, 2006. HYSPLIT 72-hour back trajectories are also shown for six origins in East Texas, at 18:00 UTC and an altitude of 300 magl.

Various plume animation tools are available that show the estimated plume tracks based on measured 1-hour average values of wind direction, ozone concentrations, or both, from the EPA AIRNow website. Figures C-15 through C-18 show slides of animations that were generated using 1-hour average ozone concentration measurements collected by surface monitors in Texas, Louisiana, Arkansas, and Oklahoma (McGaughey, 2006). The locations of the surface monitors with valid data for that hour are labeled with a "+" symbol. Similar to Figures C-13 and C-14, these animations were generated using Surfer by Golden Software to interpolate (invoking a Kriging interpolation scheme) the monitoring data to a regular grid. These images further qualitatively support the finding that elevated surface ozone concentrations in Austin were likely impacted by advection of the Houston urban plume on August 18th, 2006.

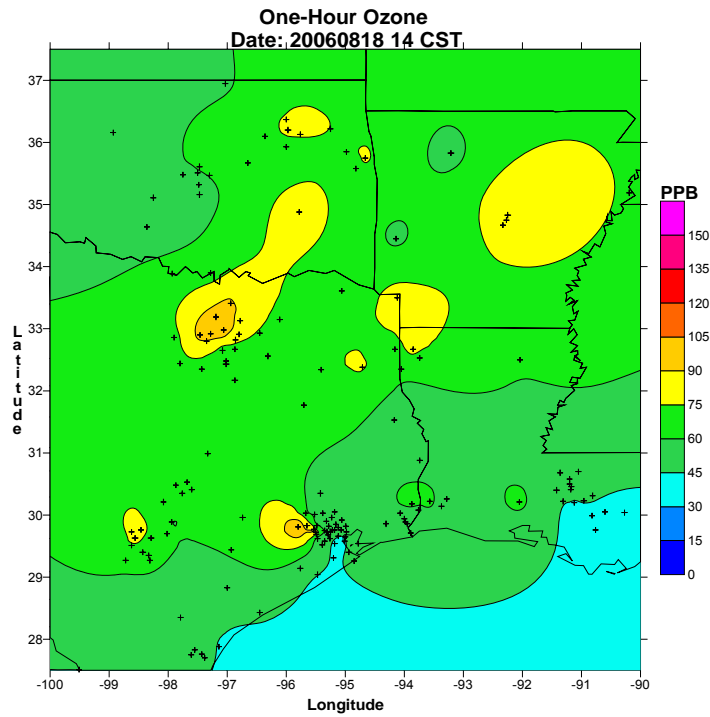


Figure C-15. Surfer contour plot of interpolated ambient 1-hour average ozone concentrations for 14:00 CST on August 18th, 2006.

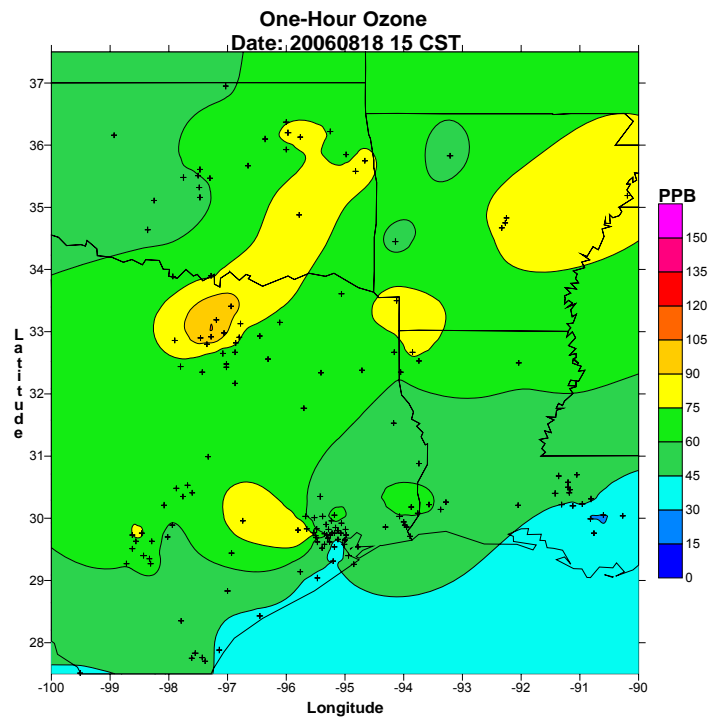


Figure C-16. Surfer contour plot of interpolated ambient 1-hour average ozone concentrations for 15:00 CST on August 18th, 2006.

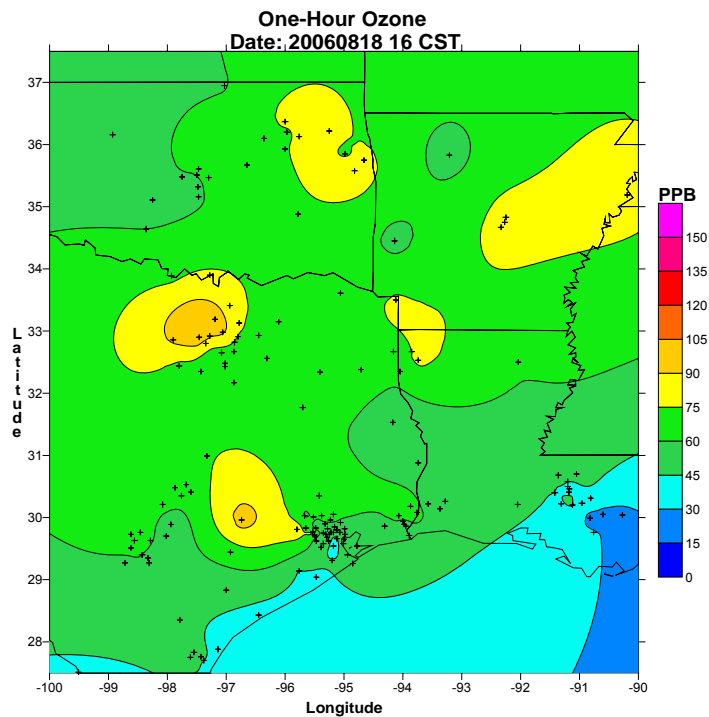


Figure C-17. Surfer contour plot of interpolated ambient 1-hour average ozone concentrations for 16:00 CST on August 18th, 2006.

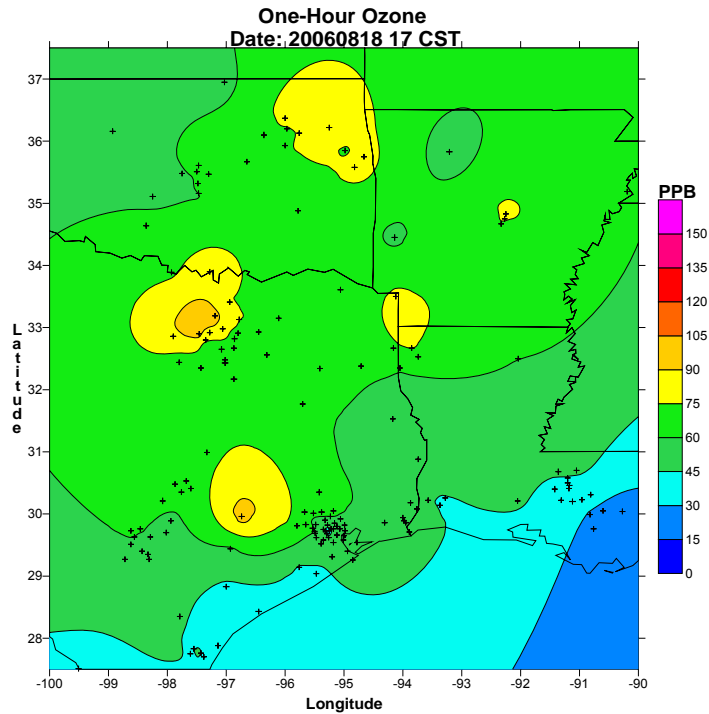


Figure C-18. Surfer contour plot of interpolated ambient 1-hour average ozone concentrations for 17:00 CST on August 18th, 2006.

C.1 REFERENCES

- Draxler, R.R. and G.D. Rolph (2003), HYSPLIT (HYbrid Single-Particle Lagrangian Integrated Trajectory), NOAA Air Resources Laboratory, Silver Spring, MD, Model access via the NOAA ARL READY website, available at <http://www.arl.noaa.gov/ready/hysplit4.html>, accessed March 2010.
- Golden Software, Surfer product description website reference, available at <http://www.goldensoftware.com/products/surfer/surfer.shtml>, accessed March 2010.
- McGaughey, G. (2006), The University of Texas Center for Energy and Environmental Resources ozone animations website reference, available at <http://bosshogg.ces.utexas.edu/animations/ozone.cfm>, accessed February 2010.
- Texas Commission on Environmental Quality (2009), “Protocol for Eight-Hour Ozone Modeling of the Houston/Galveston/Brazoria Area”, Revised report prepared by the Air Modeling and Data Analysis Section, July 2009, available at http://www.tceq.state.tx.us/assets/public/implementation/air/am/modeling/hgb8h2/doc/HGB8H2_Protocol_20090715.pdf.
- Texas Commission on Environmental Quality, website reference for CAMx simulation performance, available at <http://www.tceq.state.tx.us/implementation/air/airmod/data/hgb8h2/hgb8h2.html>, accessed March 2010.
- Texas Commission on Environmental Quality online database, available at http://www.tceq.state.tx.us/cgi-bin/compliance/monops/daily_average.pl, accessed March 2010.
- Texas Commission on Environmental Quality, website reference for Figure C-11, available at <http://www.tceq.state.tx.us/assets/public/compliance/monops/graphics/clickable/region04.gif>, accessed April 2010.
- Texas Commission on Environmental Quality, website reference for Figure C-12, available at <http://www.tceq.state.tx.us/assets/public/compliance/monops/graphics/clickable/region11.gif>, accessed April 2010.

Appendix D: CAMx Process Analysis Results for September 6th, 2000

The tables below present the complete CAMx Process Analysis (PA) results of each of the processes contributing to the sources and sinks of ozone for the hours corresponding to the flight time on September 6th, 2000, as discussed in Chapter 6. These processes (in ppb/hr) include chemistry, advection, diffusion, and deposition. Initial and final concentrations of ozone (in ppb) are also shown for each hour. Results are presented for all receptor sites as labeled in Figure 6-4. H and V indicate the direction of transport, horizontal and vertical, respectively, and negative values are indicative of ozone depletion.

Table D-1. CAMx PA results for receptor site a1 from 10:00-16:00 CST on September 6th, 2000. Initial and final concentrations of ozone are shown in units of ppb. Chemistry, advection, diffusion, and deposition terms are shown in units of ppb/hr.

Hr	Initial Conc.	Chemistry	H_ advection	H_ diffusion	H_ transport	V_ advection	V_ diffusion	V_ transport	Deposition	Final Conc.
10	77.5	21.9	-7.0	-0.9	-7.9	4.5	72.6	77.0	-65.2	103.3
11	104.2	29.7	-2.2	-1.9	-4.1	-2.1	82.3	80.2	-83.9	126.1
12	126.9	28.1	8.1	-2.9	5.2	-15.0	89.8	74.8	-97.1	137.9
13	138.5	21.4	32.2	-4.9	27.2	-46.1	99.4	53.3	-101.7	138.7
14	139.0	17.9	63.7	-4.8	58.9	-89.4	99.5	10.1	-97.4	128.6
15	128.8	6.1	85.7	-3.6	82.1	-116.2	95.6	-20.6	-85.7	110.7
16	110.5	-11.9	83.8	-2.4	81.4	-111.0	89.0	-22.0	-69.4	88.7

Table D-2. CAMx PA results for receptor site a2 from 10:00-16:00 CST on September 6th, 2000. Initial and final concentrations of ozone are shown in units of ppb. Chemistry, advection, diffusion, and deposition terms are shown in units of ppb/hr.

Hr	Initial Conc.	Chemistry	H_ advection	H_ diffusion	H_ transport	V_ advection	V_ diffusion	V_ transport	Deposition	Final Conc.
10	77.1	31.8	1.8	0.0	1.8	4.5	73.8	78.3	-86.7	102.3
11	103.1	40.2	-6.7	-0.5	-7.2	8.5	92.5	101.0	-111.8	125.4
12	126.2	36.8	-10.3	-1.3	-11.5	7.3	107.0	114.3	-129.6	136.2
13	136.7	29.2	1.6	-2.4	-0.8	-8.8	118.4	109.6	-135.6	139.2
14	139.4	25.8	28.4	-3.5	25.0	-45.3	122.4	77.1	-133.5	133.8
15	134.0	18.0	75.1	-5.4	69.8	-97.8	116.7	19.0	-121.9	118.8
16	118.7	6.1	108.0	-4.4	103.6	-130.6	100.8	-29.8	-100.9	97.8

Table D-3. CAMx PA results for receptor site a3 from 10:00-16:00 CST on September 6th, 2000. Initial and final concentrations of ozone are shown in units of ppb. Chemistry, advection, diffusion, and deposition terms are shown in units of ppb/hr.

Hr	Initial Conc.	Chemistry	H_ advection	H_ diffusion	H_ transport	V_ advection	V_ diffusion	V_ transport	Deposition	Final Conc.
10	73.1	33.4	4.0	0.1	4.1	-2.3	60.4	58.1	-68.0	100.7
11	101.5	38.2	1.6	-1.0	0.6	-1.4	74.3	72.9	-89.5	123.8
12	124.6	32.8	0.0	-1.8	-1.9	0.4	85.1	85.5	-104.8	136.3
13	136.7	24.6	-3.5	-2.4	-5.9	-2.7	93.5	90.8	-109.8	136.5
14	136.8	18.6	5.1	-2.1	3.0	-18.9	97.4	78.5	-106.9	130.0
15	130.1	11.9	30.5	-2.1	28.5	-52.6	93.9	41.3	-96.5	115.3
16	115.2	3.7	71.7	-1.8	69.9	-91.9	83.2	-8.7	-81.2	99.0

Table D-4. CAMx PA results for receptor site a4 from 10:00-16:00 CST on September 6th, 2000. Initial and final concentrations of ozone are shown in units of ppb. Chemistry, advection, diffusion, and deposition terms are shown in units of ppb/hr.

Hr	Initial Conc.	Chemistry	H_ advection	H_ diffusion	H_ transport	V_ advection	V_ diffusion	V_ transport	Deposition	Final Conc.
10	70.2	25.4	2.5	0.8	3.2	-1.4	73.1	71.7	-74.2	96.3
11	97.1	28.7	5.2	-0.2	5.0	-0.7	90.8	90.1	-99.6	121.3
12	122.1	21.9	4.8	-0.9	4.0	3.9	100.2	104.0	-117.5	134.6
13	135.1	16.8	11.5	-1.6	9.9	-2.3	110.7	108.4	-127.4	142.8
14	143.1	12.9	26.0	-3.1	22.9	-24.8	119.6	94.8	-130.9	142.9
15	143.0	8.2	47.3	-4.8	42.5	-58.5	120.5	62.0	-124.4	131.3
16	131.2	1.4	82.8	-5.2	77.5	-102.7	107.4	4.8	-105.3	109.5

Table D-5. CAMx PA results for receptor site a5 from 10:00-16:00 CST on September 6th, 2000. Initial and final concentrations of ozone are shown in units of ppb. Chemistry, advection, diffusion, and deposition terms are shown in units of ppb/hr.

Hr	Initial Conc.	Chemistry	H_ advection	H_ diffusion	H_ transport	V_ advection	V_ diffusion	V_ transport	Deposition	Final Conc.
10	72.0	12.9	5.7	-0.9	4.8	-5.0	70.6	65.6	-61.7	93.6
11	94.2	12.1	19.9	-2.3	17.6	-19.8	76.9	57.2	-74.9	106.2
12	106.8	8.6	45.0	-3.3	41.7	-42.2	84.5	42.2	-83.2	116.2
13	116.7	2.9	58.7	-5.6	53.1	-52.6	94.6	42.0	-90.4	124.3
14	124.6	-2.6	51.7	-7.4	44.2	-50.9	99.7	48.8	-93.3	121.7
15	121.7	-9.1	49.9	-5.1	44.7	-63.9	92.6	28.8	-83.5	102.6
16	102.5	-17.1	70.0	2.8	72.8	-78.4	85.5	7.0	-70.3	94.9

Table D-6. CAMx PA results for receptor site b1 from 10:00-16:00 CST on September 6th, 2000. Initial and final concentrations of ozone are shown in units of ppb. Chemistry, advection, diffusion, and deposition terms are shown in units of ppb/hr.

Hr	Initial Conc.	Chemistry	H_ advection	H_ diffusion	H_ transport	V_ advection	V_ diffusion	V_ transport	Deposition	Final Conc.
10	80.6	21.4	25.5	-0.9	24.6	-23.1	57.1	34.0	-63.6	97.0
11	97.4	17.3	39.6	-1.5	38.0	-38.1	63.4	25.3	-70.8	107.3
12	107.7	15.1	56.8	-1.8	55.0	-56.3	69.3	13.0	-75.9	115.0
13	115.3	13.2	70.0	-3.1	66.9	-75.4	73.3	-2.2	-79.2	114.1
14	114.2	8.5	63.1	-2.2	60.9	-74.5	70.8	-3.8	-74.7	105.2
15	105.0	2.5	23.0	0.5	23.5	-33.7	66.6	32.9	-67.6	96.2
16	95.9	-4.2	-6.8	0.7	-6.0	4.3	66.2	70.6	-64.7	91.6

Table D-7. CAMx PA results for receptor site b2 from 10:00-16:00 CST on September 6th, 2000. Initial and final concentrations of ozone are shown in units of ppb. Chemistry, advection, diffusion, and deposition terms are shown in units of ppb/hr.

Hr	Initial Conc.	Chemistry	H_ advection	H_ diffusion	H_ transport	V_ advection	V_ diffusion	V_ transport	Deposition	Final Conc.
10	80.5	24.0	-0.9	-0.7	-1.6	1.6	47.2	48.8	-55.2	96.5
11	97.0	19.0	13.2	-1.6	11.6	-11.6	53.0	41.3	-61.7	107.3
12	107.7	16.5	29.4	-2.3	27.0	-28.4	59.0	30.7	-67.2	114.7
13	115.1	14.7	44.7	-2.9	41.8	-47.1	64.0	16.9	-70.4	118.1
14	118.2	12.1	38.6	-2.8	35.8	-49.6	64.1	14.5	-69.4	111.3
15	111.2	7.6	1.2	0.4	1.6	-19.1	59.5	40.4	-61.8	98.9
16	98.6	2.5	-25.8	0.5	-25.3	17.5	57.7	75.2	-57.2	93.8

Table D-8. CAMx PA results for receptor site b3 from 10:00-16:00 CST on September 6th, 2000. Initial and final concentrations of ozone are shown in units of ppb. Chemistry, advection, diffusion, and deposition terms are shown in units of ppb/hr.

Hr	Initial Conc.	Chemistry	H_ advection	H_ diffusion	H_ transport	V_ advection	V_ diffusion	V_ transport	Deposition	Final Conc.
10	78.6	23.7	-12.4	-0.2	-12.6	13.0	45.0	58.0	-54.1	93.5
11	94.0	22.1	-16.4	-0.7	-17.1	16.5	49.8	66.3	-60.7	104.7
12	105.1	20.5	-18.7	-1.3	-20.0	18.2	55.0	73.2	-66.5	112.3
13	112.7	18.8	-14.3	-2.0	-16.2	13.8	58.9	72.6	-70.3	117.5
14	117.7	16.3	-10.7	-2.2	-12.9	6.7	61.4	68.0	-71.7	117.4
15	117.4	12.2	-22.6	-0.7	-23.3	9.2	58.7	67.9	-67.5	106.7
16	106.4	3.7	-33.1	1.0	-32.1	22.8	55.1	77.9	-59.7	96.2

Table D-9. CAMx PA results for receptor site b4 from 10:00-16:00 CST on September 6th, 2000. Initial and final concentrations of ozone are shown in units of ppb. Chemistry, advection, diffusion, and deposition terms are shown in units of ppb/hr.

Hr	Initial Conc.	Chemistry	H_ advection	H_ diffusion	H_ transport	V_ advection	V_ diffusion	V_ transport	Deposition	Final Conc.
10	77.3	14.5	-18.1	-0.5	-18.6	22.4	69.5	91.9	-73.5	91.5
11	92.0	13.0	-23.7	-0.8	-24.5	28.5	77.0	105.5	-84.5	101.5
12	101.9	11.4	-28.2	-1.0	-29.2	32.7	83.6	116.3	-91.9	108.5
13	108.8	8.6	-24.1	-1.0	-25.0	28.0	89.7	117.7	-96.8	113.2
14	113.3	5.0	-8.1	-0.7	-8.9	9.8	94.5	104.3	-99.3	114.5
15	114.4	-0.6	-6.2	-0.3	-6.5	0.1	94.5	94.6	-95.6	106.4
16	106.1	-9.5	-15.7	0.3	-15.4	10.8	87.2	98.0	-84.7	94.5

Table D-10. CAMx PA results for receptor site b5 from 10:00-16:00 CST on September 6th, 2000. Initial and final concentrations of ozone are shown in units of ppb. Chemistry, advection, diffusion, and deposition terms are shown in units of ppb/hr.

Hr	Initial Conc.	Chemistry	H_ advection	H_ diffusion	H_ transport	V_ advection	V_ diffusion	V_ transport	Deposition	Final Conc.
10	74.8	15.8	3.9	-0.2	3.7	-3.9	65.6	61.8	-70.4	85.8
11	86.1	14.3	15.8	-0.7	15.1	-15.4	70.9	55.5	-78.4	92.6
12	92.9	12.6	24.5	-1.0	23.5	-24.6	76.5	51.9	-83.7	97.2
13	97.3	10.4	22.1	-0.8	21.2	-25.4	81.5	56.1	-86.4	98.7
14	98.7	7.4	22.5	-0.1	22.4	-29.5	84.5	55.0	-86.2	97.4
15	97.2	3.1	18.5	0.8	19.2	-29.2	82.8	53.6	-82.1	91.0
16	90.6	-2.8	-6.3	1.0	-5.3	-0.6	77.2	76.6	-75.3	83.8

Appendix E: A Comparison of Airborne LIDAR and Surface Measurements of Ozone Concentrations on September 6th, 2000

The methodology developed for performing flux calculations of excess ozone in urban plumes by incorporating measurements from surface monitors was discussed in Section 5.2. The use of surface measurements, time averaged over one hour, in this approximation method assumes a well-mixed planetary boundary layer (PBL). In contrast, the instantaneous vertical distributions of ozone measured by airborne LIDAR show variations in the vertical distributions of concentrations. To assess the degree to which the time averaging of surface measurements captures the vertical variations in ozone levels in the PBL, this section examines surface and airborne LIDAR observations of ozone in urban plumes on September 6th, 2000. On this day, the National Oceanic and Atmospheric Administration (NOAA) DC-3 aircraft tracked two distinct plumes of high ozone concentrations, originating from industrial facilities located in the Houston Ship Channel and Texas City, as they were transported across regions to the southwest of Houston. Further details of this case study were discussed in Chapters 5 and 6.

Discrepancies between approximations of excess ozone transported in urban plumes using aircraft LIDAR observations and data from surface monitors arise due to differences in the spatial and temporal resolutions of both measurements. As described in Section 5.2, data from surface monitors were used to estimate excess ozone as the difference in 1-hour average values of ozone concentrations that are recorded in 5-minute intervals, as measured by monitors located upwind and downwind of the urban source region. With LIDAR observations, the excess ozone in urban plumes was estimated by integrating essentially instantaneous, but vertically resolved data across the horizontal and vertical plume boundaries. The LIDAR measurements provide vertical profiles of ozone concentrations, extending from the surface to approximately 2600 meters above mean sea level (mMSL), at a vertical and temporal resolution of 90 meters and 10 seconds, respectively.

The complete DC-3 flight track for September 6th, 2000, along with contours of vertically averaged ozone concentrations over a depth of 200-1000 mMSL, is presented

in Figure E-1. From approximately 16:20-22:20 UTC, the aircraft LIDAR collected measurements along multiple parallel flight transects, tracking two distinct plumes of elevated ozone levels as they were transported to the southwest of Houston.

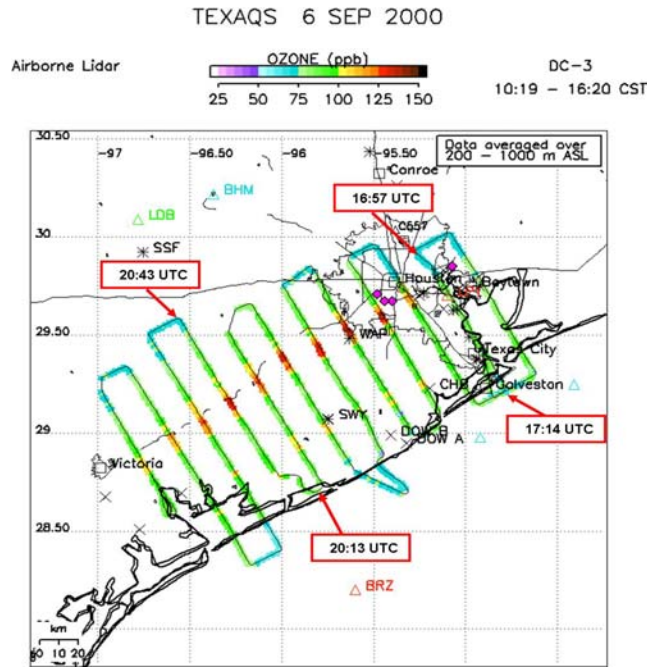


Figure E-1. Ozone concentrations (vertically averaged from 200-1000 mMSL) from the NOAA DC-3 flight on September 6th, 2000 (Senff et al., 2007). The locations of the surface monitors used for calculating ozone flux on this day are shown in magenta. The flight transects examined in this analysis are specified, corresponding to flight times from 16:57-17:14 UTC and 20:13-20:43 UTC.

LIDAR data collected during this flight were obtained from the NOAA Earth System Research Laboratory website

(http://www.esrl.noaa.gov/csd/ors/data_pages/texaqs/air_ozone.html). To provide an approximation of plume ozone levels in the well-mixed PBL, LIDAR measurements of ozone concentrations for each 10-second interval along select flight transects were vertically averaged to an altitude of approximately 1000 mMSL. Invalid LIDAR observations were noted at elevations between the surface and approximately 200 mMSL; therefore, data for the 0-200 mMSL elevation range were ignored in this analysis. The vertically averaged 10-second LIDAR measurements were compared to 5-

minute ozone concentrations measured by select surface monitors for portions of the two flight transects specified in Figure E-1.

The flight transect that was used as the basis for ozone flux retrieval on this day (results were presented in Section 5.3) corresponds to a flight time of 20:13-20:43 UTC. The surface monitors selected to provide estimates of background and peak ozone concentrations are specified in Figure E-2 (also indicated in Figure E-1 relative to the DC-3 flight track), which shows the geographic locations of all surface monitors in the Houston region that were operational in 2000. The surface monitor chosen to estimate the upwind background ozone is Mont Belvieu CAMS 610 (circled in blue). The surface monitors selected to estimate peak ozone levels are Houston Westhollow CAMS 410, Houston Croquet CAMS 409, and Houston Bayland Park CAMS 53 (circled in red).

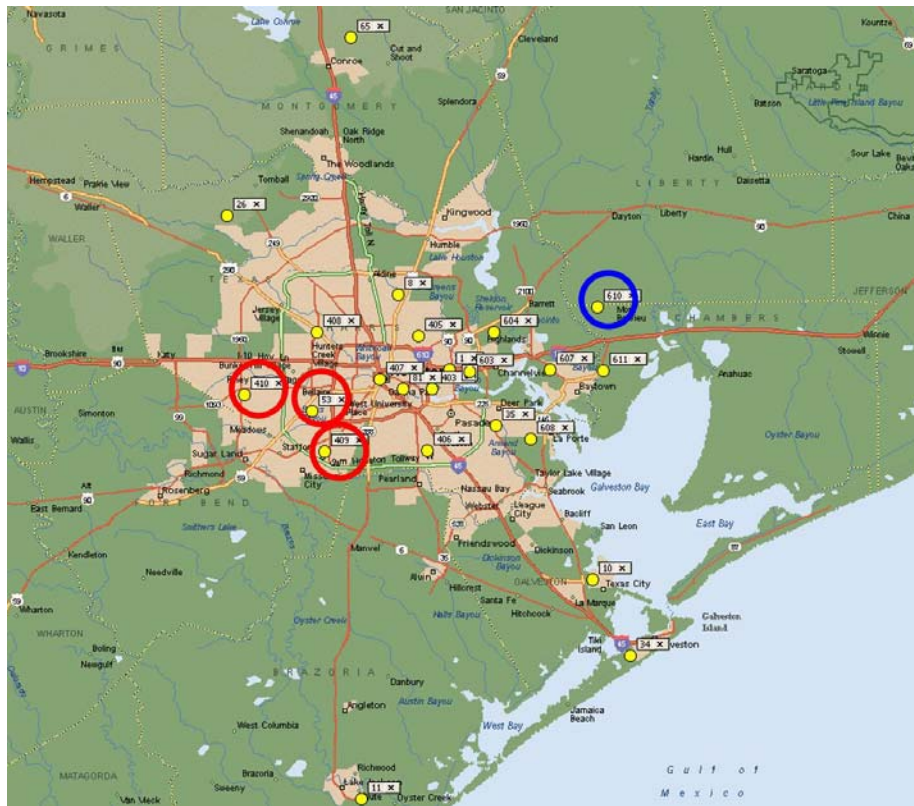


Figure E-2. Continuous Ambient Monitoring Stations (CAMS) in the Houston area that were operational during 2000 (CAPCO et al., 2004). Surface monitors that were used to estimate background and peak ozone concentrations on September 6th, 2000, are circled in blue and red, respectively.

The 10-second ozone concentrations measured by the LIDAR for the flight transect corresponding to 20:13-20:43 UTC, vertically averaged over a column depth of approximately 200-1000 mMSL, are shown in Figure E-3. The 5-minute ozone concentrations measured by the surface monitors circled in Figure E-2 (located approximately 100 km northwest of the flight transect) are also presented for 20:00-21:00 UTC, along with the corresponding mean concentration for each monitor. To further examine and compare the variations associated with the LIDAR and surface monitor measurements, portions of the flight transect were selected that are representative of peak and background ozone levels.

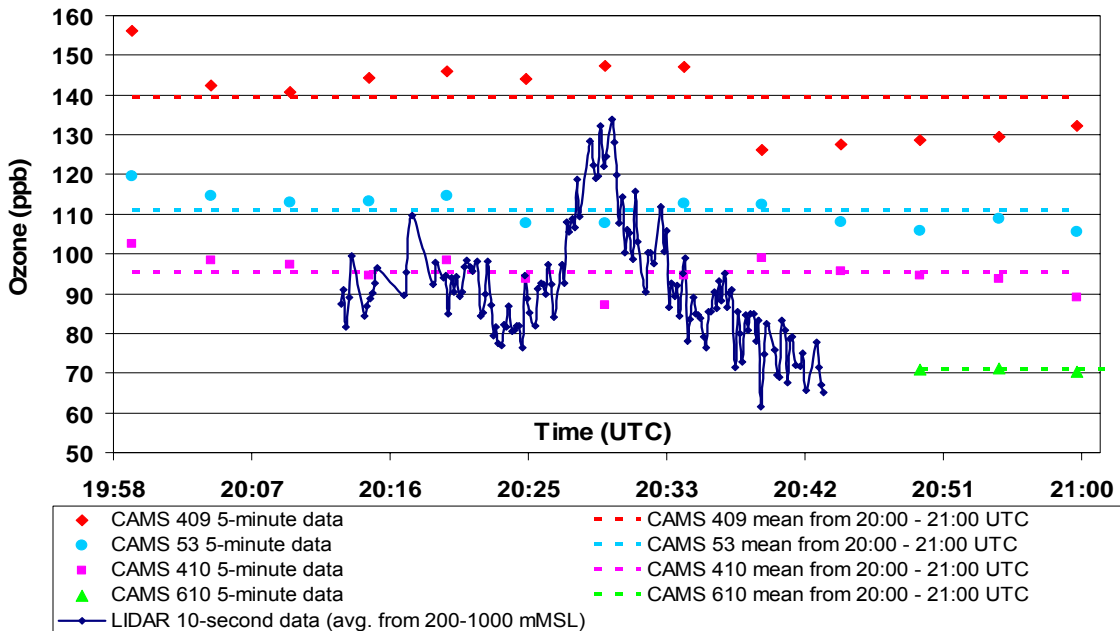


Figure E-3. Vertically averaged LIDAR and surface monitor measurements of ozone concentrations (ppb) for September 6th, 2000. Results are shown for the flight transect indicated in Figure E-1 from 20:13-20:43 UTC. The 5-minute measurements are shown for the surface monitors circled in Figure E-2. The dashed lines represent the mean ozone concentration for each surface monitor, based on 5-minute measurements from 20:00-21:00 UTC.

A comparison was performed to assess the extent to which ozone concentrations, and their time variability, measured by CAMS 409, 410, and 53 are representative of peak ozone levels aloft, as observed by the airborne LIDAR, in the advected plumes. As

shown in Figure E-3, there are thirteen 5-minute measurements recorded by each of these surface monitors over the course of the hour from 20:00-21:00 UTC. Thirteen 10-second LIDAR measurements were selected for comparison that correspond to peak ozone concentrations observed from 20:28:25-20:31:05 UTC. These selected vertically averaged LIDAR measurements are emphasized in bold dark blue in Figure E-4, which presents a portion of the flight transect shown in Figure E-3. It should be noted that the LIDAR and surface monitor measurements are identical in Figures E-3 and E-4, though they are displayed on a finer temporal scale in Figure E-4. The mean and one standard deviation of these measurements are shown as the dashed lines and error bars, respectively. While Figure E-4 only shows 5-minute surface measurements for a duration of 15 minutes, the mean and standard deviation statistics for each monitor were calculated based on the thirteen measurements recorded by that monitor from 20:00-21:00 UTC.

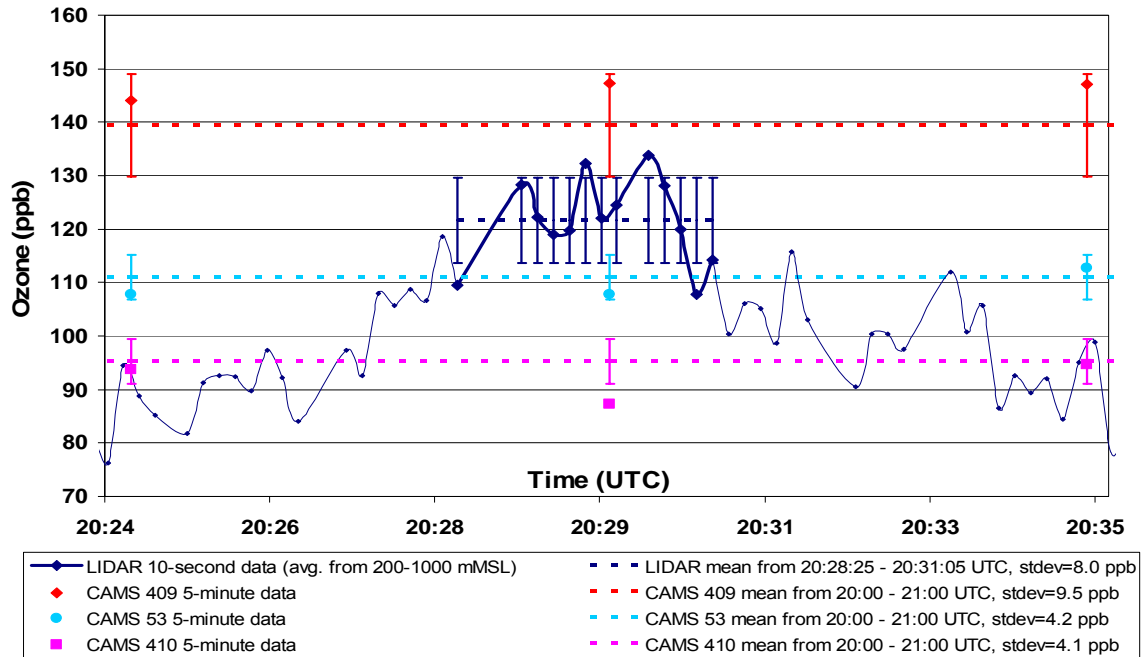


Figure E-4. Vertically averaged LIDAR and surface monitor measurements of ozone concentrations (ppb) for a portion of the flight transect from 20:13-20:43 UTC on September 6th, 2000. The mean and one standard deviation of these measurements are shown as the dashed lines and error bars, respectively. These statistics were calculated for thirteen 10-second LIDAR measurements from 20:28:25-20:31:05 UTC, and for thirteen 5-minute measurements recorded by each surface monitor (CAMS 409, 410, and 53) from 20:00-21:00 UTC.

For the data shown in Figure E-4, surface measurements from CAMS 409, 410, and 53 are in reasonable agreement with vertically averaged peak ozone concentrations observed by the LIDAR along this flight transect. As discussed in Section 5.2, the mean value of the 1-hour average concentrations measured by select downwind monitors is used to approximate peak ozone levels transported in urban plumes. Based on the 1-hour average ozone concentrations for CAMS 409, 410, and 53 (shown for each monitor in Figure E-4 as dashed lines), the mean value for this flight transect is approximately 115 ppb and is comparable to the mean of the thirteen selected LIDAR measurements (122 ppb). Furthermore, the selected LIDAR measurements exhibit variations similar to those in 5-minute surface monitor data recorded from 20:00-21:00 UTC. The standard deviations associated with these measurements are represented by the error bars in Figure

E-4 and range from 4.1-9.5 ppb for the surface monitors, which is comparable to the standard deviation of the selected LIDAR data (8.0 ppb).

A similar assessment was performed to compare airborne LIDAR and surface estimates of background ozone concentrations, and to examine the variability in these measurements. The surface monitor that was selected to approximate background ozone levels for this case study is CAMS 610 (circled in blue in Figure E-2). For the flight transect shown in Figure E-3, only three 5-minute measurements were recorded by this monitor during the hour of 20:00-21:00 UTC. Therefore, a second transect was selected downwind of CAMS 610, corresponding to a flight time of 16:57-17:14 UTC (indicated in Figure E-1). The 10-second LIDAR measurements of ozone concentrations for a portion of this transect, vertically averaged from 200-1000 mMSL, along with the 5-minute data recorded by CAMS 610 during this time, are illustrated in Figure E-5.

In order to compare the variations associated with the LIDAR and surface data, thirteen 10-second LIDAR measurements were selected to represent airborne observations of background ozone levels. These vertically averaged LIDAR measurements, collected from 16:57:55-17:00:05 UTC, are emphasized in bold dark blue in Figure E-5. The mean and one standard deviation of the selected LIDAR and CAMS 610 measurements are also shown as the dashed lines and error bars, respectively. While Figure E-5 only shows CAMS 610 data for a period of 20 minutes, the mean and standard deviation statistics associated with these data were calculated based on thirteen 5-minute measurements recorded from 16:55-17:55 UTC.

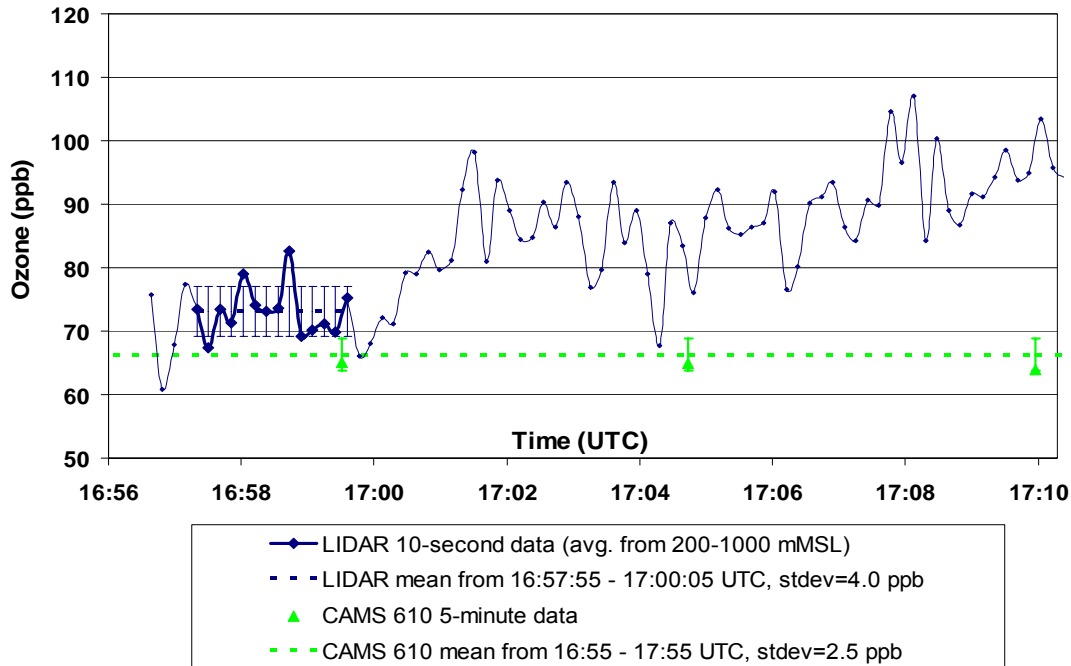


Figure E-5. Vertically averaged LIDAR and CAMS 610 surface measurements of ozone concentrations (ppb) for a portion of the flight transect from 16:57-17:14 UTC on September 6th, 2000. The mean and one standard deviation of these measurements are shown as the dashed lines and error bars, respectively. These statistics were calculated for thirteen 10-second LIDAR measurements (from 16:57:55-17:00:05 UTC) and thirteen 5-minute CAMS 610 measurements (from 16:55-17:55 UTC).

As shown in Figure E-5, the mean of the 5-minute ozone concentrations at CAMS 610 from 16:55-17:55 UTC is approximately 66 ppb. This value is comparable to the mean of the thirteen selected 10-second LIDAR measurements of background ozone, which is approximately 73 ppb. The temporal variations in these measurements are also similar; the standard deviations of the selected LIDAR and CAMS 610 data (represented by the error bars in Figure E-5) are approximately 4 ppb and 2.5 ppb, respectively. Moreover, the 5-minute measurements recorded by CAMS 610 exhibit relatively low variability throughout the afternoon hours on this day, with ozone concentrations ranging from 62-72 ppb from 17:00-23:00 UTC. These surface measurements at CAMS 610 are in good agreement with the LIDAR-derived background ozone level of 69 ppb that was implemented in the ozone flux retrieval for the flight transect shown in Figure E-3.

For the two flight transects examined in this analysis, 5-minute measurements from select surface monitors displayed good overall agreement and comparable temporal variations with 10-second airborne LIDAR measurements of plume background and peak ozone levels in the well-developed PBL. Collectively, the results presented here suggest that surface level observations on September 6th, 2000, were generally representative of the larger mixed layer over distances as far as 100 km to the southwest of Houston.

E.1 REFERENCES

The Capital Area Planning Council (CAPCO), the University of Texas at Austin, and ENVIRON International Corporation (2004), “Development of the September 13-20, 1999 Base Case Photochemical Model for Austin’s Early Action Compact”, Report submitted to the United States Environmental Protection Agency and the Texas Commission on Environmental Quality, September 2004.

National Oceanic and Atmospheric Administration Earth System Research Laboratory website reference,
http://www.esrl.noaa.gov/csd/ors/data_pages/texaqs/air_ozone.html, accessed March 2010.

Senff, C., et al. (2007), “Ozone Production and Flux Downwind of Houston and Dallas”, Presentation given at the TexAQS II Principal Findings Data Analysis Workshop, Austin, TX, May 2007, available at
http://www.tceq.state.tx.us/assets/public/implementation/air/texaqs/workshop/20070529/2007.05.30/Afternoon-1/1-O3_Production+Flux_Downwind-Senff.pdf.

Appendix F: Parameters of Ozone Flux Calculations Based on Data from Surface Monitors

This Appendix includes the parameters that were used to calculate ozone flux in urban plumes transported from DFW and Houston in 2000 and 2006 for the six case study days examined in Chapter 5. These parameters include 1-hour average ozone concentrations and wind speeds measured by surface monitors and predicted by the CAMx photochemical model, along with estimates of horizontal plume width. The methodologies implemented to calculate ozone flux by incorporating data from surface monitors and CAMx were described in Sections 5.2 and 5.4, respectively. The results of these flux calculations are shown in Table 5-5 for surface measurements and in Tables 5-6 and 5-7 for CAMx data.

F.1 ESTIMATES OF BACKGROUND AND DOWNWIND OZONE AND WIND SPEEDS

For each of the six case study days, Figures F-1 through F-6 illustrate the locations of the surface monitors that were selected to represent background and downwind ozone concentrations and wind speeds. These figures also show the NOAA aircraft flight track and contours of ozone concentrations as measured by the LIDAR, vertically averaged from approximately 200-1000 mMSL. Tables F-1 through F-6 list the 1-hour average ozone concentrations and wind speeds measured by the surface monitors (indicated in the figure that corresponds to the same case study day), as well as LIDAR measurements for the flight transect associated with the maximum calculated ozone flux (also indicated in the corresponding figure).

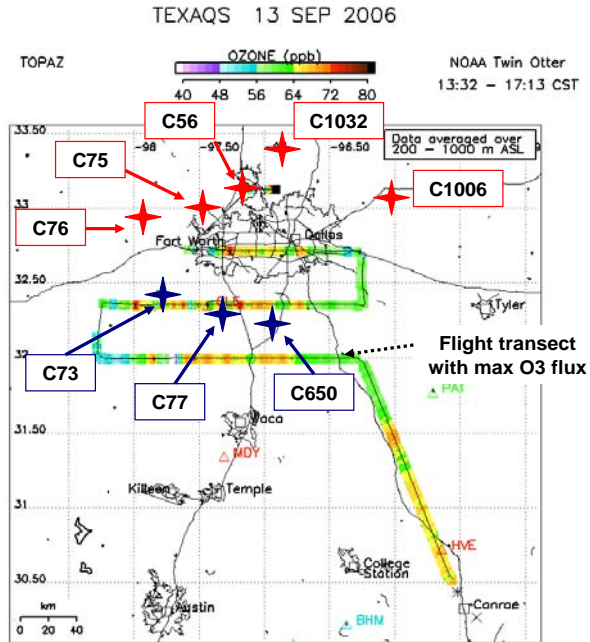


Figure F-1. Ozone concentrations from the NOAA Twin Otter flight downwind of DFW on September 13th, 2006 (Senff et al., 2007). The locations of the upwind and downwind surface monitors used to calculate ozone flux are also shown in red and blue, respectively.

Table F-1. One-hour average wind speeds (m/s) and ozone concentrations (ppb) for surface monitors upwind and downwind of the DFW area for 16:00 CST on September 13th, 2006. LIDAR-based results are also shown for this day for measurements collected along the flight transect indicated in Figure F-1, with data corresponding to a flight time of 15:50-16:30 CST.

	Surface Monitor (CAMS Number)	Surface Monitor Wind Speed (m/s)	Surface Monitor O3 (ppb)	LIDAR/Wind Profiler Estimates
Upwind	C1032	2.8	59	
	C56	2.6	60	
	C1006	2.1	57	
	C75	2.5	62	
	C76	2.4	57	
	Background O3 (ppb)		59	57
Downwind	C73	1.9	65	
	C77	3.5	69	
	C650	3.3	69	
	Elevated Downwind O3 (ppb)		68	75
Average Wind Speed (m/s)		2.7		4.6
O3 Enhancement (ppb)			9	18

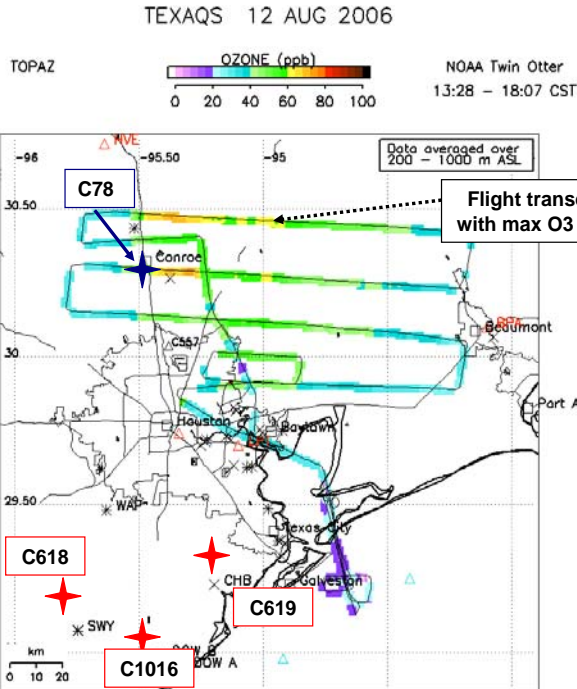


Figure F-2. Ozone concentrations from the NOAA Twin Otter flight downwind of Houston on August 12th, 2006 (Senff et al., 2007). The locations of the upwind and downwind surface monitors used to calculate ozone flux are also shown in red and blue, respectively.

Table F-2. One-hour average wind speeds (m/s) and ozone concentrations (ppb) for surface monitors upwind and downwind of the Houston area for 17:00 CST on August 12th, 2006. LIDAR-based results are also shown for this day for measurements collected along the flight transect indicated in Figure F-2, with data corresponding to a flight time of 16:57-17:34 CST.

	Surface Monitor (CAMS Number)	Surface Monitor Wind Speed (m/s)	Surface Monitor O3 (ppb)	LIDAR/Wind Profiler Estimates
Upwind	C619	4.6	17	
	C618	4.6	16	
	34	6.5	16	
	C1016	3.1	19	
	Background O3 (ppb)		17	29
Downwind	C78	3.8	51	
	Elevated Downwind O3 (ppb)		51	68
Average Wind Speed (m/s)		4.3		7.3
O3 Enhancement (ppb)			34	39

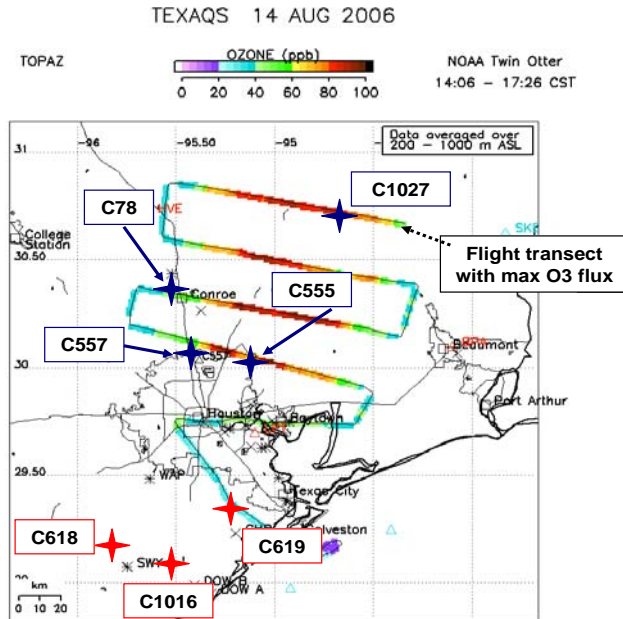


Figure F-3. Ozone concentrations from the NOAA Twin Otter flight downwind of Houston on August 14th, 2006 (Senff et al., 2007). The locations of the upwind and downwind surface monitors used to calculate ozone flux are also shown in red and blue, respectively.

Table F-3. One-hour average wind speeds (m/s) and ozone concentrations (ppb) for surface monitors upwind and downwind of the Houston area for 17:00 CST on August 14th, 2006. LIDAR-based results are also shown for this day for measurements collected along the flight transect indicated in Figure F-3, with data corresponding to a flight time of 16:59-17:26 CST.

	Surface Monitor (CAMS Number)	Surface Monitor Wind Speed (m/s)	Surface Monitor O3 (ppb)	LIDAR/Wind Profiler Estimates
Upwind	C619	4.1	17	
	C618	3.5	15	
	C34	5.1	15	
	C1016	2.8	16	
	Background O3 (ppb)		16	34
Downwind	C78	3.8	67	
	C555	N/A	48	
	C557	N/A	50	
	C1027	2.5	78	
	Elevated Downwind O3 (ppb)		61	89
Average Wind Speed (m/s)		3.5		4.5
O3 Enhancement (ppb)			45	55

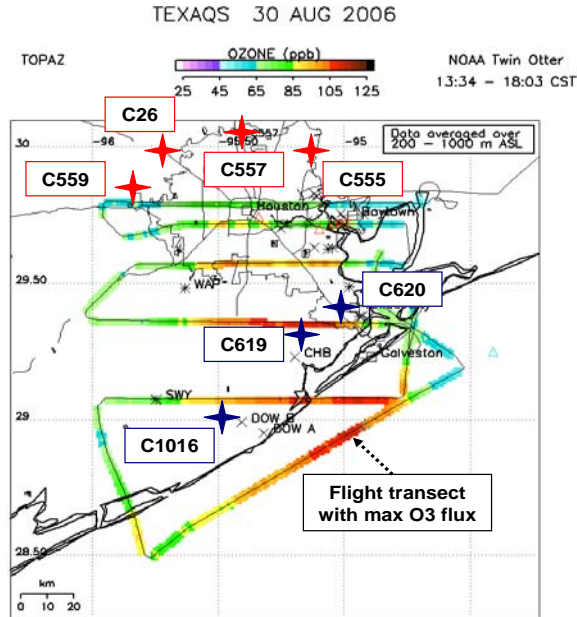


Figure F-4. Ozone concentrations from the NOAA Twin Otter flight downwind of Houston on August 30th, 2006 (Senff et al., 2007). The locations of the upwind and downwind surface monitors used to calculate ozone flux are also shown in red and blue, respectively.

Table F-4. One-hour average wind speeds (m/s) and ozone concentrations (ppb) for surface monitors upwind and downwind of the Houston area for 17:00 CST on August 30th, 2006. LIDAR-based results are also shown for this day for measurements collected along the flight transect indicated in Figure F-4, with data corresponding to a flight time of 17:10-17:43 CST.

	Surface Monitor (CAMS Number)	Surface Monitor Wind Speed (m/s)	Surface Monitor O3 (ppb)	LIDAR/Wind Profiler Estimates
Upwind	C78	3.4	60	
	C26	1.7	59	
	C555	N/A	57	
	C557	N/A	67	
	C559	N/A	62	
	Background Ozone (ppb)		61	59
Downwind	C619	1.6	88	
	C1016	1.5	88	
	C620	2.5	79	
	Elevated Downwind O3 (ppb)		85	111
Average Wind Speed (m/s)		2.2		3.8
O3 Enhancement (ppb)			24	52

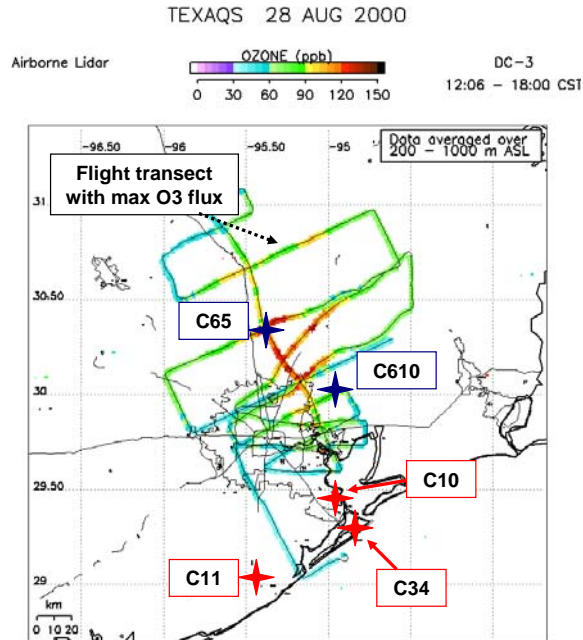


Figure F-5. Ozone concentrations from the NOAA DC-3 flight downwind of Houston on August 28th, 2000 (Senff et al., 2007). The locations of the upwind and downwind surface monitors used to calculate ozone flux are also shown in red and blue, respectively.

Table F-5. Hourly wind speeds (m/s) and ozone concentrations (ppb) for surface monitors and CAMx grid cells corresponding to the locations of these monitors, upwind and downwind of the Houston area for 16:00 CST on August 28th, 2000. LIDAR-based results are also shown for this day for measurements collected along the flight transect indicated in Figure F-5, with data corresponding to a flight time of 16:11-16:40 CST.

	Surface Monitor (CAMS Number)	Surface Monitor Wind Speed (m/s)	Surface Monitor O3 (ppb)	LIDAR/Wind Profiler Estimates	CAMx Surface/Vertically Averaged Wind Speed (m/s)	CAMx Surface/Vertically Averaged O3 (ppb)
Upwind	C11	5.0	20		5.3 / 6.2	32 / 44
	C34	5.5	26		4.7 / 5.1	42 / 45
	C10	4.2	22		5.0 / 4.7	34 / 44
	Background Ozone (ppb)		23	53		36 / 44
Downwind	C26	3.0	66		3.8 / 4.1	83 / 73
	C65	1.9	107		4.0 / 5.1	122 / 107
	Elevated Downwind O3 (ppb)		87	105		102 / 90
Average Wind Speed (m/s)		3.7		4.2	4.5 / 5.0	
O3 Enhancement (ppb)			64	52		66 / 46

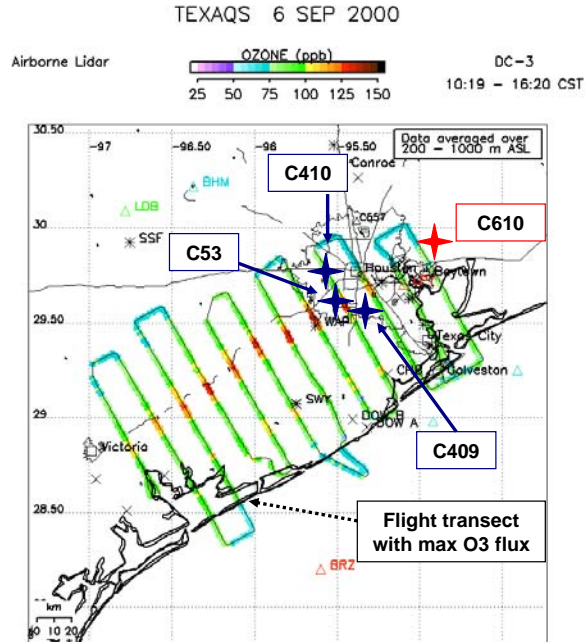


Figure F-6. Ozone concentrations from the NOAA DC-3 flight downwind of Houston on September 6th, 2000 (Senff et al., 2007). The locations of the upwind and downwind surface monitors used to calculate ozone flux are also shown in red and blue, respectively.

Table F-6. Hourly wind speeds (m/s) and ozone concentrations (ppb) for surface monitors and CAMx grid cells corresponding to the locations of these monitors, upwind and downwind of the Houston area for 14:00 CST on September 6th, 2000. LIDAR-based results are also shown for this day for measurements collected along the flight transect indicated in Figure F-6, with data corresponding to a flight time of 14:13-14:43 CST.

	Surface Monitor (CAMs Number)	Surface Monitor Wind Speed (m/s)	Surface Monitor O3 (ppb)	LIDAR/Wind Profiler Estimates	CAMx Surface/Vertically Averaged Wind Speed (m/s)	CAMx Surface/Vertically Averaged O3 (ppb)
Upwind	C610	2.4	71		4.5 / 5.7	73 / 62
	Background Ozone (ppb)		71	69		73 / 62
Downwind	C409	3.0	139		4.6 / 6.0	111 / 92
	C410	3.4	95		5.2 / 6.4	103 / 78
	C53	4.0	111		4.6 / 6.2	78 / 75
	Elevated Downwind O3 (ppb)		115	115		97 / 82
Average Wind Speed (m/s)		2.9		5.2	4.7 / 6.0	
O3 Enhancement (ppb)			44	46		24 / 19

F.2 ESTIMATES OF HORIZONTAL PLUME WIDTH

As described in Section 5.2.3, the plume width was estimated using ozone contour plots of daily maximum 1-hour average ozone concentrations, provided by the University of Houston IMAQS Air Quality Forecast (AQF) model (available at http://www.imaqs.uh.edu/ftp/AQF_usa/). For the case studies in 2006, these contour plots are shown in Figures F-7 through F-10, along with the locations of surface monitors that were selected to approximate the width of the downwind plumes. Table F-7 lists the latitude and longitude of these monitors, as well as the resulting calculated plume width.

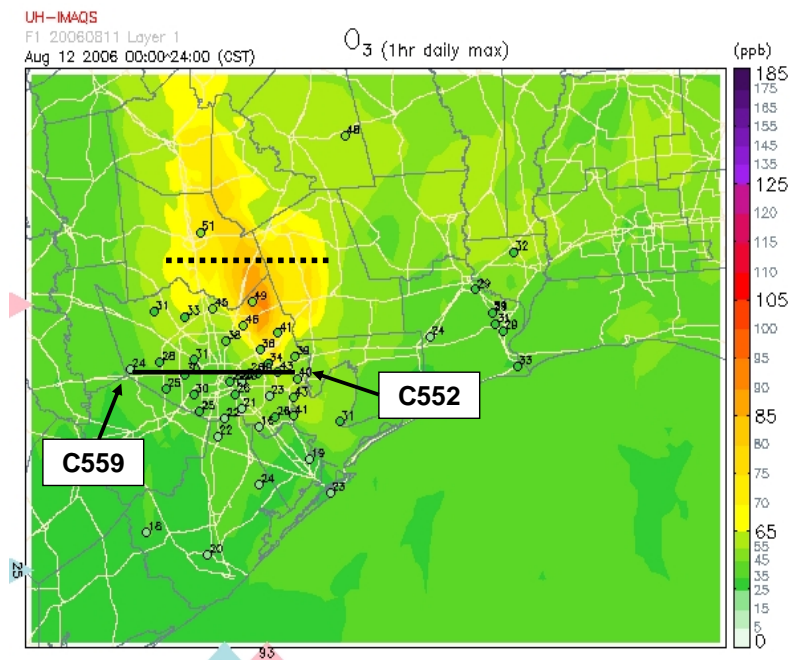


Figure F-7. Air Quality Forecast 1-hour daily maximum ozone concentrations for the Houston-Galveston 4-km modeling domain on August 12th, 2006. The surface monitors used to approximate the width of the plume (C559 and C552) are indicated.

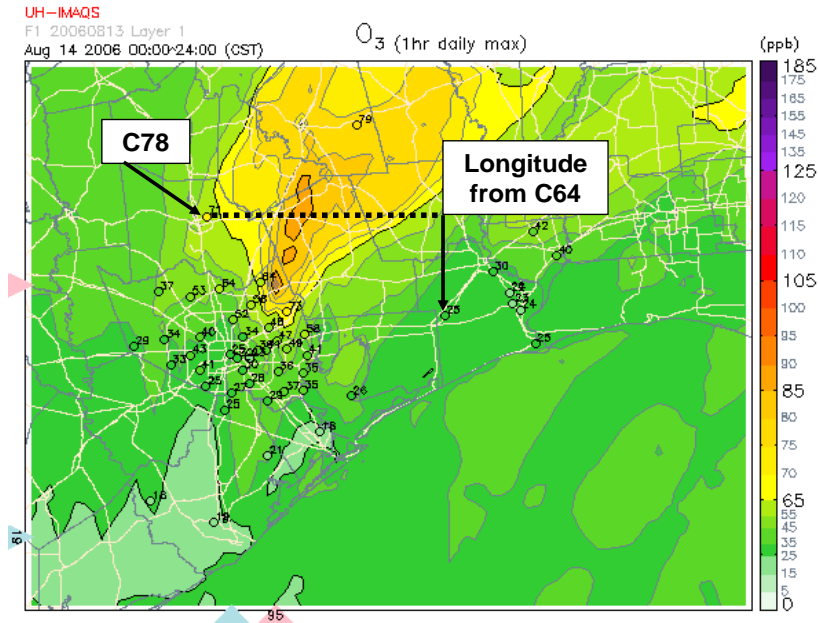


Figure F-8. Air Quality Forecast 1-hour daily maximum ozone concentrations for the Houston-Galveston 4-km modeling domain on August 14th, 2006. The surface monitors used to approximate the width of the plume (C78 and C64) are indicated.

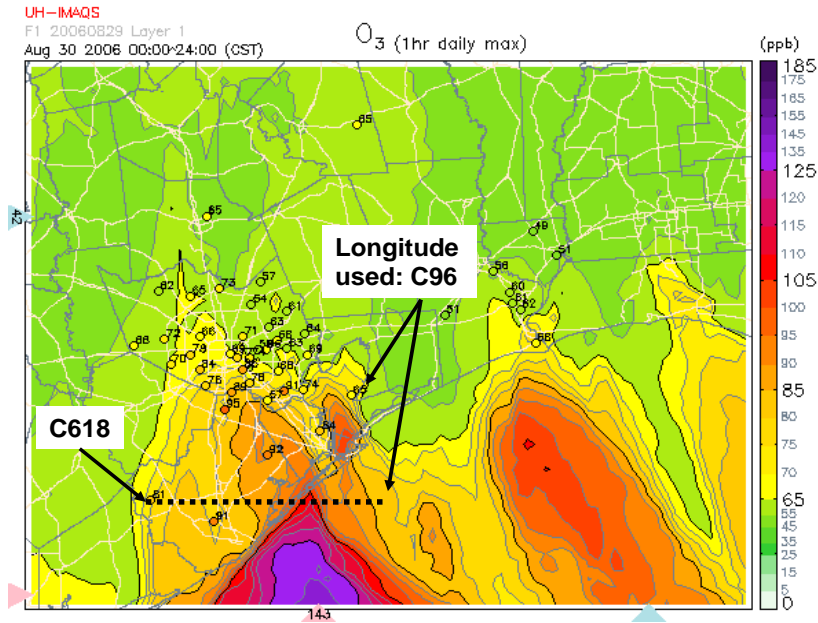


Figure F-9. Air Quality Forecast 1-hour daily maximum ozone concentrations for the Houston-Galveston 4-km modeling domain on August 30th, 2006. The surface monitors used to approximate the width of the plume (C618 and C96) are indicated.

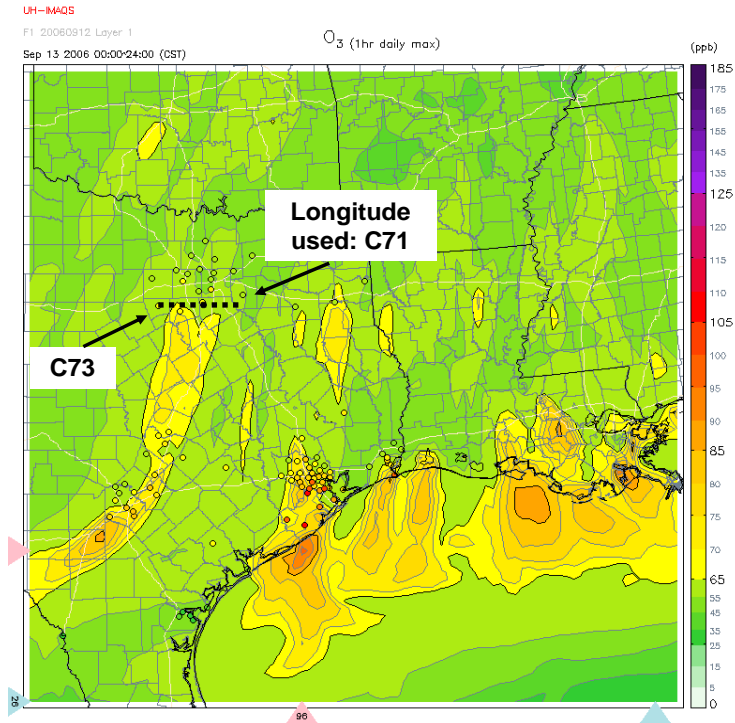


Figure F-10. Air Quality Forecast 1-hour daily maximum ozone concentrations for the East Texas 12-km modeling domain on September 13th, 2006. The surface monitors used to approximate the width of the plume (C73 and C71) are indicated.

Table F-7. Geographical coordinates of surface monitors used to estimate horizontal plume width with the AQF model, as illustrated in Figures F-7 through F-10. Approximations of plume width (in km) are shown for the 2006 case study days, along with LIDAR-derived estimated ranges of plume width (in km).

Urban Region	Date	Monitor #1	Monitor #1 Latitude	Monitor #1 Longitude	Monitor #2	Monitor #2 Latitude	Monitor #2 Longitude	Plume Width (km)	LIDAR Plume Width (km)
Houston	8/12/2006	C559	29.81	-95.81	C552	29.73	-94.99	80	122-133
Houston	8/14/2006	C78	30.35	-95.43	C64	29.86	-94.32	106	97-108
Houston	8/30/2006	C618	29.15	-95.77	C96	29.55	-94.79	95	83-108
Dallas-Ft. Worth	9/13/2006	C73	32.44	-97.80	C71	32.57	-96.32	139	144-162

As discussed in Section 5.2.3, results from the University of Houston AQF model were not available for days in 2000; therefore, the CAMx photochemical model was similarly used to approximate the plume widths on August 28th and September 6th, 2000.

The results of this approximation for September 6th, 2000, were shown in Figure 5-6. Figure F-11 illustrates ozone concentrations that were extracted for surface layer grid cells within the CAMx 4-km modeling domain for 16:00 CST on August 28th, 2000, as well as the NOAA DC-3 flight track for this day. Two grid cells were selected within the 4-km domain that correspond to approximate endpoints of the widest portion of the plume, which is characterized by predicted ozone concentrations above 85 ppb. The locations of these endpoints are indicated in Figure F-11, and the distance between these two grid cells corresponds to an estimated plume width of 72 km. Table F-8 lists the latitude and longitude coordinates for the grid cells selected to estimate plume widths on August 28th and September 6th, 2000, as shown in Figures F-10 and F-11. The range of plume widths estimated by LIDAR measurements along the flight transects for both days is also shown in Table F-8.

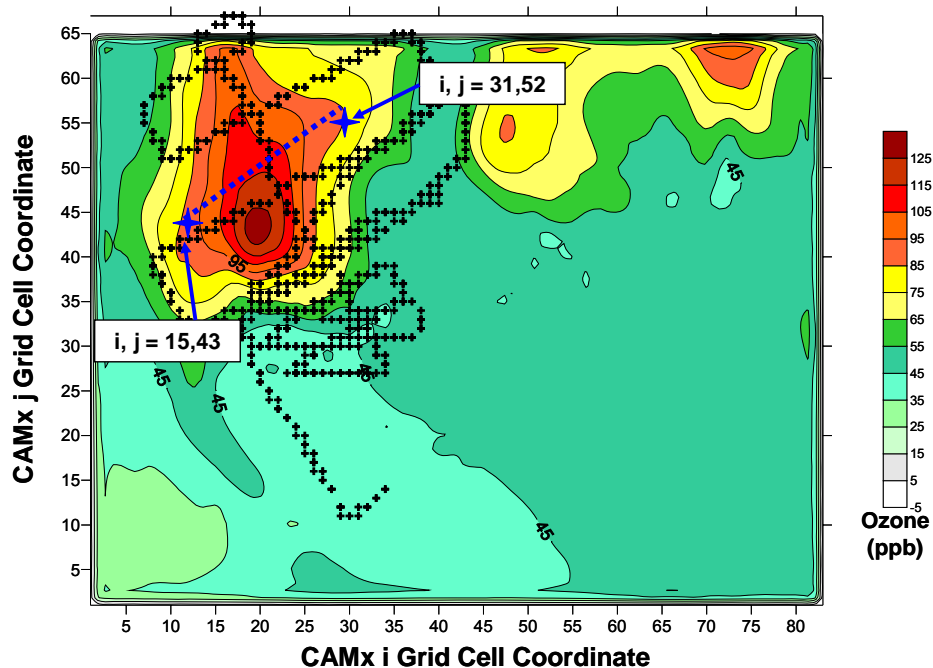


Figure F-11. Contour plot of ozone concentrations predicted by CAMx at 16:00 CST on August 28th, 2000. The x- and y-axes are in units of projected grid cell coordinates (i_j) within the CAMx 4-km modeling domain in the East-West and North-South directions, respectively. The coordinates of two CAMx grid cells that were selected to estimate the horizontal extent of the plume are indicated, and the NOAA DC-3 flight track for this day is also shown.

Table F-8. CAMx surface layer grid cell i and j coordinates, and the corresponding latitude and longitude coordinates, for the grid cells within the 4-km modeling domain that were selected to estimate plume widths on August 28th and September 6th, 2000.

		CAMx i coordinate	CAMx j coordinate	Latitude	Longitude	CAMx Plume Width (km)	LIDAR Plume Width (km)
8/28/2000	Grid Cell #1	15	43	30.25	-95.63	72	43-72
	Grid Cell #2	31	52	30.52	-94.95		
9/6/2000	Grid Cell #1	11	33	29.85	-95.86	85	61-108
	Grid Cell #2	25	13	29.19	-95.41		

F.3 REFERENCES

The University of Houston Institute for Multi-dimensional Air Quality Studies (IMAQS) Air Quality Forecast Model database, available at http://www.imaqs.uh.edu/ftp/AQF_usa/, accessed February 2007.

Bibliography

- Allen, D. T., G. McGaughey, and E. McDonald-Buller (2002), "Development of an Ozone Conceptual Model for Victoria", Final Report for Project UTA02-443, submitted to Capital Area Planning Council and TNRCC, October 2002.
- Allen, D., and J. Olaguer (2004), "State of the Science of Air Quality in Eastern Texas: Major Scientific Findings and Recommendations", Report for the Texas Environmental Research Consortium, July 31, 2004, available at <http://files.harc.edu/Projects/AirQuality/Projects/H030.2004/H30FinalReport.pdf>.
- Allen, D. T., and M.P. Fraser (2006), "An Overview of the Gulf Coast Aerosol Research and Characterization Study: The Houston Fine Particulate Matter Supersite", *Journal of the Air and Waste Management Association*, 56, 456-466.
- Allen, D.T. (2007), "Rural Monitoring for Assessing Ozone Transport into Texas", Final report submitted to the Texas Commission on Environmental Quality, New Technology Research and Development Program, satisfying tasks 1-4 of Grant Contract 582-5-65591-003, February 2007.
- Armistead, R., and R. Dennis (2000), "NARSTO critical review of photochemical models and modeling", *Atmospheric Environment*, 34, 2283-2324.
- Bowman, F.M., and J.H. Seinfeld (1994), "Ozone Productivity of Atmospheric Organics", *Journal of Geophysical Research*, 99, 5309-5324.
- Breitenbach, P. (2003), "Dallas Fort Worth Ozone: Background and Transport Issues", Briefing for Science Coordinating Committee, Texas Commission on Environmental Quality, August 2003.
- Byun, D.W., et al. (2006), "Regional Air Pollution Transport Modeling: CMAQ HDDM Simulations", HARC Project H60 Final Report, August 2006.
- Cracknell, A.P., and H. Ladson (2007), *Introduction to Remote Sensing* (2nd edition), London: Taylor and Francis, [ISBN 0849392551](#), [OCLC 70765252](#).
- Daum, P., J. Meagher, D. Allen, and C. Durrenberger (2002), "Accelerated Science Evaluation of Ozone Formation in the Houston/Galveston Area: Summary", Report to the Texas Natural Resources Conservation Commission, Austin, TX, November 13, 2002, available at <http://www.utexas.edu/research/ceer/texaqsarchive/accelerated.htm>.

- Deuel, H.P., R.E. Looker, and P.D. Guthrie (1997), "A UAM-V based threaded source-apportionment modeling system", Paper presented at the 90th Annual Meeting, Air and Waste Management Association, Toronto, Ontario, Canada, 8-13 June.
- Draxler, R.R. and G.D. Rolph (2003), HYSPLIT (HYbrid Single-Particle Lagrangian Integrated Trajectory), NOAA Air Resources Laboratory, Silver Spring, MD, Model access via the NOAA ARL READY website, available at <http://www.arl.noaa.gov/ready/hysplit4.html>, accessed March 2010.
- Dunker, A.M. (1981), "Efficient calculation of sensitivity coefficients for complex atmospheric models", *Atmospheric Environment*, 15, 1155-1161.
- Dunker, A.M. (1984), "The decoupled direct method for calculating sensitivity coefficients in chemical kinetics", *Journal of Chemical Physics*, 81, 2385.
- Dunker, A.M., G. Yarwood, J.P. Ortmann, and G. Wilson (2002a), "Comparison of source apportionment and source sensitivity of ozone in a three-dimensional air quality model", *Environmental Science & Technology*, 36, 2953-2964.
- Dunker, A.M., G. Yarwood, J.P. Ortmann, and G. Wilson (2002b), "The decoupled direct method for sensitivity analysis in a three-dimensional air quality model: Implementation, accuracy, and efficiency", *Environmental Science & Technology*, 36, 2965-2976.
- ENVIRON International Corporation (2002), "Conceptual Model of Ozone Formation in the Dallas/Fort Worth Ozone Non-Attainment Area", Final report, Novato, CA, October 2002.
- ENVIRON International Corporation (2003), "Development of Base Case Photochemical Modeling to Address 1-Hour and 8-Hour Ozone Attainment in the Dallas/Fort Worth Area", Final report prepared by Mansell, G., G. Yarwood, M. Jimenez, and T. Dinh for the Texas Commission on Environmental Quality, Novato, CA, August 2003.
- ENVIRON International Corporation (2004), User's Guide – Comprehensive Air Quality Model with extensions (CAMx), Version 4.00, Novato, CA, available at <http://www.camx.com>.
- ENVIRON International Corporation (2004), "Dallas-Fort Worth Transport Project", Final report prepared for the Houston Advanced Research Center (HARC), Novato, CA, April 2004.
- ENVIRON International Corporation (2004), User's Guide – Comprehensive Air Quality Model with extensions (CAMx), Version 4.00, Novato, CA, available at <http://www.camx.com>.

- ENVIRON International Corporation (2005), "Dallas/Fort-Worth CAMx Modeling: Improved Model Performance and Transport Assessment", Final report for HARC Project H35 (Phase 2), August 2005, available at http://www.tceq.state.tx.us/assets/public/implementation/air/am/docs/dfw/p1/H35_Phase2_FinalReport_20050831.pdf.
- ENVIRON International Corporation (2006), "Seasonal Model of Northeast Texas Ozone", Final report prepared for the East Texas Council of Governments, Novato, CA, September 2006.
- ENVIRON International Corporation (2009), User's Guide – Comprehensive Air Quality Model with extensions (CAMx), Version 4.5, Novato, CA, available at <http://www.camx.com>.
- ENVIRON International Corporation (2009), "Recent Improvements to the 2005 Ozone Model", Presentation given to the Northeast Texas Air Care (NETAC) Technical Committee, Novato, CA, April 2009, available at http://etcog.sitestreet.com/UserFiles/File/NETAC/pdf/reports/air%20quality/2009/Enclosure_TC3.pdf.
- Gao, D., W.R. Stockwell, and J.B. Milford (1995), "First-order sensitivity and uncertainty analysis for a regional-scale gas-phase chemical kinetic mechanism", *Journal of Geophysical Research*, 100, 23, 153-23, 166.
- Golden Software, Surfer product description, available at <http://www.goldensoftware.com/products/surfer/surfer.shtml>, accessed March 2010.
- Hakami, A., M.T. Odman., and A.G. Russell (2003), "High-order, direct sensitivity analysis of multidimensional air quality models", *Environmental Science & Technology*, 37, 2442-2452.
- Hakami, A., M.T. Odman, and A.G. Russell (2004), "Nonlinearity in atmospheric response: A direct sensitivity analysis approach", *Journal of Geophysical Research*, 109, D15303.
- Kemball-Cook, S., D. Parrish, T. Ryerson, U. Nopmongcol, J. Johnson, E. Tai, and G. Yarwood (2009), "Contributions of regional transport and local sources to ozone exceedances in Houston and Dallas: Comparison of results from a photochemical grid model to aircraft and surface measurements", *Journal of Geophysical Research*, 114, D00F02, doi: 10.1029/2008JD010248.
- Lawson, D.R., N.F. Robinson, S. Diaz, J.G. Watson, E.M. Fujita, and P.T. Roberts (1995), "Coastal Oxidant Assessment for Southeast Texas (COAST) Project", Final Report submitted to the Texas Natural Resource Conservation Commission, August 1995.

- Leone, J. A., and J. H. Seinfeld (1984), "Analysis of the characteristics of complex chemical reaction mechanisms: application to photochemical smog chemistry", *Environmental Science & Technology*, 18, 280–287, 1984.
- McDonald-Buller, E.C., A.A. Eusebi, Y. Kimura, M.M. Russell, and D.T. Allen (2000), "Impacts of Regional Control Strategies on Air Quality in Eastern and Central Texas: Zeroing Out Emissions in Each of the Non-Attainment and Near Non-Attainment Regions", Report submitted to the Texas Natural Resource Conservation Commission, January 2000.
- McGaughey, G., E. McDonald-Buller, and D.T. Allen (2002), "Development of an Ozone Conceptual Model for the Austin Area", Report submitted to the Capital Area Planning Council, and the Texas Natural Resource Conservation Commission, September 2002.
- McGaughey G., C. Durrenberger, E.C. McDonald-Buller, and D.T. Allen (2005), "Assessing the Performance of the CAMx Photochemical Model: A Qualitative Comparison of Observed and Simulated Ozone Plumes on September 6, 2000 within the 4-km HGA Grid Domain", Report prepared for the City of Victoria, The University of Texas at Austin Center for Energy and Environmental Resources, Austin, TX, April 2005.
- McGaughey, G., C. Durrenberger, E.C. McDonald-Buller, and D.T. Allen (2006), "Back-Trajectory Analyses on High and Low Ozone Days for the Dallas/Fort Worth and Houston/Galveston/Brazoria Ozone Nonattainment Areas for the Years 2001 through 2005", Report prepared for the TCEQ NTRD program, October 2006.
- McGaughey, G., C. Durrenberger, E.C. McDonald-Buller, and D.T. Allen (2006), "Monthly Back-Trajectory Analyses on High and Low Ozone Days for the Texas Near Nonattainment Areas for the Years 2001 through 2005", Report prepared for the City of Victoria, August 2006.
- McGaughey, G. (2006), The University of Texas Center for Energy and Environmental Resources ozone animations website reference, available at <http://bosshogg.ces.utexas.edu/animations/ozone.cfm>, accessed February 2010.
- National Oceanic and Atmospheric Administration Earth System Research Laboratory website reference, http://www.esrl.noaa.gov/csd/ors/data_pages/texaq/air_ozone.html, accessed March 2010.

- Neilsen-Gammon, J., J. Tobin, and A. McNeil (2005), "A Conceptual Model for Eight-Hour Ozone Exceedances in Houston Texas: Part I: Background Ozone Levels in East Texas", Final report for Houston Advanced Research Center, Project H-12, January 2005.
- Nielsen-Gammon, J.W., C.L. Powell, M.J. Mahoney, W.M. Angevine, C. Senff, A. White, C. Berkowitz, C. Doran, and K. Knuff (2008), "Multisensor estimation of mixing heights over a coastal city", *Journal of Applied Meteorology and Climatology*, 47, pp. 27-43, January 2008.
- Nobel, C.E., E. C. McDonald-Buller, Y. Kimura, and D.T. Allen (2001), "Accounting for spatial variation of ozone productivity in NO_x emission trading," *Environmental Science and Technology*, 35, 4397-4407.
- Northeast Texas Air Care (NETAC) (2010), "Summary of 2009 NETAC Air Quality Planning Activities", Final Report, March 2010.
- Olague, E., H. Jeffries, G. Yarwood, and J. Pinto (2006), "Attaining the 8-hr Ozone Standard in East Texas: A Tale of Two Cities", *Journal of the Air & Waste Management Association (EM)*, October 2006 Issue, 26-30.
- OTCAIR reference, available at <http://www.otcair.org/>, accessed February 2008.
- Rao, V, N. Frank, A. Rush, and F. Dimmick (2002), "Chemical Speciation of PM 2.5 in Urban and Rural Areas", National Air Quality and Emissions Trends Report, Air and Waste Management Association Air Quality Measurements Conference, November 2002.
- Schichtel, B.A., K.A. Gebhart, M.G. Barna, W.C. Malm, D.E. Day, S. Kreidenweis, and J. Collett, Jr. (2004), "Big Bend Regional Aerosol and Visibility Observational (BRAVO) Study Results: Air Quality Data and Source Attribution Analyses Results from the National Park Service/Cooperative Institute for Research in the Atmosphere", Final report prepared by the Cooperative Institute for Research in the Atmosphere, Colorado State University, Ft. Collins, CO, 2004, available at http://vista.cira.colostate.edu/improve/Studies/BRAVO/reports/FinalReport/bravofinalreport_CIRA.htm.
- Seigneur, C., B. Pun, and Y. Zhang (1999), "Review of methods for source apportionment in three-dimensional air quality models for particulate matter", *EPRI Tech. Rep. TR-112070*, Electr. Power Res. Inst., Palo Alto, CA.
- Seinfeld, J.H., and S.N. Pandis (1998), "Atmospheric Chemistry and Physics - from Air Pollution to Climate Change", John Wiley and Sons, New York, NY.

- Senff, C., et al. (2007), "Ozone Production and Flux Downwind of Houston and Dallas", Presentation given at the TexAQS II Principal Findings Data Analysis Workshop, Austin, TX, May 2007, available at http://www.tceq.state.tx.us/assets/public/implementation/air/texaqs/workshop/20070529/2007.05.30/Afternoon-1/1-O3_Production+Flux_Downwind-Senff.pdf.
- Sillman, S. (1995), "The Use of NO_y, H₂O₂, and HNO₃ as Indicators for Ozone – NO_x Hydrocarbon Sensitivity in Urban Locations", *Journal of Geophysical Research*, 100, 14,175-14,188.
- Sullivan, D.W., V.M. Torres, and M.C. Dionisio (2006), "Early Findings from a Regional Ozone and PM_{2.5} Field Study in Texas", Extended abstract #06-A-354-AWMA, submitted to the Air and Waste Management Association.
- Sullivan, D. (2009), "Effects of Meteorology on Pollutant Trends", Final report to the Texas Commission on Environmental Quality, grant activities No. 582-5-86245-FY08-01, The University of Texas at Austin Center for Energy and Environmental Resources, Austin, TX, March 2009.
- Texas Commission on Environmental Quality, LEADS website reference, available at www.tceq.state.tx.us/air/monops, accessed January 2006.
- Texas Commission on Environmental Quality (2007), personal communication, Office of the Chief Engineer.
- Texas Commission on Environmental Quality, website reference for Figures 5-14 and 5-15, available at http://www.tceq.state.tx.us/implementation/air/airmod/data/hgb1_camx_domain.html#layer, accessed February 2008.
- Texas Commission on Environmental Quality website reference for Figure 6-3, available at http://www.tceq.state.tx.us/implementation/air/airmod/data/hgb1_camx_domain.html#layer, accessed February 2008.
- Texas Commission on Environmental Quality (2008), State Implementation Plan website reference, available at <http://www.tceq.state.tx.us/nav/eq/sip.html>, accessed December 2008.
- Texas Commission on Environmental Quality, Monitoring Operations (2008), TexAQS II reference, available at <http://www.tceq.state.tx.us/nav/eq/texaqsII.html>, accessed December 2008.
- Texas Commission on Environmental Quality, Monitoring Operations (2008), Air pollution and meteorological data, available at http://www.tceq.state.tx.us/nav/data/air_met_data.html, accessed December 2008.

Texas Commission on Environmental Quality (2009), “Protocol for Eight-Hour Ozone Modeling of the Houston/Galveston/Brazoria Area”, Revised report prepared by the Air Modeling and Data Analysis Section, July 2009, available at http://www.tceq.state.tx.us/assets/public/implementation/air/am/modeling/hgb8h2/doc/HGB8H2_Protocol_20090715.pdf.

Texas Commission on Environmental Quality (2009), “Houston-Galveston-Brazoria Nonattainment Area Ozone Conceptual Model”, Draft report prepared by the TCEQ Data Analysis Team, May 2009, available at http://www.tceq.state.tx.us/assets/public/implementation/air/am/modeling/hgb8h2/doc/HGB8H2_Conceptual_Model_20090519.pdf.

Texas Commission on Environmental Quality, website reference for hourly data retrievals, available at http://www.tceq.state.tx.us/cgi-bin/compliance/monops/daily_average.pl, accessed March 2010.

Texas Commission on Environmental Quality, photochemical modeling website reference, available at <http://www.tceq.state.tx.us/implementation/air/airmod/overview>, accessed March 2010.

Texas Commission on Environmental Quality, State Implementation Plan website reference, available at <http://www.tceq.state.tx.us/nav/eq/sip.html>, accessed March 2010.

Texas Commission on Environmental Quality, 1999 Dallas-Fort Worth ozone SIP modeling website reference, available at <http://www.tceq.state.tx.us/implementation/air/airmod/data/dfw1.html>, accessed April 2010.

Texas Commission on Environmental Quality, website reference for CAMx simulation performance, available at <http://www.tceq.state.tx.us/implementation/air/airmod/data/hgb8h2/hgb8h2.html>, accessed March 2010.

Texas Commission on Environmental Quality, website reference for Figure C-11, available at <http://www.tceq.state.tx.us/assets/public/compliance/monops/graphics/clickable/region04.gif>, accessed April 2010.

- Texas Commission on Environmental Quality, website reference for Figure C-12, available at http://www.tceq.state.tx.us/assets/public/compliance/monops/graphics/clickable/regio_n11.gif, accessed April 2010.
- The Capital Area Planning Council (CAPCO), the University of Texas at Austin, and ENVIRON International Corporation (2004), “Development of the September 13-20, 1999 Base Case Photochemical Model for Austin’s Early Action Compact”, Submitted to the United States Environmental Protection Agency and the Texas Commission on Environmental Quality, September 2004.
- The University of Houston Institute for Multi-dimensional Air Quality Studies (IMAQS) Air Quality Forecast Model database, available at http://www.imaqs.uh.edu/ftp/AQF_usa/, accessed February 2007.
- The University of Texas at Austin (2004), “Analysis of the Impacts of Regional Transport on Air Quality in the Austin and Victoria Areas using Anthropogenic Precursor Culpability Assessment (APCA) Tool with the September 13-20, 1999 CAMx Photochemical Modeling Episode”, The University of Texas at Austin Center for Energy and Environmental Resources Austin, TX, October 2004.
- The University of Texas at Austin (2004), “Development of an Ozone Conceptual Model for Victoria”, Report prepared by The University of Texas at Austin Center for Energy and Environmental Resources, Austin, TX, June 2004.
- U.S. Environmental Protection Agency (1999), “Draft Guidance on the Use of Models and Other Analyses in Attainment Demonstrations for the 8-hour Ozone NAAQS”, EPA 454/R-99-004, U.S. Environmental Protection Agency, Research Triangle Park, NC.
- U.S. Environmental Protection Agency, OTAG website reference, available at <http://www.epa.gov/ttnnaqs/ozone/rto/otag/faq.html>, accessed February 2008.
- U.S. Environmental Protection Agency, AIRNow website reference, available at www.airnow.gov, accessed December 2008.
- U.S. Environmental Protection Agency, website reference for Figures 1-1 and 1-2, available at <http://www.epa.gov/ozonepollution/actions.html>, accessed March 2010.
- U.S. Environmental Protection Agency, NAAQS and Air Quality System website reference, available at <http://www.epa.gov/ttn/airs/airsaqs/>, accessed March 2010.

- Webb, A.M., C. Durrenberger, E.C. McDonald-Buller, and D.T. Allen (2002), "Texas Non-Attainment and Near Non-Attainment Zero-Out Modeling Runs for the July 7-12, 1995 episode", Report submitted to the Capital Area Planning Council and the Texas Natural Resource Conservation Commission, The University of Texas at Austin Center for Energy and Environmental Resources, Austin, TX, August 2002.
- Webb, A.M., C. Durrenberger, G. McGaughey, D.T. Allen, and E.C. McDonald-Buller (2007), "Comparison of Source Apportionment and Source Sensitivity Approaches for an Air Quality Analysis in Central and Southeast Texas", The University of Texas at Austin Center for Energy and Environmental Resources, Austin, TX, 2007.
- Wilczak J., I. Djalalova, S. McKeen, and L. Bianco (2007), "Evaluation of NMM-CMAQ and WRF-Chem during High Ozone Episodes in TexAQS-II", Presentation given at the TexAQS II Principal Findings Data Analysis Workshop, Austin, TX, May 2007, available at <http://www.tceq.state.tx.us/assets/public/implementation/air/texaqs/workshop/20070529/2007.05.31/Afternoon/2-NMM-CMAQ+WRF-Chem-Wilczak.pdf>.
- Woodrow, P. (2000), "Building Consensus among Multiple Parties: The Experience of the Grand Canyon Visibility Transport Commission", Final report prepared by CDR Associates, Boulder, Colorado.
- Yang, Y.J., J.G. Wilkinson, and A.G. Russell (1997), "Fast, direct sensitivity analysis of multidimensional photochemical models", *Environmental Science & Technology*, 31, 2859-2868.
- Yarwood, G., G. Wilson, R.E. Morris, and M.A. Yocke (1997), "User's guide to the ozone tool: Ozone source apportionment technology for UAM-IV", Report, S. Coast Air Quality Management District, Diamond Bar, CA.
- Yarwood, G., R.E. Morris, S. Lau, U. Ganesh, and G. Tonnesen (2003), "Guidance on the Application of CAMx Probing Tools", CRC Project A-37-2, Novato, CA.
- Zhang, J., and S. T. Rao (1999), "The role of vertical mixing in the temporal evolution of ground-level ozone concentrations," *Journal of Applied Meteorology*, 38, 12, 1674-1691.
- Zhang, Y., K. Vijayaraghavan, and C. Seigneur (2005), "Evaluation of three probing techniques in a three-dimensional air quality model", *Journal of Geophysical Research*, 110, D02305.

Vita

Mariana Costa Dionisio attended Bartlesville High School in Bartlesville, Oklahoma. In 1999, she entered the University of Oklahoma in Norman, Oklahoma. During her years of undergraduate studies, she was awarded the University of Oklahoma Dean's Scholarship, Minority Engineering Scholarship, Chemical Engineering Award of Excellence Scholarship, and honors such as the Chemical Engineering Sophomore and Senior of the Year in 2001 and 2004, respectively. During the summers of 2000 and 2001, she was employed in Houston, Texas, as an intern at Anadarko Petroleum Corporation and BP Amoco (now BP p.l.c.), respectively. During the summers of 2002 and 2003, she was employed as an intern for ExxonMobil in Houston, Texas. Pertaining to her work as an intern for ExxonMobil, she was awarded a scholarship from the International School of Hydrocarbon Study in 2002. She received the degree of Bachelor of Chemical Engineering with Biotechnology Option from the University of Oklahoma in May, 2004, with special distinction. In August, 2004, she entered the Ph.D program in the Graduate School at the University of Texas at Austin. She received an award honoring her work in 2009 from the Air and Waste Management Association 102nd Annual Conference & Exhibition (First Place Ph.D Platform Paper, 2009).

Permanent Email Address: mariana@che.utexas.edu

This dissertation was typed by the author.